Liquid-Vapour Phase Change and Multiphase Flow Heat Transfer in Single Micro-Channels Using Pure Liquids and Nano-Fluids

Yuan Wang

A thesis submitted for the degree of Doctor of Philosophy
The University of Edinburgh
October 2011

Declaration

I declare that this thesis has been composed by myself and is all my own work except where otherwise stated. This thesis has not been submitted for any other degree or professional qualification except as specified.

Yuan Wang
October 2011

Acknowledgments

I gratefully acknowledge the financial support of the UK Engineering and Physical Sciences Research Council and the China Scholarship Council.

I would like to thank my supervisor Dr. Khellil Sefiane for guiding and supervising my work. Dr. Khellil Sefiane has provided his expert advice and encouragement which lead me through my PhD. He also enlightens me about the importance of contribution to science and society. It has been a great pleasure working with him.

Many thanks to Professor Anthony J. Walton and the Scottish Microelectronics Centre (SMC) staff at Edinburgh for the design and fabrication of Tantalum deposits which served for transparent heating.

I am grateful to Professor Souad Harmand in the Université de Valenciennes et du Hainaut-Cambrésis. It has been a pleasure collaborating with her and her group in France. The inverse heat method Matlab program they developed was used in my research.

I would like to express my gratitude to the technicians of mechanical and electronic workshops for their support.

I am thankful to Dr. John Walker who helped conducting the atomic force microscope measurements of the micro-channel surface roughness.

I am also very thankful to my colleagues Dr. Jacqueline Barber, Dr. Christian Hutter, Dr. Dario Bogojevic, Dr. Ross Moffat, Dr. Jovana Radulovic, Danni Orejon, Alexandros Askounis, and other students in the office for their friendship, advice and support.

I thank my parents for their unwavering love. Their encouragement strengthened my faith and confidence. To my brother, you are the one who brings lots of fun to the family and who makes me enjoy English so much. I am also thankful to the friends in Edinburgh and in China who have always been supporting.

Abstract

Heat management in high thermal-density systems such as CPU chips, nuclear reactors and compact heat exchangers is confronting rising challenges due to ever more miniaturized and intensified processes. While searching for heat transfer enhancement, micro-channel flow boiling and the usage of high thermal potential fluids such as nanofluids are found to be efficient heat removal approaches. However, the limited understanding of micro-scale multiphase flows impedes wider applications of these techniques. In this thesis work, liquid-vapour phase change and multiphase flow heat transfer in micro-channels were experimentally investigated. Included are studies on the single phase friction, vapour dynamics, liquid meniscus evaporation, two-phase flow instabilities and heat transfer. An experimental system was built. Rectangular micro-channels with different hydraulic diameters (571 μm, 762 μm and 1454 μm) and cross-sectional aspect ratios were selected. Transparent heating was utilised by coating the micro-channels with a layer of tantalum on the outer surfaces. FC-72, n-pentane, ethanol, and ethanol-based Al_2O_3 nanofluids were used as working fluids. Pressures and temperatures at micro-channel inlet and outlet were acquired. Simultaneous visualisation and thermographic profiles were monitored. Single phase friction of pure liquids and nanofluids mostly showed good agreement with the conventional theory. The discrepancies were associated with hydrodynamic developing flow and the early transition to turbulent flow, but nanoparticle concentration showed minor impact. After boiling incipient, the single vapour bubble growth and flow regimes were investigated, exploring the influences of flow and thermal conditions as well as the micro-channel geometry on vapour dynamics. In addition, liquid meniscus evaporation as the main heat transfer approach at thin liquid films in micro-channels was studied particularly. Nanoparticles largely enhanced meniscus stability. Besides, flow instabilities were analyzed based on the pressure drop and channel surface temperature fluctuations as well as the synchronous visualization results. Moreover, study on flow boiling heat transfer was undertaken, the corresponding heat transfer characteristics were presented and the heat transfer mechanisms were elucidated. Furthermore, ten existing heat transfer correlations were assessed. A modified heat transfer correlation for high aspect ratio micro-channel flow boiling was proposed. The crucial role of liquid property and micro-channel aspect-ratio on flow boiling heat transfer was highlighted.

CONTENTS

LIST OF TABLES

LIST OF FIGURES

NOMENCLATURE

Symbol	Definition	
A	area	[m^2]
A_b	bubble area	[m^2]
A_c	channel cross-sectional area	[m^2]
A_w	channel surface area	[m^2]
C_D	drag coefficient	
Co	confinement number $Co = \left[\frac{\sigma}{g(\rho_L - \rho_v)d_h^2}\right]^{1/2}$	
	or	
	convection number $Co = \left(\frac{1-x}{x}\right)^{0.8} \cdot \left(\frac{\rho_v}{\rho_L}\right)^{0.5}$	
C_p	specific heat capacity	[$J \cdot kg^{-1} \cdot K^{-1}$]
d	diameter	[m]
d_{in}	channel inner depth or channel inner diameter	[m]
d_h	channel hydraulic diameter	[μm]
d_l	thickness of liquid film	[m]
d_{wall}	thickness of channel wall	[m]
E	correlation constant	
F	correlation constant	
F_D	drag force	[N]
F_{HP}	force due to hydrodynamic pressure	[N]
F_P	the force due to liquid-vapour interface pressure difference	[N]
F_S	surface tension force	[N]
f	friction factor	[N]
g	gravitational acceleration	[$kg \cdot m \cdot s^{-2}$]
g_c	gravitational constant	6.673×10^{-11} $m^3 \cdot kg^{-1} \cdot s^{-2}$
G	mass flux	[$kg \cdot m^{-2} \cdot s^{-1}$]
h	heat transfer coefficient	[$W \cdot m^{-2} \cdot K^{-1}$]
h_C	convective heat transfer coefficient	[$W \cdot m^{-2} \cdot K^{-1}$]
H	parallel plates gap	[m]
h_{fg}	latent heat of vaporization	[$J \cdot g^{-1}$]
I	current	[A]
K	loss coefficient	
k	thermal conductivity	[$W \cdot m^{-1} \cdot K^{-1}$]
L	length	[m]
L_b	bubble length	[m]

L_C	characteristic length,	[m]
L_{df}	hydrodynamic developing flow entrance length	[m]
L_{df}^{+}	dimensionless hydrodynamic developing flow entrance length	
l_c	capillary length, $l_c = \sqrt{\frac{\sigma}{g(\rho_L - \rho_v)}}$	[m]
M	molecular weight	
$\dot{m}$	mass flow rate	$kg \cdot s^{-1}$
N	correlation constant	
P	pressure	[Pa]
P_r	reduced pressure	
P_w	wetted perimeter of the channel cross-section	[m]
ΔP_{cd}	hydrodynamic developing flow region pressure	[Pa]
ΔP_{cf}	friction pressure drop in micro-channel	[Pa]
ΔP_f	friction pressure drop in connecting pipe	[Pa]
ΔP_s	sudden expansion and contraction pressure drop	[Pa]
ΔP_{Total}	total measured pressure drop	[Pa]
Po	Poiseuille number	
q	heat flux	$[kW \cdot m^{-2}]$
q_{evp}	bubble evaporation heat flux	$[kW \cdot m^{-2}]$
q_{ONB}	heat flux for onset of nucleation	$[kW \cdot m^{-2}]$
Q	heat	[J]
Q_{evp}	heat used for evaporation	[J]
R	tube radius or vapour bubble radius	[m]
R_b	bubble radius	[m]
R_c	cavity mouth radius	[m]
R_E	equivalent radius	[m]
R_P	surface roughness parameter	[μm]
S	correlation constant or sensitivity matrix in inverse heat method	
T	temperature	[K]
T_W	plate wall temperature	[K]
T_{sat}	liquid saturation temperature	[K]
T_∞	quiescent temperature (fluid temperature far from the surface of the object)	[K]
ΔT_{sup}	wall superheat, T_W - $T_{sat,}$ when $T_W > T_{sat}$	[K]
ΔT_{sub}	inlet subcooling, T_{sat} - $T_{W,}$ when $T_W < T_{sat}$	[K]
t	time	[s]
t_c	bubble growth critical time	[s]
u	velocity	$[m \cdot s^{-1}]$
U	voltage	[V]
V_b	bubble volume	$[mm^3]$

$\dot{V}$	volume flow rate	[ml·min^{-1}]
W_b	bubble width	[mm]
W_{in}	channel inner width	[mm]
X	Martinelli parameter: $X = \left(\frac{1-x}{x}\right)^{0.9} \cdot \left(\frac{\rho_v}{\rho_L}\right)^{0.5} \cdot \left(\frac{\mu_L}{\mu_v}\right)^{0.5}$	
x	glass plate thickness or vapour quality	[mm]
z	stream-wise distance from channel inlet	
z_0	distance required for the liquid to reach saturation temperature when flowing in the micro-channel	

Subscripts

avg	average
b	bubble
c	channel
conv	convective
cor.	correlation calculated
cut-off	cut-off values
eff	effective
envi	environmental
evp	evaporation
exp.	experimental
in or i	input, inlet, inner
L	liquid
local	local
m	mean value
nb	nucleate boiling
nf	nanofluid
out or o	output, outer
pipe	parameter in the connection pipe of the loop
pump	pump provided parameter
rad	radiative
rms	root mean square
s	solid
sat	saturated
sub	subcooled working condition
suf	surface
sup	superheatered working condition
tp	two-phase
v	vapour
w or wall	channel wall parameter

w,in	inner wall	
w,out	outer wall	

Greek symbol

α	channel aspect ratio	
	or thermal diffusivity	$[m^2 \cdot s^{-1}]$
β	thermal expansion coefficient	
ε	emissivity	
μ	dynamic viscosity	[Pa·s]
ρ	density	$[kg \cdot m^{-3}]$
σ	surface tension	$[N \cdot m^{-1}]$
σ	bubble aspect ratio, $\sigma = L_b/W_b$	
λ_c	capillary length	[mm]
δ	boundary layer thickness	
ϕ	heat transfer efficiency	
	or volume fraction of nanoparticles	
ϕ_L^2	two-phase frictional multiplier	
θ	contact angle	°
v	kinematic viscosity	$[m^2 \cdot s^{-1}]$
ω	Stefan-Boltzmann constant	5.6704×10^{-8} $W \cdot m^{-2} \cdot K^{-4}$

Dimensionless parameter

Bi	Biot number	$Bi = \frac{hL}{k}$
Bl	Boiling number	$Bl = \frac{q}{Gh_{fg}}$
Bo	Bond number	$Bo = (\frac{d_h}{l_c})^2$
Eo	Etovos number	$Eo = \frac{g\Delta\rho d^2}{\sigma}$
Fr	Froude number	$Fr = \frac{G^2}{\rho_L^2 g d}$
Ja	Jacob number	$Ja = \frac{\rho_L C_{PL}(T_W - T_{sat})}{\rho_v h_{fg}}$
Pr	Prandtl number	$Pr = \frac{C_p \mu}{k}$
Re	Reynolds number	$Re = \frac{\rho u_L d}{\mu_L}$
We	Weber number	$We = \frac{G^2 d}{\rho\sigma}$

Chapter 1

Introduction

Energy has become the single most important issue facing humanity in the next fifty years following the diminishing availability of fossil fuels and increasing concerns on global warming. Among all the forms of energy used today, over 70% are produced in or through the form of heat. In the principle of thermodynamic cycle or in many industrial systems, heat must be transferred either to add energy to the system or to remove the energy produced by the system. Considering the rapid increase in energy demand worldwide, the heat transfer processes enhancement and the irreversibility (due to the friction and heat losses) reduction, have become increasingly important tasks. Heat removal and management in high heat flux systems such as nuclear fusion, fuel cells, Micro-Electro-Mechanical Systems/Nano-Electro-Mechanical Systems (MEMS/NEMS), and micro chemical reactors present challenges on both spatial and time scales.

Attempts are underway to create miniaturized cooling systems and to make possible the realization of complete Systems-on-a-Chip (SoC), referring to the integration of all components of a computer or other electronic systems into a single chip. Figure 1-1 is a package on package (PoP) system-on-a-chip designed by Apple® (Clark [1]). The Apple® A4 processor contains an ARM Cortes-A8 CPU core paired with a PowerVR SGX 535 graphic processor (GPU) and is built on a Samsung® 45-nanometer (nm) silicon chip ([2]). The high-performance, low-power system-on-a-chip which provides fast running clock rate is one of the key specifications of the popular gadget ipad®. More intensely-integrated chips are expected according to the growing market needs and users requirements.

Figure 1-1. Apple® A4 processor: designed by Apple and manufactured by Samsung on a Samsung's 45-nanometer silicon chip ([2])

Advanced electronic devices that provide SoC capability can potentially generate high heat fluxes which with conventional cooling systems will lead to high chip operating temperatures and accelerated device failure. Therefore, thermal management which can provide high heat dissipation is a major focal point in the development of next

generation electronic systems such as central processor units (CPU). Figure 1-2 gives the projected CPU heat flux each year of the last decade and the corresponding module cooling technology limits (Smith [3]). The exponentially growing chip heat flux exceeds the limit of the conventional cooling methods of single phase convection and heat conduction. During the past decade, the predicted rapid growth of chip heat flux has been verified. Even much higher heat fluxes were reached. For instance, Sung and Mudawar [4] reported a heat dissipation of over 1000 $W \cdot cm^{-2}$.

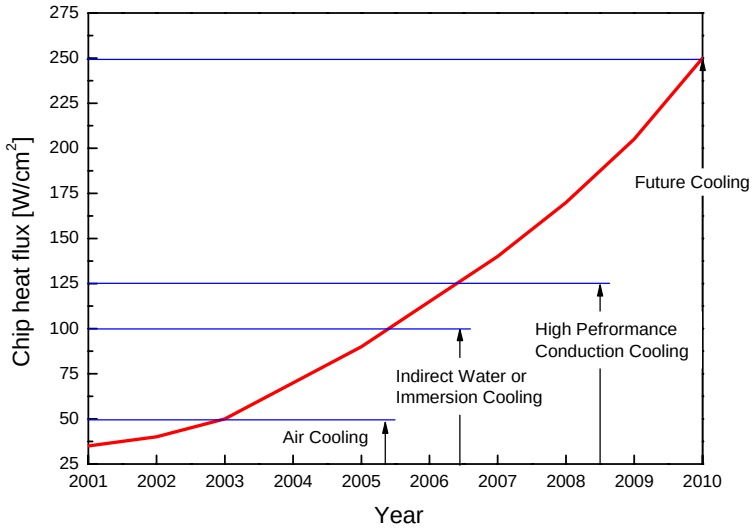

Figure 1-2. Increasing projected chip heat flux and module cooling technology limits (Smith [3])

Many technologies are under development to transport heat within the equipment to allow it to be dissipated into the surroundings via conduction, natural convection, radiation, two-phase change, etc. In recent years, many innovations of modern materials and technologies have increased the thermal conductivity by including additional materials with attractive thermal properties. For example, the thermal conductivity of diamond is the highest among all materials found in nature. It is reported that high-quality single crystals of diamond have a thermal conductivity of 1800 $W \cdot m^{-1} \cdot K^{-1}$ at room temperature and the thermal conductivity for a variety of diamond films on a silicon substrate ranges from 600 $W \cdot m^{-1} \cdot K^{-1}$ to 1200 $W \cdot m^{-1} \cdot K^{-1}$.

The technology and methodology to use for the thermal management of industrial systems are strongly linked to the range of heat transfer coefficient needed to guarantee the efficiency and reliability (life time and degradation) of the devices. The heat transfer coefficient range for the thermal management method is shown in Figure 1-3.

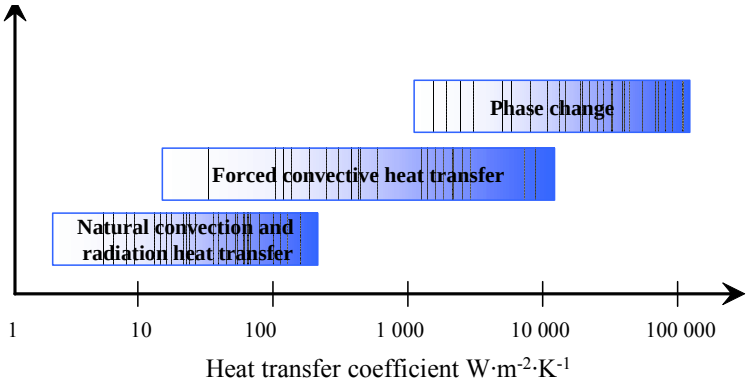

Figure 1-3. Heat transfer coefficients for thermal management methods (moderate temperature)

It has been realized that due to the increased heat generation, the widely used fan cooling method using forced convective by air as the working fluid, is no longer suitable for high heat fluxes greater than 10^5 $W \cdot m^{-2}$ (Kakac *et al.* [5]). Besides, there are problems such as noise, electrical failure, and high power consumption. More effective cooling methods have been developed by making use of the liquid-vapour phase change process.

Boiling as a liquid-vapour phase change process is found to be a potential candidate for heat dissipation. In comparison to those single-phase cooling solutions, boiling provides high heat transfer capacity through the latent heat of vaporization rather than the traditional thermal conductivity. Besides, boiling can maintain the heated surface at a relatively low temperature and avoid system failure. Because of these outstanding performances, boiling is considered promising in the thermal management of some tensely packaged electronic devices and energy conversion systems, such as compact evaporators and heat exchangers.

The direct immersion cooling, named as pool boiling, has been suggested as an alternative to the forced convective air cooling method for the electronics devices. Liquids have advantages of higher thermal conductivity, density, and specific heat over air, ensuring higher heat removal capacity. It is also feasible to maintain a low boiling surface temperature by reducing the saturation pressure of the working liquid. In pool boiling, water is a desirable liquid since it has a high latent heat of vaporization, high thermal conductivity, and is non-toxic and non-flammable. Figure 1-4 gives an example of a pool boiling for electronic components. Pool boiling involves heat transfer from the electronic component to a stagnant pool of liquid, through an intermediate material. As there is an intermediate material it is possible to use water as the working fluid. The

liquid will vaporise, allowing high heat transfer rates to be obtained. The vapour will then come into contact with a further heat sink, give up its latent heat of vaporisation, and the liquid formed will return to the pool by gravity. The maximum heat transfer coefficient for boiling water is 4×10^4 $W\cdot m^{-2}\cdot K^{-1}$. The corresponding maximum heat fluxes are compared with the liquid forced convection heat fluxes in Figure 1-5. Dramatic increase of heat transfer capacity is shown when phase change is involved.

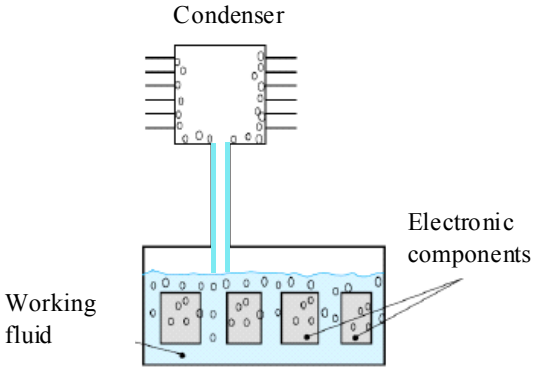

Figure 1-4. Pool boiling (Petit [6])

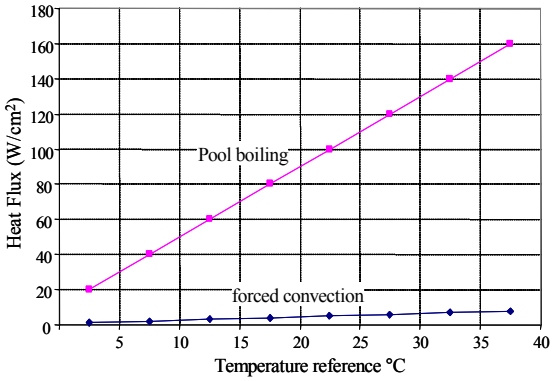

Figure 1-5. Boiling heat fluxes comparison between pool boiling and forced convection (Petit [6])

Another type of boiling is induced during the forced convective flow, namely flow boiling. One of the popular topics is flow boiling in micro-channel heat sinks. Micro-channel heat sink is a component or assembly that transfers heat of the system by using micro-channels as the flow passages. Reducing the channel dimension in cooling system offers appreciable advantages such as high heat transfer coefficient, high compactness and small quantity of working liquid thanks to the high surface-to-volume ratio. There are several classification criteria for the channel, but micro-channels normally have inner diameters in the range 1 μm – 1000 μm. Heat fluxes as high as 3×10^6 $W\cdot m^{-2}$ are obtained

using micro-channels, compared to 2×10^6 $W\cdot m^{-2}$ with mini-channels, the diameters of which are usually 1 mm – 3 mm.

Micro-channel flow boiling involves a liquid coolant being forced through micro-channels underneath an electronic chip or integrated circuit board. Boiling of the fluid maximizes the obtainable heat fluxes. Ideally a closed loop system containing a pump and a condenser would be utilised (Figure 1-6).

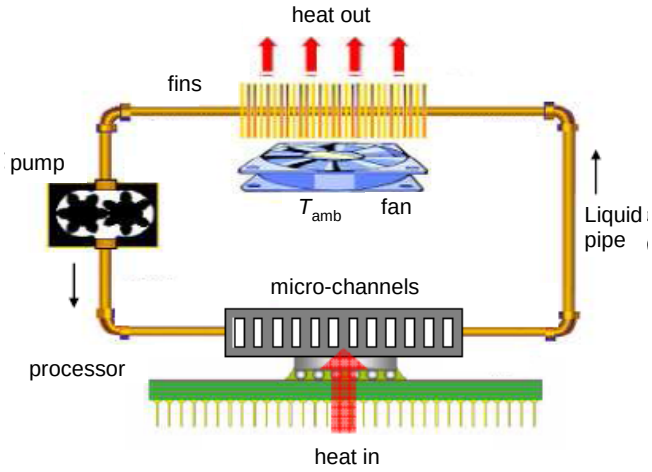

Figure 1-6. Schematic drawing of micro-channel flow boiling equipments (Gillot [7])

Micro-channel heat sinks undergoing two-phase heat transport can provide very high heat transfer rates while maintaining the wall temperature relatively uniform, and have therefore been investigated as an attractive solution for the cooling of high-power electronics. Since the working fluid in the micro-channels may be in direct contact with the electronics, the stringent material requirements prohibit the use of water. Hence the use of dielectric liquids has drawn recent attention for these applications. There are some low-boiling point dielectric fluoro-coolants developed by the 3M™ Fluorinert™ Electronic Liquids such as FC-87, FC-72, FC-84 and FC-77 which have the saturation temperatures of 30°C, 56°C, 80°C and 97°C at atmospheric pressure. The low boiling points of these liquids ensure the moderate device temperatures while permitting the heat discharge to the ambient air stream.

For decades, researchers have been working on various directions related to flow boiling heat transfer, including the onset of boiling, vapour dynamics and flow patterns in the micro-channel system, and the corresponding heat transfer characteristics during the boiling. Experimental parameters such as heat and flow conditions, working liquid, inlet liquid temperature, channel surface roughness and channel geometry are found to be influential on the boiling heat transfer characteristics in micro-channels. Circular

tubes are widely used in macro-scale evaporation, but non-circular channels are more common in micro-scale applications because of the fabrication issues. The boiling in micro-channels with geometries such as triangular, trapezoidal and rectangular have been probed more or less. Even so, a wider channel geometry range is necessary, especially when people found that channels with high aspect ratio[1] cross-section have outstanding advantages such as high area-to-volume ratio, decreased pressure drop and increased heat transfer. Additionally, investigations on flow boiling instabilities have been widely conducted with the awareness of the undesired consequences which are caused by the temperature and pressure oscillations and the occurrence of hot-spots. In order to improve the performances of micro-channel heat sinks, a thorough understanding of the heat transfer mechanisms is necessary. Prediction tools for heat transfer coefficient and the flow instabilities are also of paramount importance.

Apart from the idea of optimising the cooling devices designs, enhancing the heat transfer capacity of the fluid itself is also a method to achieve higher heat dissipation ability. The inherent limitation of liquid thermal conductivity can be largely extended by adding metal and metal oxides particles, the thermal conductivities of which are several orders higher than the liquids (see Figure 1-7).

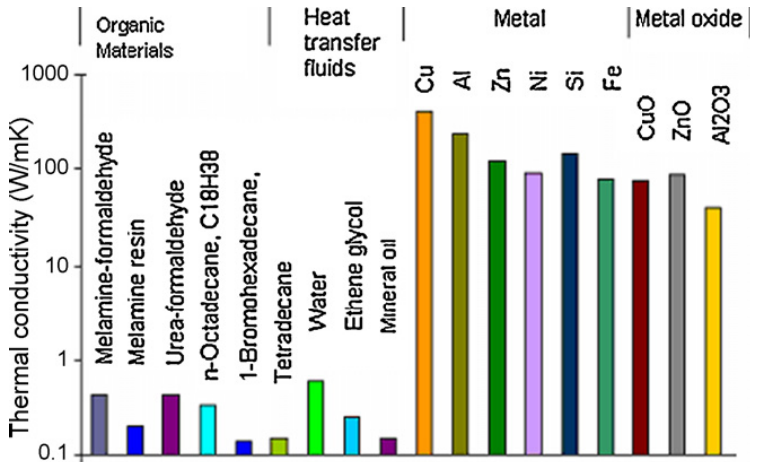

Figure 1-7. Comparison of the thermal conductivity of common liquids, polymers and solids (Wen *et al.* [8])

Actually, the idea of adding particles in liquids can be traced back to more than a century ago when Maxwell [9] formulated a theoretical basis and predicted a high

[1] In the present study, for a channel cross section with a width W_{in} and a depth d_{in}, the channel aspect ratio α is considered to be high when $\frac{\text{MAX}(W_{\text{in}}, d_{\text{in}})}{\text{MIN}(W_{\text{in}}, d_{\text{in}})} \geq 10$ or $\frac{\text{MIN}(W_{\text{in}}, d_{\text{in}})}{\text{MAX}(W_{\text{in}}, d_{\text{in}})} \leq 0.1$.

thermal conductivity of the particle-liquid suspension. However, large scale sedimentation, pipe fouling, erosion and the risen pressure drop stood in the way of the popularity of the particle-liquid suspension technique. Owing to the technological limitations of the particle manufacturing, only micro-scale particles were available and particle dimension could not go smaller than micro-scale. Additional particles started to become prospective when it was feasible to reach nano-scale. Nanofluids can continuously maintain the steady-suspension-state for a long time without experiencing serious sedimentation meanwhile fouling and erosion are substantially reduced. Because of these appealing advantages, nanofluids draw increasing attention of the researchers. Figure 1-8 shows the rapid growth of nanofluids investigations from 1998 to 2008 (Wen *et al.* [8]). Further growth can be expected as the potential nanofluid applications spread. However, the understanding of nanofluids is still far from enough. Fundamental investigations on nanofluids hydrodynamic and thermal performances are of great necessity to enrich the knowledge of this area.

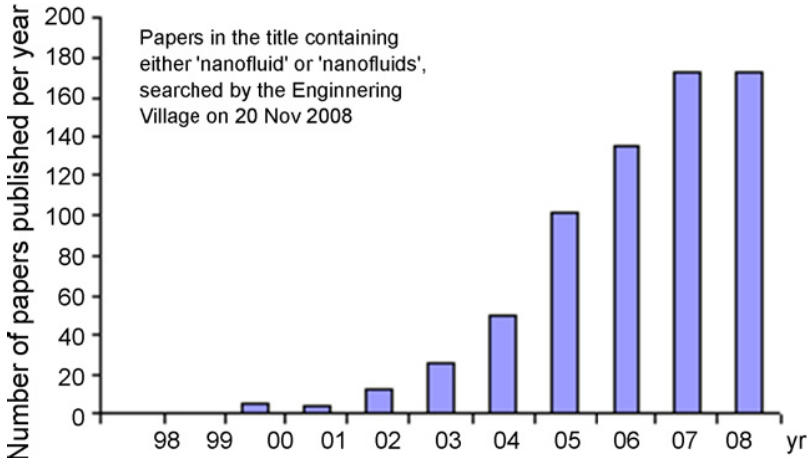

Figure 1-8. Growth of publications by the nanofluids community (Wen *et al.* [8])

In general, micro-channel flow boiling as an effective cooling technique is not quite well understood. Basic experimental studies on this area are required before micro-channel heat sinks can be employed in wider ranges of applications. In particular, abnormal channel geometries such as high aspect ratio cross-section still lack of exploration, the corresponding flow and heat transfer characteristics in which are waiting to be extensively investigated. Besides, the novelty of heat transfer enhancement by using nanofluids should also be highlighted. The huge potential market of nanofluids cooling calls for more concentration on this area. Based on these motivations, the present study takes a fundamental approach on liquid-vapour phase change and flow boiling heat

transfer in micro-channels with pure liquids and nanofluids. The thesis is organized as follows:

- Chapter 1 introduces the research background.
- Chapter 2 reviews the liquid-vapour phase change, flow and heat transfer with pure liquids and nanofluids in micro-channels
- Chapter 3 describes the experimental facilities and data reduction.
- Chapter 4 presents the results of single phase friction factors in the unique micro-channel geometry obtained using pure liquids and nanofluids.
- Chapter 5 concentrates on the liquid-vapour phase change and vapour dynamics, especially single vapour bubble evolution in micro-scale space.
- Chapter 6 examines the meniscus evaporation in vertical high aspect ratio micro-channels using pure liquids and nanofluids.
- Chapter 7 investigates the hydraulic instabilities during flow boiling in single micro-channels using synchronous data acquisition including high speed visualisation, infrared thermography and NI DAQ measurements.
- Chapter 8 discusses the distinctive flow boiling heat transfer characteristics in the high aspect ratio micro-channel geometry and proposed modifiec correlation based on the obtained experimental data..
- Chapter 9 summarizes the general conclusions of this thesis and the future work.

Chapter 2

Overview of liquid-vapour phase change, flow and heat transfer in mini- and micro-channels

2.1. Introduction

Boiling and heat transfer in micro-channels and their applications in micro-system cooling are becoming increasingly important because of the extremely high requirement of heat dissipation capacity in miniaturized and intensified processes. Though phase change and heat transfer have already been utilized in systems such as nuclear reactor cooling systems, heat exchangers, power stations and Micro- Electro-Mechanical Systems /Nano-Electro-Mechanical Systems (MEMS/NEMS), heat management is still confronting demanding challenges in high thermal density devices owing to insufficient knowledge of heat transfer mechanisms at different conditions.

Boiling is known as a liquid-vapour phase changing process in a liquid layer above a heated surface and/or in a superheated liquid layer adjacent to the heated surface. There are mainly two types of boiling which have been widely investigated: flow boiling which is induced in forced convective flow while pool boiling refers to natural convection (Kandlikar *et al.* [10]).

Flow boiling in narrow space such as mini- and micro-channels can be significantly different from the well-established conventional flow boiling heat transfer because of the possible change in the dominant forces such as surface tension force (Thome [11]). The decrease of dimension is experimentally identified to promote heat transfer capacities to some extent. However, the two-phase pressure drop imposes a restriction on the lower limit of cross-sectional dimension of ~50 μm due to limited pumping power. Therefore the optimization of channel dimension for different heat dissipation requirements is becoming increasingly necessary.

For decades, investigators have been working on various directions related to flow boiling heat transfer. There are several exhaustive reviews on single phase and two-phase flow boiling heat transfer in micro-channels which provided a basic idea of the differences between macro-scale and micro-scale, comprehensively summarized the remarkable experimental and numerical outcomes and pointed out the directions of further explorations (*e.g.* Mehendale *et al.* [12], Kandlikar [13], Bergles *et al.* [14], Thome [15], Thome [16], Cheng *et al.* [17]). The present overview mostly concentrates on the experimental investigations on liquid-vapour phase change in mini- and micro-scale space, including the macro- to micro-scale transition, vapour dynamics, flow boiling and heat transfer. In addition, some of the existing heat transfer correlations are

assessed. Besides, the usage of nanofluids as an innovative heat transfer enhancement method is still in an early stage. Some of the experimental studies on nanofluids are also included.

2.2. Macro- to micro-scale transition

Numbers of studies on flow boiling have been conducted within small passages. Evident deviations from macro-scale flow boiling data were pointed out to highlight the presence of macro- to micro-scale transition and the necessity of seeking for a micro-scale threshold.

According to previous investigations, it has been implied that there exists a scale-boundary beyond which the flow and heat transfer would behave differently. Most directly from the visualisation, stratified-wavy flow and fully stratified flow gradually disappeared as the channel diameter decreased (Thome [11]), indicating the diminishing effect of gravity when the channel dimension reduced. Besides, heat transfer characteristics are different in channels with small diameters. Yan and Lin [18] studied flow boiling with R134a in a small pipe (inner diameter d_{in} = 2.0 mm) and reported that the evaporation heat transfer coefficient in small pipe was about 30% – 80% higher than that in larger pipes (hydraulic diameter $d_h \geq 8.0$ mm). Moreover, Owhaib *et al.* [19] investigated the saturated boiling of R134a in vertical circular tubes with internal diameters of 1.7 mm, 1.224 mm and 0.826 mm. They described that the heat transfer coefficient increases as tube diameter decreases. Consoli [20] also showed the similar dependency of heat transfer coefficients of R-245fa on channel diameter. In addition, critical heat flux (CHF) obtained in smaller channels were found to deviate from macro-scale correlations (Qu and Mudawar [21]). The above results reinforced the existence of macro- to micro-scale transition.

So far, several macro- to micro- transition criteria have been proposed. The most direct way of classifying the channels is based on the channel dimension. Some recommended classifications are listed below:

Mehendale *et al.* [12]

conventional channels	$d_h > 6$ mm
macro-channels	1 mm < d_h < 6 mm
meso-channels	100 μm < d_h < 1 mm
micro-channels	1 μm < d_h < 100 μm

Kandlikar and Grande [22]

conventional channels	$d_h \geq 3$ mm
mini-channels	200 μm $\leq d_h <$ 3 mm
micro-channels	10 μm $\leq d_h <$ 200 μm
transitional channels	0.1 μm $< d_h <$ 10 μm
transitional micro-channels	1 μm $< d_h \leq$ 10 μm
transitional nano-channels	0.1 μm $< d_h \leq$ 1 μm
molecular nano-channels	$d_h \leq$ 0.1 μm

The channel diameter was also compared with the bubble nucleation scale. Lin and Pisano [23] defined the micro-channel threshold as the moment when bubble nucleation was suppressed and no bubble could form in the channel. The nucleation radius is defined as:

$$R_{\text{nuc}} = \frac{2\sigma}{\Delta T_{\text{nuc}} (\mathrm{d}P/\mathrm{d}T)_{\text{sat}}} \tag{2-1}$$

where ΔT_{nuc} is nucleation superheat and σ is the liquid surface tension.

Based on pioneering investigations on heat transfer in confined space under different conditions, Suo and Griffith [24] recommended a channel diameter criterion that $\lambda / d \geq 3.3$, where λ is named Laplace constant, defined as:

$$\lambda = \sqrt{\frac{\sigma}{g(\rho_{\text{L}} - \rho_{\text{v}})}} \tag{2-2}$$

Moreover, Kew and Cornwell [25] suggested that the channel could be considered to be in micro-scale when the confinement number Co exceeded 0.5. The confinement number is defined as:

$$Co = \left[\frac{\sigma}{g(\rho_{\text{L}} - \rho_{\text{v}}) d_{\text{h}}^2} \right]^{1/2} \tag{2-3}$$

where g is the gravitational acceleration, d_h is the hydraulic diameter of the channel, σ is the surface tension of the liquid and ρ_L and ρ_v are the liquid and vapour density respectively.

Another criterion was proposed by Brauner and Maron [26] that micro-scale starts when:

$$Eo \le (2\pi)^2 \tag{2-4}$$

where Eo is the Etovos number calculated as $Eo = \frac{g\Delta\rho d^2}{\sigma}$, d is the channel diameter, $\Delta\rho$ is the liquid and vapour density difference.

Others suggested that the macro- to micro-scale transition should be related with bubble departure diameter (Jacobi and Thome [27]). However, the utilised bubble departure diameter correlations were mostly derived from pool boiling. Considering the fact that liquid flow would accelerate the bubble departure, it was realised that using the bubble departure diameter as a criterion in flow boiling will overestimate the transition channel diameter.

Cheng *et al.* [28] proposed a micro-channel classification criterion based on the Bond number, which is given by:

$$Bo = \left(\frac{d_h}{l_c}\right)^2 \tag{2-5}$$

where d_h is the channel hydraulic diameter, l_c is the capillary length defined as:

$$l_c = \sqrt{\frac{\sigma}{g(\rho_L - \rho_v)}} \tag{2-6}$$

Bond number is actually a different statement of the Etovos number. According to Cheng *et al.* [28], channels could be classified as follows: (1) micro-channel (Bo < 0.05, gravity effect can be neglected), (2) mini-channel (0.05 < Bo < 3, surface tension becomes dominant while gravity effect is small), and (3) macro-channel (Bo > 3, surface tension is small compared with the gravitational force).

Recently, Li and Wu [29] defined a non-dimensional number $Bo \times Re_L^{0.5}$ by taking into account of both Bond number and Reynolds number of the liquid. They argued that $Bo \times Re_L^{0.5}$ presents the relative importance of surface tension, body force, viscous force

and inertia force, and $Bo \times Re_L^{0.5}$ = 200 can be set as the conventional-to-micro/mini-channel criterion. The micro/mini-channel phenomena dominated when $Bo \times Re_L^{0.5}$ < 200.

In spite of the attempts to identify the macro- to micro- transition threshold summarized above, a clarified universal criterion is still not well established due to lack of reliable experimental data in various micro-channel geometries. Further experimental investigations on flow boiling heat transfer in some abnormal channel geometries are essential for building a more comprehensive database and deducing a more global macro- to micro- transition criterion.

2.3. Bubble dynamics in mini- and micro-channel flow boiling

Bubble nucleation has been studied for more than five decades (Zuber [30]). Because of the rising need of precise heat transfer models, the investigation on vapour formation and dynamic under flow conditions became more attractive since 1990s. Bubble dynamics are a series of behaviours including bubble nucleation, bubble growth and evolution such as departure, lift-off and release frequency (Dhir [31]). A knowledge of vapour dynamic is crucial for heat transfer modelling, and is also important in applications such as burnout condition prediction in nuclear reactor, boiling enhancement in heat exchangers and power stations as well as the high-powered micro-electronic devices in MEMS (Straub [32], Robinson and Judd [33]).

Existing experimental data in the open literature show the significant discrepancies between bubble dynamics in flow boiling and pool boiling. Kandlikar *et al.* [34] experimentally investigated the bubble growth rate in subcooled flow boiling of water under near atmospheric pressure. Bubbles were nucleated from cavities with known sizes. A narrow rectangular channel (3 mm × 50 mm) was used. Bubble growth rate obtained in flow boiling was compared with pool boiling results. The comparison showed substaintial difference in bubble departure radii and cavity size. The increasing flow velocity activated smaller cavities, and the bubble departure radii were reduced . The time scale for a bubble to grow to a size of 10^{-6} m in pool boiling was ~ 0.1 ms, but in flow boiling it was 100 ms. Additionally, effects of bulk liquid temperature (60°C to 80°C), flow velocity (Reynolds number ranged from 1290 to 5160) and heated surface

temperature (100°C to 120°C) on bubble temporal radius were studied. An increase of growth rate was encountered for increasing flow velocity and wall superheat, and for decreasing subcooling of the bulk liquid.

Zeitoun and Shoukri [35] conducted the experiments on upward flow boiling of water within a narrow annular channel. They made the point that the significant void fraction in subcooled upward flow boiling was the consequence of the increase of bubble size owing to less condensation. Besides, effects of local subcooling and heat flux on bubble mean diameter were found to be similar with Kandlikar *et al.* [34]. Moreover, mass flux influenced the bubble diameter differently before and after the net vapour generation (NVG) point, which was the transition from highly subcooled region to slightly subcooled region.

Nucleation in small space was found to be a highly non-equilibrium process by X.F.Peng *et al.* [36]. They analyzed the thermodynamic of phase transition in micro-channel flows and proposed a new criterion of nucleation, considering thermodynamics and the relation between bubble growth interaction and microchannel geometry. "Evaporating spacing" hypothesis was built on the theory bases of their study, but more experiments were required to support the theoretical conclusions.

Flow direction was also influential on bubble growth and detachment. Thorncroft *et al.* [37] examined the bubble growth and detachment in vertical upward and downward flow in a 12.7 mm inner diameter square duct. The main difference between upward flow and downward flow was that bubble slided in upward flow without lift-off, but in downward flow, bubble lift-off was regularly observed. Accordingly, it was also found that bubble sliding could enhance the heat transfer at the heated surface because the heat transfer coefficient in upward flow was much higher than downward flow. Besides, vapour bubble growth, departure diameter and lift-off diameter were captured at very low subcooling (ΔT_{sub} = 1.0°C to 5.0°C). The relation of the bubble behaviours to Jacob number ($Ja = \frac{\rho_L C_{PL}(T_W - T_{sat})}{\rho_v h_{fg}}$) were described.

Moshe *et al.* [38] reported the bubble nucleation and growth in a viscous Newtonian liquid in a shear flow. They argued that the existence of vacuum was insufficient to trigger the boiling in viscous flow. Instead, a critical shear rate was suggested as the onset of boiling. Besides, bubble growth rate was found increased at higher shear rate and lower pressure. It was believed that the bubble growth was a result of mass transfer rather than hydrostatic pressure change.

In the study of vapour dynamics, more precise visualizations could be achieved by employing more than one camera. Maurus *et al.* [39] studied the bubble and void fraction in subcooled flow boiling of water at low pressure. Two CCD cameras were positioned perpendicular to each other to obtain simultaneous visualization results within a 40 mm × 40 mm rectangular channel. This optical design enabled more accurate measurements of void fraction and bubble distribution. The effects of heat flux and mass flux on bubble population and density, spacing between two bubbles and bubble size distribution have been explored. A model of void fraction was presented as a function of height above the heater. Moreover, heated length of the test section was found to affect the void fraction.

As the dimension of the channel reduced to micro-scale, the bubbles growing in small space sometimes showed distinct behaviours owing to confinement and the increasing predominance of liquid properties.

In addition to the effects of bulk temperature, flow direction, flow velocity and surface temperature summarized above, channel geometry was also influential on bubble dynamic in mini- and micro- channels (Kandlikar [13]). The importance of comparing bubble size with channel size has been emphasized. Subsequently Bond number and Boiling number have been considered as the transition criterion from individual bubble flow to confined bubble flow. The sensitivity of wall temperature on bubble growth rate was also reported. However, bubble departure diameter appeared more dependent on flow velocity than the wall temperature.

G.Hetsroni *et al.* [40] discussed bubble growth in parallel triangular micro-channels with a base of 200 μm to 310 μm and the base angle 55°. Both streamwise and spanwise growths of the bubbles were studied. Bubbles started to move into the exit manifold after occupying 70% of the channel cross section. The moving velocity then experienced a sharp increase in streamwise direction, about three-fold increase during a time interval about 0.003 s. However, the explanation of the rapid expression before filling the entire channel cross-section was not clarified.

Cubaud and Ho [41] used liquid/gas mixture in 200 μm and 525 μm micro-channels. Bubble velocity and slip ratio (defined as the ratio of gas velocity to liquid velocity) were measured. Wettability was highlighted to have a significant effect on flow pattern because of the small channel size.

Lee *et al.* [42] and Li *et al.* [43] published detailed experimental results on bubble dynamics in single and multi- trapezoidal micro-channels (d_h = 41.3 μm). Effects of heat

flux and mass flux on bubble growth rate, initial bubble radius and bubble departure diameter were concluded based on a wide range of test conditions. Bubbles were captured to grow at constant rate except some unusual cases during which the bubble growth was approaching exponential. Moreover, they compared the experimental bubble radii with predictions from Cooper model where the bubble radius was proportional to the square root of time. Deviations indicated the absence of micro-layer underneath the growing bubble. Similar growth trends were found when bubbles grew in the multi-micro-channels. In their study, inertia force was believed to be dominant during linear bubble growth and the exponential growth of vapour slug was considered to be governed by thin liquid film evaporation.

Bubble growth, bubble detachment, lift-off and post lift-off behaviours in micro-channels have also been studied by Situ *et al.* [44], Frank *et al.* [45] and Owhaib *et al.* [46]. Some macro-scale physical laws were found no longer available in micro-scale.

Recently, Agostini *et al.* [47] and Revellin *et al.* [48] experimentally and theoretically studied the elongated bubble confined in micro-channels with hydraulic diameters of 509 μm and 790 μm. The bubble relative velocity to the homogeneous flow was found to be a function of bubble/liquid slug length, and increased with bubble length until a plateau was captured. In the research of Wu *et al.* [49] with a horizontal flat heat exchanger, bubble growth rate was obtained at different inlet fluid velocities but only slight variations were found. The authors also discussed the bubble departure and bubble lift-off behaviours at various flow velocities. Both of the two radii decreased with increasing mean flow velocity. Moreover, Lee and Mudawar [50] reported that high subcooling greatly reduced bubble departure diameter and void fraction.

Duhar *et al.* [51] managed to acquire the n-pentane micro-bubble temporal equivalent radius and centre position within a shear flow in a horizontal channel (1 m long, 8 cm wide, and 1 cm high). Bubble detachment radius increased with Jacob number, but hardly depends on the flow velocity. An expression for temporary bubble radius was proposed as a function of liquid thermal diffusivity and Jacob number, and was proportional to the square root of time. They also presented an equation for bubble detachment radius specifically for small heaters with an overheat temperature up to 20°C.

So far, various results of bubble dynamics were reported but with very limited reliable explanations, especially the explanation on single bubble behaviours in confined space. Bubbles growing in mini- and micro-channels were behaving differently compared with those in conventional structures. However, the majority of existing

studies with regular-shaped micro-channels concentrated more on bubble detachment, lift-off and post lift-off behaviours instead of exploring the single bubble growth, let along single bubble growth in high aspect ratio micro-channels. Micro-channels with high aspect ratio cross-section were previously acknowledged to be able to reduce thermal resistance by Tuckerman and Pease [52], and are becoming attractive thanks to the large surface-to cross-sectional area ratio and reduced vapour side pressure drop as well as an increased vapour side heat transfer (Mokrani *et al.* [53]). Recently, Barber *et al.* [54] discussed confined bubble in high aspect ratio micro-channels. However, limited experimental data are still calling for extensive explorations in high aspect ratio micro-channels.

2.4. Flow boiling in mini- and micro-channels

2.4.1 Flow patterns during two-phase flow boiling

Flow boiling heat transfer and two-phase pressure drop are closely related with the liquid and vapour phase distribution within the micro-channels. In flow boiling, the two-phase flow patterns change along the heated surface due to vapour production. With the aid of high speed photography techniques, it is feasible to visualise the flow patterns during flow boiling. Various types of patterns have been identified by different researchers, but the most widely described were bubbly flow, slug flow, churn flow, annular flow and drop flow in vertical tubes (Figure 2-1 and Figure 2-2) and bubbly flow, plug flow, slug flow, wavy and annular flow in horizontal tubes (Figure 2-3). Due to varying experimental conditions, especially the geometries of the flow passages, several distinctive flow patterns have been mentioned. In horizontal channels, for example, stratified flow disappeared when gravity became negligible compared with surface tension, shear and inertia forces within the flow. Flow patterns were also classified into sub-categories according to detailed observations. In Figure 2-4 (Serizawa *et al.* [55]), transition flow occurred when bubble coalescence took place and vapour slugs existed among bubbles, transforming from bubbly flow to slug flow; coalescence of slugs was noted as liquid ring flow (or throat-annular flow in Saisorn *et al.* [56]) and frothy annular flow with bubbles underneath the large vapour core of annular flow. Besides, Cubaud and Ho [41] named the wedging flow which consisted of slug-droplets and annular-droplets. It should be noticed that the wedging flow was different from the widely

reported Taylor bubble flow (Xu *et al.* [57]); Xu *et al.* [57] observed air/water flow in vertical rectangular channels with variable channel gaps (0.3 mm, 0.6 mm-1.0 mm). The comparison of flow patterns among different sized rectangular channels revealed that in larger channels with a gap of 1.0 mm and 0.6 mm, bubbly flow, slug flow, churn-turbulent flow and annular flows were observed. However, when channel gap was 0.3 mm, flow patterns could be identified as cap-bubbly flow, slug-droplet flow, churn flow and annular-droplet flow. The decrease of channel gap significantly changed the liquid vapour distribution. Moreover, wispy flow was captured at relatively high mass flow rate, during which the entrained droplets attached on the channel wall and formed wisps in the centre of the vapour core (Harirchian and Garimella [58]). In some other studies, bubbly flow was also named as dispersed flow (by Arcanjo *et al.* [59]), while slug flow, elongated bubble flow and churn flow were all classified into intermittent flow.

Two-phase boiling in parallel micro-channels exhibited different flow patterns in different channels as a result of the unevenly distributed mass flux. Megahed and Hassan [60] described that from side channel to centre channel, flow turned from wispy-annular flow to churn flow and then became liquid-vapour slug flow. Therefore more complexities would be expected when generating a flow pattern map for the multi-micro-channel system.

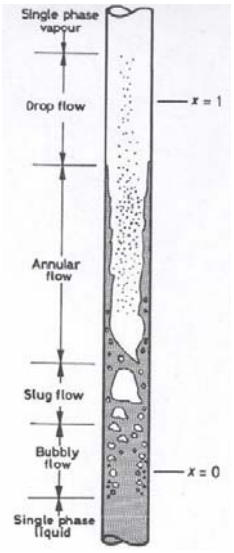

Figure 2-1. Flow patterns in a vertical tube evaporator (Collier [61])

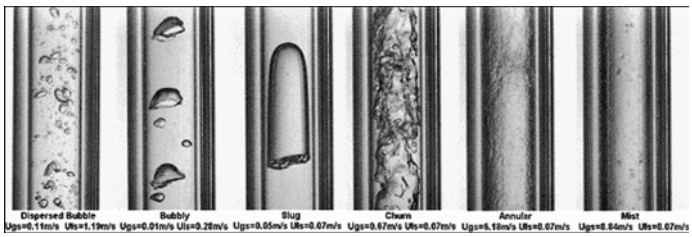

Figure 2-2. Flow patterns observed in vertical tubes with d = 4.26 mm at P = 10 bar, working liquid: R134a (Huo *et al.* [62])

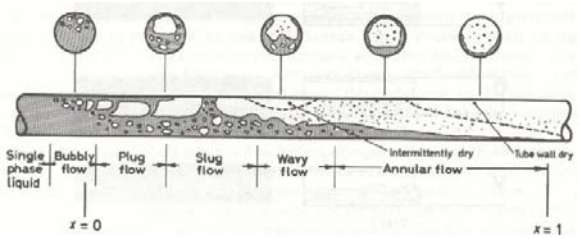

Figure 2-3. Flow patterns in a horizontal tube evaporator (Collier [61])

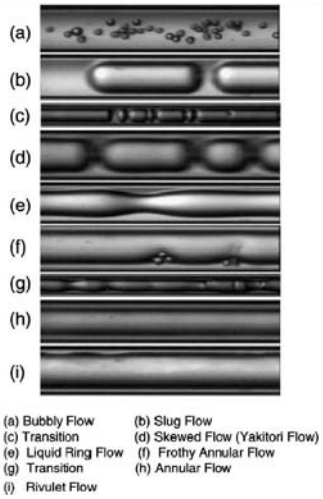

Figure 2-4. Flow patterns observed during air/water flow in horizontal tubes with d = 100 μm (Serizawa *et al.* [55])

Flow pattern transitions have also been discussed. For instance, Xu *et al.* [57] found that the flow regime transition occurs at lower gas flow rate. Ichikawa *et al.* [63] performed the interface motion analysis and proposed a series of driving force variables for microfluidics in rectangular micro-channels. The dimensionless variable of driving force, which was related to the liquid dynamic contact angle with the channel surface enabled the prediction of interface motion for any sized rectangular micro-channels. Huh and Kim [64] used deionized and degassed water and found that flow patterns distributed differently in different locations along the d_h = 100 μm rectangular channel. Observations showed that in the middle of the channel, bubbly and elongated bubbly flow prevailed, but elongated slug flow/annular flow was the main flow regime near the channel exit.

Recently, Kandlikar [65] conducted the scale analysis of different forces on flow pattern transition of water and FC-77. Scale effects of inertia force, surface tension force, shear force, gravity and evaporation momentum forces were discussed, which emphasized the dominance of surface tension and evaporation momentum forces. Encouraging results of flow region transitions were provided. Elongated bubble/slug flow pattern was seen to be prevailing in micro-channels. Besides, the authors also admitted the impacts of channel size and shape on transition criteria and the necessity to modify their flow pattern transition map to accommodate these factors with further experimental data. Furthermore, a comprehensive flow pattern map with quantitative transition criteria was proposed by Harirchian and Garimella [66]. A wide range of experimental parameters (mass flux in the range of 225 $kg \cdot m^{-2} \cdot s^{-1}$ – 1420 $kg \cdot m^{-2} \cdot s^{-1}$ and heat flux in the range of 25 $kW \cdot m^{-2}$ – 380 $kW \cdot m^{-2}$) and channel dimensions (cross-sectional area in the range of 0.009 mm^2 – 2.201 mm^2) were covered. The quantitative transition criteria were described with non-dimensional boiling parameters based on boiling number, Bond number and Reynolds number. However, this criterion was merely developed for FC-77. It could be better generalized and be expanded to other fluids if more well-characterized data were available.

However, for the study on flow pattern, most of these existing results were obtained in circular tubes (Saisorn *et al.* [56], Arcanjo *et al.* [59], In and Jeong [67], Kawahara *et al.* [68], and Celata *et al.* [69]), square channels (Cubaud and Ho [41]) or low aspect ratio rectangular channels (Megahed and Hassan [60], Huh and Kim [64] and Harirchian and Garimella [58]) and trapezoidal channels (Lee *et al.* [42] and Chen and Cheng [70]). Only very limited studies utilised channels with high aspect ratio (Xu *et al.* [57], σ = 40, 20 and 12; Barber *et al.* [54], σ = 10, and Wu *et al.* [71], σ = 9.668). It is imaginable that flow patterns in high aspect ratio micro-channel perform differently. It was also observed that flow turned into annular flow shortly after the onset of nucleate boiling due to the confinement of the narrow channel gap. Therefore, the corresponding hydrodynamic and thermal performances are expected to be distinctive.

2.4.2 Flow instabilities during two-phase flow boiling

The two-phase instability was firstly described by Ledinegg [72]. There were several reviews concerning the two-phase flow instabilities, such as Boure *et al.* [73], Tadrist [74] and Kakac and Bon [75]. The flow instability can be defined as an unstable flow

condition induced by the dynamic interaction between the internal and external systems and has various types or modes with different mechanisms (Kandlikar *et al.* [76]). Flow instabilities are classified into three main categories (see Table 2-1).

Table 2-1. Classification of flow instabilities in boiling channel system (Kandlikar *et al.* [76])

Category	Pattern	Mechanism	Feature
Negative resistance instability	Flow excursion or Ledinegg instability	Negative damping in 1st-order system	Transitional, significant flow maldistribution appears in parallel-channel system
	Pressure drop oscillation	Dynamic interaction between flow excursion and accumulation mechanism of mass and momentum	Relaxation oscillation with large amplitude and long period
Time-delayed feedback instability	Density wave oscillation	Propagation delay of void wave (kinematic wave) and feedback effect provide negative damping	Oscillation, period comparable with residence time, appears in positive resistance region of pressure drop vs. flow rate
Thermal non-equilibrium instability	Geysering Chugging	Insufficient nucleation sites bring about large superheat followed by violent boiling or condensation	Relaxation oscillation if liquid refilling mechanism exists

It is essential to identify flow instability prior to further investigations. Kew and Cornwell [77] suggested the threshold of instability to be when the initial bubble diameter approached the channel hydraulic diameter. Kennedy *et al.* [78] defined the onset of instability according to the pressure drop versus mass flux trend, *i.e.* the demand curve. The relative minimum point of the demand curve was considered as the onset of flow instability. A further criterion was proposed by Celata *et al.* [69] who described the flow as unstable when not only the back and forth movement of bubbles but also reverse flow were observed.

Various types of instabilities and corresponding unstable flow behaviours in micro-scale flows have been published in literature. The tendency that instabilities are more severe in micro-channels than macro-channels could be expected, as individual bubbles are more influential on the local pressures in smaller internal volume (Zhang *et al.* [79]). Flow instabilities were proved to cause pressure drop fluctuations and to deteriorate the heat transfer during flow boiling in uniformly heated micro-channels (Hetsroni *et al.*

[80]). The pressure fluctuation consequently resulted in fluctuating channel wall temperatures.

So far, there is no theoretical criterion to identify stable and unstable boiling. Several stability criteria were proposed in the previous studies based on experimental data with the aid of visualization as well as synchronous pressure and temperature measurements.

Brutin *et al.* [81] suggested a stability diagram in term of heat flux versus mass flow rate (Figure 2-5). The steady state referred to a low pressure drop fluctuation amplitude (< 1 kPa) and no characteristic oscillation frequency; while the unsteady state was defined by a high fluctuation amplitude (> 1 kPa) and a characteristic frequency of a peak amplitude-to-noise amplitude ratio higher than 20.

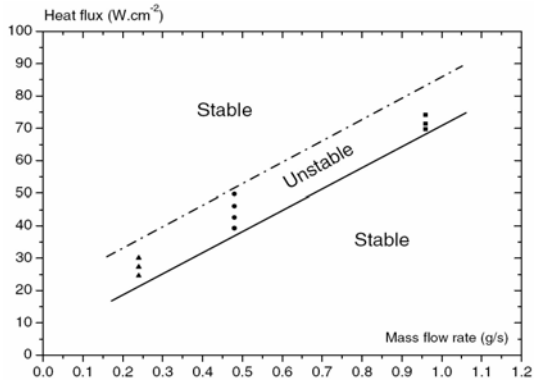

Figure 2-5. Stability diagram of heat flux as a function of mass flow rate in a 0.5 mm ×4 mm ×50 mm mini-channel (Brutin *et al.* [81])

Chang and Pan [82] studied the two-phase flow instability for boiling in a micro-channel heat sink with 15 parallel rectangular channels (d_h = 86.3 μm), the width and depth of which were 99.4 μm and 76.3 μm respectively. They suggested that the amplitude of pressure drop oscillation might be used as an index for the occurrence of reverse flow. They pointed out that reverse flow to inlet chamber would occur when the deviation between the maximum and the minimum pressure drops became larger than 6 kPa. Additionally, the stability map in term of inlet subcooling number versus phase change number showed conspicuous difference from that in an ordinarily sized channel. Only a very narrow region of stable two-phase flow or mild two-phase flow oscillations was near the zero vapour quality line. In an ordinarily sized channel, on the other hand, unstable region occupied the upper right part of the map.

Unstable flow boiling was also classified into two sub-types according to the oscillation period length (Wang *et al.* [83], Figure 2-6 (a) and (b) for single channel and

parallel channels respectively). Based on the visualization results, it was found that the unstable flow boiling with long-period oscillation was induced by the transition from annular flow to mist flow. On the other hand, the unstable flow boiling with short-period oscillation was a result of vapour expansion.

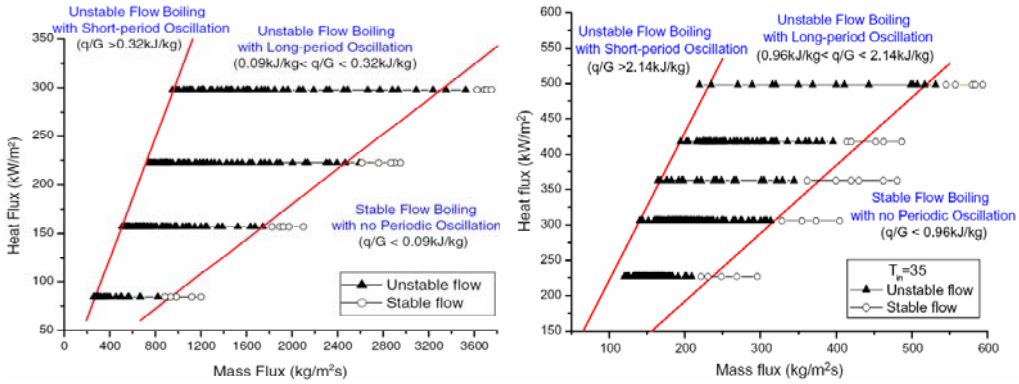

(a) **(b)**

Figure 2-6. (a) Stable and unstable flow boiling regimes in single micro-channel, (b) Stable and unstable flow boiling regimes in parallel micro-channels (Wang *et al.* [83])

Wang and Cheng [84] tested the water boiling in a single trapezoidal channel with a hydraulic diameter of 155 μm. They suggested the exit vapour quality to be the stable and unstable flow regimes criterion. A critical vapour quality of 0.013 was proposed, above which the flow would turn into unstable. This critical exit vapour quality was experimentally obtained and was independent of inlet fluid temperature, heat flux, mass flux, working fluid and the test section geometry. The authors also highlighted that lower mass flux would induce higher channel wall temperature, larger temperature and pressure drop fluctuation amplitudes as well as longer oscillation periods.

Even for unstable flows, the instability behaviours varied from time to time. Balasubramanian and Kandlikar [85] found that the pressure drop magnitude and the dominant frequency of pressure drop fluctuation increase with increasing wall temperature. However, the frequency decreased after the surface temperature became higher than 109°C. On the contrary, different trend of fluctuation frequency was reported by Muwanga *et al.* [86] where decreasing oscillation frequency was found at higher heat flux. Comparisons of the experimental parameters used in these two studies showed the differences in channel dimension and the amount of channels, surface materials and mass fluxes. Further experimental investigations are needed to further explore the dependency of flow instability on applied heat flux.

There are also some other parameters which were found influential to the two-phase flow stability. Effects of inlet conditions on two-phase flow pressure fluctuation amplitude and frequency were discussed by Brutin and Tadrist [87]. Two types of inlet conditions were fabricated. The first corresponded to the constant liquid velocity at the mini-channel entrance which was called the confinement case; the second was to provide a constant velocity at the syringe outlet by connecting a buffer tank between the syringe and mini-channel. The second inlet condition corresponded to the compliant case. For all the inlet Reynolds numbers ($0 < Re < 10{,}000$) and heat fluxes (15.7 $kW \cdot m^{-2}$ – 125.6 $kW \cdot m^{-2}$), the fluctuation amplitude was much smaller in the confinement case, but the oscillation frequencies were higher in the compliant case.

In addition, differences between single channel and parallel channels were evidenced by some researchers.

Ding *et al.* [88] believed that less upstream compressible volume was required in single channel to initiate pressure-drop instability than in parallel channels. Therefore it was easier to detect the flow instability in single micro-channel.

Wang *et al.* [83] conducted the separate flow boiling experiments in eight parallel micro-channels and in a single micro-channel with water. All the channels had the identical trapezoidal cross-section and a hydraulic diameter of 186 μm. They emphasized the much longer temperature fluctuation in single channel than in parallel channels which they believed was a result of the significant flow interaction from neighboring parallel channels.

Singh *et al.* [89] experimentally studied the pressure drop characteristics in parallel trapezoidal micro-channels with a hydraulic diameter of 109 μm over a wide range of heat flux and mass flux. For both single channel and multi-channel conditions, averaged pressure drop increased with increasing heat flux for a constant mass flux. It was noticed that the fluctuations in parallel channels were not as periodic as in single channel. Nevertheless, higher pressure drop was found in parallel channels, reinforcing the explanation that fluctuation was caused by periodic bubble formation and departure.

Moreover, flow instability was found to be affected by other experimental parameters such as surface roughness. Bhide *et al.* [90] compared the two-phase pressure drop and stability in smooth micro-channels with hydraulic diameters of 45 μm, 65 μm and a rough micro-channel with a hydraulic diameter of 70 μm. They concluded that for rougher surface conditions, more nucleation sites induced larger amount of bubbles in two-phase flow. Therefore the transition from nucleate boiling bubbly flow to annular

flow would be completed in a shorter period. Compared with bubbly flow, annular flow was much steadier. Thus the oscillation was largely suppressed.

Recently published investigations revealed some new flow instability characteristics. A fluctuation minimum with increasing heat flux was firstly reported by Singh *et al.* [89]. The pressure fluctuation showed peculiar trends which firstly increased, then dropped to a minimum and kept on increasing as heat flux increased. This was different from previous studies which mostly showed monotonic increase in pressure fluctuation with increasing vapour quality (Hetsroni *et al.* [91] and Muwanga *et al.* [86]). Additionally, the transitions between flow patterns showed different stabilities depending on the heat flux and mass flux (Celata *et al.* [69]). Stable alternation was observed at high or very high heat flux and mass flux conditions while oscillating flow with instabilities were captured at low heat flux and mass flux. Besides, system instability owing to the usage of constant flow pump, a buffer tank, and a constant heating pre-heater should also be considered in micro-channel systems (Lee and Yao [92]).

In addition, the improvement of experimental setups plays an important role in further exploring the flow instabilities. Barber *et al.* [93] managed to obtain simultaneous measurements of channel wall temperature in conjunction with local flow visualization and pressure drop measurements across a high aspect ratio micro-channel with the aid of infrared camera and transparent heating technique. Data acquisition synchronization and noble transparent heating technique are helpful in disclosing the complex internal flow boiling in micro-channels.

2.4.3 Flow boiling heat transfer characteristics in micro-channels

Micro-scale heat transfer has become attractive during the last three decades since the pioneering work of Tuckerman and Pease [52]. Large numbers of studies have been conducted on flow boiling heat transfer in small flow passages. The heat transfer characteristics and corresponding heat transfer mechanisms are the major topics. Besides, further explorations on heat transfer enhancement are also attractive. In this part of literature review, some remarkable experimental studies are summarized in Table 2-2, including the experimental conditions, dominant heat transfer mechanisms and remarks.

Table 2-2. Review of general experimental investigations on boiling heat transfer in small flow passages (horizontal)

author(s) [reference] (year)	channel dimension; hydraulic diameter d_h (mm)	working liquid; mass flux G [kg·m^{-2}·s^{-1}]; heat flux q [kW·m^{-2}]	vapour quality x	pressure; temperature and others	heat transfer mechanism	remarks of heat transfer characteristics
Peng and Wang [94] (1993)	3 parallel, rectangular; (0.6 mm × 0.7 mm); d_h = 0.646	deionized water;		P = 1 atm; T_{sub} = 40°C - 70°C u_L: 1.5 m·s^{-1} - 4.0 m·s^{-1}	nucleate boiling	Temperature overshoot was observed by increasing heat flux; distinct effects of u_L and T_{sub} were found in single phase region but not in the nucleate boiling region.
Tran *et al.* [95] (1996)	single, circular and rectangular; d_h = 2.46 and 2.4	R12; G: 44-832; q: 3.6-129	0-0.94	P_{sat} = 8.25 bar; Bl: 0.0002-0.0016	nucleate boiling	Heat transfer coefficient h increased with q but was independent of G or x; No significant influence of d_h was found.
Bao *et al.* [96] (2000)	single, circular; d_h = 1.95	R11, R123; G: 50-1500; q: 5-200	0-0.9	P_{sat} = 2.94 bar -5.09 bar	nucleate boiling	Heat transfer coefficients were independent of G and x, but were strong functions of q and P_{sat}.
Lin *et al.* [97] (2001)	single, circular; d_h =1.1, 1.8 and 2.8, rectangular (square); d_h = 2	R141b; G:15-3500; q: 1-300	0-1.0	P_{in} = 1.0 bar-3.0 bar; Bl: 0.00022-0.00078	transfer from nucleate boiling to convective boiling	Average h was largely affected by q and x, but slightly increased with G in the convective region; h reached a peak at x = 0.05-0.1, then decreased with increasing x; channel diameter and geometry affected heat transfer after dry-out occurrence; Dryout prone to occur under increased confinement; transform from nucleate boiling to convective boiling happened at higher quality in smaller tubes.
Warrier *et al.* [98] (2002)	5 parallel, rectangular; d_h = 0.75	FC-84; G: 557-1600; q: 0-59.9	0-0.55	T_{in} = 26°C, 40°C and 60°C; Bl: 0.00043-0.00089		For a given heat flux, h decreased with x in low x range, but was independent of x in high quality range.
Yu *et al.* [99] (2002)	single, circular; d_{in} = 2.98	water; G: 50-200	0-1.0	P = 2 bar; T_{in}: up to 80°C	Nucleate boiling was dominant till vapour quality reached 0.5.	Heat transfer was heat-flux-dependent but essentially mass-flux-independent, which was significantly different from the large-sized channels; CHF decreased with decreased mass flux.

(continued)

Qu and Mudawar [100] (2003)	21 parallel, rectangular, (0.231mm× 0.713mm); d_h = 0.349	water; G: 135-402	0-0.2		convective boiling	h decreased with x in all the vapour quality range. Besides, h strongly depended on G, but only weakly relied on q; Note: similar trend was reported by Bhide *et al.* [90], but Bhide *et al*. did not consider forced convection heat transfer to be dominant because of the decreasing trend of h on x. Instead, they emphasized the effects of thermal instabilities.
Yen *et al.* [101] (2003)	single, circular; d_{in} = 0.19, 0.30 and 0.51	HCFC123, FC72; G: 50-300; q: 1-13	0-1.0	P_{system} = 1.10 bar-1.25 bar for 0.51 mm ID and 1.35 bar-1.45 bar for 0.19 mm ID; Bl:~ 0.0006	nucleate boiling with minor convective boiling contribution	Superheat occurred at low Boiling number, indicating a heat flux threshold for nucleation cavity activation. In saturated boiling, h monotonically decreased with increasing x, but was independent of G. Annular flow prevailed in micro-tubes.
Huo *et al.* [62] (2004)	single, circular; d_h = 4.26 and 2.01	R134a; G:100-500; q: 13-150	0-0.9	P_{in} = 8-12 bar	transfer from nucleate boiling to convective boiling	h versus x trends varied with channel sizes. Smaller channel lowered the vapour quality corresponding to the peak h; For larger channel, x = 0.45-0.5, but for the smaller channel, x = 0.2-0.3; dependence of h on x increased with increasing q. Succeedingly, the effect of q diminished, transferring to the convective boiling domination.
Steinke and Kandlikar [102] (2004)	6 parallel, trapezoidal, average dimension: (0.214 mm ×0.2 mm); d_h = 0.204	water; G: 157-1782; q: 5-930	0-1.0	T_{in} = 22°C	nucleate boiling	A heat flux of 930 kW·m^{-2} was achieved with a high heat transfer coefficient of 192 kW·m^{-2}·K^{-1}. Two-phase heat transfer coefficient decreased with increasing vapour quality.
Greco and Vanoli [103] (2005)	single, circular; d_{in}= 6	R410A, R404A; G: 290-1100; q: 11-39	0-1.0	P_{sat} = 3 bar-12 bar	nucleate boiling	Nucleate boiling and liquid convection dominance varied with vapour quality and the flow conditions: for high q and high P_{sat}: nucleate boiling was dominant; For low q and low P_{sat}: convective boiling was dominant. Effect of working liquid changed with P_{sat}: at low P_{sat}, h of R410 was larger than that of R404A, but the difference decreased as P_{sat} was higher.

(continued)

Lee and Mudawar [104] (2005)	53 micro-slots; (0.231 mm ×0.713mm)	R134a; G: 127-654; q: 159-938	0.26-0.87	P_{in}= 1.44 bar-6.60 bar	annular film evaporation in medium to high quality	Bubbly flow and nucleate boiling occurred only at x_e < 0.05 and at very low q. For 0.05 < x_e < 0.55 or 0.55 < x_e < 1.0, annular film evaporation dominated; as x_e increased, slope of h versus x_e reduced from steep to almost zero.
Saitoh *et al.* [105] (2005)	single, circular; d_h = 0.51, 1.12 and 3.1	R134a; G: 150-450; q: 5-39	0-1.0 inlet x = 0-0.2	T_{sat} = 5°C, 10°C and 15°C	Nucleate boiling was dominant in low quality region and forced convective evaporation was dominant in high quality region.	Critical vapour quality (CVQ) was decreased by decreasing channel diameter; In smaller channel, flow approached homogeneous flow and the effect of G decreased, but the effect of T_{sat} became more considerable.
Yun *et al.* [106] (2005)	single, circular; d_h = 0.98 and 2.0	CO_2; G: 500-3570; q: 7-48	0-1.0	T_{sat} = 0, 5°C and 10°C		Heat transfer coefficient before the CVQ was a strong function of q at all G, but G had an impact restrained by Weber number value. CVQ decreased with increasing q, then kept constant for higher q; post-CVQ region showed negligible effect of q and no significant effect of channel diameter on heat transfer. The heat transfer after CVQ was explained by the partially dried liquid film and rate of liquid droplets in the vapour core.
Chen and Garimella [107] (2007)	10 parallel, rectangular, (0.504 mm ×2.5 mm); d_h = 0.839	FC-77; G: 30 ml·min^{-1}-50 ml·min^{-1}; q: 0-240		$P_{channel}$ = 1 atm		Different flow rates resulted in different wall temperatures. For low wall temperature, higher h was achieved at lower flow rate. In fully developed boiling region, T_w weakly depended on q, *i.e.* very small increase of T_w caused rapid increase of q, indicating an appreciable heat dissipating capacity.
Choi *et al.* [108] (2007)	single, circular; d_h = 1.5 and 3.0	CO_2; G: 200-600; q: 20-40	0-1.0	T_{sat} = 10°C	nucleate boiling in low x region	Insignificant effects of G and x were found in low vapour quality region; geometric effects must be considered because laminar flow appeared during flow boiling in small tubes.

(continued)

Díaz and Schmidt [109] (2007)	single, rectangular, (0.3 mm ×12.7 mm); d_h = 0.586	water and ethanol; G: 50-500; q: up to 400	-0.1-0.7	P_{in} = 1.13 bar-2.60 bar	water: nucleate boiling; ethanol: both nucleate and convective boiling	Different heat transfer characteristics in water and ethanol were found: for water, h decreased with x from x = 0; For ethanol, h increased with x in high quality region and low heat flux, h decreased at high heat fluxes.
Huh and Kim [64] (2007)	single, rectangular; d_h = 0.10	water; G: 90, 169, 267; q: 200-500	0-0.4		nucleate boiling	Although nucleate boiling was dominant, the observed flow pattern was similar to the conventional annular flow.
Liu and Garimella [110] (2007)	single, rectangular; channel I: (275 μm ×636 μm); channel II: (406 μm ×1063 μm)	water; G: 221-1283; q: 0-1290	0-0.2	T_{in} = 67°C - 95°C	nucleate boiling	Inlet liquid temperature T_{in} and flow velocity affected ONB, but became less influential afterward; Contribution of convective component was suppressed by boiling heat transfer from fully developed boiling region. Wall temperature T_w near channel exit dropped lower than those at upstream locations due to reduced T_{sat} after saturated boiling.
Agostini *et al.* [111] (a) (2008)	67 parallel, rectangular, (0.223 mm ×0.68 mm); d_h = 0.336	(a). R236fa; G:281-1501;q: 36-2210	(a). 0.02-0.75	(a). P_{sat} = 2.73 bar	(a) nucleate boiling	(a) At low q, low x and low G, h increased with x but independent of q or G; At medium q, h was independent of x and increased with q but weakly changed with G; At very high q, h weakly increased with G but decreased with further increase of q; convective boiling did not exist.
Agostini *et al.* [112] (b) (2008)		(b). R245fa ; G: 281-1501; q: 36-2900	(b). 0-0.78	(b). P_{sat} = 1.41 bar-2.73 bar	(b) nucleate boiling and convective boiling	(b) Heat transfer coefficient h increased with P_{sat} but was independent of T_{sub}; For low q: h increased with x but was independent of q or G; for medium q: h increased with q and slightly increased with G, but was independent of x; while for high q: h decreased with q and x but increased with G.
Bertsch *et al.* [113] (2008)	17 parallel, rectangular; d_h = 1.09	HFC-134a; G: 20.3-81; q: 0-200	0-1.0	P_{sat} = 4.7, 5.5 and 7.5	nucleate boiling	No obvious temperature overshoot was observed in the boiling curves; h increased with q and G, and strongly depended on x. CVQ was around 0.2; The decrease of d_h lowered the CVQ; The effect of P_{sat} was negligible.

(continued)

Lee and Garimella [114] (2008)	parallel micro-channel array, rectangular; (102 μm - 997 μm × 400 μm)	water; G: 46 ml·min^{-1}-126 ml·min^{-1}; q: 10-340	-0.02-0.20	T_{in} = 90.6°C - 95.1°C	transfer from nucleate boiling to convective boiling	No temperature overshoot was observed in the boiling curves measured at five stream-wise locations at a given G and q. Local h increased linearly with q for low to medium q, but for higher q, h became insensitive to q, indicating a transition from nucleate boiling dominance to convective boiling dominance.
Bertsch *et al.* [115] (2009)	17 parallel, rectangular; d_h = 1.09; 33 parallel, rectangular; d_h = 0.54	R134a and R245fa; G: 20-350; q: 0-220	-0.2-0.9	T_{sat} = 8°C - 30°C; P_{sat} = 1.25bar-7.5 bar	nucleate boiling	Heat transfer coefficient h was a strong function of q and x but only slightly changed with G and P_{sat}; smaller channel slightly enahnced heat transfer; Compare with previous study Bertsch *et al.* [113] where CVQ was 0.2, CVQ = 0.5 in the present study, showing that CVQ was higher at higher G.
da Silva Lima *et al.* [116] (2009)	single, circular, copper; d_{in} = 13.84	R134a; G: 300-500; q: 7.5-17.5	0.01-0.99	T_{sat} = 5°C, 15°C and 20°C	nucleate boiling and convective boiling	Newly found that for slug flow, heat transfer was not a simple juxtaposition of nucleate and convective boiling , but that the integration of these two heat transfer mechanisms was also a function of flow parameters such as mass flux and geometrical modifications the flow was suffering. h increased with T_{sat} at low x region.
In and Jeong [67] (2009)	single, circular; d_h = 0.19	R123 and R134a; G: 314,392, 470; q: 10,15,20	0.2-0.85	P_{sat} = 1.58 bar, 2.08 bar for R123 and 9 bar, 11 bar for R134a	transfer from nucleate boiling to convective boiling	Strong effect of G was shown on h versus x trends at low P_{sat}, but increase of G resulted in deterioration of h at high quality region; effect of q was different for the two liquids: for R123: h increased with q, effect of q was more profound for higher x; while for R134a, effect of q was reduced as x increased. The decline of the effect of heat flux was more evident as G was higher.
Kuznetsov and Shamirzaev [117] (2009)	10 parallel, rectangular, (0.64 mm ×2.05 mm); d_h = 0.975	water; G: 17, 51; q: 30-150	0-0.8	$P_{channel}$ = 1atm	nucleate boiling and liquid film evaporation	Negligible effect of G was found. When G was low, liquid film evaporation became dominant. Effect of q decreased as G decreased.
Ong and Thome [118] (2009)	single, circular; d_h = 1.03	R134a, R236fa and R245fa; G: 200-1600; q: 2.3-250	0-1.0	T_{sat} = 31°C	nucleate boiling and convective boiling	Heat transfer coefficient h depended on q, G and x but not on T_{sub}; h increased with x even in annular flow region; significant differences were found in the three liquids due to different surface tensions.

(continued)

Saisorn *et al.* [56] (2010)	single, circular; d_h = 1.75	R134a; G: 200-1000; q: 1-83	0-1.0	P_{sat} = 8 bar - 13 bar		Channel average h_{avg} increased with q till a peak then h_{avg} decreased after partial dry-out occurred; h decreased as P_{sat} was higher but was independent of G and x; Five flow regimes were observed.
Hamdar *et al.* [119] (2010)	single, square; d_h = 1.0	HFC-152a; G: 200-600; q: 10-60	0-1.0	P_{sat} = 6 bar	nucleate boiling	Heat transfer coefficient h was a strong function of q but was independent of x and strictly independent of G; Boiling curves were also independent of G.

The above studies have covered wide ranges of flow and thermal conditions in various channel geometries, the reported heat transfer mechanisms in which can generally represent the current understanding of flow boiling heat transfer in mini- and micro-channels. Among the outcomes, there are some key aspects which are worth emphasizing, such as the effects of working liquids and channel dimension.

Bao *et al.* [96] made the point that the difference in heat transfer coefficients for R-11 and HCFC123 flow boiling in fine passage are not profound under the same condition. However, different conclusions were drawn by Greco and Vanoli [103] that effect of working liquid changes with saturation pressure P_{sat}. They pointed out that at low saturation pressure, heat transfer coefficient of R410 is larger than that of R404A but the difference decreases as P_{sat} gets higher. The authors believed that under lower evaporation pressure, higher convective contribution in R410 was achieved because of the higher liquid conductivity and lower vapour density of R410. As P_{sat} became higher, the higher vapour density as well as a lower surface tension and latent heat of vaporization of R404A were the key reasons for a higher nucleate boiling contribution.

Díaz and Schmidt [109] used water and ethanol as working liquids and reported different heat transfer characteristics. In water flow, heat transfer coefficient decreased with vapour quality from zero while nucleate boiling was dominating. In ethanol flow, however, heat transfer coefficient increased with vapour quality in high vapour quality low heat flux and decreased with vapour quality at high heat flux condition. Both nucleate boiling and convective boiling were said to be dominating. However, the reason of the discrepancies between water and ethanol was not mentioned.

Bertsch *et al.* [115] explained that the higher molecular mass and surface tension of R245fa resulted in the different heat transfer performance from that of R134a.

Ong and Thome [118] also highlighted the difference in fluid surface tension as the major reason of the evidently different heat transfer performances among R134a, R236fa and R245fa.

As discussed in the previous literature, thermophysical properties of the working liquids played an important role in heat transfer. In small scale flow passages, the influence of surface tension became more crucial. Besides, latent heat of vaporisation and liquid viscosity were also substantial. Basically, liquids with greater liquid/vapour density ratio, higher latent heat and larger thermal diffusion coefficients required higher heat flux to initiate nucleation (X.F.Peng *et al.* [36]). After the onset of nucleation, liquids with lower surface tension and lower latent heat of vaporisation prone to induce higher heat transfer coefficients (Greco and Vanoli [103]).

The effect of channel dimension on boiling heat transfer has been focused under the spotlight. Several studies have been conducted in channels with different diameters. Some found no significant effect of d_h (Tran *et al.* [95] and Yun *et al.* [106]), but in most of the studies, channel diameter (inner diameter (ID) for circular tube and hydraulic diameter d_h for rectangular or other non-circular-shaped channels) was reported to be more or less influential.

X.F.Peng *et al.* [36] described dramatically high superheats for liquid nucleation when the micro-channel was sufficiently small. Boiling nucleation was noticed to become sensitive to channel size in micro-scale channels.

Yen *et al.* [101] tested three circular tubes with the ID of 0.19 mm, 0.30 mm and 0.51 mm. They also found the onset superheat, which was the wall superheat before onset of nucleation, increased with decreasing tube diameter because the confined space limited the number of cavity sites. Moreover, the behaviours of heat transfer coefficient versus vapour quality were noticed to be completely different from those in conventional sized channels where heat transfer coefficient h increased with vapour quality x till $x <$ 0.9. The decrease of channel diameter lowered the value of x at which h began to decrease. The similar results were also published by Huo *et al.* [62], Saitoh *et al.* [105] and Bertsch *et al.* [113]. In addition, the decrease of channel hydraulic diameter was pointed out to increase the heat transfer performance of the passage (Bertsch *et al.* [115]).

A number of studies in recent years have also attempted to better understand the flow boiling heat transfer characteristics in micro-channels with different cross-sectional geometries.

Yen *et al.* [120] visually observed the convective boiling in single micro-channel with different cross-sectional shapes. Circular and square cross-sections with similar hydraulic diameters were chosen. It has been observed that in the square channel, both nucleation bubble number and local heat transfer coefficients increased with decreasing vapour quality because the corners of square channel served as nucleation sites. On the other hand, heat transfer coefficients in circular channel were lower. Combining the results presented by Tran *et al.* [95] in circular and rectangular channels, where the heat transfer differences between different-shaped channels were diminished when channel ID was larger, it could be concluded that the effect of channel cross-sectional shape was eliminated in larger channels due to the relatively less important role of channel corners. Meanwhile the larger surface area in larger channels became more influential.

The critical role of channel cross-sectional geometry has been extensively investigated by Harirchian and Garimella [121]. Seven different silicon pieces containing channels with depths ranging from 100 μm to 400 μm and widths ranging from 100 μm to 5850 μm were tested with perfluorinated dielectric fluid FC-77. A critical threshold channel cross-sectional area A_c = 0.089 mm^2 was identified. When $A_c \geq 0.089$ mm^2, h was independent of the micro-channel size. While in small micro-channels where bubble confinement was visible, higher heat transfer coefficient was achieved in low heat flux region (see Figure 2-7) and heat transfer was enhanced by decreasing the channel cross-sectional area. However, channel aspect ratio was not considered as the determining geometric factor which affects boiling heat transfer. Moreover, it was concluded that forced convection and liquid film evaporation were the dominant heat transfer mechanisms in smaller channels.

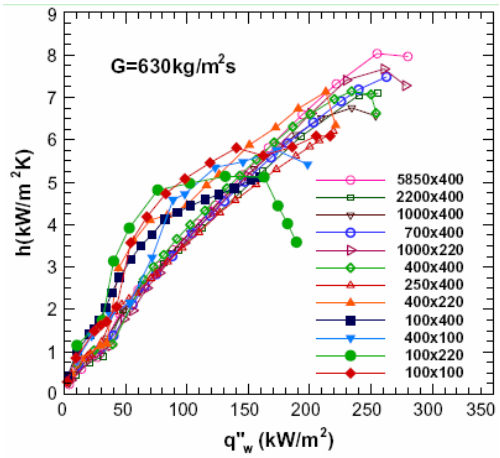

Figure 2-7. Effect of microchannel dimension (μm × μm) on heat transfer coefficients (Harirchian and Garimella [118])

Other aspects such as the channel surface structure treatment on heat transfer also attracted people's attention since 1970s (Oktay and Schmekenbecher [122]). For high-powered electronic components, liquid cooling with direct contact by using dielectric liquids has been considered as a prospective option. However, associated with the high heat removal capacity, the high wall superheat required for boiling onset was expected owing to the high wettability of dielectric liquid (Honda *et al.* [123]). Many studies have been conducted addressing the effect of surface structures on boiling heat transfer. In the study of Honda *et al.* [123], both micro-pin-finned and submicro-scale roughness surfaces provided considerable heat transfer enhancement compared to a smooth chip in the nucleate boiling region. Consequently the surfaces treatment has been widely studied in order to achieve boiling heat transfer enhancement. Surface treatment was also suggested to ease the boiling initiation (Honda and Wei [124]). There were various surface structure develop methods. Figure 2-8 gives some examples of the previously studied surface micro-structures (Honda and Wei [124]).

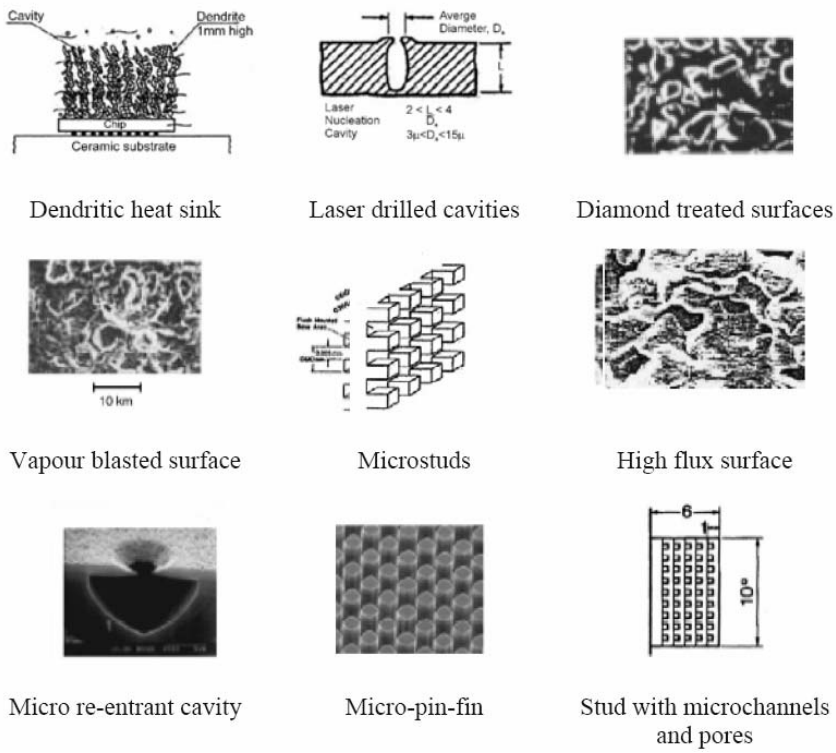

Figure 2-8. Examples of surface microstructures (Honda and Wei [124])

It was encouraging to know that micro-structure were effective in decreasing boiling onset superheat. Moreover, Honda and Wei [124] suggested that microporous structures

were most effective in enhancing nucleate boiling while micro-pin-fins were most effective in increasing the critical heat flux.

Particularly, Ma *et al.* [125] examined the effect of fin height with micro-pin-finned chips. Heat transfer was confirmed to be further enhanced by increasing the height of the fins. In the later investigation of Yuan *et al.* [126], flow and thermal conditions became more influential for micro-pin-finned surfaces rather than the smooth surface. The enhancement of heat transfer was believed to be a consequence of the increased surface area on the micro-pin-finned chips.

Shou-Shing Hsieh and Chih-Yi [127] recently conducted an experiment with a micro-channel heat sink containing 75 parallel 100 μm × 200 μm channels with 200 cavities of different angles. The enhancement ratio was calculated based on a comparison of the structured surfaces to the plain surfaces. An optimal cavity angle (θ) of 90° with an enhancement performance ratio of 1.4 was presented.

However, the heat transfer enhancement mechanism with microstructure surfaces is still debatable while the effect of wetting fluids and the role of wetting contact angle require deeper exploration.

Furthermore, other experimental parameters such as the channel orientation and the dissolved gas have been found influential on heat transfer characteristics. Studies have been conducted in inclined channel (Hetsroni *et al.* [128]) and different oriented surfaces (Honda and Wei [124] and Misale *et al.* [129]). It was evidenced that the effect of confinement plays a more important role in horizontal and upwardly oriented channels, thus providing higher efficiency of heat transfer.

Concerning the effect of dissolved gas in the working liquid, a remarkable decrease in boiling incipient superheat was captured by Honda *et al.* [123] when there was dissolved gas. Steinke and Kandlikar [130] tested the flow boiling using water with different levels of dissolved air. At 1 atm, the surface boiling incipient temperature was lower when oxygen contents were higher. A newly observed behaviour showed a slight reduction in heat transfer when bubble nucleation started. The dissolved air was blamed for forming an insulating layer of bubbles on the heated surface to reduce the heat transfer after boiling incipient. Honda and Wei [124] also pointed out an enhancement of heat transfer in gas-dissolved FC-72 at low heat fluxes. For high heat flux conditions, however, heat transfer performances were similar to those of the degassed FC-72.

The review in this session summarised the key experimental investigations on flow boiling heat transfer characteristics in mini-and micro-channels. As can be seen, there

are still large disagreements among researchers as to the different experimental methodologies, the effects of various experimental parameters on heat transfer characteristics and most importantly, the heat transfer mechanisms during flow boiling.

2.4.4 Saturated flow boiling heat transfer correlation

A large number of two-phase heat transfer correlations have been developed from existing experimental databases. Table 2-3 includes a group of popular saturated flow boiling heat transfer correlations and the corresponding mean absolute error (MAE) reported in their studies.

Table 2-3. Summary of saturated flow boiling heat transfer correlations in macro-, mini- and micro-channels

Reference (Year)	Experimental Parameters	Correlation for local h	MAE[1] (%)
Chen [131] (1966)	water and organic fluids; vertical tubes; u_L = 0.061-4.481 m·s^{-1}; x = 0.01-0.71; P = 0.56-35.28 bar; macro-tube and annulus	$h_{tp} = Fh_{sp} + Sh_{nb}$ $h_{sp} = 0.023(Re_L)^{0.8} \cdot (Pr_L)^{0.4} \cdot (k_L / D)$ $h_{nb} = 0.00122\left(\frac{k_L^{0.79} C_{p,L}^{0.45} \rho_L^{0.49} g_c^{0.25}}{\sigma^{0.5} \mu_L^{0.29} h_{fg}^{0.24} \rho_v^{0.24}}\right) \cdot (\Delta T)^{0.24} \cdot (\Delta P)^{0.75}$ $F = (1 + 1/X^{0.5})^{1.78}$, $S = 0.9622 - 0.5822\left[\tan^{-1}\left(\frac{Re_L F^{1.25}}{6.18 \times 10^4}\right)\right]$ X: Martinelli parameter , $X = \left(\frac{1-x}{x}\right)^{0.9} \cdot \left(\frac{\rho_v}{\rho_L}\right)^{0.5} \cdot \left(\frac{\mu_L}{\mu_v}\right)^{0.5}$ $Re_L = \frac{G(1-x)d_h}{\mu_L}$, $Pr_L = \frac{C_{p,L} \cdot \mu_L}{k_L}$	12

(continued)

[1] $\mathrm{MAE} = \frac{1}{N} \cdot \sum \left(\left| h_{\mathrm{exp.}} - h_{\mathrm{cor.}} \right| / h_{\mathrm{exp.}} \right) \times 100\%$

Shah [132] (1982)	water and refrigerants (R11, R12,R22, R502); vertical and horizontal tubes; d = 5.0-15.8 mm; G = 70-11071 kg·m^{-2}·s^{-1}; q = 90-1215 kW·m^{-2}; x = 0-0.7; macro-channels	$h_{tp} = \max(F, S) h_{sp}$ $h_{sp} = 0.023(Re_L)^{0.8} \cdot (Pr_L)^{0.4} \cdot (k_L / D)$ For N >1.0, $S = 1.8 / N^{0.8}$, $F = 230 Bl^{0.5}$ for $Bl > 3\times10^{-5}$, or $F = 1 + 46 Bl^{0.5}$ for $Bl < 3\times10^{-5}$ For $0.1 < N \le 1.0$, $S = 1.8 / N^{0.8}$, $F = E \cdot Bl^{0.5} \exp(2.74 N^{-0.1})$ For $N \le 0.1$ $S = 1.8 / N^{0.8}$, $F = E \cdot Bl^{0.5} \exp(2.74 N^{-0.15})$ where E = 14.7 for $Bl \ge 11\times10^{-4}$ or E = 15.43 for $Bl < 11\times10^{-4}$ $N = Co$ for $Fr_L \ge 0.04$ or $N = 0.38 Fr_L^{-0.3} Co$ for $Fr_L < 0.04$ $Bl = \frac{q}{G h_{fg}}$ $Co = \left(\frac{1-x}{x}\right)^{0.8} \cdot \left(\frac{\rho_v}{\rho_L}\right)^{0.5}$, $Fr = \frac{G^2}{\rho_L^2 g d}$	
Gungor and Winterton [133] (1986)	water, refrigerants, ethylene glycol; horizontal and vertical up and downward flow; d_{in} =2.95-32 mm; G = 12.4-61518.0 kg·m^{-2}·s^{-1}; q = 0.35-91534 kW·m^{-2}; x = 0-1.73; macro-channels	$h_{tp} = F h_{sp} + S h_{nb}$ $h_{sp} = 0.023(Re_L)^{0.8} \cdot (Pr_L)^{0.4} \cdot (k_L / D)$ $F = 1 + 24000 Bl^{1.16} + 1.37(1/X)^{0.86}$ $h_{nb} = 55 Pr^{0.12} (-\log_{10} Pr)^{-0.55} M^{-0.5} q^{0.67}$ $S = 1/(1 + 1.15\times10^{-6} F^2 Re_L^{1.7})$ For horizontal tube and Froude number Fr < 0.05: $F = F Fr^{(0.1-2Fr)}$ and $S = S\sqrt{Fr}$	
Kandlikar [134] (1990)	water, refrigerants, neon and nitrogen; vertical and horizontal; d_h = 4.6-32 mm; G = 13-8179 kg·m^{-2}·s^{-1}; q = 0.3-2280 kW·m^{-2}; x = 0.001-0.987; P = 0.6-64.2 bar; macro-channels	$h_{tp} = \max(F, S) \cdot h_{sp}$ $h_{sp} = 0.023(Re_L)^{0.8} \cdot (Pr_L)^{0.4} \cdot (k_L / D)$ For convective boiling: $F = 1.136 Co^{-0.9} f(Fr_L) + 667.2 Bl^{0.7}$ For nucleate boiling: $S = 0.6683 Co^{-0.2} f(Fr_L) + 1058 Bl^{0.7}$ $Co = \left(\frac{1-x}{x}\right)^{0.8} \cdot \left(\frac{\rho_v}{\rho_L}\right)^{0.5}$ F_{fL}: fluid-dependent parameter; Co: convection number $f(Fr_L) = 1$ for $Fr_L \ge 0.04$ or $f(Fr_L) = (25\ Fr_L)^{0.3}$ for Fr_L < 0.04 Extension of the correlation (Kandlikar and Balasubramanian [135] (2004)) neglects channel orientation in mini-channels, thus Froude number effect is deleted.	13.0-23.2
Liu and Winterton [136] (1991)	d_h = 2.95-32 mm; G = 12.4-8179.3 kg·m^{-2}·s^{-1}; q = 0.349-2620 kW·m^{-2}; x = 0.0-0.948; superheat: 0.2-62.2 K, T_{sub} = 0.1-173.7 K, Fr = 2.66×10^{-4}-2240 reduced pressure: 0.0023-0.895,Re = 568.9-875000; macro-channels	$h_{tp} = F h_{sp} + S h_{nb}$, $h_{sp} = 0.023(Re_L)^{0.8} \cdot (Pr_L)^{0.4} \cdot (k_L / D)$ $F = \left[1 + x Pr_L \left(\frac{\rho_L}{\rho_v} - 1\right)\right]^{0.35}$ $h_{nb} = 55 P_r^{0.12} \cdot (-\log_{10} P_r)^{-0.55} \cdot M^{-0.5} \cdot q^{0.67}$ $S = 1/(1 + 0.055 F^{0.2} Re_L^{0.16})$ For horizontal tube and Froude number Fr < 0.05: $F = F \cdot Fr^{(0.1-2Fr)}$ and $S = S\sqrt{Fr}$	

(continued)

Lee and Lee [137] (2001)	R113; single, rectangular with aspect ratio: 0.1, 0.05 and 0.02; d_{in} = 0.4-2.0 mm, W_{in} = 20 mm; G = 50-200 kg·m^{-2}·s^{-1}; q = 0-15 kW·m^{-2}; x =0.15-0.75; mini- and micro-channels	$h_{tp} = F \cdot h_{sp}$ $h_{sp} = 8.235\begin{pmatrix}1-2.0421\alpha+3.0853\alpha^2-2.4765\alpha^3\\+1.0578\alpha^4-0.1861\alpha^5\end{pmatrix}$ $F = 10.3\alpha^{0.398}\phi_L^{0.598}$, $Re_L \le 200$, α: channel aspect ratio; $\phi_L^2 = 1+\frac{C}{X}+\frac{1}{X^2}$, X: Martinelli parameter $C = 6.185\times10^{-2} Re_L^{0.726}$	deviation: ±20%
Warrier *et al.* [98] (2002)	FC-84; 5 parallel, rectangular; d_h = 0.75 mm; G = 557-1600 kg·m^{-2}·s^{-1}; q = 0-59.9 kW·m^{-2}; x =0-0.55; T_{in} = 26, 40 and 60 °C; mini- and micro-channels	$h_{tp}/h_{sp\_FD} = 1+6.0Bl^{1/16}-5.3(1-855Bl)x^{0.65}$ h_{sp_FD} : fully developed single phase heat transfer coefficient for laminar flow	maximum difference: ±28%
Zhang *et al.* [138] (2004)	water,R11,R12,R113; circular and rectangular; vertical and horizontal; d_h = 0.78-6.0 mm; G = 23.-2939 kg·m^{-2}·s^{-1}; q = 2.95-2511 kW·m^{-2}; P = 1.01-12.1 bar; macro- and mini-channels	generalized Chen correlation: $h_{tp} = Fh_{sp} + Sh_{nb}$ $\begin{cases}h_{sp} = (k_L/d_h)\max(Nu'_{sp,v}, Nu_{sp,t}),\ Re_L < 2300, \text{horizontal}\\h_{sp} = (k_L/d_h)\max(Nu'_{sp,v}, Nu),\ Re_L < 2300, \text{vertical}\\h_{sp} = (k_L/d_h)Nu_{sp,t},\ Re_L \ge 2300, \text{both horisontal and vertical}\end{cases}$ $h_{nb} = 0.00122\left(\frac{k_L^{0.79}C_{p,L}^{0.45}\rho_L^{0.49}g_c^{0.25}}{\sigma^{0.5}\mu_L^{0.29}\lambda^{0.24}\rho_v^{0.24}}\right)\cdot(\Delta T_{sat})^{0.24}\cdot(\Delta P_{sat})^{0.}$ $F = \max(0.64\phi_L, 1), S = f(Re)$	18.3
Lee and Mudawar [104] (2005)	water, R134a; 53 parallel rectangular, 0.231×0.713mm^2; G = 127-654 kg·m^{-2}·s^{-1}; q = 159-938 kW·m^{-2}; P_{in} = 1.44-6.60 bar; x = 0.001- >1; micro-channels	x = 0-0.05: $h_{tp} = 3.856X^{0.267}h_{sp,L}$ $X^2 = \frac{(dP/dz)_L}{(dP/dz)_v}$, $h_{sp,L} = \frac{Nu_3 k_L}{d_h}$ $X_{vv} = \left(\frac{\mu_L}{\mu_V}\right)^{0.5}\cdot\left(\frac{1-x}{x}\right)^{0.5}\cdot\left(\frac{v_L}{v_v}\right)^{0.5}$ $X_{vt} = \left(\frac{f_L Re_v^{0.25}}{0.079}\right)^{0.5}\cdot\left(\frac{1-x}{x}\right)^{0.5}\cdot\left(\frac{v_L}{v_v}\right)^{0.5}$ $Re_v = \frac{Gxd_h}{\mu_v}$	11.6
		x = 0.05-0.55: $h_{tp} = 436.48Bl^{0.522}We_L^{0.351}X^{0.665}h_{sp,L}$ $Bl = \frac{q}{Gh_{fg}}$, $We_L = \frac{v_L G^2 d_h}{\sigma}$	11.9
		x = 0.55-1.0: $h_{tp} = \max\{(108.6X^{1.665}h_{sp,v}), h_{sp,v}\}$ $h_{sp,v} = \frac{Nu_3 k_v}{d_h}$ for laminar gas flow $h_{sp,v} = 0.023Re_g^{0.8}Pr_g^{0.4}$ for turbulent gas flow	16.1
Yun *et al.* [106] (2005)	CO_2 and refrigerants; circular and rectangular; d_h = 0.79-2.92 mm; G = 44-3571.0 kg·m^{-2}·s^{-1}; q = 2.22-128.6 kW·m^{-2}; Pr = 0.045-0.87	before critical vapour quality: $h = 16.26q^{0.72}Pr^{0.88}$	38

(continued)

Liu and Garimella [110] (2007)	water; rectangular mini-channels, 0.275 × 0.636 and 0.406 × 1.063 mm^2; G = 221-1283 kg·m^{-2}·s^{-1}; q < 1290 kW·m^{-2}; x = 0-0.2	saturated boiling : $h_{tp} = Fh_{sp} + Sh_{nb}$ $F = (\phi_L^2)^{1/4}\left(\frac{\mu_{tp}}{\mu_L}\right)^{0.105}\left(\frac{C_{p,tp}}{C_{p,L}}\right)^{1/4}\left(\frac{k_{tp}}{k_L}\right)^{3/4}$ $S = \exp[36.57 - 55746/(Re_L F^3) - 3.4\ln(Re_L F^3)]$ $h_{nb} = h_o F_{PF}\left(\frac{q''}{q_0''}\right)^n\left(\frac{R_p}{R_{p0}}\right)^{0.133}$ F_{PF} : pressure correction factor $F_{PF} = 1.73P_r^{0.27} + \left(6.1 + \frac{0.68}{1-P_r}\right)P_r^2$, P_r: reduced pressure	16.7
Bertsch *et al.* [139] (2009)	water, refrigerants, FC-77 and nitrogen; circular and rectangula; d_h = 0.16-2.92 mm; G = 20-3000 kg·m^{-2}·s^{-1}; q = 0.4-115 kW·m^{-2}; T_{sat} = -194-97 °C; x = 0-1; confinement number: 0.3-4.0; mini- and micro-channels	$h_{tp} = h_{nb}\cdot(1-x) + h_{conv,tp}\cdot\left[1 + 80(x^2 - x^6)\cdot e^{-0.6Co}\right]$ $h_{nb} = 55P_r^{0.12-0.2\log_{10}R_p}\cdot(-\log_{10}P_r)^{-0.55}M^{-0.5}q^{0.67}$, R_p : surface roughness parameter, μm P_r : reduced pressure $h_{conv,tp} = h_{conv,L}\cdot(1-x) + h_{conv,v}\cdot x$ $h_{conv,L} = \left(3.66 + \frac{0.0668\cdot\frac{d_h}{L}Re\cdot Pr}{1 + 0.04\cdot\left[\frac{d_h}{L}Re\cdot Pr\right]^{2/3}}\right)\cdot\frac{k_L}{d_h}$ $h_{conv,v}$ is calculated using the properties of saturated vapour instead	30

Reference (Year)	**Experimental Parameters**	**Correlation for global *h***	**MAE (%)**
Lazarek and Black [140] (1982)	G = 125-750 kg·m^{-2}·s^{-1}; q = 14-380 kW·m^{-2}; static pressure: 1.3-4.1 bar *Re*: 860-5500 *Bl*: 2.3×10^4 - 76×10^4 ; mini- and micro-channels	$h_{tp} = 30Re^{0.857}Bl^{0.714}k_L/d_h$ $Re = \frac{GD}{\mu_L}$ $Bl = \frac{q}{Gh_{fg}}$	
Tran *et al.* [95] (1996)	R12; single, circular and rectangular; d_h = 2.4-2.92 mm; G = 44-832 kg·m^{-2}·s^{-1}; q = 3.6-129 kW·m^{-2}; x =0-0.94 reduced pressure: 0.045-0.20 bar nucleate boiling dominant; mini-channels	$h = (8.4\times10^5)(Bl^2We_L)^{0.3}\cdot\left(\frac{\rho_L}{\rho_v}\right)^{-0.4}$	15

Based upon the correlations in Table 2-3, some modifications and extensions were made to better satisfy the newly obtained heat transfer data or to cover more comprehensive experimental conditions. For instance, Yu *et al.* [99] fitted new values of the coefficient and index in the Tran *et al.* [95]'s correlation. Kandlikar and

Balasubramanian [135] extended the range of applicability of the Kandlikar [134] correlation to low (below 3000) and very low (below 100) Reynolds number by recognising the convective boiling contribution as well as the increased nucleate boiling contribution. Schwarzkopf *et al.* [141] modified Chen [131]'s correlation by taking into account of the laminar entry length effect and boiling enhancement factor based on fluid properties. The modified correlation better estimated the heat transfer coefficients for flow boiling in meso-channels (d_h = 1.55 and 1.17 mm).

In addition to the summarized correlations, there are also a number of numerical models proposed to predict flow boiling heat transfer. For example, Kew and Cornwell [25] established a model for the prediction of heat transfer coefficients for fluid evaporating in a single channel. Thome *et al.* [142] developed a three-zone flow boiling heat transfer model which described the transient variation in local heat transfer coefficient during the sequential and cyclic passages of liquid slug, evaporating elongated bubble and a vapour slug. The authors compared the predicted local heat transfer coefficients to the flow boiling experimental data coving seven fluids: R11, R12, R113, R123, R134a, R141b and CO_2 in tubes with d_{in} = 0.77 mm – 3.1 mm. The model was found to predict 67% of the database within ± 30% (Dupont *et al.* [143]).

However, most of the micro-channels used in the previous studies were circular tubes, trapezoidal, square and low aspect ratio rectangular micro-channels. There is very limited work in literature using high aspect ratio micro-channels. More efforts on flow boiling in high aspect ratio micro-channels are of tremendous necessity. The experimental database of high aspect ratio micro-channels is still waiting to be enlarged in order to bridge this gap and to develop more global correlations for flow boiling heat transfer predictions.

2.5. Review on experimental studies on nanofluids

The need for a more effective heat transfer system is always rising as the operational speed of the high-thermal density devices is strictly limited by the cooling rate. In addition to the heat transfer enhancement methods regarding cooling system configuration, novel ideas of improving heat transfer capacity by using advanced fluids with greater potential to provide better thermal characteristics came out. However, the inherent limitation of the current utilised heat transfer liquids is the relatively low

thermal conductivity. Water possesses the highest thermal conductivity among all the fluids we use today. On the other hand, most metals or metal oxides have much higher thermal conductivities (Bejan and Kraus [144]). Therefore it is logical to enhance thermal conductivity by adding solid particles into the pure base liquid (Wen *et al.* [8]). Since Maxwell [9], researchers have made great efforts to break the heat transfer limitations by dispersing millimetre- or micron-sized particles in liquids. However, rapid sedimentation, erosion, clogging and high-pressure drop caused by these particles stood in the way of making this technology more practical.

Fortunately, the development of modern nanotechnology has enabled the production of nano-scale metallic ort non-metallic particles (Das *et al.* [145]). Liquids with nanometer-sized solid particles exhibit excellent stability and do not experience large scale sedimentation thanks to the size effect and Brownian motion of the nanoparticles. Nanofluids as a colloidal mixture of nanoparticles (1-100 nm) and a base liquid (nanoparticle fluid suspensions) was firstly phrased and brought into sight by Choi and Eastman [146] to introduce a new type of fluids with outstanding thermal properties. Fouling and pipe erosion were greatly reduced and stable suspension could be achieved in which the effective thermal conductivity of the fluid was greatly enhanced (Eastman *et al.* [147]). A substantial increase in thermal conductivity of nanofluids was confirmed by numerous experimental and theoretical studies (Choi and Eastman [146], Lee *et al.* [148], Wang *et al.* [149], Xuan and Roetzel [150], Choi *et al.* [151], Xie *et al.* [152], Kumar Das *et al.* [153], Hwang *et al.* [154], Garg *et al.* [155], Lee *et al.* [156], Li *et al.* [157], Murshed *et al.* [158], Wensel *et al.* [159]).

Various types of nanoparticles have been reported in literature including metallic particles (Cu, Al, Fe, Au, and Ag) (Xuan and Li [160], Patel *et al.* [161], Hong *et al.* [162], Garg *et al.* [155], Li *et al.* [157],), non-metallic particles (Al_2O_3, CuO, Fe_3O_4, TiO_2, SiC and ZrO_2) (Zhu *et al.* [163], Lee *et al.* [156], Hwang *et al.* [164], Rea *et al.* [165], Duangthongsuk and Wongwises [166], Williams *et al.* [167], Chopkar *et al.* [168], Trisaksri and Wongwises [169]), carbon nanotube (CNT) (Choi *et al.* [151], Park and Jung [170, [171]) and nanodroplets (Li *et al.* [172]). Some commonly used base liquids are water, oil, acetone, decene and ethylene glycol. There are also some recent studies on refrigerant-based nanofluids (Trisaksri and Wongwises [169], Park and Jung [170, [171]).

The presence of nanoparticles may be influential on the pressure drop characteristics of single phase and flow boiling within small-scale channels and consequently affect the overall performances of heat exchangers or cooling systems.

Several investigations were conducted on the pressure drop and the friction factor during nanofluids convective flow, among which the laminar entrance flow region and fully developed flow region (Hwang *et al.* [164], Rea *et al.* [165]), transition flow (Sharma *et al.* [173], Dong and Leyuan [174]) as well as the turbulent flow (Xuan and Li [175], Williams *et al.* [167], Sharma *et al.* [173], Duangthongsuk and Wongwises [166], Fotukian and Nasr Esfahany [176]) have been concentrated on respectively. Dong and Leyuan [174] studied the single phase forced convection of Al_2O_3-water nanofluids in circular minichannels (d_{in} = 1.09 mm) and reported an increase of friction factor with increasing nanoparticle concentration. However, the nanoparticle effect was vanished at higher Reynolds number range. They described a prolonged hydraulic developing length and an early transition from laminar to turbulent flow using nanofluids. The pressure drop penalty was also reported by Fotukian and Nasr Esfahany [176] using CuO-water nanofluids in an annular tube with d_{in} = 5 mm and d_{out} = 32 mm. In contrast, there are also a number of studies that showed no or minor pressure drop rise by using nanofluids (Li and Xuan [177], Rea *et al.* [165], Pawan *et al.* [178] and Duangthongsuk and Wongwises [166]), especially for dilute nanofluids. It was argued that nanofluids can be treated as homogeneous fluids and the conventional friction factor correlations can be extended to nanofluids. It is worth noticing that the aforementioned studies were mostly carried out in conventional or mini-scale circular tubes. Nanofluid convective flow in micro-scale channels with different cross-sectional geometries need to be explored.

The knowledge of nanofluid boiling is still very limited, the majority of which were conducted in pool boiling. Vassallo *et al.* [179] studied the silica-water nanofluids boiling on a 0.4 mm diameter horizontal NiCr wire. Nano-particles and micro-particles were used and it was reported that the CHF increased for both types of particles. However, heat transfer enhancement was not observed in nucleate boiling. Remarkable CHF enhancement (~ 200%) was also described by You *et al.* [180] using distilled-deionized water-based Al_2O_3 nanofluids, the particle concentration of which ranged from 0 to 0.05 $g \cdot L^{-1}$. Besides, different bubble dynamics were observed. Compared with pure water, the size of the bubbles was increased and the bubble frequency was decreased in saturated nanofluids. Among the very limited studies on refrigerant-based nanofluids, Park and Jung [170] and Park and Jung [171] examined pool boiling heat transfer using carbon nanotube (1.0 vol.%) suspended in R22, R123, R134a and water and achieved significant heat transfer enhancement (up to 36.6% at low heat flux). Nevertheless, Trisaksri and Wongwises [169] chose TiO_2-R134b nanofluids and reported that boiling

heat transfer coefficient decreased with increasing particle concentrations, especially at higher heat flux. Even though the majority of the studies confirmed remarkable enhancement of CHF (Vassallo *et al.* [179], You *et al.* [180], Bang and Soon [181], Milanova and Kumar [182], Kim *et al.* [183] and Kim *et al.* [184]), controversial conclusions of the effects of nanoparticles on nucleate boiling heat transfer were reported by different researchers. The heat transfer was found to be deteriorated (Das *et al.* [185], Trisaksri and Wongwises [169], Chopkar *et al.* [168]), unaffected (Vassallo *et al.* [179], You *et al.* [180],) or increased (Witharana [186], Liu *et al.* [187], Park and Jung [170, 171]) by higher particle concentration. Hence, further investigations are required to better understand the nanofluids boiling heat transfer mechanisms.

There are a few studies published on flow boiling heat transfer with nanofluids in microchannels. Vafaei and Wen [188] discussed the effect of nanoparticles on critical heat flux during subcooled flow boiling of aqueous based alumina nanofuilds in a 510 μm single microchannel. Critical heat flux was found to increase with increasing mass flux. Compared with pure de-ionized water, an increase of ~ 51% in the critical heat flux was achieved under very low nanoparticle concentrations (0.1 vol.%). Furthermore, detailed observations on boiling surface showed that as the particle concentration increased, fouling effect was more profound at channel outlet, resulting in changed surface conditions. Thus the nanoparticle deposition and the consequent surface modification were argued to be responsible for CHF enhancement. Finally it was pointed out that nanoparticle deposition may generate hotspots on the channel surface and prevent the dryout from spreading due to increasing wettability, therefore a pinhole type failure would occur.

Kim *et al.* [189] evaluated the CHF enhancement using water-based Al_2O_3 nanofluids. Similarly, the CHF of Al_2O_3 nanofluids was enhanced up to ~ 70% in the flow boiling compared to de-ionized water. CHF increased with increasing mass flux but CHF enhancement ratio did not show any trend toward increasing mass flux. As a result of the deposition of Al_2O_3 nanoparticles on the tube inner surface, the CHF enhancement contributed to the enhanced wettability of the liquid film onto the heater surface. Interestingly, since no significant change of CHF was captured when Al_2O_3 nanoparicles concentration increased from 0.001 vol.% to 0.1 vol.%, the authors assumed that the effect of deposition may already become saturated at a concentration of 0.001 vol.%. Hence, examinations on nanofluids with very low concentration ($\leq 10^{-4}$ vol.%) were suggested to confirm this assumption.

Henderson *et al.* [190] used refrigerant-based nanofluids to investigate the effect of nanoparticles on flow boiling heat transfer coefficient during flows in a horizontal tube (d_{in} = 7.9 mm) at low vapour quality ranges. In order to prepare the nanofluids, the authors tested various nanofluids combinations and found that for the tested base fluids (water, ammonia, hydrocarbons, HFCs and HCFCs), none of the other fluids could suspend noncoated particles as good as water. Besides, compared with the common base liquids such as water and ethylene glycol, a remarkably rapid agglomeration and settling of common nanoparticles were observed in refrigerants. Moreover, nanoparticles with hydrophobic surface treatments (fumed silica and coated alumina) were found to be the most prospective options for two-phase flow boiling experiments with direct particle loading. In their heat transfer experiment, direct dispersion of SiO_2 nanoparticles in R-134a and CuO nanoparticles in a mixture of R-134a and polyolester oil were selected as the two testing nanofluids. In R-134a/SiO_2 nanofluids, a systematic decrease in convective boiling heat transfer coefficient with nanoparticle seeding was evidenced and the decrease was more profound in the 0.5% suspension than the 0.05% suspension. No conclusion on nanoparticle effect was drawn due to limited data. However, it was assured that the effect of nanoparticles was statistically significant because the heat transfer degradation was beyond the experimental uncertainty. Even though the original reason behind heat transfer degradation was unclear, the quality of nanoparticle dispersion was considered to be partially responsible. On the contrary, excellent dispersion was achieved for R-134a and polyolester oil mixture-based CuO nanofluids. More than 100% heat transfer enhancement was achieved, indicating the appealing potential for heat transfer enhancement with refrigerant/lubricant mixtures.

Although nanofluids were reported to have improved the liquid thermal performances than the pure liquids while induced very little pressure drop rise, the application of nanofluids is still in its infancy. Many questions in the controversial heat transfer characteristics still need to be answered. For instance, in similar flow passage geometries and under similar flow and thermal conditions, the dependency of heat transfer coefficients on vapour quality, heat flux and mass flux various in different studies. Extensive theoretical and experimental explorations are urged to dig further in the nanofluids flow and heat transfer mechanisms.

2.6 Conclusions

The above overview on liquid-vapour phase change and flow boiling heat transfer summarizes a number of criteria of channel system classification, vapour dynamics, flow instabilities and varying trends of heat transfer characteristics as well as the proposed correlations with respect to diverse conditions. Moreover, the usage of nanofluids as an innovative method for heat transfer enhancement starts to become attractive. The aforementioned studies reinforce that the flow boiling heat transfer in micro-channels could be vastly different from that in the conventional-sized channels. The experimental data in micro-channels indicate that there are still many controversies about the flow instabilities and heat transfer mechanisms. Some macro-scale physical laws are found no longer available in micro-scale. It is also realised that the understanding of vapour dynamics in confined space is still not enough, especially in the channels with geometries such as high aspect ratio cross-section. Due to the lack of experimental data, the development of boiling heat transfer modelling in micro-scale is therefore constrained. Even though there are a number of correlations proposed for heat transfer in various conditions, a more global method to calculate the flow boiling heat transfer in micro-channels is still not well established. Most of the previous studies were conducted in regular channel geometries such as circular, trapezoidal, square and low aspect ratio rectangular micro-channels. The experimental database with a wider range of channel geometries is waiting to be enlarged. Furthermore, the application of nanofluids is currently in a very early stage. Explanations to the controversial hydraulic and thermal characteristics of nanofluids are still not clarified. So the extensive theoretical and experimental investigations on nanofluids should be conducted to better understand the nanofluids hydraulic behaviours and heat transfer mechanisms.

The present study concentrates on liquid-vapour phase change in micro-scale space and the flow boiling heat transfer in different-sized high aspect ratio rectangular mini- and micro-channels, aiming to dig further in the boiling and heat transfer mechanisms as well as flow instabilities in the unique channel geometry. This study will take a fundamental approach on studying boiling in mini-and micro-channels, based on the simultaneous measurements of pressure drops, local temperature profiles across the channel surfaces and synchronous visualisation of the boiling phenomena. Experimental data in the present study will also contribute to enlarge the boiling heat transfer database in order to help build more precise theoretical models for future predictions. The investigations on flow and evaporation of nanofluids in high aspect ratio micro-channels are of significant importance to contribute to the knowledge.

Chapter 3
Experimental facilities

3.1. Introduction

An experimental system was designed for the investigation on liquid-vapour phase change, flow boiling and heat transfer in single micro-channels with pure liquids and nano-fluids. The experimental system consisted of three main parts: first and foremost was the setup for flow boiling and heat transfer in single rectangular micro-channel. The bubble dynamics, flow instabilities, and flow boiling heat transfer characteristics were concentrated on. Particularly, in the study of single bubble growth, a separate test rig was built to study the single bubble growth confined between two parallel glass plates without liquid flow. Thirdly, because of the significant role of liquid film evaporation in the liquid-vapour phase change and heat transfer processes, another experimental setup was constructed to specifically investigate the meniscus evaporation in a micro-channel.

Each part of the experimental system is introduced individually. Besides, properties of the working liquids and the preparation of nanofluids are provided. Some of the general data reduction as well as the experimental parameter uncertainties are also presented in this chapter.

3.2. Experimental facilities

All the setups could be mounted in a 1m×1m×1m plexiglass box, which could provide a stable and controllable testing environment. The ambient temperature inside the plexiglass box was controlled by a thermal regulation system. Each set of facilities are introduced as follows.

3.2.1. Flow boiling in single micro-channel test loop

In practical point of view, flow boiling is essential for enhancing heat dissipation capacity. Experimental investigations on flow boiling in single micro-channel were conducted to explore the liquid-vapour phase change, vapour dynamics and heat transfer characteristics in single micro-channels. An integrated experimental setup including a syringe pump, micro-channel test section, a high speed camera and an infrared (IR)

camera was mounted in the plexiglass box. Figure 3-1 and Figure 3-2 provide the details of the experimental apparatus for flow boiling in single micro-channel.

A heater was positioned on top of the plexiglass box to control the inside temperature. A syringe pump was used to deliver the working liquid through the flow loop at a pre-set constant flow rate. The liquid was vigorously degassed for one hour to remove dissolved gases prior to entering the flow loop, and was eventually condensed into a glass reservoir. The reservoir was connected to the open air outside the plexiglass box. The inlet liquid temperature was controlled via the control of the ambient temperature of the box.

Thermocouples and pressure transducers were located at the inlet and outlet of the channel to measure the corresponding temperatures and pressures. A National Instruments® system was used for data acquisition. Meanwhile, a high speed camera NanoSense MKIII® was installed above the test section to provide synchronized visualisation. A Fiber Optic back light was put under the test section to provide a constant and uniform light source for lumination. In addition, an infrared camera ThermoVision® 900 was utilized to obtain the temperature profiles across the channel outer surface during flow boiling.

The setups are introduced in detail as follows addressing to Figure 3-3 – Figure 3-11.

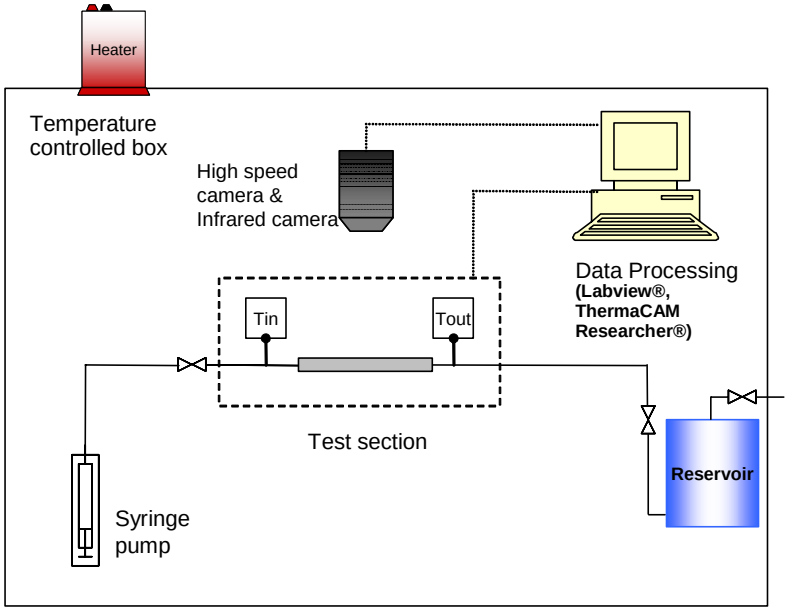

Figure 3-1. Schematic drawing of the flow boiling in single micro-channel experimental setup

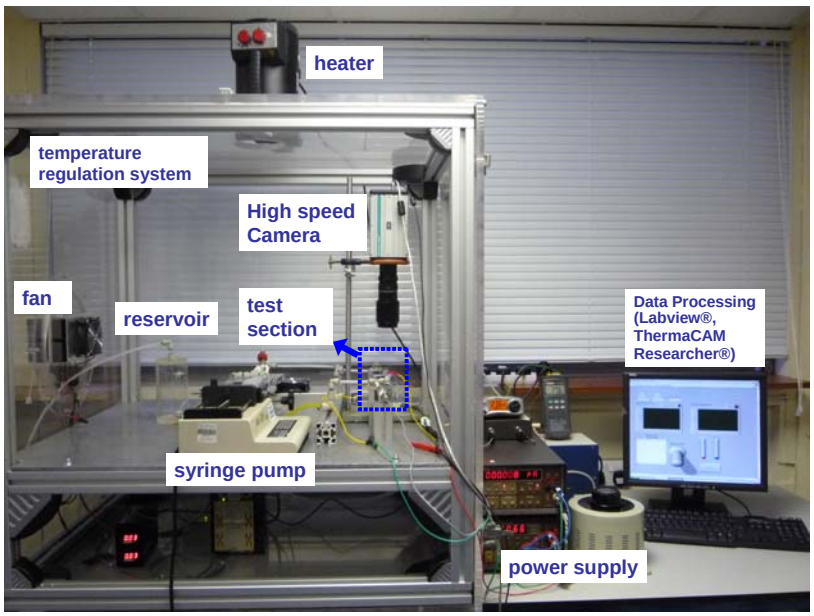

Figure 3-2. Photograph of the flow boiling in single micro-channel experimental setup

3.2.1.1. Temperature regulation system

A Honeywell® Turbo fan heater (Figure 3-3) was used to manage the temperature inside the plexiglass box. The heater could provide continuous heating, the strength of which was adjustable. In order to maintain a uniformly distributed temperature field inside the box, a fan (Figure 3-4) was used to help circulate the air in the box. Meanwhile, temperature was displayed using several thermometers and digital thermocouples, which were put at different locations inside the box to make sure that the temperature distribution was uniform before conducting the experiment.

Figure 3-3. Honeywell® TURBO fan heater

Figure 3-4. Fan on the plexiglass box wall

3.2.1.2. Degassing system

Working liquid was degassed vigorously for one hour prior to entering the flow loop. The degassing system was designed as in Figure 3-5. Liquid was added in the degassing glass chamber through the top entrance, and was heated by the bottom heating coil. The vapour was condensed by the cooling water coil on top of the chamber meanwhile the dissolved gases were expelled from a vent on the chamber top cover. Finally the degassed working liquid was released via a valve on the chamber bottom and was ready for testing.

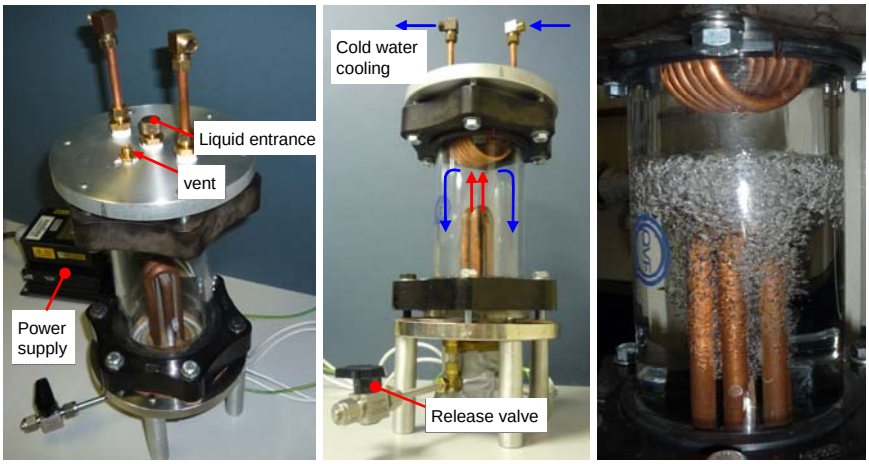

Figure 3-5. Degassing system

3.2.1.3. Transparent heating and visualization system

The use of transparent heating offered a real advantage for visualisation during flow boiling in micro-channels. The conductive coating of the micro-channel, which provided the novel transparent heating, was fabricated in the Scottish Microelectronic Centre (SMC) based in the University of Edinburgh. Sputtering technique was selected to provide a uniformly distributed coating on the channel outer surface. Different metal

deposit thicknesses were tested. The coating resistance and transparency for visualization were the main considerations. Tantalum was eventually selected due to the capacity in SMC. The thickness of the tantalum layer was optimized to ensure sufficient transparency for visualization while providing enough energy for heating. According to the technicians in SMC, the coating film thickness should be about 45 Angstroms, and the resistance ranged from 3 kΩ – 10 kΩ.

Figure 3-6 is the Oxford Plasmalab 400 Sputtering System used for micro-channel coating fabrication. A nozzle spayed directly on a target wafer where the micro-channels were held. The channels needed to be rotated manually to ensure that both external surfaces were covered with deposit.

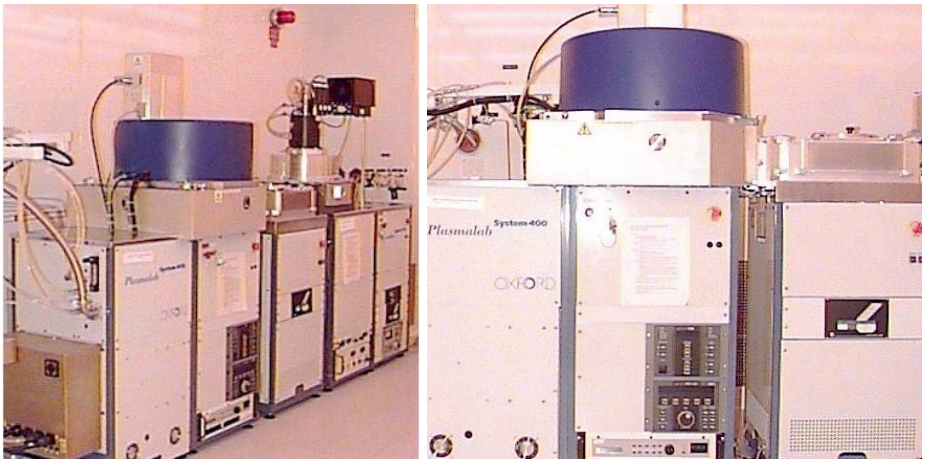

Figure 3-6. The Oxford Plasmalab 400 Sputtering System

Visualization results were undertaken via a high speed camera NanoSense MKIII® (Figure 3-7). The camera has a maximum frame rate of 1040 fps at full resolution 1280 pixel × 1024 pixel. The resolution could be edited to focus on the entire channel or a particular area of interest. The maximum camera speed could be extended with reduced resolution. A Navitar® ZOOM 7000 Close Focus Macro Lens (Figure 3-8) was used. In the present study, the rate of the camera was set from 500 fps to 3000 fps depending on different visualisation requirements. A Fiber-Lite® illuminator and Fiber Optic back light (Figure 3-9) were put under the test section to provide a constant and uniform light intensity without releasing heat to interfere the thermal field around the test section.

Figure 3-7. NanoSense® MKIII high speed camera

Figure 3-8. Navitar® ZOOM 7000 Close Focus Macro Lens

Figure 3-9. Dolan-Jenner Industries Fiber-Lite® illuminator and Fiber Optic back light

3.2.1.4. Thermography system

Because of the fragility of the micro-channels and the requirement of transparent heating, advantages of infrared thermography, such as non-contact and non-destructive, made the IR camera a better option than commercial thermocouples for channel wall temperature measurements. ThermoVision® 900 infrared camera (Figure 3-10) was used to record the temperature profiles across the micro-channel outer surface. It has a resolution of 204 pixel × 88 pixel and an accuracy of ±1°C or ±1% for different temperature ranges. The highest camera speed was 7 fps and was employed in all the experiments. The ThermaCAM Researcher Professional® software was used to analyze the IR image sequences. Table 3-1 and Table 3-2 list the specifications and the

measurement performances of the infrared camera. Details of how the infrared camera works are shown in Appendix A.

Figure 3-10. ThermoVision® 900 Infrared Camera

Table 3-1. Infrared camera ThermoVision® 900 SW scanner performance

detector type	2 × SPRITE, serial scanning
cooling system	thermal-electrically cooled
spectral response	2-5.4 micron
frame frequency	7 Hz
line frequency	3.5 kHz
lines/frame	128 (88 lines at high frequency)
samples/line	204
spatial resolution	140 elements per line (50% modulation, interpreted in the processor to provide an image of 204 pixel × 88 pixel)

Table 3-2. Infrared camera measurement performance

temperature range	-20°C to +500°C range1: -20°C – 80°C range2: 0 – 150°C range3: 50°C – 250°C range4: 100°C – 500°C
sensitivity at 30 °C	0.1°C
accuracy	±1°C (range 1) or ±1% (range 2-4)

3.2.1.5. Fluid delivery system

The degassed working fluid was delivered into the test section by a syringe pump (Figure 3-11). FORTUNA® OPTIMA® glass syringes (60 ml) were used. The glass syringes were chosen because of the low thermal expansion coefficient (in the order of 10^{-6} K^{-1}) and its compatibility with the working liquids. The volume flow rate of the syringe pump was calibrated before being used (see calibration chart in Appendix B). The accuracy of the syringe pump was 0.996. The mass flux accordingly depended on the cross-sectional area of the micro-channel and the desired volume flow rate.

Figure 3-11. Cole-Parmer® 74900 dual-syringe pump with FORTUNA® OPTIMA® Glass syringe (60 ml)

3.2.1.6. Data acquisition system

A National Instruments® data acquisition system was used to acquire the inlet and outlet pressures as well as the temperatures. Voltage and temperature data were acquired via a NI SCXI-1600 USB Data Acquisition and Control Module, a NI SCXI 1303 32-channel isothermal terminal block (see Figure 3-12) and a LabView® software interface. This configuration provided a 166 $kS \cdot s^{-1}$ maximum sampling rate. The SCXI 1303 module was selected because of its isothermal design and high-precision CJC sensor.

Figure 3-12. National Instruments® Data Acquisition Unit and SCXI-1303 connection

A pair of Omega® PXM219 series pressure transducers were utilised to acquire the inlet and outlet pressures. The common specifications of the pressure transducers are listed in Table 3-3. Pressure transducers were calibrated, the calibration charts of which can be found in Appendix B. A pair of K type thermocouples was also fixed at the channel inlet and outlet for local liquid temperature measurements. A photograph of the test section with pressure transducers and thermocouples connections is shown in Figure 3-13.

Table 3-3. Common Specifications of the Omega PXM219 pressure transducers

gauge pressure range	0 – 2.5 bar
output	0 – 10 Vdc
accuracy	0.25% (full scale, including linearity, hysteresis and repeatability)
response time	2 ms typical
operating temperature	-54°C – 121°C

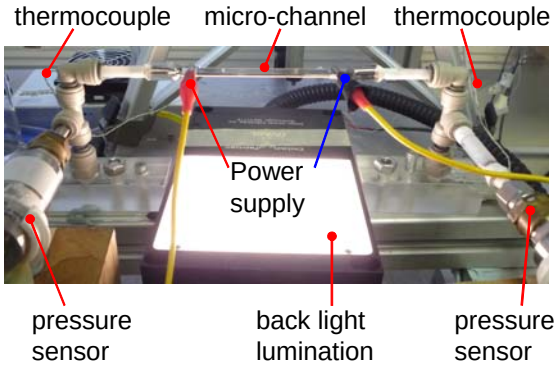

Figure 3-13. Micro-channel test section connected with pressure transducers and thermocouples

3.2.2. Micro-channel test section

The flow boiling test sections were rectangular borosilicate glass channels, which were purchased from VitroCom®. Borosilicate glass is widely used in laboratory thanks to its excellent thermal properties with low coefficient of expansion and high softening point. It also offers a high level of resistance towards the attack from water, acids, salt solution, organic solvent and halogens (Höhmann and Stephan [191]). Some physical properties of borosilicate glass are listed in Table 3-4.

Table 3-4. Physical properties of borosilicate glass (Höhmann and Stephan [191])

coefficient of expansion (20°C-300°C)	3.3×10^{-6} K^{-1}
density	2.23 g·cm^{-3}
specific heat (20°C)	750 J·kg^{-1}·K^{-1}
thermal conductivity (20°C)	1.14 W·m^{-1}·K^{-1}
thermal diffusivity	6.816×10^{-7} m^2·s^{-1}
Young's Modulus (25°C)	6400 kg·mm^{-2}
softening point	820°C

Selected channel geometries in the present study are listed in Table 3-5. The cross-sectional aspect ratio is the ratio of channel inner width to inner depth, *i.e.* $\alpha = W_{in} / d_{in}$. The heated channel length was 80 mm. A layer of tantalum was sputtered on the channel outer surface to provide thermal energy when both ends of the layer were connected to a

DC power supply. Figure 3-14 is a schematic drawing of the micro-channel test section. The channel was then sealed in the test section using plastic tubes, PTEF thread seal tape as connected with John Guest® push-pull fittings. The high aspect ratio channels and heating technique were previously used in the doctoral study of Barber [192] and following publications Barber *et al.* [93], Barber *et al.* [54]. The present study uses the transparent heating technique but the channels are horizontally positioned compared with the vertical channels in [54, 93 and 191]. Besides, the analysis on heat transfer, evaporation, and the use of nanofluids in the high aspect ratio micro-channel geometry have never been conducted previously.

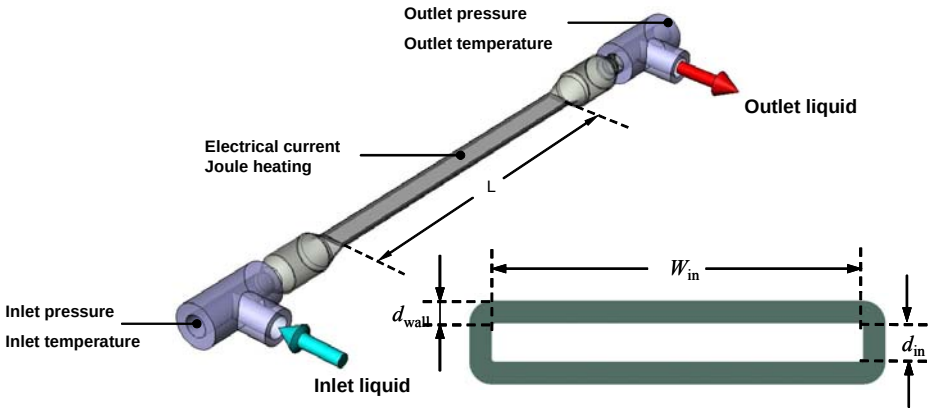

Figure 3-14. Schematic drawing of the test section and the channel cross section geometry

Hydraulic diameter d_h is commonly used as the characteristic length of the micro-channel to enable the comparisons between channels with different cross-sectional geometries. Hydraulic diameter is calculated as:

$$d_h = \frac{4A_c}{P_w} = \frac{2W_{in}d_{in}}{W_{in}+d_{in}} \quad (3\text{-}1)$$

where A_c and P_w are the area and wetted perimeter of the channel cross-section.

It is worth mentioning that micro-channels normally have inner diameters in the range 1 μm – 1000 μm. In the present study, the confinement of the channel depth is dominant and the channel depth is used for channel size classification. The hydraulic diameter is simply a way to report the flat geometry to a more conventional circular geometry and has no physical implications. The channel depth ranges from 0.3 mm – 0.8 mm. Besides, the confinement number based on the channel hydraulic diameter is in the

range of 0.54 – 3.05, confirming that the channels can be considered as micro-channels according to Kew and Cornwell [25] .

Table 3-5. Selected channel geometries in the present study

channel	d_h [μm]	W_{in} [mm]	d_{in} [mm]	α	d_{wall} [mm]
1	571	6.0	0.3	20	0.3
2	762	8.0	0.4	20	0.4
3	1454	8.0	0.8	10	0.54

The channel internal surface roughness was analyzed by atomic force microscope (AFM). The channel surface was found to be highly smooth. As in Figure 3-15, the roughness of the channel inner surface is within ± 0.1 μm. Minor variations of surface roughness were found in different channels. In average, all the tests were conducted on very smooth surfaces and a roughness parameter of R_p = 0.1 μm was used for heat transfer calculation.

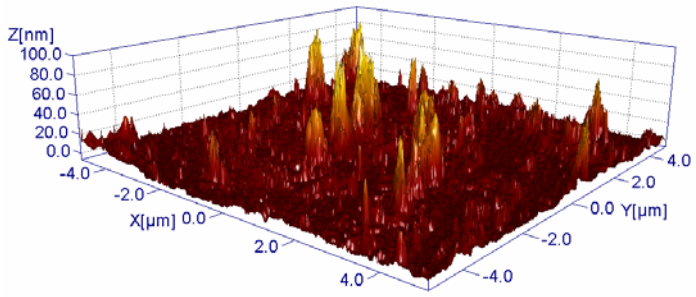

Figure 3-15. AFM image of micro-channel inner surface

Using the facilities described in session 3.2.1 and 3.2.2, the flow boiling and heat transfer in single micro-channel including the liquid-vapour phase change, single bubble growth, flow instabilities and heat transfer characteristics were experimentally investigated.

3.2.3. Confined bubble between two parallel plates

Apart from the single bubble growth which was captured during flow boiling in micro-channel, an extra test rig was designed to study the vapour bubble growth confined in micro-scale space without liquid flow. Fundamental experiments on confined bubble between two parallel plates could provide basic prospective on the vapour dynamics without interference from neighbouring bubbles or the shear effect of the liquid flow. As

in Figure 3-16, the rig consisted of two parallel plates with an adjustable gap. The gap was maintained by clamping a piece of foil between the plates. Thus the thickness of the foil determined the plate gap. In the present study, the tested gaps were 114 μm and 250 μm. A hole was drilled at the center of the bottom plate. A resistor was then attached under the hole and was powered by a DC power source to heat up the liquid around the hole, so that a vapour bubble could be generated at the specified location. In addition, an adhesive gauge tape was attached on the plate for spatial calibration. A CCD camera (SONY® XCD-X710 Firewire) ran at the speed of 30 fps to capture the growth of the bubble. The camera speed was sufficiently high to capture the bubble growth confined between the plates because the superheating and subcooling degrees of the plates were relatively low and the bubbles were growing slowly. After acquiring the visualization videos, ImagePro.® software was used for image processing. The temperatures of the parallel plates were controlled by changing the ambient temperature in the box and maintained at different levels of subcooling and superheating for each working liquid. Figure 3-17 shows the main components of the setups. Degassed FC-72 and n-pentane were the selected working liquids because of the low boiling points. The gap between the parallel plates was entirely filled with the working liquid. The edge of the gap between the two plates was left semi-open to ensure a constant pressure experiment. All the tests were conducted at atmospheric pressure.

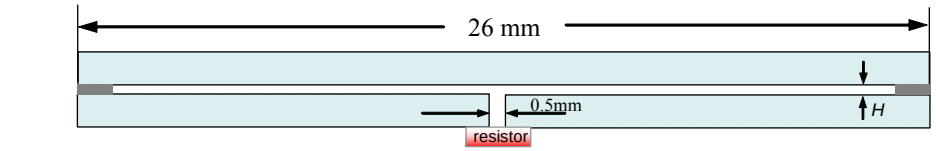

(a)

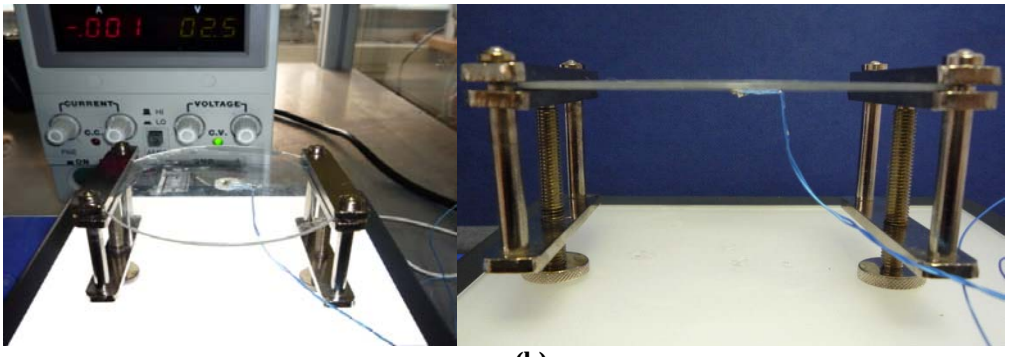

(b)

Figure 3-16. Parallel plates test section: (a) schematic drawing of the cross-sectional view, (b) test section assembly

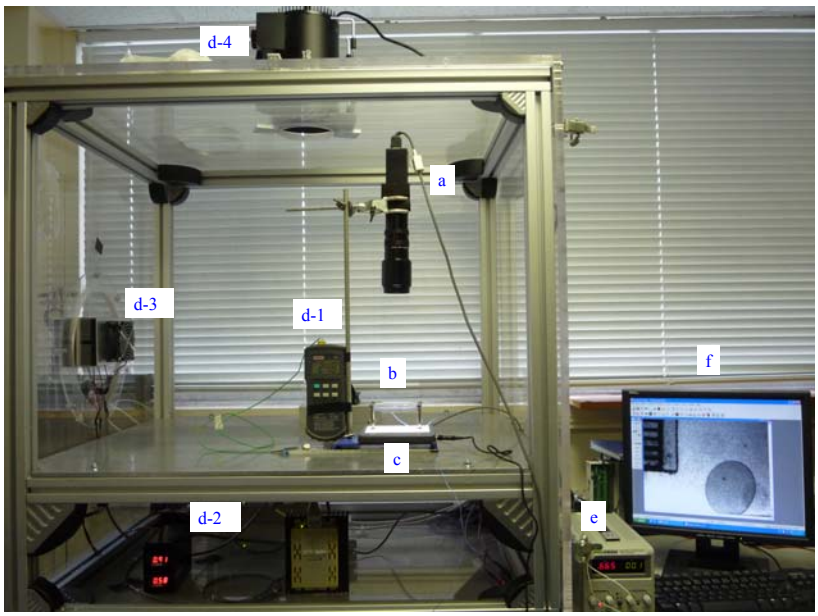

Figure 3-17. Experimental apparatus for confined bubble between two parallel plates: (a) CCD camera, (b) test section, (c) back light, (d-1~d-4) thermal regulation system, (e) power supply for the resistor, (f) image processing system

3.2.4. Meniscus evaporation in micro-channel

The spatial limitation of the micro-channel manifested the prevailing role of surface tension in micro-scale space. Furthermore, the micro-channel geometry had some influence on the liquid-vapour interface properties. Fundamental investigations on the interface could better understand the vapour dynamics and evaporation heat transfer mechanisms in micro-channel. It is of great importance to particularly focus on the meniscus behaviours during the evaporation in micro-channel. In order to do this, a test rig was built to be able to obtain visualisation results and channel wall temperature profiles at and around the meniscus, as shown in Figure 3-18. The experimental components including the high speed camera, infrared camera, syringe pump and micro-channel test-section were the same as those used in the flow boiling experiments which were introduced in session 3.2.1 and session 3.2.2.

The main interest of this part of experiments was the meniscus behaviours when confined in a high aspect ratio rectangular micro-channel. However, it was found that the steady meniscus was difficult to maintain if the channel was horizontally positioned. In addition, when the channel was horizontal, the thin-film region would extend to the channel exit and occasionally merge with the condensed liquid in the connecting pipe. Therefore, in order to obtain an immobile meniscus for long-time observation, the micro-

channel was vertically positioned. The channel bottom was connected to a syringe which could be considered as a reservoir; the other side of the channel was open to the air. There is an enlarged schematic drawing of the vertical test section in Figure 3-18. The channel surface coating was connected to a DC power supply for transparent heating. However, during the experiment, it was noticed that condensed liquid in the non-heated top-pipe would flow back to the test section. This backflow could be vaporised while rewetting on the channel wall, but part of it would still reach the meniscus and cause unexpected disturbance. Hence a resistor was used as a wrap heater on the top-pipe to avoid the condensed liquid backflow.

Pure ethanol and ethanol-based Al_2O_3 nanofluids were used to study the effect of nanoparticles on the evaporation rate and interface stability.

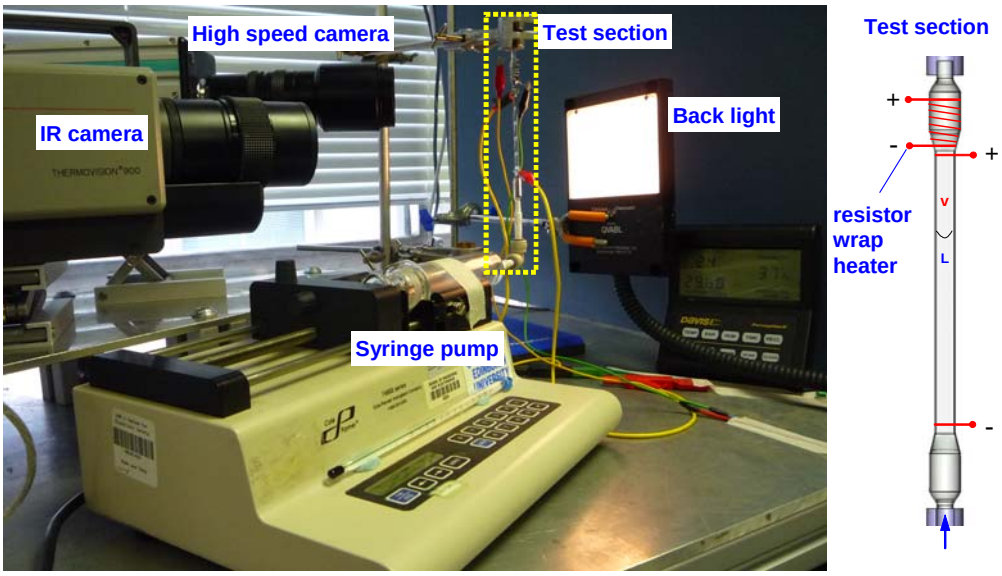

Figure 3-18. Experimental apparatus for meniscus evaporation in vertical micro-channel with an enlarged drawing of the test section

3.2.5. Working liquids properties

Different liquids were used in different parts of the present study. FC-72 and n-pentane were used in confined bubble between parallel plates tests. FC-72 and ethanol were chosen in the single micro-channel flow boiling tests. For the evaporation in vertical micro-channel experiments, however, ethanol and ethanol-based Al_2O_3 nanofluids with one concentration were tested so far. Further investigations with nanofluids are expected in the future work. Moreover, FC-72, ethanol and ethanol-based Al_2O_3 nanofluids were all used in the single phase tests, which were conducted prior to the two-phase flow

boiling experiments to check the experimental system availability and the validity of the conventional friction theory in micro-channel.

FC-72 is an appealing candidate for direct immersion cooling because it is chemically and electrically (high dielectric strength) compatible with microelectronic components (Mudawar and Maddox [193]). Ethanol and n-pentane were used in the present study for comparison and to examine the effect of liquid properties. From the secure point of view, all the selected liquids have moderate boiling points, therefore the channel wall temperature could be maintained at a moderate level during the experiments. Table 3-6, Table 3-7 and Table 3-8 list some of the thermophysical properties of FC-72, n-pentane and ethanol. Several key physical properties are compared in Figure 3-19 by equaling the properties of FC-72 as 100 (%), hence the corresponding property percentages of n-pentane and ethanol can be calculated and the differences can be highlighted.

Table 3-6. Properties of FC-72 (Consolini [194] and Yaws [195])

Properties	**FC-72 at 25°C, 1 atm**
boiling point	56°C
critical pressure	1.83×10^{6} Pa
latent heat of vaporisation (at normal boiling point)	88 $J\cdot g^{-1}$
liquid density	1680 $kg\cdot m^{-3}$
molecular mass	338.04 $g\cdot mol^{-1}$
vapour density	13.86 $kg\cdot m^{-3}$
vapour-liquid density ratio ρ_v / ρ_L	0.00825
kinematic viscosity	3.8×10^{-7} $m^2\cdot s^{-1}$
liquid dynamic viscosity μ_L	0.00064 Pa·s
vapour dynamic viscosity μ_v	7.19×10^{-6} Pa·s
liquid specific heat	1052.85 $J\cdot kg^{-1}\cdot K^{-1}$
liquid surface tension	0.01 $N\cdot m^{-1}$
thermal conductivity	0.05725 $W\cdot m^{-1}\cdot K^{-1}$

Table 3-7. Properties of n-pentane (Yaws [195])

Properties	**n-pentane at 25°C, 1 atm**
boiling point	36.1°C
critical pressure	3.36×10^{6} Pa
latent heat of vaporisation (at normal boiling point)	356.8 $J\cdot g^{-1}$
liquid density	621.3 $kg\cdot m^{-3}$
molecular mass	72.15 $g\cdot mol^{-1}$
vapour density	3.06 $kg\cdot m^{-3}$
vapour-liquid density ratio ρ_v / ρ_L	0.00493
kinematic viscosity	3.64×10^{-7} $m^2\cdot s^{-1}$
liquid dynamic viscosity μ_L	0.000226 Pa·s
vapour dynamic viscosity μ_v	7.32×10^{-4} Pa·s

liquid specific heat	158.274 $J \cdot kg^{-1} \cdot K^{-1}$
liquid surface tension	0.01549 $N \cdot m^{-1}$
thermal conductivity	0.148 $W \cdot m^{-1} K^{-1}$

Table 3-8. Properties of ethanol (Yaws [195])

Properties	**ethanol at 25°C, 1 atm**
boiling point	78.4°C
critical pressure	6.3×10^{6} Pa
latent heat of vaporisation (at normal boiling point)	846 $J \cdot g^{-1}$
liquid density	787.3 $kg \cdot m^{-3}$
molecular mass	46.07 $g \cdot mol^{-1}$
vapour density	1.5 $kg \cdot m^{-3}$
vapour-liquid density ratio ρ_v / ρ_L	0.00191
kinematic viscosity	1.34×10^{-6} $m^2 \cdot s^{-1}$
liquid dynamic viscosity μ_L	0.001057 Pa·s
vapour dynamic viscosity μ_v	1.04×10^{-5} Pa·s
liquid specific heat	2440 $J \cdot kg^{-1} \cdot K^{-1}$
liquid surface tension	0.02339 $N \cdot m^{-1}$
thermal conductivity	0.1694 $W \cdot m^{-1} \cdot K^{-1}$

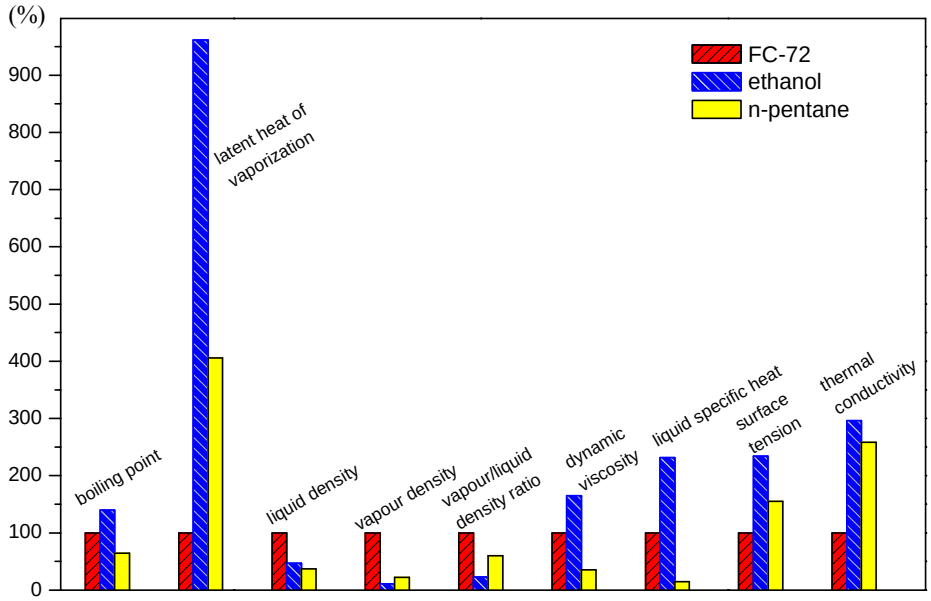

Figure 3-19. Percentage comparisons among the properties of FC-72, ethanol and n-pentane

3.2.6. Preparation of nano-fluids

Nanofluids were used to in the single phase flow tests and the investigation on evaporation in single micro-channels.

Nanoparticles (Sigma Aldrich®) were purchased in powder form. Figure 3-20 shows the nano-particles available in the lab. Aluminium oxide nanoparticles were firstly used

in the present study. The particle size was less than 50 nm according to the manufactures specifications.

The nano-fluid concentration was described in volume percentage, noted as vol.%. Nano-fluids were prepared by measuring the required mass of nano-particles using a microbalance (Figure 3-21) and dispersing the nanoparticles into the known volume of base liquid (ethanol was used in the present study). In order to achieve a good suspension, the fluids were mixed by an ultrasonic bath (Figure3-22) for three hours prior to testing.

Figure 3-20. Nano-particle samples available in the lab

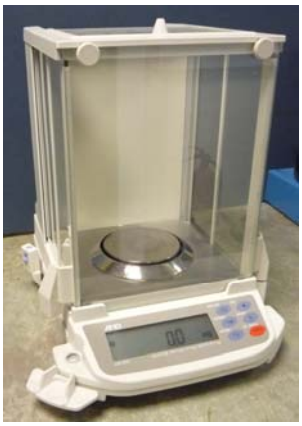

Figure 3-21. A&D GR-202-EC analytical balance used for nano-particle measurements

Figure 3-22. SKU:RK100H Sonorex Super Ultrasonic Bath - 3.0 Litre with Heater

A magnetic stirrer (Figure 3-23) was also used for nano-fluids dispersion. Nano-fluids solutions which were made by magnetic stirrer and ultrasonic bath were compared. Figure 3-24 – Figure 3-27 are the comparisons of nano-fluids with two different concentrations. The stability difference is more detectable for the 0.01 vol.% solution. It can be found that sedimentation occurred easier in the nano-fluids made by magnetic stirrer. Ultrasonication ensured better suspension stability. Therefore, ultrasonic bath was used for nano-fluids preparation. Most importantly, the nano-fluids made by ultrasonic bath could stay well-suspended for at least 7 hours, which was long enough to sustain sufficient stability for each set of experiment.

The physical properties of nanofluids such as density and dynamic viscosity which are needed for the related data reduction can be found in Chapter 4.

Figure 3-23. VELP® T.ARE Heating magnetic stirrer, F20520170

0 h 1 h 3 h 5 h 7 h

Figure 3-24. Ethanol-based Al_2O_3 nano-fluids, 0.01 vol.%, made by magnetic stirrer

0 h 1 h 3 h 5 h 7 h

Figure 3-25. Ethanol-based Al_2O_3 nano-fluids, 0.01 vol.%, made by ultrasonic bath

0 h 1 h 3 h 5 h 7 h

Figure 3-26. Ethanol-based Al_2O_3 nano-fluids, 0.1 vol.%, made by magnetic stirrer

0 h 1 h 3 h 5 h 7 h

Figure 3-27. Ethanol-based Al_2O_3 nano-fluids, 0.1 vol.%, made by ultrasonic bath

3.3. Data reduction

3.3.1. Mass flux

The mass flux was determined from the volume flow rate and the cross-sectional area of the micro-channel:

$$G = \frac{\dot{V}\rho_L}{A_c} \quad \textbf{(3-2)}$$

where $\dot{V}$ is the volume flow rate set by the syringe pump, ρ_L is the liquid density and A_c is the channel cross-sectional area.

In the present study, mass flux tested for single phase pressure drop ranged from 0 to 2170.9 $kg \cdot m^{-2} \cdot s^{-1}$. For two-phase flow boiling tests, the applied mass fluxes were set at 11.2 $kg \cdot m^{-2} \cdot s^{-1}$, 22.4 $kg \cdot m^{-2} \cdot s^{-1}$ and 44.8 $kg \cdot m^{-2} \cdot s^{-1}$ for each micro-channel. The conditions were selected because there are small amount of boiling heat transfer data at low mass flux conditions and the low mass flux conditions have the merit of minimal pressure drop.

3.3.2. Channel wall temperature processing

Efforts have been exerted to reasonably obtain reliable temperature data from the thermographic measurements for heat transfer calculation and analysis. Figure 3-28 shows an example of a map of wall temperature acquired by the infrared camera. Temperature varies across the surface area and increases in the flow direction. 17 equidistant locations along the channel axial direction were selected, the lines of which are illustrated in Figure 3-28. To show the spatial temperature variation, three averaged temperatures at upstream, middle-stream and downstream are plotted in Figure 3-29. All three spatial averaged temperatures show periodic fluctuation in time. The downstream temperature fluctuates at higher amplitude.

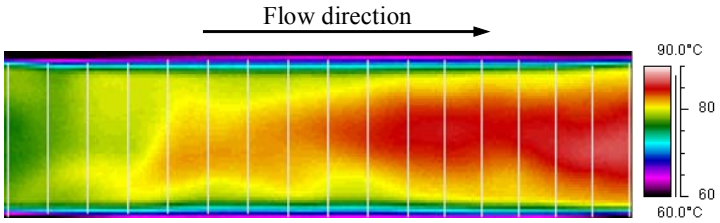

Figure 3-28. An example of transient channel wall temperature profile acquired by the infrared camera

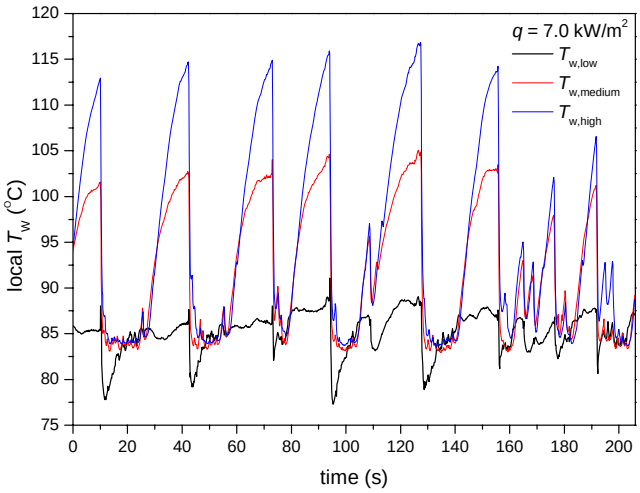

Figure 3-29. Temporal channel wall temperature fluctuation (d_h = 1454 μm at G = 11.2 kg·m^{-2}·s^{-1} and q = 7.0 kW·m^{-2})

The aim of the present study was to extract data to be able to plot boiling curves and averaged heat transfer coefficients. To do this, the average channel wall temperatures were required to be estimated from the transient wall temperatures. In order to assess the sensitivity of the average temperature to the averaging method used, the temporal temperature data were averaged using three methods. Firstly, arithmetic mean was applied on the entire temperature data group, expressed as:

$$\overline{T}_{\mathrm{W}} = \frac{1}{N}\sum_{i=1}^{N} T_{\mathrm{W},i} \tag{3-3}$$

where N is the total number of data point.

The average temperature could also be computed as:

$$\overline{T}_{\mathrm{W}} = \frac{1}{\tau}\int_0^{\tau} T_{\mathrm{W}}(t)\mathrm{d}t \tag{3-4}$$

where τ is the time during which the data group was obtained. In the present study, the data acquisition for each test usually lasted for 200 s – 400 s while the wall temperature fluctuation period was found to be less than 20 s. Since τ was much higher than the fluctuation period, the influence of τ on the mean wall temperature could be neglected.

Two numerical methods, *Simpson's Rule* and *Newton-Cotes Formula* (Butt [196]) were used to solve the integration in eq. (3-4).

Simpson's Rule was applied for the solution of $\int_0^{\tau} T_{\mathrm{W}}(t)dt$ using the following approximation:

$$\int_0^{\tau} T_{\mathrm{W}}(t)\mathrm{d}t \approx \frac{\tau - 0}{n}\left[\frac{T_{\mathrm{W}}(\tau) + T_{\mathrm{W}}(0)}{2} + \sum_{k=1}^{n-1} T_{\mathrm{W}}\left(k\frac{\tau - 0}{n}\right)\right] \tag{3-5}$$

where $n = \dfrac{\tau}{\mathrm{d}t}$.

Newton-Cotes Formula: $\int_0^{\tau} T_{\mathrm{W}}(t)\mathrm{d}t$ was also computed using the closed Newton-Cotes formula of degree n, calculated as:

$$\int_0^{\tau} T_{\mathrm{W}}(t)\mathrm{d}t \approx \frac{\tau}{n}\sum_{i=0}^{n} w_i T_{\mathrm{W}}(t_i) \tag{3-6}$$

where $t_{\mathrm{i}} = i\mathrm{d}t$ with $\mathrm{d}t$ (named as the step size) equals to τ / n. The w_i are called weights, and are derived from the Lagrange basis polynomials:

$$w_i = \int_0^{\tau} \prod_{\substack{k=0 \\ k \neq i}}^{n} \left(\frac{t-k}{i-k} \right) \mathrm{d}t \tag{3-7}$$

The averaged temperature data obtained using the *Simpson's Rule* and *Newton-Cotes Formula* were compared with the arithmetic mean results. As can be seen in Table 3-9, the differences among these three methods are insignificant. Besides, arithmetic mean is the simplest and least time-consuming among the three. Thus, arithmetic mean method is chosen as the temperature averaging method in the present study. The averaging of pressure data which was needed in Chapter 4 was also implemented using the arithmetic mean.

Table 3-9. Comparison of the temperature averaging methods

Method	Maximum deviation from the results calculated in Method 1 (%)
1. Arithmetic mean	0
2. Simpson's Rule	1.75
3. Newton-Cotes	0.61

3.3.3. Heat loss and heat flux

The effective heat Q_{eff} applied on the test section was calculated from the power supply and heat loss to environment. The total power Q supplied by a DC power supply was simply computed as $Q = UI$, where U and I are voltage and current.

For single phase, effective heat transferred to the liquid was estimated from the channel inlet and outlet temperatures:

$$Q_{\text{eff}} = C_{p,\text{L}} (T_{\text{out}} - T_{\text{in}}) \dot{m} \tag{3-8}$$

where $\dot{m}$ is the mass flow rate (kg·s^{-1}), $C_{p,\text{L}}$ is the specific heat capacity of the liquid, T_{in} and T_{out} are the inlet and outlet liquid temperatures respectively.

The heat flux was calculated as $q = Q_{\text{eff}} / A$, where A is the channel internal surface area. Successively the heat transfer efficiency $\phi = Q / Q_{\text{eff}}$ could be obtained.

For two-phase boiling, heat loss was estimated considering the convective loss Q_{conv} and radiative loss Q_{rad}.

The convective loss can be calculated in equation (3-9):

$$Q_{\text{conv}} = h_{\text{conv}} A_{\text{W,out}} (T_{\text{W,avg}} - T_{\text{envi}}) \quad \textbf{(3-9)}$$

where h_{conv} is the convective heat transfer coefficient of air and was estimated using the empirical correlations of natural convection external flow conditions. The calculation was conducted using the parameters of air at 25°C. The required properties of air were the properties at an averaged temperature of the channel wall temperature and the ambient temperature; $A_{\text{W,out}}$ is the outer surface area of the micro-channel surface. According to the channel geometry in Figure 3-14:

$$A_{\text{W,out}} = 2L(W_{\text{in}} + 2d_{\text{wall}}) + 2L(d_{\text{in}} + 2d_{\text{wall}}) \quad \textbf{(3-10)}$$

where L is the channel heated length.

$T_{\text{W,avg}}$ is the average channel wall temperature and T_{envi} is the environment temperature within the box. The radiative loss is calculated as:

$$Q_{\text{rad}} = \varepsilon \omega A_{\text{W,out}} (T_{\text{W,avg}}^4 - T_{\text{envi}}^4) \quad \textbf{(3-11)}$$

where ε is the total emissivity of the micro-channel tantalum deposit, and ω is the Stefan-Boltzmann constant (5.6703×10^{-8} $\text{W}\cdot\text{m}^{-2}\cdot\text{K}^{-4}$). About the emissivity of tantalum, there are only emissivity values in very high temperature ranges from literature (Malter and Langmuir [197], Allen *et al.* [198], Milošević *et al.* [199]). Since ε increases with increasing temperature, and ε was reported to be 0.136 at 1000 K (Malter and Langmuir [197]), in the present study, ε is approximated to be 0.1. Actually the calculated ε at 25°C already dropped to zero (Milošević *et al.* [199]). The calculated Q_{rad} was very low compared with the total heat Q_{eff}, thus the approximation of ε and Q_{rad} would not bring remarkable error to the heat loss calculation.

Thus $Q_{\text{eff}} = Q - Q_{\text{conv}} - Q_{\text{rad}}$ and the heat flux applied on the test section is $q = Q_{\text{eff}} / A$.

Heat transfer efficiencies $\phi = Q_{\text{eff}} / Q$ obtained in each channel at different mass fluxes were different. Each test condition was repeated 25 times, then the averaged heat transfer efficiencies were obtained and plotted in Figure 3-30.

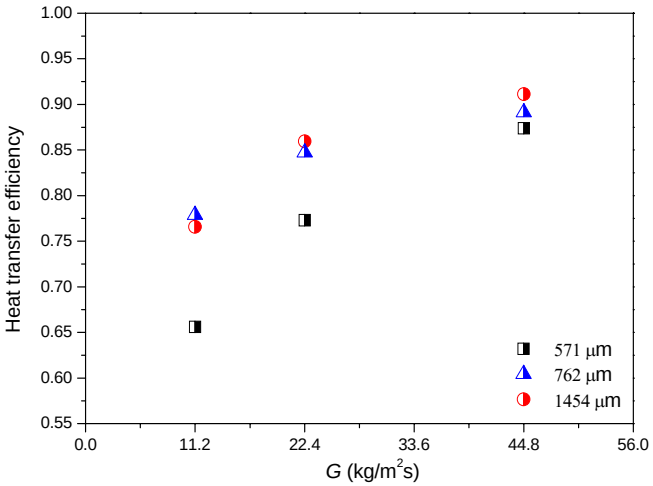

Figure 3-30. Heat transfer efficiency for each micro-channel at three different mass fluxes

It should be noticed that the infrared camera only measured the channel outer surface temperature profiles. Thus it is necessary to calculate the elapse time for the internal wall to reach the temperature of the external wall. The thickness of channel deposit was negligible compared with channel wall thickness. Then an estimation of elapse time can be simply calculated as,

$$t = \frac{(d_{\text{wall}})^2}{\alpha_{\text{W}}} \tag{3-12}$$

where d_{wall} is the channel wall thickness, α_{W} is the thermal diffusivity of the channel wall, computed as:

$$\alpha_{\text{W}} = \left(\frac{k}{\rho C_p} \right)_{\text{borosilicate}} \tag{3-13}$$

where k, ρ and C_p are the thermal conductivity, density and specific heat capacity of borosilicate glass respectively. α_{W} is 6.816×10^{-7} $m^2 \cdot s^{-1}$ for borosilicate, thus elapse time is found to be in the range of 0.13 s – 0.43 s depending on different channel wall thicknesses, which is relatively short compared with the time needed for the liquid to travel through the entire channel, t_t.

$$t_{\mathrm{t}} = \frac{L}{u} \tag{3-14}$$

Where L is the channel length and u is the liquid velocity in the channel.

Therefore, the temperature profile difference between the channel external and internal wall is neglected.

Besides, the calculation of Biot number allowed studying the temperature uniformity within the channel body by comparing the conduction resistance to the convection resistance. Biot number is calculated as:

$$Bi = \frac{h_{\mathrm{c}} d_{\mathrm{w}}}{k_{\mathrm{channel}}} \tag{3-15}$$

where h_{c} is the convective heat transfer coefficient in the fluid at the channel inner surface, and was estimated using the fully developed laminar flow in rectangular channel correlation (Shah and London [200]) with parameters of the working liquid at saturation temperature. d_{W} is the channel wall thickness and k_{channel} is the thermal conductivity of the channel body. Following the calculations, Biot number was found to be 0.076 – 0.184. Uniform temperature within the channel could be assumed according to M.Thirumaleshwar [201]. It is necessary to emphasis that, because of the unique geometry of the micro-channels, this is simply an estimate of the convective heat transfer coefficient. There maybe other ways to calculate h_{c} and consequently the Biot number. Thus the measured channel outer wall temperatures were used for heat transfer calculation. The calculations of heat transfer coefficient, local liquid temperature and vapour quality can be found in Chapter 8.

3.4. Uncertainty analysis

The experimental uncertainties mainly came from pump velocity, input power, channel dimension and temperature measurements. According to the standard uncertainty analysis of R.Taylor [202], uncertainties of channel surface area, mass flux, heat flux, heat transfer coefficient and vapour quality were estimated. Maximum uncertainties are summarized in Table 3-10:

Table 3-10. Experimental parameters and calculated results uncertainties

Parameter	Maximum Uncertainty
pressure	0.25%
pump volumetric velocity	0.5%
voltage	0.2%
current	0.5%
channel depth and thickness	10%
channel length and width	2%
IR camera measured temperature	1%
channel surface area	5.4%
channel hydraulic diameter	5.8%
bubble length and width	4%
mass flux	10.2%
heat flux	5.4%
pressure drop	0.5%
flow velocity	12.5%
friction factor	19%
bubble aspect ratio	8%
bubble nose and tail velocity	8%
bubble equivalent radius	8%
evaporation heat flux	16%
local liquid temperature	16.3%
heat transfer coefficient	17.2%
vapour quality	16.2%

3.5. Conclusions

An experimental system has been built to study the liquid-vapour phase change, flow boiling and heat transfer in single micro-channels. The three parts of the system have been introduced in detail, corresponding to the investigations on the flow boiling heat transfer in single micro-channels, single bubble between two parallel plates without liquid flow, and the meniscus evaporation in vertical micro-channels. The test sections were a number of high aspect ratio rectangular borosilicate glass micro-channels. The fabrication of the micro-channel transparent heating technique has been described. FC-72, n-pentane, ethanol and ethanol-based nanofluids are used as working liquids, the properties and preparation of which have been presented. The selected working fluids were all compatible with the connections and tubing of the setups. Besides, some general data reduction and the experimental parameter uncertainties have been provided in this chapter.

Chapter 4

Single phase friction factor in micro-channels

4.1. Introduction

As the use of micro-channel flow passage for heat dissipation is becoming more popular in various applications in industry, medicine and space (Sefiane *et al.* [203], Johannes *et al.* [204]), the performances of the micro-channel flow systems become more crucial. Any enhancement in the hydraulic and thermal characteristics of the micro-channel flow passages could help improve the cooling efficiency, reduce the costs of the applications and bring some remarkable practical benefits. Flows in micro-channel passages inevitably involve the dynamics of fluids. However, the availability of conventional friction theory in micro-scale flow passages is still an unclosed topic.

Efforts have been made to analysis the friction factor, the transition from laminar to turbulent flow and the convective heat transfer during single phase liquid flow in micro-channels. Comprehensive reviews on micro-channel single phase flow can be found (Papautsky *et al.* [205], Morini [206], Steinke and Kandlikar [207]). Experimental investigations on single phase pressure drop in micro-channels published from 1981 to 2004 have been covered. Some have achieved good agreement with friction theory for conventional channel. Conspicuous discrepancies between micro-channel flow friction and conventional channel flow friction were reported in several studies (Harley *et al.* [208], Rahman and Gui [209], Peng and Peterson [210], Mala and Li [211], Rahman [212]). On the contrary, fully developed Poiseuille number $C = fRe$ was found lower than the theoretically predicted values (Pfahler *et al.* [213]). Steinke and Kandlikar [3] corrected the pressure drop data which were claimed to show great discrepancy with conventional theory by considering the entrance and exit loss as well as the developing flow pressure loss, and better agreements were achieved. Furthermore, Peng and Peterson [210] presented fRe as a function of Reynolds number for friction factor in rectangular micro-channels. In the function there was an aspect-ratio-dependent empirical coefficient, the dependency of which was not clarified. In fact, the crucial role of channel aspect ratio on single phase liquid flow friction needs to be further analyzed, especially upon the results obtained in high aspect ratio channels.

Early transition from laminar flow to turbulent flow has also been focused. Morini [206] published an exhaustive review on single phase convective flow. Early transition from laminar flow to turbulent flow has been previously reported (X.Wang and F.Peng

[214] , Peng and Peterson [210], Peng and Peterson [215], Peng and Peterson [216], Mala and Li [211], Jiang *et al.* [217] and Bucci *et al.* [218]). The critical Reynolds number at which the flow drifted away from laminarity was considered to rely on the channel wall roughness and micro-channel hydraulic diameter.

In addition, the need for a more effective heat transfer system is increasing so drastically that people start using nanofluids in the micro-scale passages. It is conceivable that the additional nanoparticles in liquids might affect the fluids dynamics. Experimental investigations of convective flow with nanofluids were overviewed in Chapter 2, session 2.5. More experiments on single phase flow in micro-channels with high-aspect-ratio geometry are necessary for enlarging the friction factor database of micro-scale flows.

In the present study, single phase flow tests were conducted prior to the two-phase flow boiling experiments mainly to check the validity of experimental setups, data measurements and data reduction. Single phase pressure drop with pure liquids and nanofluids was obtained; Darcy friction factor was calculated and compared with the fully developed laminar flow correlation. The hydrodynamic developing entrance length in the micro-channel was analyzed based on theoretical correlation. Based on the Poiseuille number, early transition from laminar flow to turbulent flow was also discussed. Besides, effects of liquid properties on pressure drop were investigated. Different fluids were used, including ethanol,FC-72, and four concentrations of ethanol-based Al_2O_3 nanofluids. Friction factors of FC-72 and ethanol were compared to examine the influences of liquid physical properties while the comparisons among pure ethanol and ethanol-based nanofluids intend to highlight the effect of nanoparticles. Furthermore, the influence of channel geometry on single phase friction factor has been emphasized.

4.2. Experimental setup and procedure

Single phase flow tests were conducted prior to the two-phase flow boiling experiments to examine the setup availability. The experimental setups described in Chapter 3, session 3.2.1 and 3.2.2 were utilised. Single phase pressure drop data in single micro-channel were obtained. There was no heat flux applied on the micro-channel during the single phase test. FC-72, ethanol, and ethanol-based Al_2O_3 nanofluids with four different

particle concentrations: 0.01 vol.%, 0.05 vol.%, 0.1 vol.% and 0.5 vol.% , were used as working fluids in the present study. The pure liquids were vigorously degassed for one hour before entering the flow loop to remove the dissolved gases. The degassed pure ethanol was later used as the base fluid of the nanofluids. Micro-channels with three different hydraulic diameters were selected, the dimensions and cross-sectional aspect ratio of which are listed in Chapter 3, Table 3-5.

During single phase flow, the inlet and outlet pressures of the micro-channel test section were measured via a pair of pressure transducers located at the channel entrance and exit. The pressure readings were taken with a National Instrument® Data Acquisition card at a predetermined acquisition frequency of 200 Hz. The offset pressures resulted from the background noises were recorded prior to each test when the channel was filled with stagnant working fluid. Then the offset pressures were subtracted from the acquired raw data. Darcy friction factor was calculated and compared with the predictions of conventional theory. In addition, effect of nano-particle concentration on single phase friction factor was discussed.

After each test with nanofluids, all the components in the entire flow loop including connecting pipes, valves, reservoir and micro-channel test section were thoroughly cleaned by running water, ultrasonic bath and compressed air in order to remove the nanoparticle deposition on the channel inner surface.

A series of single phase pressure drop measurements were taken as increasing the volume flow rate from 1 $ml \cdot min^{-1}$ to 144 $ml \cdot min^{-1}$, which were limited by the pumping capacity. Experiments at each series of flow rate in each micro-channel were repeated for three times on different days. It was found that the deviations among the pressure drops were less than 5%. The minor deviations indicated the good reproducibility of the experiment. Then the three groups of pressure drop results in each test series were averaged and used for friction factor calculation.

4.3. Data reduction

4.3.1. Pressure drop

The difference between inlet and outlet pressures was noted as the total pressure drop ΔP_{Total}. However, the frictional pressure drop must be corrected by subtracting the entrance and exit loss, loss due to sudden expansion and contraction, and the developing

loss from ΔP_{Total}. The micro-channel and the connection pipes are schematically illustrated in Figure 4-1. The rectangular test section was fabricated in the working loop by gradually connecting to circular pipes.

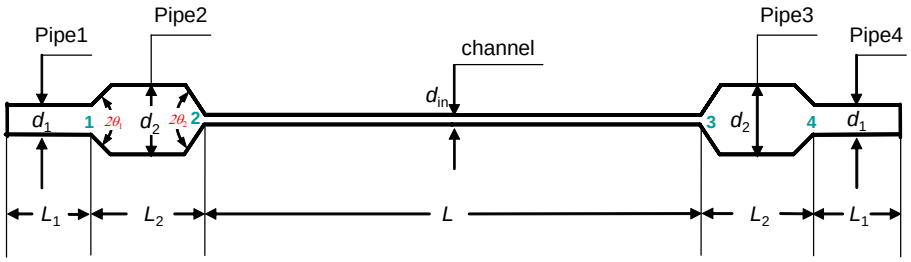

Figure 4-1. Micro-channel test section and connecting pipes showing the locations of expansion and contraction

The direct pressure drop ΔP_{Total} includes friction loss in the micro-channel and Pipe 1 – Pipe 4 as well as the minor loss due to sudden expansion or contraction at pipe connections and the loss in hydrodynamic developing flow. The raw pressure drop comprised the following components:

$$\Delta P_{\text{Total}} = \sum_{\text{n=1,2,3,4}} \Delta P_{\text{fn}} + \sum_{\text{n=1,2,3,4}} \Delta P_{\text{sn}} + \Delta P_{\text{cd}} + \Delta P_{\text{cf}} \quad \textbf{(4-1)}$$

where $\sum_{\text{n=1,2,3,4}} \Delta P_{\text{fn}}$ is the sum of friction loss in the four connection circular pipes calculated as (White [219]):

$$\Delta P_{\text{fn}} = f \frac{L_{\text{n}}}{d_{\text{in,n}}} \cdot \frac{\rho u_{\text{pipe}}^{\ 2}}{2}, \quad \text{n} = 1,2,3,4 \quad \textbf{(4-2)}$$

where L_{n} and d_{in} are the length and inner diameter of the pipes, ρ is the liquid density, u_{pipe} is the liquid velocity within the pipes and f is the Darcy friction factor in circular tube calculated as $f = 64/Re$.

$\sum_{\text{n=1,2,3,4}} \Delta P_{\text{sn}}$ is the loss due to sudden expansion and contraction at pipe connections, (illustrated as locations 1, 2, 3 and 4 in Figure 4-1) and is estimated as:

$$\Delta P_{sn} = K_n \frac{\rho u_n^{\,2}}{2}, \mathrm{n} = 1,2,3,4 \quad \textbf{(4-3)}$$

where u_n is the velocity head at each location, K_n are the loss coefficients. Though the glass pipes and the micro-channel test section are gradually connected, the cone angle is very large, *i.e.* $2\theta \approx 180\,°$. Thus it can be considered as the sudden expansion and contraction situations. According to White [219], for the sudden expansion from a small pipe with a diameter of d to a large pipe with a diameter of D, there is a theoretical equation for the sudden expansion loss coefficient, note that K_n is based on the velocity head in the small pipe.

$$K_n = \left(1 - \frac{d^2}{D^2}\right)^2, \mathrm{n} = 1 \text{ and } 3 \quad \textbf{(4-4)}$$

In the present study, sudden expansion is encountered at location 1 and 3. The channel hydraulic diameter is used as the diameter d of the test section. It can be calculated that $K_1 = 0.79$ and $K_3 = 0.991$, 0.986 and 0.948 for the 571 μm, 762 μm and 1454 μm channel respectively.

For the sudden contraction, on the other hand, there is an empirical correlation for the contraction loss coefficient:

$$K_n \approx 0.42\left(1 - \frac{d^2}{D^2}\right), \mathrm{n} = 2 \text{ and } 4 \quad \textbf{(4-5)}$$

Sudden contraction is encountered at location 2 and 4. Accordingly, $K_4 = 0.37$ and $K_2 = 0.418$, 0.417 and 0.409 for the channels with d_h = 571 μm, 762 μm and 1454 μm respectively.

Additionally, pressure drop in hydrodynamic developing region in the micro-channel is noted as ΔP_{cd} and is calculated according to the correlation for developing laminar flow in circular tube by Shah and London [220]:

$$\Delta P_{cd} = \frac{1}{2}\rho u^2 \left(13.74\sqrt{L_{df}^+} + \frac{1.25 + 64L_{df}^+ - 13.74\sqrt{L_{df}^+}}{1 + 0.00021(L_{df}^+)^{-2}}\right) \quad \textbf{(4-6)}$$

where L_{df}^{+} is dimensionless hydrodynamic developing flow entrance length based on the hydrodynamic developing entrance length L_{df}:

$$L_{df}^{+} = \frac{L_{df} / d_{in}}{Re} \tag{4-7}$$

where d_{in} is the inner diameter of the circular tube. In the present study, the hydraulic diameter of the rectangular channel is used for the calculation.

According to Shah and London [200], the values of L_{df}^{+} can be computed as:

$$\begin{aligned} L_{df}^{+} &= 0.0565 \quad \text{for } Re > 400; \\ L_{df}^{+} &= 0.0565 + \frac{0.60}{Re(1+0.035Re)} \quad \text{for } Re < 400 \end{aligned} \tag{4-8}$$

Thus, $\Delta P_{cf} = \Delta P_{Total} - \sum_{n=1,2,3,4} \Delta P_{fn} - \sum_{n=1,2,3,4} \Delta P_{sn} - \Delta P_{cd}$ is the frictional pressure loss within the channel in fully developed flow region. It is worth noting that in the present study, when Reynolds number is high, the hydrodynamics entrance length is longer than the channel length in the 1454 μm micro-channel, thus ΔP_{cf} is the frictional pressure drop in developing flow conditions after subtracting the above non-frictional losses $\sum_{n=1,2,3,4} \Delta P_{fn}$ and $\sum_{n=1,2,3,4} \Delta P_{sn}$.

Darcy friction factor is then calculated as:

$$f = \frac{2\Delta P_{cf} d_h}{\rho u^2 L} \tag{4-9}$$

where d_h is the micro-channel hydraulic diameter, ρ is the liquid density, u is the mean liquid velocity in the micro-channel and L is the channel length.

According to the calculation, the minor losses increase with increasing Reynolds number, and the relevant importance of $\sum_{n=1,2,3,4} \Delta P_{fn}$, $\sum_{n=1,2,3,4} \Delta P_{sn}$ and ΔP_{cd} changes in the ranges of 0.16 % – 0.25 %, 0.01 % – 0.35 %, and 0.81 % – 32.1 % respectively, thus the frictional pressure drop is 67.4 % to 98.9 % of the measured total pressure drop. Besides,

the uncertainty of friction factor is estimated to be 19 % (as shown in Table 3-10 in Chapter 3).

4.3.2. Liquid velocity and Reynolds number

The liquid velocity in micro-channel is estimated according to the channel cross-section geometry and the volumetric flow rate. Then the liquid Reynolds number is calculated using the liquid velocity and the channel hydraulic diameter.

$$u = \frac{\dot{V}}{A_c} \tag{4-10}$$

$$Re = \frac{\rho u d_h}{\mu} \tag{4-11}$$

where the hydraulic diameter d_h is defined to be four times of cross-sectional area divided by the perimeter of the cross section; ρ and μ are the liquid density and viscosity respectively.

4.3.3. Nanofluids properties for correlation

Two properties of the nanoparticle suspensions involved in calculating the friction factor are density and dynamic viscosity of the nanofluids, which are different from the original pure liquid because of the additional particles. For the nanoparticle suspension, the effective density is estimated following Xuan and Roetzel [150]:

$$\rho_{nf} = \phi\rho_p + (1-\phi)\rho_f \tag{4-12}$$

where ϕ is the volume fraction of nanoparticles, ρ_p and ρ_f are the densities of the nanoparticle material and the base liquid respectively.

There exist a few theoretical formulas to calculate the nanofluid viscosity. In the present study, the extended Einstein's equation by Brinkman [221] is used to estimate the effective viscosity of nanofluids with moderate particle concentrations:

$$\mu_{nf} = \mu_f \frac{1}{(1-\phi)^{2.5}} \quad \textbf{(4-13)}$$

where μ_{nf} is the effective viscosity of the nanofluid with a particle volume fraction of ϕ, and μ_f is the pure liquid viscosity.

4.4. Results and discussions

4.4.1 Single phase friction factor of FC-72

Single phase tests were conducted prior to two-phase flow boiling. Pressure drop across the test section was obtained based on the pressure measurements. Pressures at channel inlet and outlet were directly captured by pressure transducers via NI DAQ card and written as readable files. Pressure drop cross the channel was then the difference between inlet and outlet pressures. At a given mass flux, constant pressure drop with minor noises were acquired. Figure 4-2 gives an example of the obtained pressure drop in the micro-channel with d_h = 1454 μm at G = 44.8 kg·m^{-2}·s^{-1}. For each test, the measurement of the pressure data lasted for at least 150 s and then the arithmetic mean value of the pressure drop ($\overline{\Delta P} = \frac{1}{N}\sum_{i=1}^{N}\Delta P_i$, where N is the amount of the data points) was used for friction factor calculation.

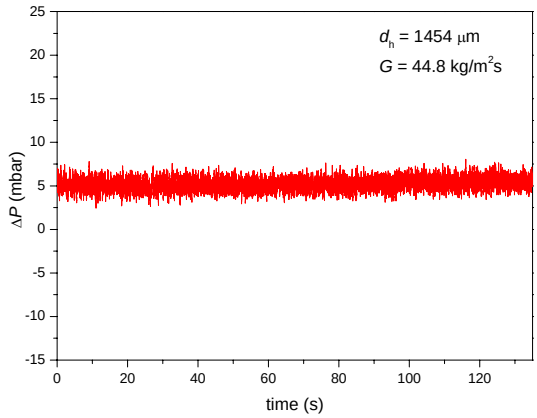

Figure 4-2. Pressure drop in the channel with d_h = 1454 μm at G = 44.8 kg·m^{-2}·s^{-1}

The frictional pressure drop in the single phase micro-channel flow is plotted against the Reynolds number in Figure 4-3. The comparisons among the results of FC-72 in all

the three channels highlight the effect of channel dimension on the pressure drop. As per the Poiseuille Law, it is as expected that the pressure drop increases with increasing Reynolds number and decreasing channel hydraulic diameter.

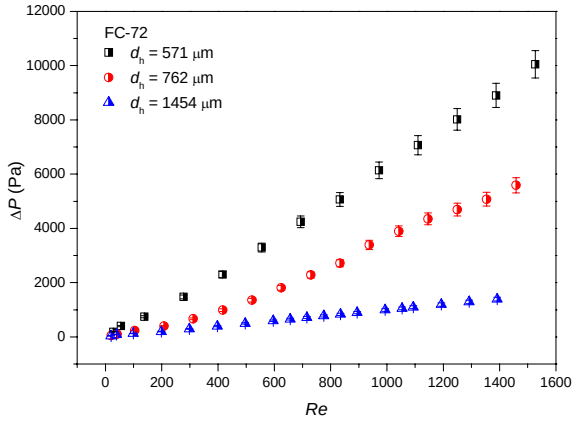

Figure 4-3. Frictional pressure drop in the three micro-channels; FC-72

Succeedingly, the single phase friction factor is plotted against the corresponding Reynolds number. The acquired friction factor was compared with the fully developed laminar flow friction factor for conventional rectangular channels (Shah and London [200]), which is given as a function of Reynolds number and the channel aspect ratio:

$$f = (96/Re)\begin{pmatrix} 1-1.3553\alpha+1.9467\alpha^2-1.7012\alpha^3 \\ +0.9564\alpha^4-0.2537\alpha^5 \end{pmatrix} \quad \textbf{(4-14)}$$

where α ($\alpha < 1$) is the channel cross-sectional aspect ratio. If the aspect ratio is greater than one, the reciprocal is taken to use.

Friction factor versus Reynolds number for FC-72 is plotted in Figure 4-4 and Figure 4-5. Figure 4-4 (a) and (b) are the friction in the 571 μm and 762 μm channel respectively. The results obtained in the 1454 μm channel are separately plotted in Figure 4-5 for detailed discussions. The solid lines in Figure 4-4 are the predictions from eq. (4-14) which gives $f = 89.9/Re$ for both 571 μm and 762 μm channels. Good agreements are achieved in the 571 μm and 762 μm micro-channels within ± 10%. The maximum Reynolds numbers terminate at 1391 to 1943 due to the limitation of the pumping capacity.

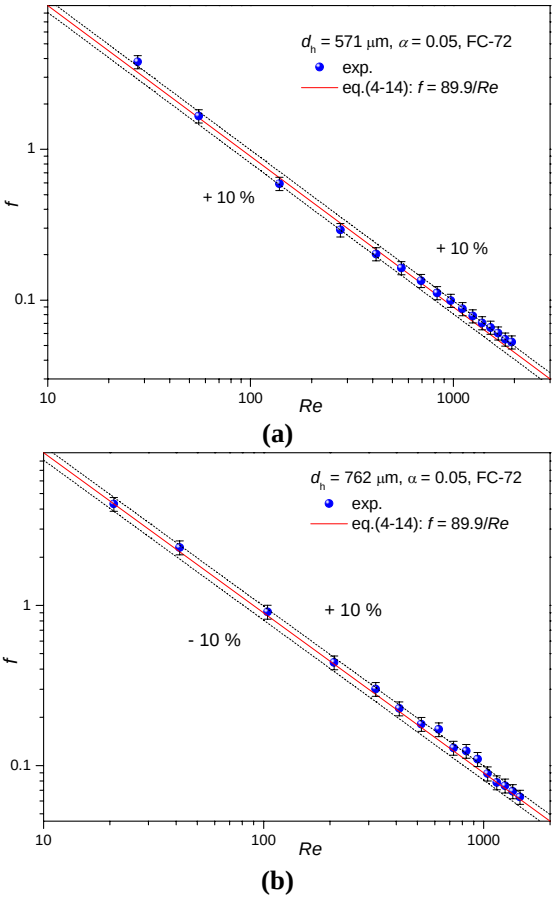

Figure 4-4. Comparisons of the measured friction factors with conventional friction correlations in the channels with (a) d_h = 571 μm, (b) d_h = 762 μm; FC-72

The friction factors in the channel with d_h = 1454 μm do not agree with the predictions from eq. (4-14) and stay above the predicted friction factors beyond 30% as in Figure 4-5. Interestingly, the deviation between the friction factor and the predictions increase as the Reynolds number rises. The dependency of f on Re was also reported by Peng *et al.* [222] and Peng and Peterson [210]. Peng and Peterson [210] proposed an empirical correlation for single phase friction factor in microchannels in the following form:

$$f = \frac{C}{Re^{1.98}} \tag{4-15}$$

where C is the empirical coefficient for laminar flow and is related with the micro-channel geometric configuration. Eq. (4-15) is plotted in Figure 4-5 as the black dash line and the coefficient C = 2310.3 is obtained by fitting to the present data. However,

large deviations are still found. Better agreement is achieved by modifying both of the coefficients in eq. (4-16):

$$f = \frac{C_1}{Re^{C_2}} \tag{4-16}$$

where C_1 and C_2 are the modified empirical coefficients based on present experimental data and are fitted to be 317.76 and 1.11 respectively.

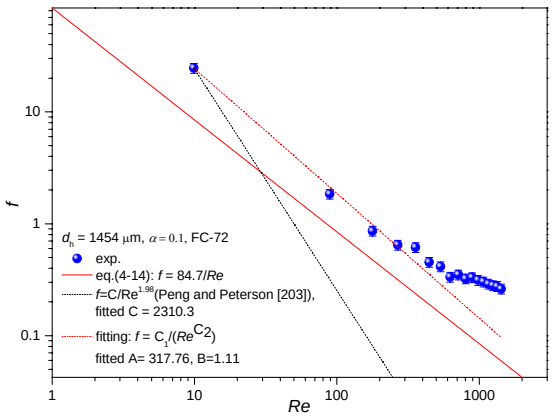

Figure 4-5. Comparisons of the measured friction factors in the 1454 μm micro-channel with conventional friction correlations; FC-72

Moreover, according to eq. (4-7) and eq. (4-8), the hydrodyanmic developing entrance length can be estimated as:

$$L_{\mathrm{df}} = d_{\mathrm{in}}\left(0.0565Re + \frac{0.6}{1+0.035Re}\right) \tag{4-17}$$

The hydrodynamic developing entrance lengths in each channel are shown in Figure 4-6. It is found that in the 1454 μm channel, the entrance length becomes longer than the available channel length from Re = 980 and afterward. Thus for Re > 980, the flow in the entire channel test section is developing in nature. This probably partly explains the deviation of f at high Re region from the conventional theory for fully developed flow in the 1454 μm channel.

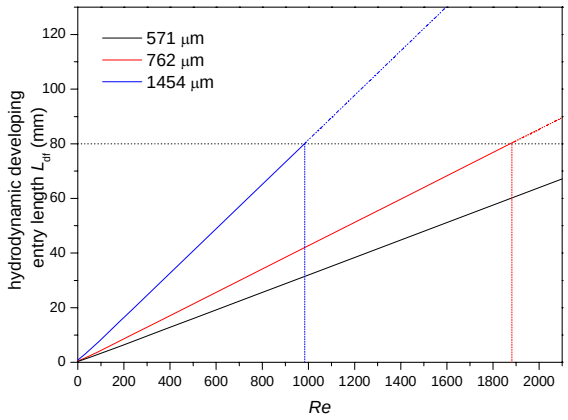

Figure 4-6. Hydrodynamic developing entrance length in the three micro-channels; FC-72

However, for those friction factors measured at relatively low Reynolds number, the fully developed friction factors in the 1454 μm channel are also greater than the predictions. In order to avoid the equipment error, all the 1454 μm channels available in the lab have been examined, and the same fiction factor magnitude scale within ± 5% was obtained. Further experiments with wider ranges of channel dimensions and inner surface roughness are necessary to clarify the reasons for the deviation from conventional friction theory in the 1454 μm in low Reynolds number region.

Furthermore, Poiseuille number (*Po*) is plotted against Reynolds number. Poiseuille number is constant in laminar flow. Any increase of Poiseuille number implies the deviation from laminarity and will contribute to the transition to turbulent flow. In Figure 4-7, Poiseuille numbers in the 571 μm and 762 μm channels are independent of Reynolds number. The red dash lines are the theoretical values calculated using eq. (4-14) ($fRe = 89.9$ for both of the channels). In Figure 4-7 (a), there is a dip of Po at low Re region. The reason of the dip is unclear but it is within the uncertainties. It can be assured that the liquid flows in 571 μm and 762 μm channels are laminar.

However, in Figure 4-7 (c), the *Po* versus *Re* curve of the 1454 μm channel shows a conspicuous increase at the Reynolds number ranging from 600 – 700, indicating the commencement of transitional flow. This transition inception is much earlier than the conventional flow where the transition normally takes place at *Re* = 2300. Early transition from laminar to turbulent flow in micro-channels has been previous reported by [210, 211, 215-218, 222]. Effects of channel geometry, hydraulic diameter and aspect ratio were highlighted. It has been pointed out that the critical Reynolds number for the transition decreases with decreasing hydraulic diameter. On the contrary, in the present study, the hydraulic diameter changing from 571 μm to 762 μm showed no significant

influence on the flow laminarity, but the critical *Re* decreased when hydraulic diameter increased to 1454 μm, the aspect ratio of which was lower than the other two channels.

Moreover, the experimentally obtained *Po* in the 1454 μm channel is much higher than the predictions from Blasius equation for smooth surface turbulent pipe flow (White [219]). In Figure 4-7 (c), the *Po* is increasing with *Re* following $fRe = 1.65Re^{0.75}$. The deviation may be caused by the channel surface roughness and, more importantly, the high-aspect-ratio cross-sectional geometry. Velocity boundary layer developments on different channel surfaces might have significant variations due to the high-aspect-ratio. Thus the corresponding flow field is expected to be much more complex than in the conventional circular tube. So far, the reason why the friction increases with increasing hydraulic diameter and decreasing cross-sectional aspect ratio is still unclear. More experiments with high-aspect-ratio micro-channels are needed to seek for the explanations.

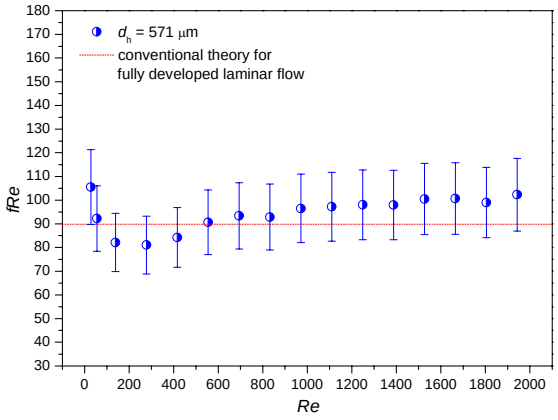

(a)

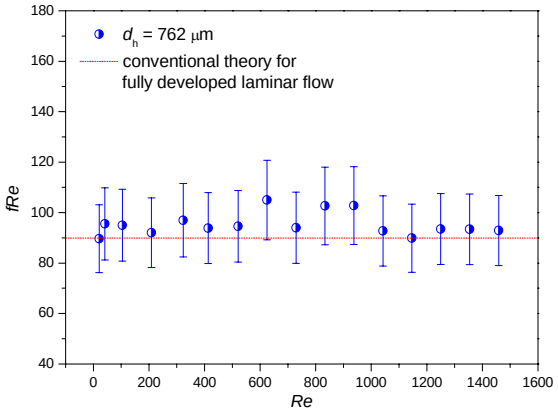

(b)

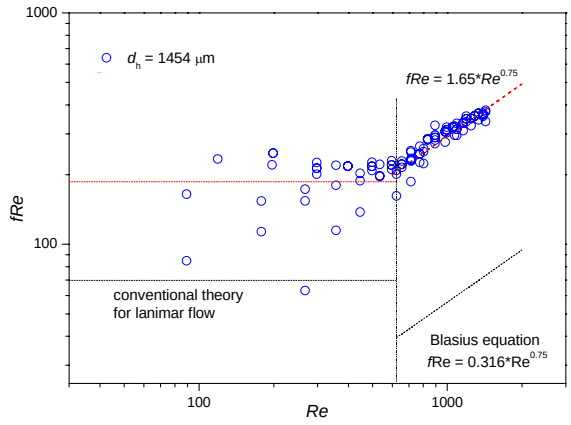

(c)

Figure 4-7. Poiseuille number ($Po = fRe$) versus Reynolds number for the channels with (a) d_h = 571 μm, (b) d_h = 762 μm, (c) d_h = 1454; FC-72

Based on the above analysis, the flow in 1454 μm channel can be classified into three stages as shown in Figure 4-8. At low Reynolds number ($0 < Re < 600$) , the flow is laminar flow and will be fully developed somewhere inside the channel; for $600 \le Re < 980$, the flow starts to drift away from laminarity but still will be fully developed somewhere inside the channel; For $Re > 980$, turbulent developing flow will be encountered.

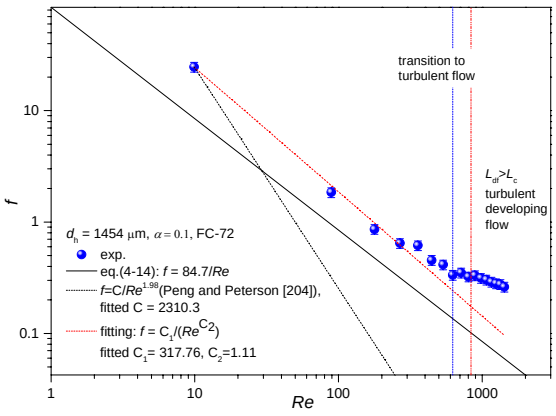

Figure 4-8. Comparisons of the measured friction factors in the 1454 μm micro-channel with conventional friction correlations and flow classification; FC-72

4.4.2 Single phase friction factor of ethanol

In order to investigate the effect of working fluids on single phase pressure drop, ethanol was also used, and the corresponding friction factors obtained in the three micro-channels are plotted in Figure 4-9 (a)-(c). The experimental data are compared with the predictions of eq.(4-14). Similarly, better agreements are achieved in the 571 μm and

762 μm channels than in the 1454 μm channel. The experimental data fall in the range of ±20% of the theoretical predictions in 571 μm and 762 μm channels. It is noticed that measured friction is lower than the theoretical predictions in the 571 μm and 762 μm channels, but the increasing channel size has an enhancing effect on the friction factor. Additionally, the friction factor data are fitted to the correlation $f = C/Re$, where C is an empirical coefficient. Correspondingly the fitted C increases from 75.3 to 124.6 when channel hydraulic diameter increases from 571 μm to 1454 μm.

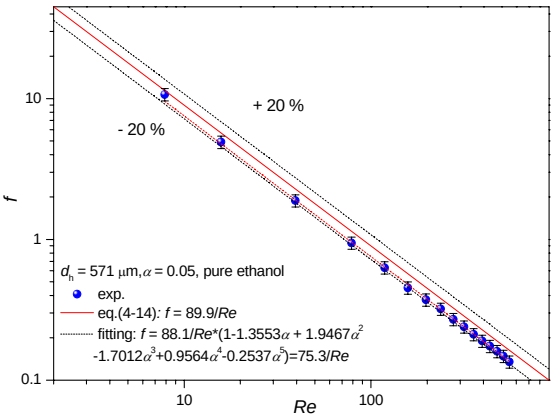

(a)

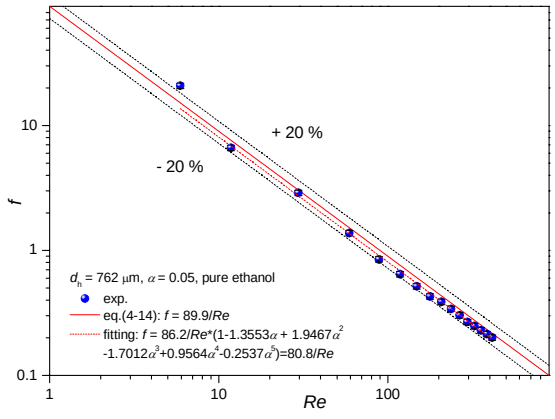

(b)

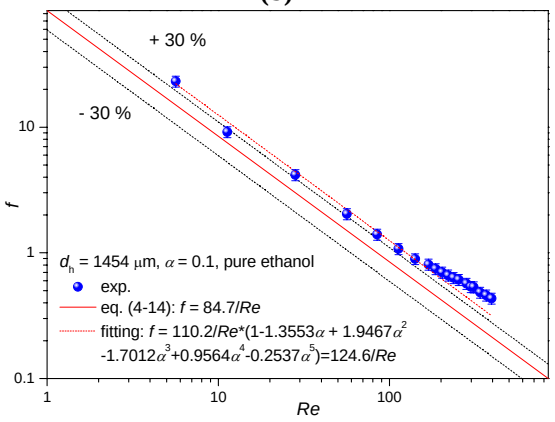

(c)

Figure 4-9. Comparisons of the measured friction factors with conventional friction correlations in the channels with (a) d_h = 571 μm, (b) d_h = 762 μm, (c) 1454 μm; ethanol

Poiseuille numbers in the tested Reynolds number range for ethanol are also obtained. Similarly, in Figure 4-10, Poiseuille number versus Reynolds number trends in 571 μm and 762 μm channels stay approximately constant but lower than the conventional theory predictions as illustrated in Figure 4-10 (a) and (b). All the data points in 1454 μm channel are plotted in Figure 4-10 (c). No obvious increase of *Po* is found. Thus the early transition was not achieved in the current Reynolds number range ($Re < 394$) for ethanol.

Wider ranges of Reynolds number with different working fluids in high-aspect-ratio micro-channels are essential to clarify the causes of the early transition and the deviation from the conventional theory.

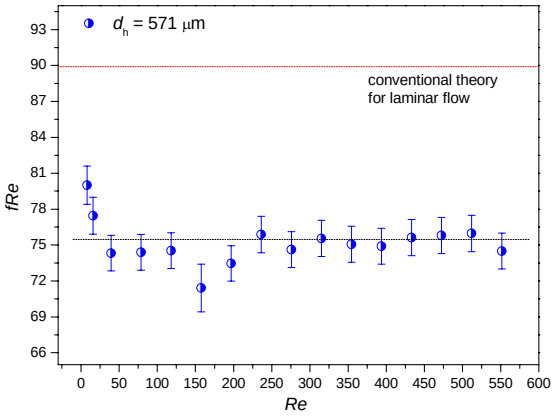

(a)

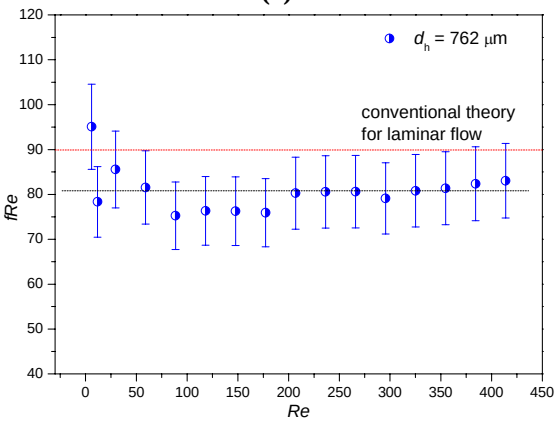

(b)

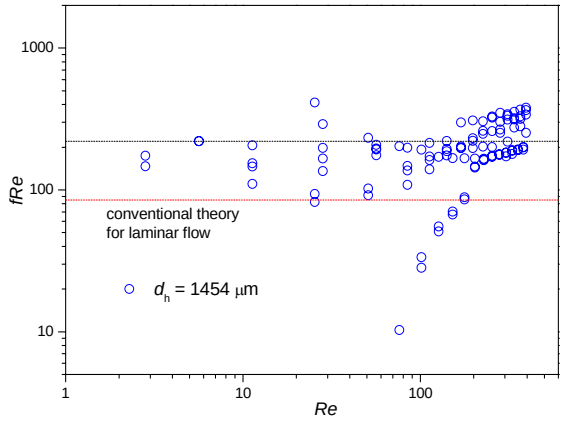

(c)

Figure 4-10. Poiseuille number ($Po = fRe$) versus Reynolds number for the channels with (a) d_h = 571 μm, with error bar, (b) d_h = 762 μm, with error bar, (c) d_h = 1454 μm, all data points; ethanol

Figure 4-11 exhibits the friction factor comparisons between FC-72 and ethanol. Because the tested Reynolds number ranges of FC-72 are higher than that of ethanol, only part of the Reynolds number ranges where both of the liquids can reach are compared. A lower friction factor of ethanol is found. This can be explained according to the liquid property comparison in Figure 4-12. The liquid dynamic viscosity of FC-72 is 65.16% lower than ethanol while the liquid density of FC-72 is 53.14 higher than ethanol. These differences in liquid physical properties result in a much lower liquid velocity of FC-72 than ethanol at the same Reynolds number. According to eq. (4-9), the friction factor is inversely proportional to the square of liquid velocity. Therefore the friction factor of FC-72 is expected to be higher than ethanol within the same Reynolds number range. In addition, the friction factor difference between FC-72 and ethanol becomes greater for larger channel. The larger channel cross-sectional area of the larger-sized channel contributes to the further reduction of liquid velocity, which causes more significant friction deviation. However, it can be seen from Figure 4-11 that, the difference between the friction factors is diminished as Reynolds number increases. So the influence of liquid physical properties is more profound in low Reynolds number region.

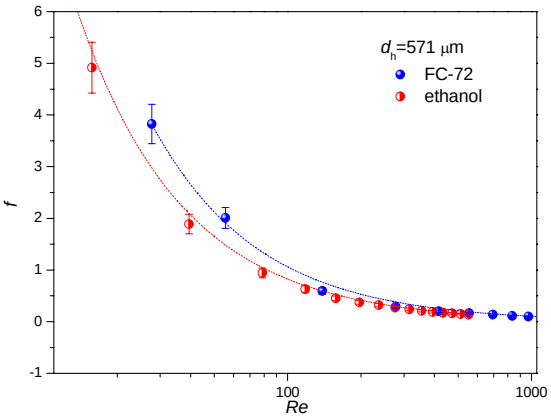

(a)

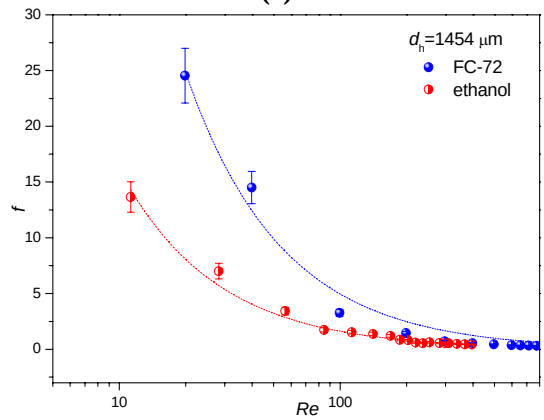

(b)

Figure 4-11. Friction factor versus Reynolds number comparisons between FC-72 and ethanol in the channels with (a) d_h = 571 μm, (b) d_h = 1454 μm

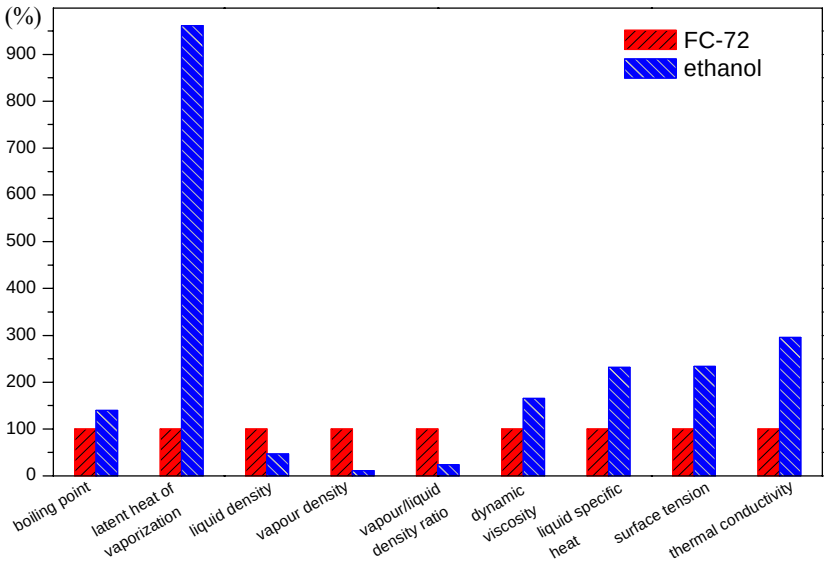

Figure 4-12. Physical property comparisons between FC-72 and ethanol

4.4.3 Single phase friction factor of nano-fluids

In order to explore the friction factor of nanofluids and the validity of conventional friction factor correlations, the friction results of pure ethanol were used as the reference to compare with those of the ethanol-based Al_2O_3 nanofluids. Four different particle volume fractions were tested to reveal the influence of particle concentration on the single phase friction factor in high aspect ratio micro-channels.

Figure 4-13 (a) to (c) show the friction factor versus Reynolds number in the three channels respectively. Nano-particle volume fractions are 0 (*i.e.* pure ethanol), 0.01 vol.%, 0.05 vol.%, 0.1 vol.% and 0.5 vol.%.

The influence of nanoparticles on single phase friction factor is insignificant under the test conditions in the present study. This indicates that the tested nanofluids can be considered as dilute suspensions. Some differences can be found in different channels. In the 571 μm channel, as shown in Figure 4-13 (a), results of all the five concentrations nearly overlap and are all predicted by the conventional theory within ±30%. Better agreement with the predictions can be found at lower Reynolds number region, but the friction slightly drops below the prediction when *Re* is higher. The impact of nanoparticle concentration is slightly more detectable in low Reynolds number region. In the 762 μm channel (Figure 4-13 (b)), the nanoparticle effect is vanished at higher Reynolds number range. Difference among the friction factors of different-concentrated nanofluids is more obvious in the low Reynolds number region. However, the effect of concentration is not conclusive. It can also be noticed that as *Re* increases, the friction factors of nanofluids gradually become lower than the pure ethanol results.

Similar with the observed trends with pure FC-72 and ethanol, the friction using nanofluids in the 1454 μm channel show the poorest agreement with the conventional theory predictions. Most of the data fall outside the $\pm 30\%$ range. Moreover, the effect of nanoparticle concentration is more detectable in low *Re* region. At $Re = 2.82$, the friction factor increases as particle volume fraction increases from 0.01 vol.% to 0.5 vol.%. The result that friction is an increasing function of Reynolds number is expected because of the increased viscosity. However, as Reynolds number grows, the influence of particle fraction becomes difficult to tell. The five groups of data eventually converge and overlap.

The insignificant effect of nanoparticle concentration on single phase friction factor was previously reported by Li and Xuan [177], Rea *et al.* [165], Pawan *et al.* [178] and Duangthongsuk and Wongwises [166] with conventional or mini-scale circular tubes, especially for dilute nanofluids. This implies that nanofluids can be treated as

homogeneous fluids and the conventional friction factor correlations can be extended to nanofluids.

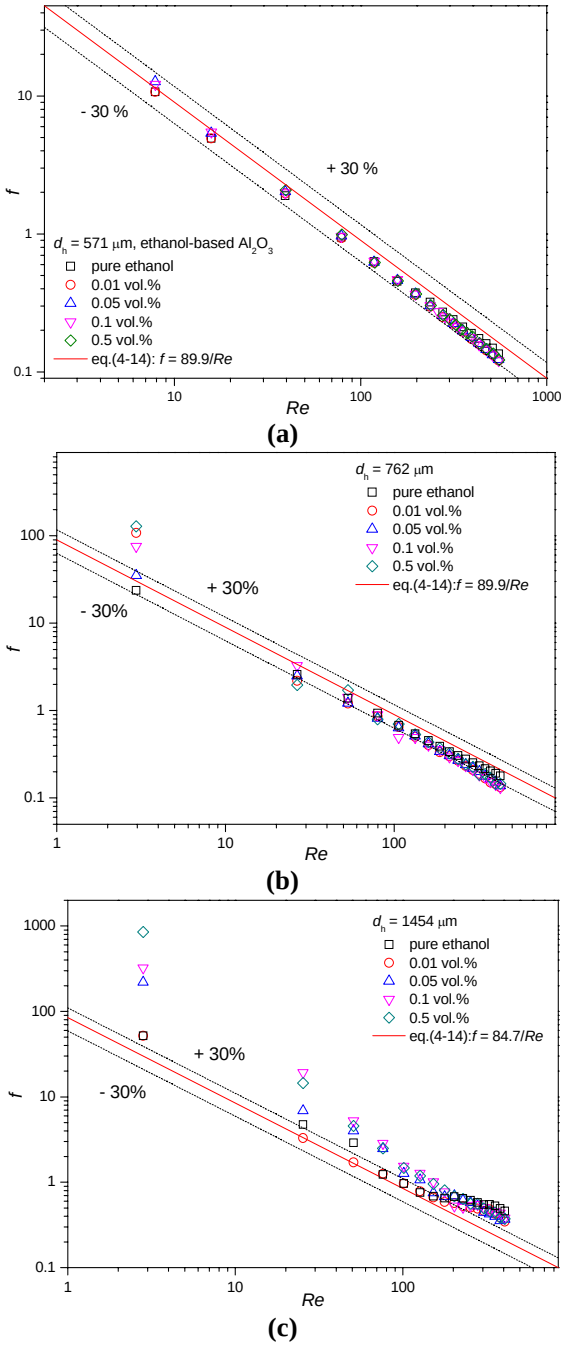

Figure 4-13. Comparisons of the measured friction factors with conventional friction correlation (a) d_h = 571 μm, (b) d_h = 762 μm, (c) d_h = 1454 μm; ethanol-based Al_2O_3 nanofluids

According to Figure 4-13, it is found that as becoming overlapped at higher Reynolds number region, the friction factors of nanofluids become slightly lower than the friction factor of pure ethanol. One possible reason is that at high Reynolds number,

the nanoparticle suspension is flowing rapidly, thus it can be considered that a layer of particles constantly stays above the channel inner surface under the continuous supply of nanofluids. Consequently the contacting area between the fluid and the channel surface is reduced, so are the friction factors. However, this explanation could only be checked by further experiments with wider ranges of nanoparticle concentrations, nanoparticle sizes, Reynolds numbers and channel geometries. In addition to the possible influences from the particle deposition and the changes of surface condition, the nanoparticles also affect the viscosity of the suspension. Viscosity is increased with increasing particle concentration according to the existing correlations in Xuan and Roetzel [150]. However, the particle concentrations in the present study were relatively low, thus only minor changes of viscosity is found for using different correlations, the consequent variations of single phase friction factor are insignificant.

4.5. Conclusions

In the study presented in this chapter, single phase pressure drop measurements have been conducted to examine the availability of the experimental setups, to investigate the effects of working fluids properties as well as the micro-channel geometry on friction factor, and to discuss the validity of the conventional friction theory on micro-channel flow and nanofluids flow. Single phase flow experiments have been carried out in three high aspect ratio rectangular micro-channels with the hydraulic diameters of 571 μm, 762 μm and 1454 μm. FC-72, ethanol, and ethanol-based Al_2O_3 nanofluids of four different particle volume fractions (0.01 vol.%, 0.05 vol.%, 0.1 vol.% and 0.5 vol.%) were used as the working fluids.

First of all, the single phase pressure drop is an increasing function of Reynolds number and a decreasing function of the channel hydraulic diameter.

It is found that for all the tests of ethanol and most of the tests of FC-72 as well as nanofluids, the single phase friction factors in the micro-channels agree with the conventional friction theory within ±10% – ±30%, indicating the validity of the set-ups for further two-phase flow tests. Specifically, the friction factors obtained in the 1454 μm channel derive from the conventional theory trend, showing not only higher values

but also a dependency of f on Re. A modified friction correlation is proposed: $f = \frac{C_1}{Re^{C_2}}$, where C_1 and C_2 are fitted to be 317.76 and 1.11 respectively.

In the channel with d_h = 1454 μm, hydrodynamic developing entrance length is longer than the channel length from Re > 980 and afterward. For Re > 980, the flow in the entire channel test section is developing in nature.

Besides, in the 1454 μm channel, early transition from laminar flow to turbulent flow occurs, the critical Reynolds number at which the flow drifts away from laminarity ranges from 600 to 700. Critical Reynolds number decreases when channel hydraulic diameter increases to 1454 μm and when the aspect ratio decreases to 10 (or increases to 0.1). Channel surface roughness and channel cross-sectional aspect-ratio are considered to be crucial for the velocity boundary layer development in micro-channels.

In the 1454 μm channel, at low Reynolds number ($0 < Re < 600$) , the flow is laminer and will be fully developed somewhere inside the channel; for $600 \le Re < 980$, the flow starts the transition to turbulent but will also be fully developed somewhere inside the channel; For $Re > 980$, turbulent developing flow will be encountered in the channel.

In addition, effects of liquid physical properties have been highlighted by comparing the friction factors obtained with FC-72 and ethanol. The lower viscosity and higher liquid density of FC-72 than ethanol result in lower friction factor of ethanol than FC-72 within the same Reynolds number region. However, the influence of liquid physical properties is more profound in low Reynolds number region.

Comparisons between the pure ethanol and ethanol-based nanofluids show that, the added Al_2O_3 nanoparticles have minor effect on single phase friction factor. This indicates that the tested nanofluids can be considered as dilute suspensions. Besides, the friction factor of nanofluids is slightly lower than that of pure ethanol at high Reynolds numbers. One possible reason is that the contacting area between working fluid and the channel surface is reduced at high Reynolds numbers. Moreover, the friction factors acquired in the 571 μm and 762 μm micro-channels with nanofluids can agree with the predictions within ±30%. This implies that nanofluids can be treated as homogeneous fluids and the conventional friction factor correlations can be extended to nanofluids.

However, single phase flow is not the major task of the present research project. The study stepped forward to the two-phase part. In the future, in order to clarify the friction factor during single phase nanofluids flow in micro-channels, more experiments are

required to look for the explanations of the reduced friction at higher Reynolds numbers. It will also be helpful to be able to probe the inner surface condition to unveil how the nanoparticles distribute and deposit on the channel surface during and after the flow. Moreover, wider ranges of micro-channel geometry with the unique high aspect ratio cross section will help to build a more conclusive database.

Chapter 5

Liquid-vapour phase change and vapour dynamics in micro-scale space

5.1. Introduction

The flow and heat transfer characteristics of flow boiling in micro-channels are closely related with the liquid and vapour phase distribution within the micro-channels. For instance, energy from the heated surface, which is stored in the thermal boundary layer adjacent to the surface, is eventually used for evaporating the surrounding liquid and thus induces boiling. Therefore, bubble nucleation, growth, deformation and vapour motions are responsible for transporting the energy from heated surface and are associated with the heat transfer rate enhancement (Robinson and Judd [33]).

Using the high speed camera, the onset of boiling was captured, the flow regimes during the flow boiling were observed, and the single bubble growth was focused on in particular. The study on single bubble growth consisted of two parts: bubble growing between two parallel plates and bubble growing during flow boiling in a single micro-channel. The evolution of bubble equivalent radius revealed a three-stage bubble growth mode, the dominant mechanisms of which were discussed. Moreover, the effects of heat flux, mass fluxes, channel gap and the channel geometry on bubble growth were examined. The influences of these experimental parameters on bubble aspect ratio could help clarifying the dominant heat transfer mechanisms. Furthermore, evaporation heat flux based on bubble growth rate was investigated.

5.2. Experimental setup and procedure

The experimental setups described in Chapter 3 session 3.2.1 and session 3.2.2 were used in the present investigation of vapour dynamics during flow boiling in a single micro-channel. All the experiments were conducted at atmospheric pressure. FC-72 and ethanol were used as working liquids. Prior to entering the flow loop, liquids were vigorously degassed for one hour to remove the dissolved gases. Meanwhile, the plexiglass box was heated up and maintained at 25°C. Then the working liquid was delivered into the flow loop by a syringe pump at the desired flow rates. Transparent heating was utilised, providing controllable heat input on the channel. The liquids were eventually collected in a reservoir after passing the test section. The fluid inlet and outlet temperatures were measured. The boiling process was synchronously visualized via the

high speed camera, then Image Pro® software helped to analyze the visualization results. Table 5-1 lists the test conditions of the present study.

Table 5-1. Experimental conditions for the investigation of vapour dynamic during flow boiling in a single micro-channel

FC-72			ethanol		
channel d_h [μm]	Heat flux q [kW·m^{-2}]	Mass flux G [kg·m^{-2}·s^{-1}]	channel d_h [μm]	Heat flux q [kW·m^{-2}]	Mass flux G [kg·m^{-2}·s^{-1}]
571 762 1454	0 – 18.31	11.2, 22.4 and 44.8	1454	0 – 15.0	11.2 and 22.4

For the particular study on single bubble growth, apart from the single bubble results obtained from the micro-channel flow boiling, the setup which was introduced in Chapter 3 session 3.2.3 was also utilized to examine the single bubble growth between two parallel plates without liquid flow. FC-72 and n-pentane were the selected working liquids. The effect of plate temperature on the bubble growth was examined. Box ambient temperature was controlled to adjust the plate temperature to examine the effect of plate temperature on bubble growth. Both plates were controlled to be subcooled or superheated compared to the saturation temperatures of the working liquids. The subcooling ΔT_{sub} and superheating ΔT_{sup} were obtained as:

$$\Delta T_{sub} = T_{sat} - T_W \quad \textbf{(5-1)}$$

$$\Delta T_{sup} = T_W - T_{sat} \quad \textbf{(5-2)}$$

where T_{sat} is the saturation temperature of the liquid and T_W is the plate temperature.

The bubble size at different levels of subcooling and superheating at two different plates gaps were obtained. The tested conditions are listed in Table 5-2.

Table 5-2. Experimental ranges of the bubble growth between two parallel plates

liquid	H = 114 μm		H = 250 μm	
n-pentane	ΔT_{sub} (°C)	ΔT_{sup} (°C)	ΔT_{sub} (°C)	ΔT_{sup} (°C)
	20.1	1	20.1	1
	11.1	3	11.1	2
	3.6	4 5	3.6	3
	0.6		0.6	

FC-72	ΔT_{sub} (°C)	ΔT_{sup} (°C)	ΔT_{sub} (°C)	ΔT_{sup} (°C)
	36.1	1	36.1	1
	20.1	2	20.1	2
	11.1	3	11.1	3
	3.6		3.6	
	0.6		0.6	

5.3. Data reduction

5.3.1. Bubble equivalent radius

The bubble equivalent radius is calculated from the measured bubble area A_b using Image Pro.® software. Assuming that the bubble is confined in the channel depth-wise direction (Figure 5-1), *i.e.* the bubble fills the channel depth during the entire growth and there is no liquid film between the bubble and the channel top and bottom surfaces. The bubble volume V_b is therefore the product of bubble area A_b and channel inner depth d_{in}. The bubble equivalent radius R_E is then calculated as the radius of a sphere of equivalent volume:

$$V_b = A_b d_{in} \tag{5-3}$$

$$V_b = \frac{4}{3}\pi R_E^{\,3} \tag{5-4}$$

$$R_E = \left(\frac{3}{4\pi}V_b\right)^{1/3} \tag{5-5}$$

Figure 5-1. Schematic drawing of a vapour bubble confined by the micro-channel depth

5.3.2. Evaporation heat flux

The amount of heat required for the bubble to grow ΔV_b during a period of Δt is:

$$Q_{\text{evp}} = \rho \cdot \frac{\Delta V_{\text{b}}}{\Delta t} \cdot h_{\text{fg}} \tag{5-6}$$

where h_{fg} is the latent heat of vaporisation.

For a growing bubble, the heat transferred per unit area per unit time for the bubble expansion, *i.e.* the evaporation heat flux is calculated as:

$$q_{\text{evp}} = \frac{Q_{\text{evp}}}{A_{\text{suf}}} \tag{5-7}$$

where A_{suf} is the surface area of the bubble. From Figure 5-2, the bubble surface area can be estimated as:

$$A_{\text{suf}} = 2A_{\text{b}} + 2d_{\text{in}}(W_{\text{b}} + L_{\text{b}}) \tag{5-8}$$

where A_{b}, W_{b}, L_{b} are the bubble area, bubble width and bubble length respectively.

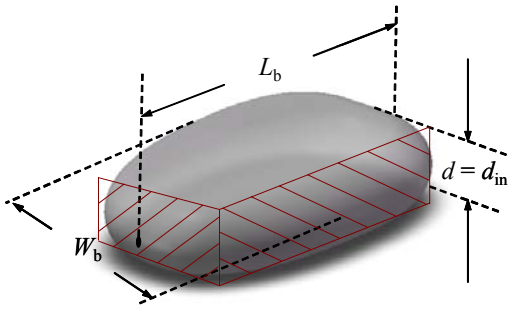

Figure 5-2. A drawing of a single bubble showing the bubble width, length and depth

5.4. Results and discussions

5.4.1. Onset of nucleation (ONB) and the following flow regimes

According to the AFM measurement of the channel internal surface roughness in Chapter 3, Figure 3-15, the mean roughness of the channel inner surfaces was R_{p} = 0.1 μm. Moreover, there might be micro- and nano-scale impurities entrained in the liquid flow because no filter was used prior to the test section for liquid purification. The usage

of filter in the flow loop was avoided in the present study due to limited pumping capacity. Therefore, in spite of the excellent surface smoothness and the usage of degassed working liquids, there would be entrapped air or vapour in the cavities or crevices, scratches on the channel inner wall and the entrained motes in the liquids. Since the temperature was the highest at the channel surface, formation of a vapour embryo was most likely to occur at the solid-liquid interface. According to Carey [223], bubble nucleation in the present study can be characterised as *heterogeneous nucleation*, which is the nucleation at the interface between a metastable phase and another (usually solid) phase that it contacts. This type of nucleation is different from *homogeneous nucleation*, which occurs completely within the superheated liquid.

Nucleation might start from these nuclei at relatively low temperatures, usually a few to several degrees higher than the saturation temperature of the liquids. When the channel wall was uniformly heated, there was a thin, moderately superheated liquid layer adjacent to the inner surface. Nucleation would take place when the bubble embryo at the cavity could grow from evaporation. This can be better understood by considering a conical crevice. Most surface crevice cross-sectional profiles are somewhat conical according to Hsu and Graham [224]. Figure 5-3 shows a conical cavity with a radius of R_c at mouth. The smallest curvature radius of the bubble is when $R_b = R_c$. The vapour pressure required to maintain the bubble at equilibrium is calculated from Young-Laplace Equation:

$$P_v - P_L = \frac{2\sigma}{R_c} \tag{5-9}$$

From Clausius-Clapeyron relation, during the phase change,

$$T_L - T_{sat} = \frac{T_{sat}(P_L - P_v)(V_L - V_v)}{h_{fg}} \approx \frac{T_{sat}(P_v - P_L)}{\rho_v h_{fg}} \tag{5-10}$$

Thus,

$$T_L - T_{sat} = \frac{2\sigma T_{sat}}{\rho_v h_{fg} R_c} \tag{5-11}$$

where P_v and P_L are the pressures of vapour phase and liquid phase, σ is the surface tension, T_L is liquid temperature and ρ_v is the vapour density (Ghiaasiaan [225]).

Eq. (5-11) provides the least liquid superheating required for nucleation in uniformly heated liquid, which was called as the incipient superheat by Kandlikar *et al.* [10]. In practice, the liquid temperature adjacent to the heated surface may not be completely uniform. Thus, a higher wall superheat is needed for nucleation.

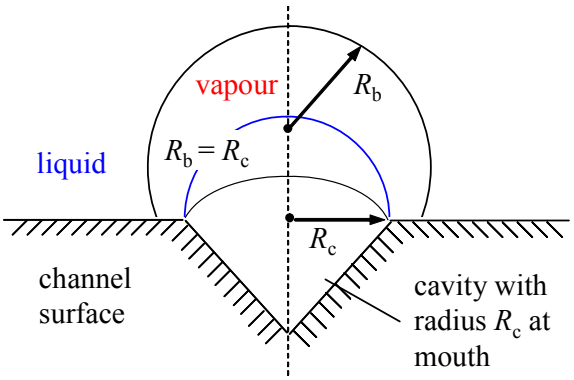

Figure 5-3. Bubble activation as the bubble radius of curvature changes

Take FC-72 for example, the liquid superheating using eq. (5-11) and the average surface roughness R_P = 0.1 μm was calculated to be 9.18°C. The corresponding liquid temperature was 65.18°C. This prediction agreed with the experimental measurements which showed an outlet liquid temperature range of 58°C – 66°C before nucleation.

In the present study, the power applied on the micro-channel was gradually increased until boiling occurred. Three mass fluxes were tested in each channel, the corresponding heat flux required for nucleation, noted as q_{ONB} are shown in Figure 5-4. It is observed that q_{ONB} is observed to increases with increasing mass flux. This is consistent with the previous observation of Bertsch *et al.* [115]. It can be explained that for a higher mass flux, the convective heat transfer is strengthened, resulting in a relatively lower channel wall temperature. Consequently, more heat is required to irritate nucleation. It is also found that q_{ONB} is higher for larger micro-channel size. Besides, the incipient superheat is increased at higher mass flux. For instance, FC-72 flows in the channel with d_h = 571 μm at G = 44.8 kg·m^{-2}·s^{-1}, the measured outlet liquid temperature was around 63.5°C but for a lower mass flux of 22.4 kg·m^{-2}·s^{-1}, the measured outlet liquid temperature right before incipient was 58.5°C.

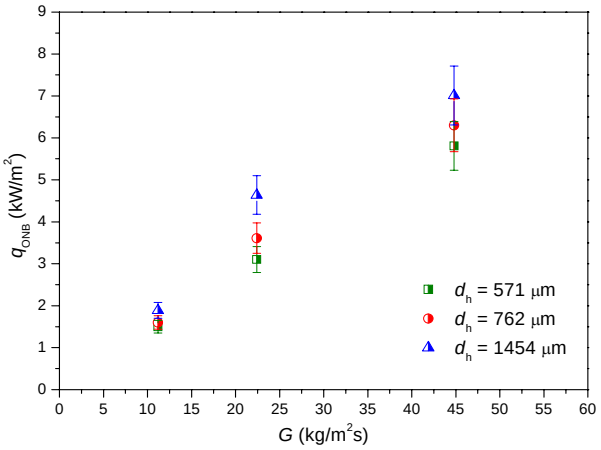

Figure 5-4. Onset of nucleate boiling (ONB) heat fluxes at G = 11.2 kg·m^{-2}·s^{-1}, 22.4 kg·m^{-2}·s^{-1} and 44.8 kg·m^{-2}·s^{-1} in the micro-channels with d_h = 571 μm, 762 μm and 1454 μm

In order to illustrate the liquid superheating, the heat flux required for the liquid to reach the saturation temperature was calculated, noted as q_{HFS}. Assume that all the effective heat flux on the channel surface is used for heating up the liquid. This leads to the following energy balance:

$$q_{HFS} = \frac{C_p G A_c (T_{sat} - T_{in})}{A_{W,out}} \quad \textbf{(5-12)}$$

where C_p is the liquid specific heat, A_c and $A_{W,out}$ are the channel cross sectional area and channel outer surface area; T_{sat} and T_{in} are the saturation temperature and inlet temperature of the liquid respectively.

In Figure 5-5, the straight line shows the q_{HFS} at each mass flux. The difference between q_{ONB} and q_{HFS}, which increases with mass flux, is the heat source for incipient superheat. This agrees with the experimental measurements. The heat losses to the surrounding and that the spatial thermal coupling modifies the local temperature could partially explain the difference and the increasing deviation with the estimated slope line.

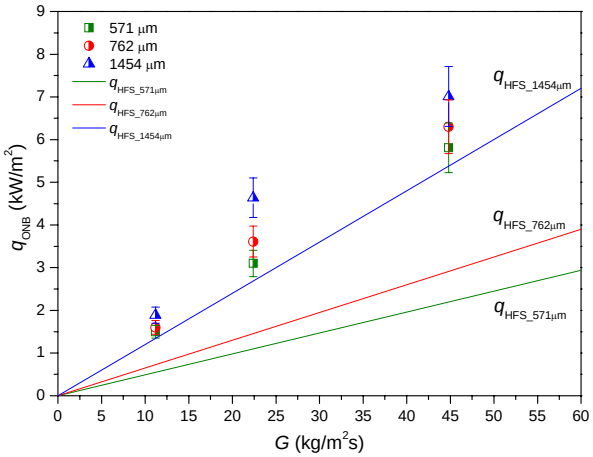

Figure 5-5. Comparison between onset of nucleate boiling heat flux (q_{ONB}) and heat flux for saturation (q_{HFS})

After the onset of nucleation, both vapour and liquid occupied the channel. Various flow regimes were observed. The flow regimes conspicuously replied on the flow and thermal conditions. Figure 5-6 gives an example of the flow regimes at relatively high flow rate. First, the nucleation appears near the channel exit and then the bubble expands rapidly. Due to the largely increased vapour volume inside the channel, the upstream liquid is blocked outside the entrance of the channel and the inlet pressure increases. The consequent liquid backflow caused by the rapid vapour expansion is called recoiling. In the meantime, liquid droplets are entrained in the vapour due to the fast vapour core movement. Under the continuous delivery of the pump, upstream fresh liquid starts to enter the channel again after gathering enough potential to provide a sufficiently high pressure. Liquid re-wetting is observed accompanied by large amount of tiny nucleation. This is because that the pre-existing nuclei, which have not been previously activated, become newly irritated due to the sudden decrease of pressure during the re-wetting. As a result of the high aspect ratio channel cross section, bubbles are suppressed by the channel gap shortly after inception and grow rapidly in the channel axial direction. The unique channel geometry determines that the major flow regimes transfer from bubbly flow to slug and annular flow in a very short span of time. It is also observed that vapour coalesces at downstream. The vapour core is then gradually pushed out of the channel and a new cycle of nucleation happens again at the near-exit site. However, for most of the heat fluxes, large amount of vapour exists in the channel hence the main flow regimes are slug-annular and annular flow. The periodic growth and release of vapour bubbles at an active nucleation site is usually termed as the *ebullition cycle* (Carey [226]).

Periodic nucleation (shown in Figure 5-6 and Figure 5-7) can be observed in most of the tests in the present study.

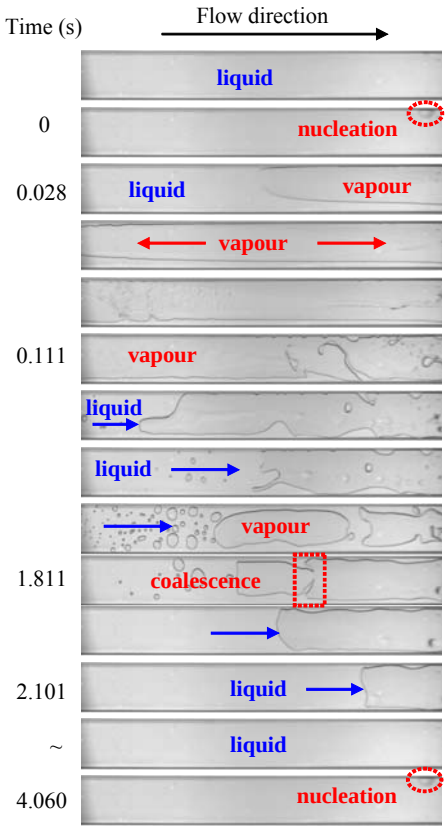

Figure 5-6. Flow regimes during flow boiling in the channel with d_h = 762 μm at G = 44.8 kg·m^{-2}·s^{-1} and q = 5 kW·m^{-2}; FC-72, camera speed: 1000 fps

In addition, nucleation took place at different locations along the flow direction at different heat fluxes. Figure 5-7 and Figure 5-8 are the flow regimes in the channel with d_h = 1454 μm at q = 5.16 kW·m^{-2} and 8.13 kW·m^{-2} respectively. Apparently, nucleation appears closer to the channel inlet when heat flux is higher. Considering that all the effective heat on the channel is used for heating up the liquid, it is understandable that the higher the heat flux is, the higher the local liquid temperature becomes, thus the easier the pre-existing cavities are activated as nuclei.

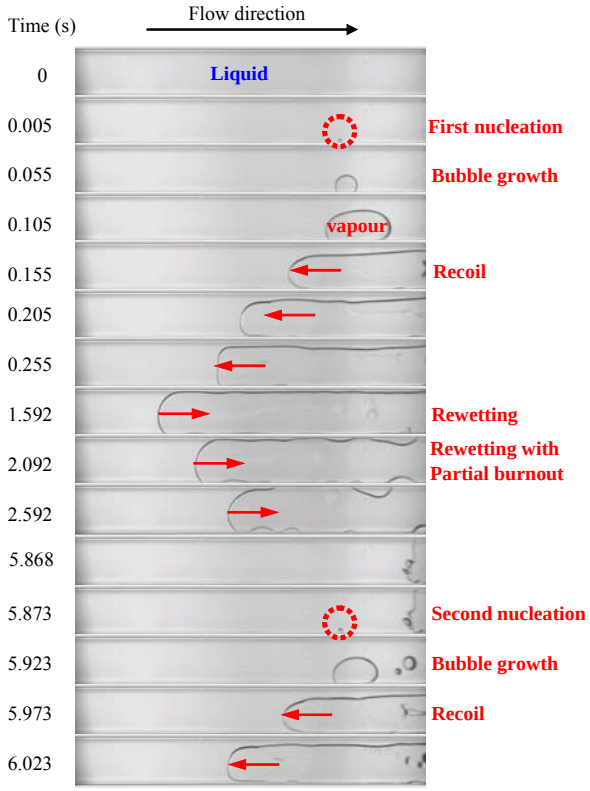

Figure 5-7. Periodic nucleation, re-coiling and re-wetting in the channel with d_h = 1454 μm at G = 22.4 kg·m^{-2}·s^{-1} and q = 5.16 kW·m^{-2}; FC-72, camera speed: 1000 fps

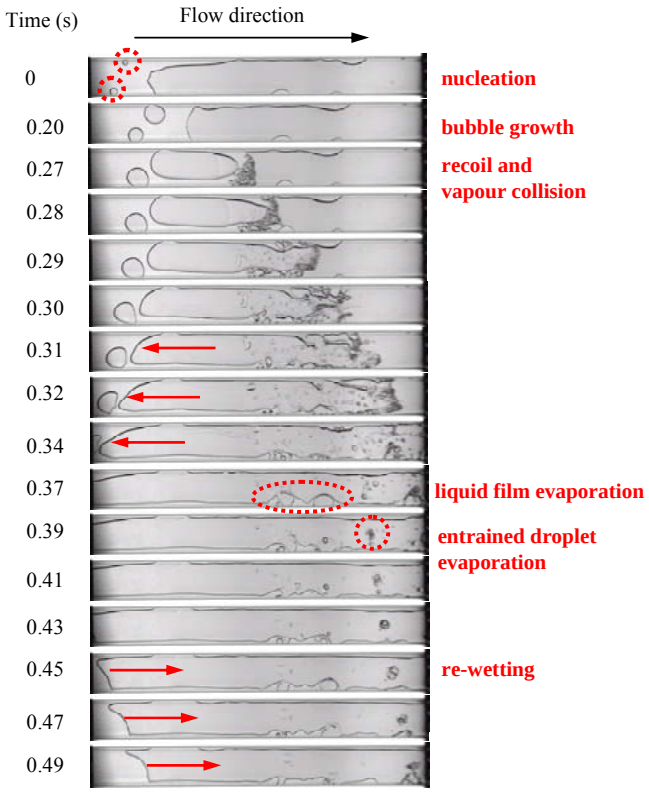

Figure 5-8. Nucleation, bubble growth, re-coiling and re-wetting with vapour collision in the channel with d_h = 1454 μm at G = 22.4 kg·m^{-2}·s^{-1} and q = 8.13 kW·m^{-2}; FC-72, camera speed: 1000 fps

Flow regimes of the flow boiling in high aspect ratio micro-channels are distinctive from the commonly observed flow patterns reported in regular channel geometries (as reviewed in Chapter 2, session 2.4.1). Figure 5-9 shows some typical flow regimes obtained in the high aspect ratio micro-channel. Flow turns into slug and annular flow shortly after the onset of nucleate boiling due to the confinement of the narrow channel gap. During the slug flow, fierce collision is noticed between two vapour slugs or when the liquid re-wets the channel. As the vapour continues to expand, the vapour core moves at a relatively high speed compared with the liquid velocity. Therefore, liquid droplets are entrained in the vapour and the wispy-annular flow is observed. There exists a thin layer of liquid film between the vapour core and the channel inner surface. The liquid film evaporation becomes predominant in the annular flow. It can be seen that the thickness of the liquid film gradually decreases in the flow direction. Partial dry-out occurs occasionally as a result of the liquid film vanishment.

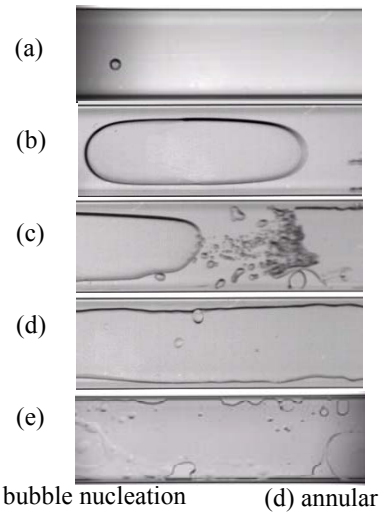

Figure 5-9. Typical flow regimes in high aspect ratio rectangular micro-channel, d_h = 1454 μm, σ = 10; FC-72, camera speed: 1500 fps

In the wispy-annular flow, the entrained droplets in vapour core are usually observed to behave in two different ways. First, when the heat flux is at a relatively low level, the liquid droplets will gather on the channel side-wall (as shown in Figure 5-10) because the surface temperature gradually reduces from channel centre line to the side-wall edge. Figure 5-10 demonstrates the deposition of the entrained liquid onto the channel side-wall. It is also noticed that the liquid-vapour interface between the vapour

core and the thin liquid layer is disturbed by the droplet deposition. Occasionally the deformed interface will activate the nuclei in the vicinity of the interface. Therefore, random nucleation at the liquid vapour interface is observed.

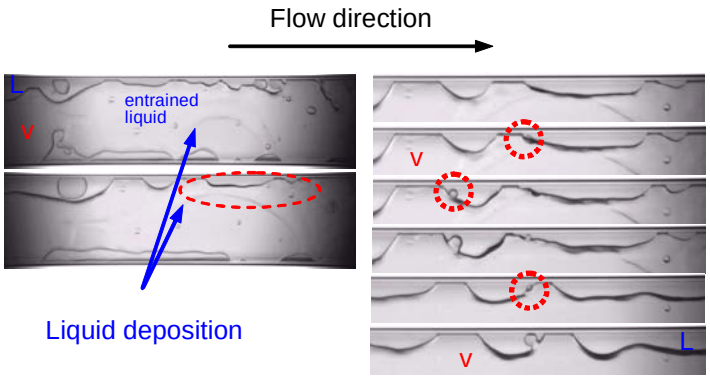

Figure 5-10. Liquid droplet deposition in wispy-annular flow at low heat flux and the corresponding interface disturbance, d_h = 1454 μm, G = 44.8 kg·m^{-2}·s^{-1}, q = 10.50 kW·m^{-2}; FC-72, camera speed: 3000 fps

When a high heat flux is applied on the channel, the liquid droplets will evaporate fiercely before reaching the channel side-wall. Figure 5-11 shows a series of the frames acquired at the heat flux of 18.31 kW·m^{-2} in the 1454 μm channel. The camera speed was 3000 fps, providing clear insight of the boiling. The vaporisation of entrained liquid droplets can be observed, especially at downstream. It is also found that when the channel is under a very high heat flux, intensive boiling occurs in the channel. The boiling is so intense that the fresh liquid is insufficient for evaporation. Therefore partial dry-out occurs (as can be seen in Figure 5-11). At the same time, large scale nucleation occurs within the remaining liquid. Since the heat transfer characteristics are vastly deteriorated by the partial dry-out, local hot-spots on the channel surface will appear which can cause system breakdown. In the present study, the tantalum coating layer on the channel outer surface would vanish if exposed under high heat flux for a long time. Therefore, high heat fluxes are not recommended for long-time experimental testing.

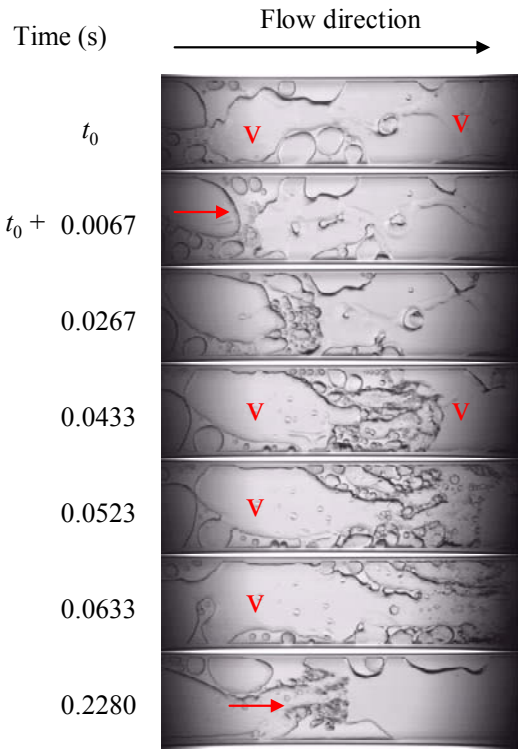

Figure 5-11. Vapour collision with large-scale nucleation and droplet evaporation in the channel with d_h = 1454 μm at G = 44.8 kg·m^{-2}·s^{-1} and q = 18.31 kW·m^{-2}; FC-72, camera speed: 3000 fps

5.4.2. Single bubble growth

The heat transfer during nucleation is determined by the vapour bubble growth on the heated surface. The temperature distribution from the heated surfaces to the liquid-vapour interface is schematically depicted in Figure 5-12. The heat is conducted from the channel outer surface to the inner surface, and then stored within a thin thermal boundary layer adjacent to the surface via liquid convection. Then from the incipient of nucleation, the liquid gives up its latent heat and consumes the stored heat for vaporization. The temperature of the interface is considered to be maintained at the saturation temperature. Besides, the flow regimes transitions and the corresponding local heat transfer largely depend on the fluid motions caused by the bubble growth. In order to obtain the insight into the heat transfer mechanisms during boiling, it is necessary to understand the single bubble growth. First of all, the single bubble growth between two parallel plates was examined. The plates were controlled to be subcooled or superheated to examine the bubble collapse or bubble growth when confined in micro-scale space. In this chapter, only the results of bubble growth between superheated plates were presented. The bubble

collapse results for subcooled plates can be found in Appendix D. Then the bubble growth captured during flow boiling was also concentrated on.

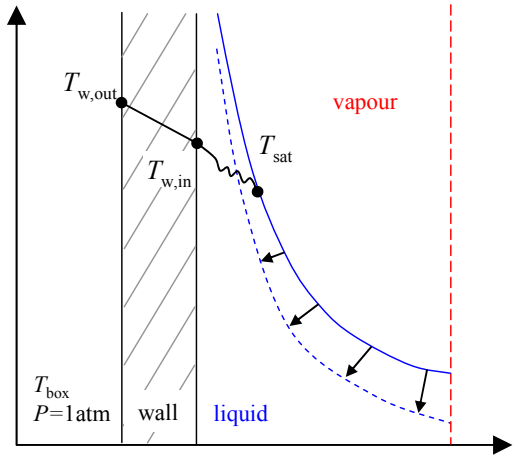

Figure 5-12. Schematic drawing of the temperature distribution from the outer wall to the liquid-vapour interface

5.4.2.1 Single bubble growth between two superheated parallel plates

Using the setup introduced in Chapter 3, session 3.2.3, a bubble was generated at the manually-created cavity on the plate. A resistor was attached below the cavity to provide local high temperature so that a bubble would be easily generated at the desired location. It is worth noting that the power supply of the resistor was immediately switched off when a bubble embryo was observed. Thus the influence of the resistor on the plate temperature could be neglected. Sometimes the bubble also randomly appeared at other locations where there existed some cavities and scratches on the plate surface. Since the temperature could be considered uniform across the plates, the location of the bubble had no essential effect on the growth result. Figure 5-13 is a series of sequences of n-pentane vapour bubble growing between two parallel plates with a gap H = 114 μm at a superheating of ΔT_{sup} = 4°C. Bubble area is measured and then the corresponding equivalent radius R_E is calculated and plotted in Figure 5-14. Bubble radius firstly increases linearly, and then turns into exponential growth, the transition to which occurs earlier with higher superheating degree. When ΔT_{sup} = 5°C, the bubble starts exponential growth at around 9.333 s, but when ΔT_{sup} = 4°C, the exponential growth is postponed till 19.333 s. Due to space limit of the plates, the exponential increase for the bubbles growing at ΔT_{sup} = 1°C and 3°C is not captured.

Moreover, the plate gap is also influential to the bubble growth rate. For a constant plate superheating, the bubble size increases faster when the channel gap increases from 114 μm to 250 μm. The increased growth rate can be seen in Figure 5-15.

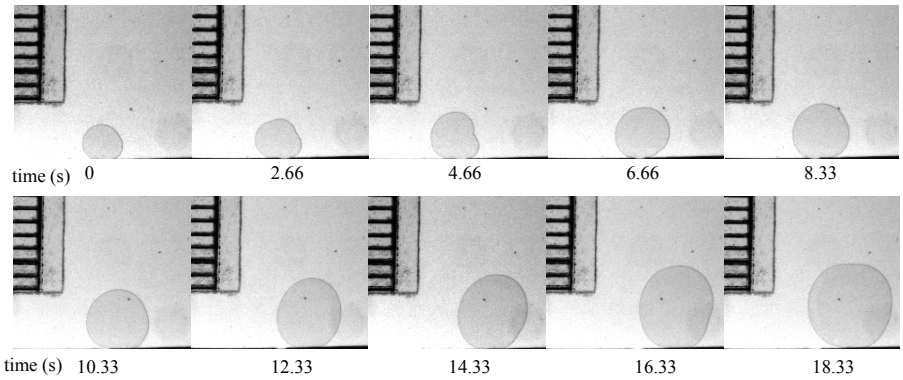

Figure 5-13. n-pentane vapour bubble growth between superheated plates, ΔT_{sup}= 4°C, H = 114 μm, camera speed: 30 fps

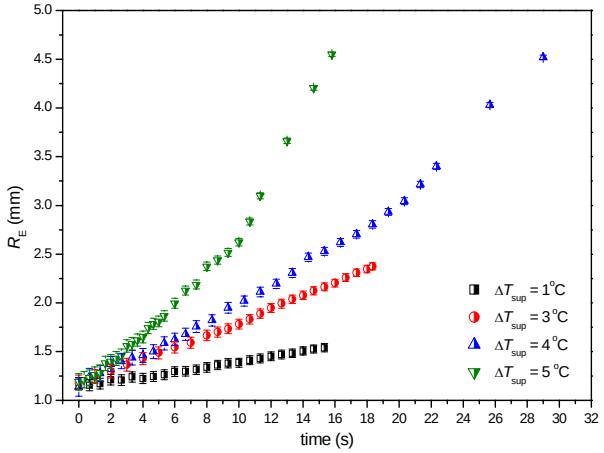

Figure 5-14. n-pentane bubble equivalent radius evolution at different levels of superheating, H = 114 μm

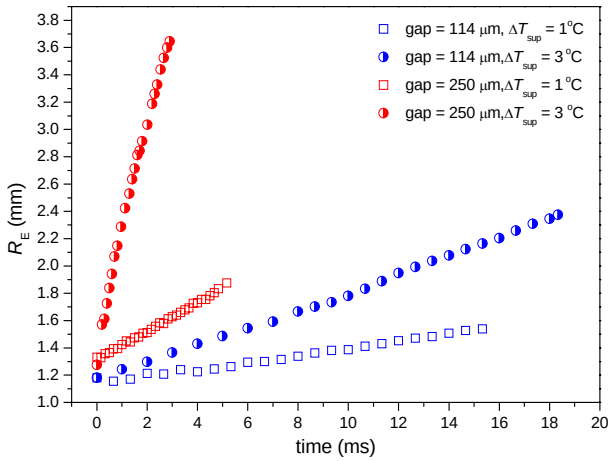

Figure 5-15. Effect of plate gap on the bubble growth rate, n-pentane

Figure 5-16 shows the FC-72 vapour bubble growth at three superheating levels. Similar linear trends are noticed and it is also easy to find the promoting effect of superheating on bubble growth rate. However, FC-72 bubble diameter keeps on increasing linearly without turning into exponential growth even after 40 s. This significant difference with n-pentane highlights the necessity to compare the physical properties of the two working liquids.

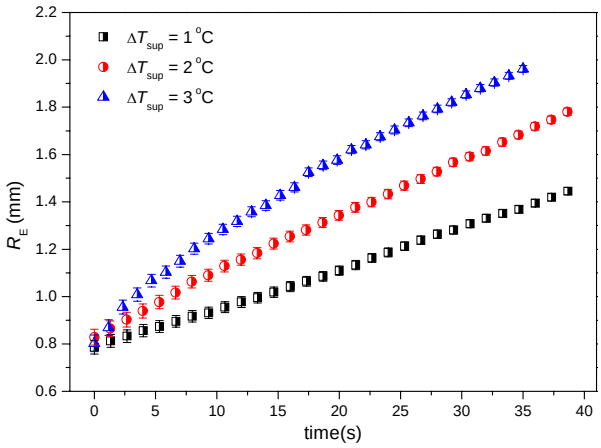

Figure 5-16. FC-72 bubble equivalent radius evolution at different levels of superheating, H = 114 μm

The physical properties of n-pentane and FC-72 are compared in Figure 5-17 using the properties of FC-72 as a reference and the corresponding property percentages of n-pentane can be calculated. The liquid specific heat of n-pentane is only 15% of that of FC-72. Therefore it costs much less heat for n-pentane temperature to increase, thus the superheated liquid layer for evaporation appears quicker. Besides, FC-72 has a lower surface tension than n-pentane. The consequent higher wettability essentially obstructs the FC-72 vapour spreading.

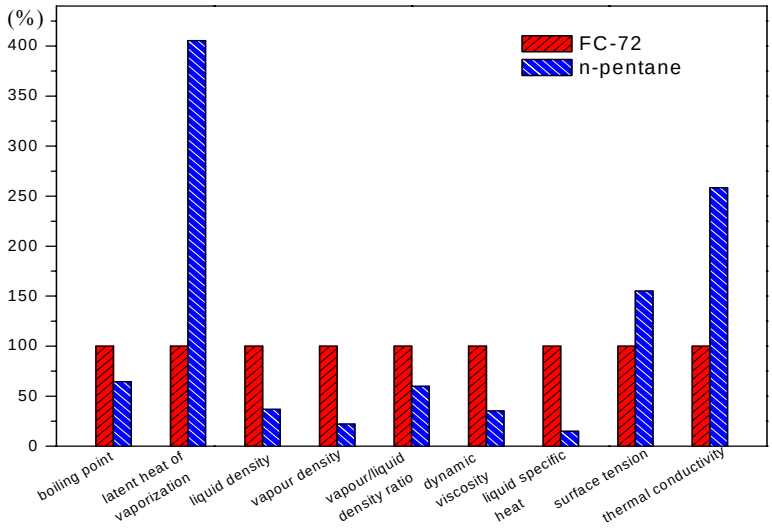

Figure 5-17. Physical property comparisons between FC-72 and n-pentane

5.4.2.2 Single bubble growth during flow boiling in micro-channels

To further explore the bubble growth mechanisms, single bubble generated during flow boiling was concentrated on. It has been previously reported by Chang and Pan [82] that the length of bubble oscillates in unstable flow. So it is essential to note that the target bubbles were all single bubble growing without interrupted by the instabilities such as neighbouring bubbles and/or the obvious reverse flow.

Onset of nucleation (ONB) and bubble growth were captured with the aid of high speed camera. The nucleation occurred either on the channel side-wall or in the channel centre, depending on the locations of the nuclei. Figure 5-18 shows the nucleation and bubble growth observed from top view. Two bubbles are growing at different locations within the channel. Bubble first grows asymmetrically till a moment beyond which the bubble length begins rapid growth. After occupying 78% – 90% of the channel width, the bubble becomes elongated in the flow direction. During the growth, bubble front is moving at a higher speed than the bubble tail. Drag force from the surrounding liquid on the liquid-vapour interface is responsible for the bubble deformation. Since there is no force acting in the width-wise direction, bubble growing on the side-wall does not lift off from the surface. All the bubbles grow and move in the channel axial direction. Meanwhile, liquid droplets are entrained in the bubbles due to the rapid movement of the vapour core.

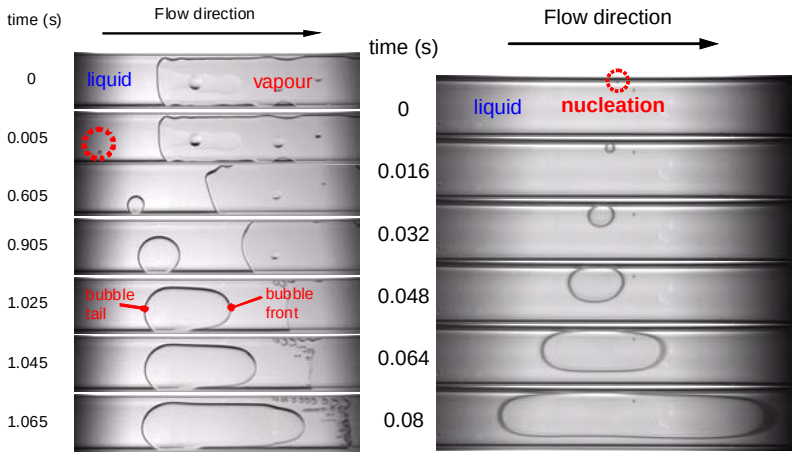

Figure 5-18. Bubble growth visualization results at G = 22.4 kg·m^{-2}·s^{-1}; FC-72, (a) d_h = 1454 μm, q = 5.95 kW·m^{-2}, (b) d_h = 571 μm, q = 3.50 kW·m^{-2}, camera speed: 1000 fps

The motion of the bubble could be better understood after performing a force analysis on the bubble interface.

First of all, it is assumed that the bubble fully fills the channel depth. As illustrated in Figure 5-19, the bubble interface is under the joint effect of the following forces: F_S, the surface tension force; F_P, the force due to liquid-vapour interface pressure difference; F_{HP}, the force due to hydrodynamic pressure and F_D, the drag force from the surrounding liquid. Forces acting on the bubble in x and y directions are:

$$\sum F_x = F_D - F_{Px} + F_{Sx} \tag{5-13}$$

$$\sum F_y = F_{Sy} - F_{Py} - F_{HP} \tag{5-14}$$

For a bubble with the radius of R_E confined between a channel gap d_{in}, the forces in eq. (5-13) and (5-14) can be estimated from:

$$F_D = \frac{1}{2} C_D \cdot u^2(x) \cdot (2R_E d_{in}) \rho_L \tag{5-15}$$

$$F_{HP} = \frac{1}{2} \rho_L \cdot u^2(x) \cdot (2R_E d_{in}) \tag{5-16}$$

$$F_P = (P_v - P_L) A = \frac{2\sigma}{R_E} \cdot (2\pi R_E d_{in}) = 4\sigma\pi d_{in} \tag{5-17}$$

$$F_S = 2\pi\sigma R_E \tag{5-18}$$

where C_D is the drag coefficient, $u(x)$ is the liquid velocity, and σ is the liquid surface tension.

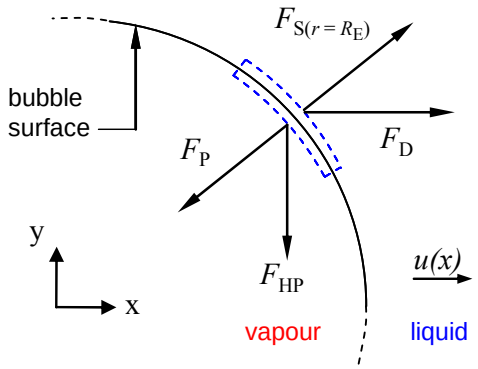

Figure 5-19. Schematic diagram of the force analysis on a growing bubble interface within the micro-channel (after confined by the channel depth)

The bubble growth in channel width-wise and stream-wise directions depends on the forces $\sum F_y$ and $\sum F_x$ respectively. As the bubble size increases, F_D, F_{HP} and F_S increases. Moreover, due to no-slip condition, liquid flow speed increases from channel side-wall to the centre line. Therefore the bubble width growth is supposed to increase because the increase of F_{HP} is hindered by the gradually reduced liquid velocity when the interface is approaching the channel wall. However, the bubble width growth is retarded due to the limitation of channel width. On the other hand, the bubble became elongated in stream-wise before occupying the entire channel width when the effect of drag force was no longer insignificant. Since the magnitude of the drag force increases as approaching the channel centre, the bell-shape bubble is observed. In addition, channel depth is believed to have essential effect on bubble geometry according to (5-15) – (5-17).

In the present study, the time of the bubble rapid elongation commencement is named as critical time, denoted as t_c and is obtained when bubble length growth rate starts deviating from bubble width growth rate (Figure 5-20). It is found that t_c is reduced by increasing heat flux and decreasing mass flux (Figure 5-21). It is also worth mentioning that the onset time is chosen when bubbles have the same initial size so that the time-related results in each test are comparable.

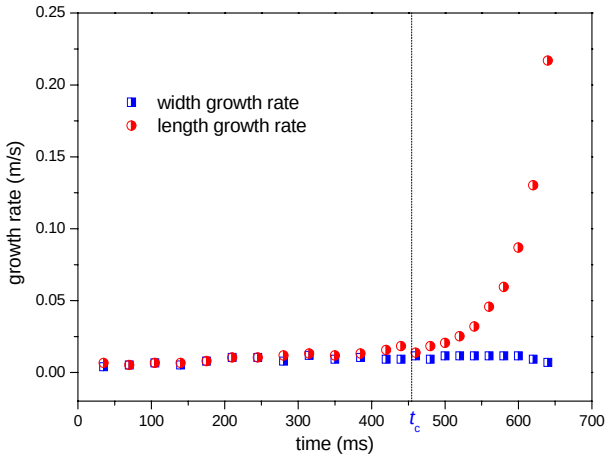

Figure 5-20. Bubble width growth rate and length growth rate comparison, in the channel with d_h = 1454 μm at G = 22.4 kg·m^{-2}·s^{-1} and q = 5.95 kW·m^{-2}; FC-72

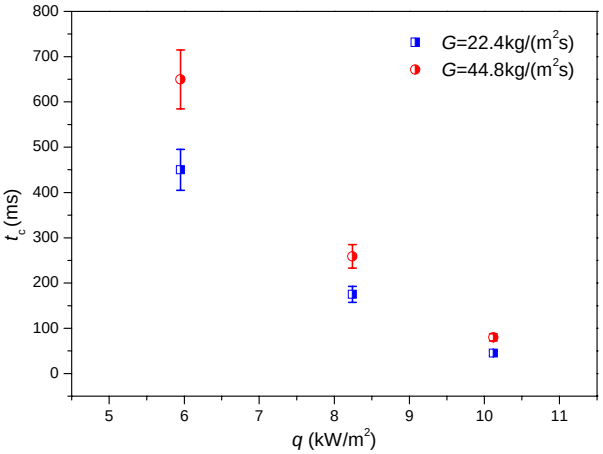

Figure 5-21. Critical time versus heat flux at two different mass fluxes in the channel with d_h = 1454 μm; FC-72

Bubble equivalent radius, calculated as in eq. (5-5), was also discussed. Figure 5-22 is the temporal bubble equivalent radius evolution during boiling in the channel with d_h = 762 μm at q = 5.95 kW·m^{-2} and G = 44.8 kg·m^{-2}·s^{-1}. A typical three-stage bubble growth mode is revealed. Bubble equivalent radius R_E firstly grows proportionally to the square root of time till t_{c1}. Then the growth turns into linear when bubble is confined by the channel depth. The linear growth is then followed by a rapid exponential growth usually behaves as the elongation in the flow direction. The critical time for elongation commencement is noted as t_{c2} (t_{c2} is the corresponding t_c in Figure 5-20 and Figure 5-21).

In previous investigations, bubble growing proportionally to the square root of time has been reported in pool boiling (Lee *et al.* [227], Frank *et al.* [45]) and some flow boiling cases (Kandlikar *et al.* [34], Duhar *et al.* [51]). In the present study, however, this type of growth was not captured in the bubble growth between two parallel plates due to

very narrow plate gap and was only captured in a few flow boiling cases, because the bubble only grows proportional to the square root of time for a very short span of time before being confined by the channel depth. As in Figure 5-22, the bubble radius is proportional to the square root of time till $2R_E \approx 0.3922$ mm, which approximately equals to the depth of the 762 μm channel. When bubble diameter approaches the channel depth, bubble immediately turns into linear growth. The exponential growth starts from bubble elongation and then the bubble quickly fills the channel. Because the channel depth is very small compared with channel width, the first stage of growth is very short. For the majority of the measurements, only the linear and exponential stages were captured. Figure 5-23 illustrates the three-stage growth and the corresponding vapour distribution in the channel cross-sectional view.

According to the Rayleigh-Plesset equation (Brennen [228]) for bubble dynamic, the thermal term will gain magnitude gradually as the bubble grows and will ultimately affect the growth in a major way. The time needed for the thermal term to gain a same order of magnitude with the inertial term is called as first critical time. The first critical time is given as:

$$t_{c1} = \frac{(P_v - P_\infty)}{\rho_L} \cdot \frac{1}{\Sigma} \tag{5-19}$$

where Σ is a function of liquid temperature,

$$\Sigma(T_L) = \frac{h_{fg}^2 \rho_v^2}{\rho_L^2 C_{PL} T_\infty \alpha_L^{1/2}} \tag{5-20}$$

where ∞ represents the properties of the ambient, α_L is the thermal diffusivity of the liquid.

If the bubble growth time exceeds the first critical time, the bubble will turn to thermally controlled growth and the bubble radius is estimated as:

$$R(t) = C \cdot Ja(\alpha_L t)^{1/2} \tag{5-21}$$

where C is a constant ranges from $\sqrt{\pi}$ to $\sqrt{3\pi}$; Ja is Jacob number. In this case, the bubble grows proportional to the square root of time, corresponding to the first stage of the three-stage growth mode.

Then, as the bubble is confined by the channel depth, heat transfer mainly takes place on the bubble surrounding area. The effects of various forces described in eq. (5-15) – (5-17) become more dominant as the bubble size increases. The bubble is then deformed and become elongated when drag force is no longer negligible.

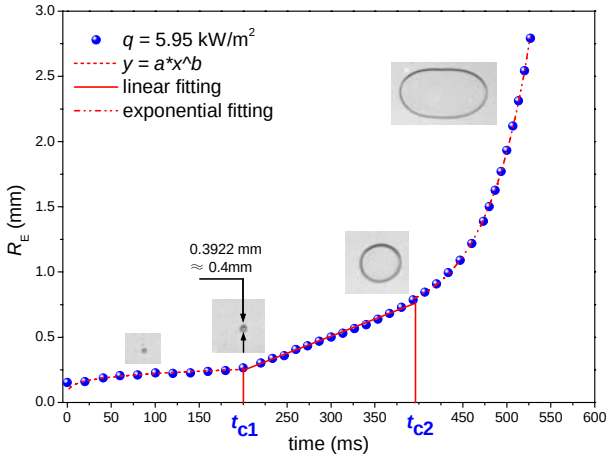

Figure 5-22. Bubble equivalent radius in the 762 μm channel showing the three typical stages of bubble growth and two critical times, G = 44.8 kg·m^{-2}·s^{-1} and q = 5.95 kW·m^{-2}; FC-72

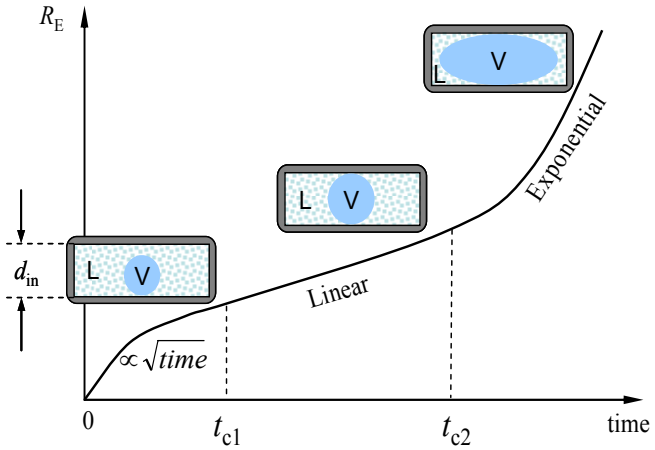

Figure 5-23. Drawing of the three-stage bubble growth and the corresponding vapour distribution in the channel cross-sectional view

The effect of heat flux on bubble growth rate is shown in Figure 5-24. Bubbles growing at four heat fluxes in d_h = 1454 μm channel are presented. Only the linear and exponential stages are seen in the comparison because the scale of t_{c1} is too short compared with t_{c2} for most of the cases. Apparently, bubble equivalent radius growth is

accelerated by the increased heat flux. The dash line in Figure 5-24 represents the critical time at which bubbles turn from linear growth to exponential growth. The measurements and analysis on bubble equivalent radius were also conducted on the bubbles growing in channels with d_h = 571 μm and 762 μm. Similar bubble growth mode and that the growth rate increases with increasing heat flux were also found in the 571 μm and 762 μm channels. Figure 5-25 (a) and (b) show an example of the visualization results of bubble growth in the 762 μm channel and the calculated equivalent radius at four different heat fluxes.

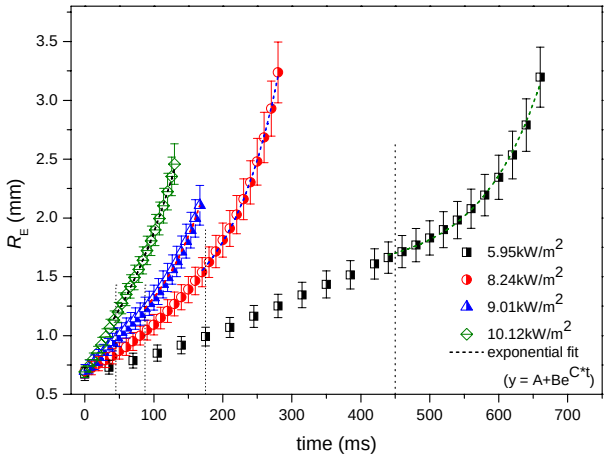

Figure 5-24. Bubble equivalent radius at different heat fluxes in the 1454μm channel, G = 22.4 kg·m^{-2}·s^{-1}; FC-72

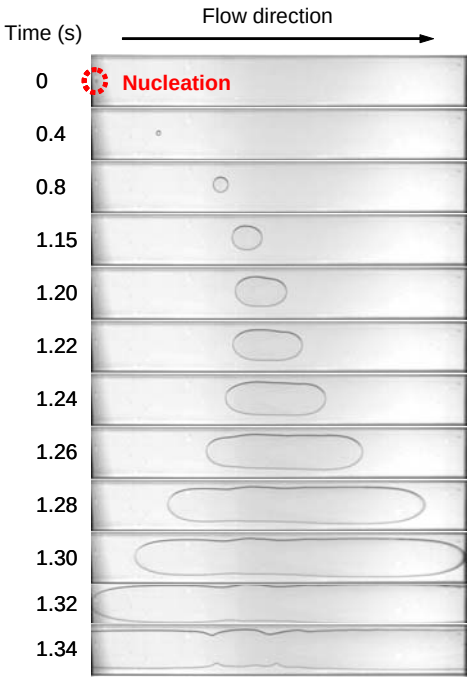

(a)

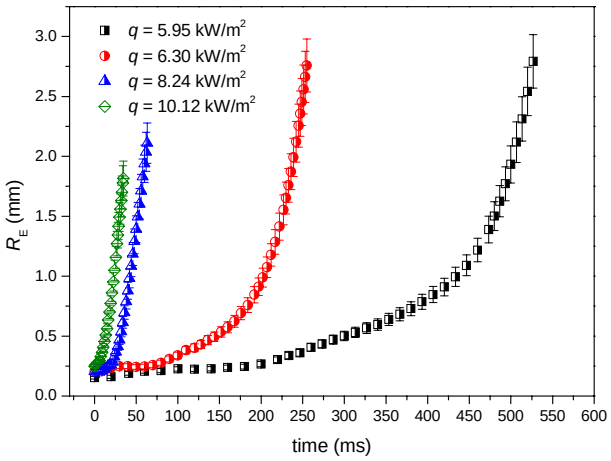

(b)

Figure 5-25. Single bubble nucleation and growth: (a) nucleation occurs at channel centre wall in the channel with d_h = 762 μm at G = 22.4 kg·m^{-2}·s^{-1} and q = 5.95 kW·m^{-2}, camera speed: 1000 fps (b) Bubble equivalent radius at different heat fluxes in the 762 μm channel at G = 22.4 kg·m^{-2}·s^{-1}; FC-72

5.4.2.3. Bubble aspect ratio and bubble geometry

Subsequently, the bubble aspect ratio is focused on to further reveal the bubble geometry evolution. Bubble aspect ratio σ is calculated as $\sigma = W_b/L_b$, where W_b and L_b are the bubble width and length respectively, as illustrated in Figure 5-26. Figure 5-27 gives the examples of the temporal bubble aspect ratio at two heat fluxes. As can be seen, σ firstly fluctuates around 1 within ±10% – ±20%. The slight fluctuation of bubble aspect ratio is probably caused by the channel inner surface non-smoothness which induces variations of radius curvature along the bubble interface. Therefore the vapour pressure distribution along the bubble surface is not uniform according to Young-Laplace Equation.

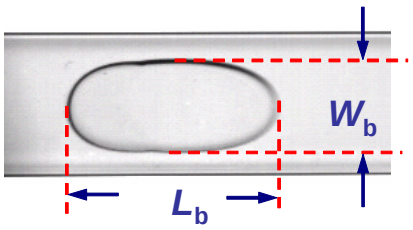

Figure 5-26. Bubble width and bubble length

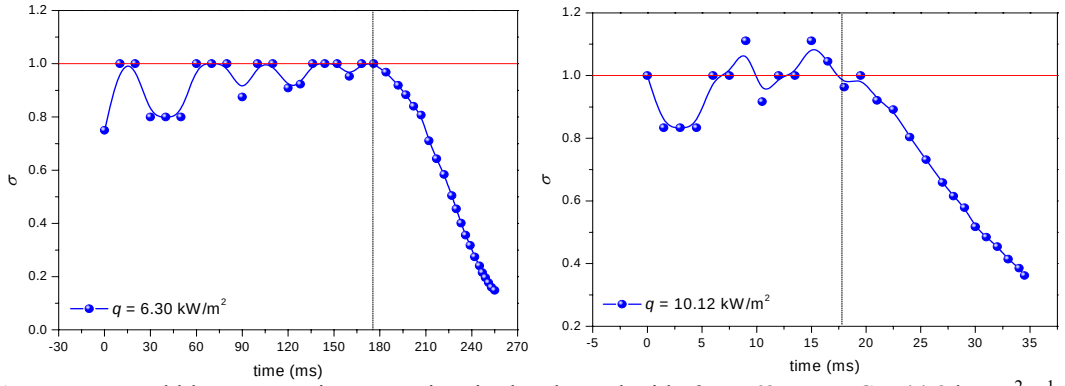

Figure 5-27. Bubble aspect ratio versus time in the channel with d_h = 762 μm at G = 44.8 kg·m^{-2}·s^{-1}, q = 6.30 kW·m^{-2} and q = 10.12 kW·m^{-2}; FC-72

The temporal aspect ratio at different heat fluxes and mass fluxes in 762 μm and 1454 μm channel are plotted in Figure 5-28 (a) and (b). The results obtained in the 571μm channel are excluded due to different heat flux range. Comparisons of aspect ratio at different heat fluxes show that the aspect ratio drops earlier at higher heat flux, indicating a higher growth rate and hence an earlier transition from linear growth to rapid exponential growth. After aspect ratio drops, the increase of heat flux increases the absolute value of the slope. Thus bubble is further elongated at higher heat flux. Besides, the effect of mass flux is shown in Figure 5-28 (b). Bubble is less elongated for lower mass flux as the slope of bubble aspect ratio at G = 44.8 kg·m^{-2}·s^{-1} is slightly higher than that at G = 22.4 kg·m^{-2}·s^{-1}. The slope of bubble aspect ratio curves S_σ obtained in the 762 μm and 1454 μm channels are summarized in Table 5-3 and Table 5-4 respectively. The increase of heat flux is more influential on the aspect ratio slope than the increase of mass flux, indicating the bubble growth after elongation is thermally controlled. Furthermore, it is noticed that S_σ is much higher in the 762 μm channel than in the 1454 μm channel. This implies the important role of channel geometry on bubble growth.

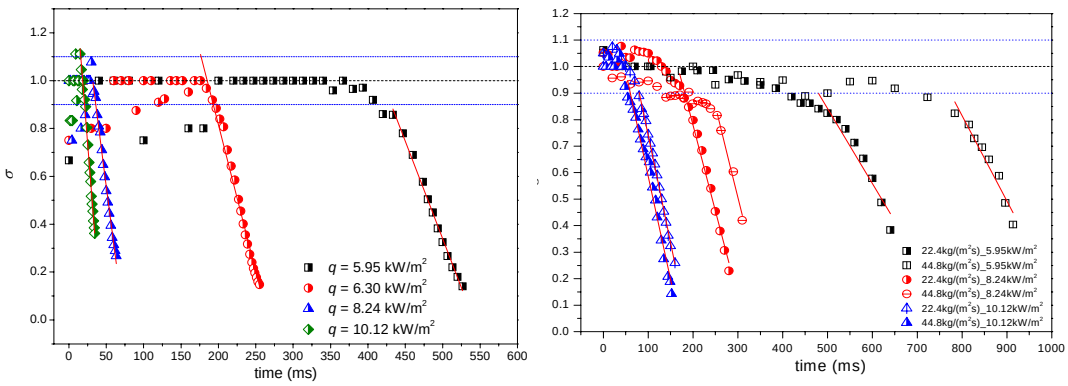

(a) (b)

Figure 5-28. (a) Bubble aspect ratio at different heat fluxes at G = 44.8 kg·m^{-2}·s^{-1}, d_h = 762 μm; (b) bubble aspect ratio at different heat fluxes for both G = 22.4 kg·m^{-2}·s^{-1}, and 44.8 kg·m^{-2}·s^{-1}, d_h = 1454 μm; FC-72

Table 5-3. Bubble aspect ratio slope comparison, d_h = 762 μm, G = 44.8 kg·m^{-2}·s^{-1}; FC-72 (for σ>1)

q (kW·m^{-2})	$S_\sigma \times 10^2$
5.95	-0.81
6.30	-1.23
8.24	-2.41
10.12	-3.95

Table 5-4. Effect of heat flux and mass flux on the bubble aspect ratio slope, d_h = 1454 μm; FC-72 (for σ>1)

q	$S_\sigma \times 10^3$	
(kW·m^{-2})	G_1 = 22.4 kg·m^{-2}·s^{-1}	G_2 = 44.8 kg·m^{-2}·s^{-1}
5.95	-2.83	-3.20
8.24	-6.48	-6.85
10.12	-7.85	-8.11

In order to emphasize the influence of channel geometry on the bubble geometry evolution, the bubble width is plotted against the bubble length. All the bubbles in the three channels at the same mass flux are included in Figure 5-29. Figure 5-29 presents the bubble width versus length at ranges of heat fluxes at G = 44.8 kg·m^{-2}·s^{-1} in the three micro-channels. As can be seen, in each tested channel, neither mass flux nor heat flux has significant effect on bubble geometry progression regardless of time. Bubbles with the same width have almost the same length. Only slight variation can be found at moderate bubble size, in consistent with the minor changes in aspect ratio slope discussed above.

Bubbles also show different width versus length trends for the channels with different cross sectional geometries. Channels with d_h = 571 μm and 762 μm have the same aspect ratio. The cross-sectional similarity manifests the dominant effect of channel size. Bubbles are further elongated when d_h = 571 μm. For 762 μm and 1454 μm channels, both channel widths are 8.0 mm. Therefore, channel depth is believed to have the major influence. As can be seen in Figure 5-29, bubbles with the same width are longer in the 762 μm channel. The decrease of channel depth has promoted the bubble elongation. This is consistent with the force analysis which also implies the appreciable effect of the channel depth.

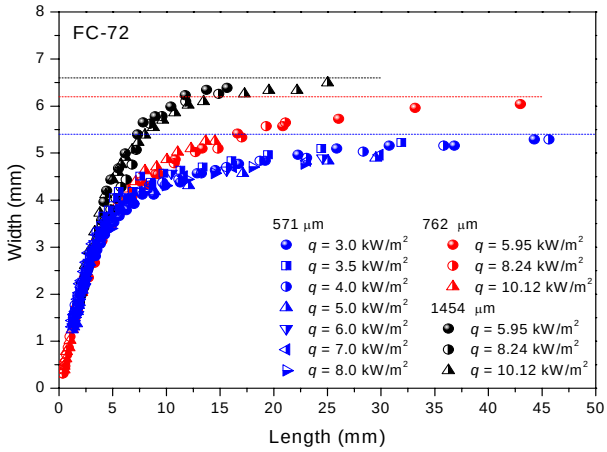

Figure 5-29. Bubble width versus length during flow boiling in three micro-channels at G = 44.8 kg·m^{-2}·s^{-1} and ranges of heat fluxes; FC-72

5.4.3. Evaporation heat transfer

The heat transferred for the evaporation of the surrounding liquid of the bubble was calculated based on the bubble volume growth rate and the latent heat of vaporization. The evaporation heat flux q_{evp} was computed as in eq. (5-7) and compared with the applied heat flux on the channel in Figure 5-30 (a). Apparently, not all the applied heat flux is used for vaporization. It seems that part of the heat is "stored" in the liquid adjacent to the heated channel surface instead of being used effectively for vaporization. Take q = 5.95 kW·m^{-2} for instance, less than 30% of heat flux is expended for evaporation within the first 250 s. This reveals that part of the heat is "stored" in the liquid and is used to increase the liquid temperature at the early stage of bubble growth.

It is also found that the calculated heat flux for evaporation becomes higher than the applied heat flux as the bubble grows. This could be explained that the heat previously "stored" in the bulk liquid is "released". Due to decreased local pressure, the local saturation temperature of the bulk liquid is lower than that of the upstream locations. The superheating level becomes relatively high, thus evaporation is intensified and the "stored" heat could be considered as an extra heat source for evaporation. Evaporation heat fluxes at different mass fluxes are also compared. In Figure 5-30 (b), as expected, increasing mass flux is shown to decrease the heat transferred for evaporation. It is understandable because at higher mass flux, the surrounding liquid is promptly replaced by the fresh liquid from upstream. Therefore the temperature of the surrounding liquid is lower. Consequently less heat is used for evaporation.

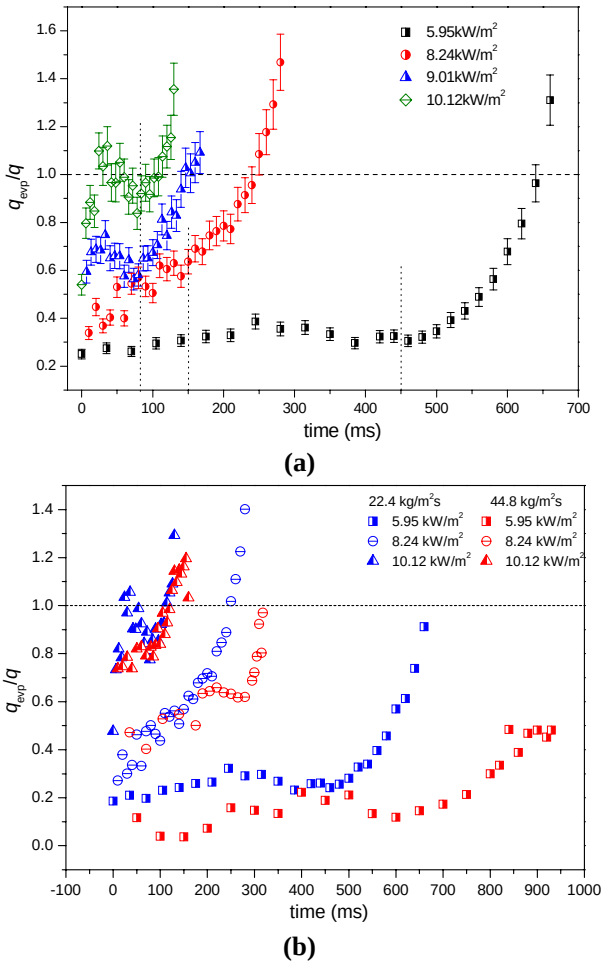

Figure 5-30. Bubble evaporation heat flux in the 1454 μm channel; FC-72, (a) Effect of heat flux, G = 22.4 kg·m^{-2}·s^{-1}, (b) Effect of mass flux

It is worth noting that due to the large aspect-ratio rectangular channel geometry, there is only very limited space for the bubble to grow in channel depth-wise direction. During the bubble growth, some vapour blankets and/or dry-out probably have already appeared on the top and bottom channel surfaces. It is also noticed that during the boiling, channel wall has much higher temperature than the boiling point of the working liquid. The high channel wall temperature confirms the existence of vapour blanket and/or dry-out. So the radiation from the heated channel inner wall becomes unnegligible. The radiation from the channel wall also partially contributes to the vaporisation.

5.5. Conclusions

In the study presented in this chapter, the onset of liquid-vapour phase change was captured. Succeedingly, the single vapour bubble growth in micro-scale space has been

investigated with and without liquid flow. FC-72 and n-pentane bubbles firstly grew between two parallel superheated plates. Then extensive investigations were conducted for bubble growth during flow boiling of FC-72 and ethanol in high aspect ratio rectangular micro-channels with the hydraulic diameters of 571 μm, 762 μm and 1454 μm at ranges of heat fluxes and mass fluxes. Transparent heating technique was utilised. Based on the high speed visualisation results and the corresponding evaporation heat transfer analysis, the following conclusions are drawn:

The heat flux required for the onset of nucleation q_{ONB} is increased with increasing mass flux and in larger-sized micro-channel. Onset of nucleation becomes increasingly deviated from the heat required for liquid to reach the saturation temperature. The heat losses to the surrounding and that the spatial thermal coupling modifies the local temperature could partially explain the increasing deviation. Besides, the incipient superheating is higher at higher mass flux.

The succeeding flow regimes in the present study show distinctive features. The unique high aspect ratio micro-channel geometry accelerates the rapid transition from bubbly flow to slug and annular flow in the channel. The main flow regimes are slug and annular flow, annular flow and wispy-annular flow with evaporating liquid film and entrained liquid droplets due to rapid vapour core movement.

Single bubble growth plays an important role in the flow regime transition and the local heat transfer. The study on single bubble growth consists of two main parts:

First of all, the bubble growth rate increases with plate superheating when growing between two parallel plates without flow. The physical properties of liquids such as liquid specific heat and surface tension are crucial for bubble growth. Besides, the increasing plate gap is found to accelerate the bubble growth rate.

For the bubble growth during flow boiling, a typical three-stage bubble growth mode is revealed. Before reaching the channel depth, the bubble grows proportionally to the square root of time. Then bubble size grows linearly and finally turns into exponential when bubble width occupies 78% – 90% of the channel width as a result of the appreciable drag force impact in the flow direction. The stage when bubble grows proportional to the square root of time is not captured in parallel plate tests due to narrow gap and is relatively short compared with the entire bubble life time during the growth in flow boiling. Bubble linear growth is dominated by liquid inertia force and the exponential growth is dominated by heat transfer via liquid film evaporation. The liquid flow contributes to accelerating the transition from linear growth to exponential growth.

Besides, qualitative force analysis explains that the bell-shape bubble is formed by the non-uniform liquid velocity distribution along the channel width-wise due to no-slip condition.

The time of the bubble rapid elongation commencement is named as critical time, which is the time when rapid exponential growth starts. Critical time decreases with increasing heat flux and decreasing mass flux, or with increasing plate superheating in the parallel plates experiments.

Moreover, bubble aspect ratio ($\sigma = W_b/L_b$) first maintains at 1 within $\pm$ 10% – 20% and then drops drastically. During the bubble elongation, increasing heat flux increases the aspect ratio slope; mass flux has minor effect on the bubble aspect ratio. Heat flux and mass flux do not significantly affect the heat transfer mechanism during single bubble growth but only change the bubble evolution speed. However, bubble geometry progression is found sensitive to the channel cross-sectional geometry. Bubble elongation is promoted in channels with smaller hydraulic diameter as well as smaller channel depth.

Based on bubble growth rate, the evaporation heat flux is obtained. Data show that only part of the applied heat flux is used for evaporation. Heat is "stored" to increase the liquid temperature. Evaporation heat flux increases with increasing heat flux and decreasing mass flux. Interestingly, evaporation heat flux finally becomes higher than the total applied heat flux. This is a consequence of the local saturation temperature reduction due to the sudden pressure drop. The previously "stored" heat is released and serves as an extra heat source for vaporization.

Chapter 6

Evaporating meniscus in single micro-channels

6.1 Introduction

Thermal management in micro-systems is confronting demanding challenges in the miniaturisation and intensification of the processes. In the applications such as micro heat pipes, compact heat exchangers, capillary pumped loops (CPLs), fuel cells and porous media drying, the thin liquid film evaporation is believed to be the dominant heat transfer mechanism (Potash Jr and Wayner Jr [229]). Particular attention has been dedicated to study the evaporation in the vicinity of the meniscus triple line. The triple line represents the boundary between liquid-vapour-solid phases. During intensive evaporation near the triple line, very high heat flux can be reached and a remarkable temperature gradient could be achieved (Potash Jr and Wayner Jr [229] and Hemanth *et al.* [230]). Consequently, the temperature-dependent surface tension shows a gradient which promotes the thermocapillary convention near the triple line. The evaporation from the meniscus and the capillary convection near the contact line are of significant importance in the heat and mass transfer processes. For instance, Stephan and Hammer [231] once pointed out that the microscale heat and mass transfer in nucleate boiling strongly depends on vapour-liquid phase equilibrist of a thin liquid film adsorbed between the heated wall and the vapour bubble.

When the liquid is in contact with the solid surface, the extended meniscus could be divided into different regions. Stephan [232] divided the liquid film between vapour and heated wall into macro-region, micro-region and the absorbed film based on the interface curvature: the interface curvature is almost constant in macro-region, but sharply turns in the micro region and eventually approaches zero in the adsorb film.

Potash Jr and Wayner Jr [229] modelled the transport processes that occurred in a two-dimensional evaporating meniscus and the adsorbed thin film on a superheated flat glass plate immersed in a liquid. It was assumed that the local heat flux across the meniscus is fixed by the thermal resistance of the liquid. The change of the meniscus profile was found to produce a pressure drop which circulates fluid flow and sustains the evaporation. It was also shown that in the non-evaporating region, the liquid sticks to the channel surface under the strong intermolecular forces; disjoining pressure (or the long range molecular force) dominates in the transition or the thin-film region while in the intrinsic meniscus region, the capillary force is prevailing (as in Figure 6-1, Park *et al.* [233], Wang *et al.* [83] and Wang *et al.* [234]) . The disjoining pressure was the

consequence of the pull of the adhesion force between the adsorbed liquid molecules in the thin liquid film and the tube wall, *i.e.* the liquid-solid interfacial force and it led to the liquid flow in the thin liquid region.

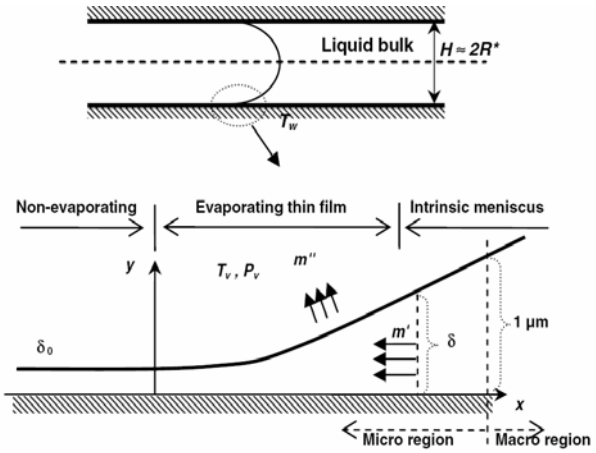

Figure 6-1. Schematic diagram and coordinate system for an evaporating thin film in a channel ([83, 232, 233])

Attempts had been made to explore the meniscus movement and the heat transfer during the thin film evaporation in confined space.

Preiss and Wayner [235] experimentally studied the characteristics of an evaporating ethanol meniscus formed at the exit of a glass capillary tube. They found that the meniscus profile was a function of the evaporation rate and the initial hydrostatic head. This agreed with the assumption that the fluid flow at the meniscus changes the meniscus profile and eventually leads to the liquid pressure variation. Besides, the meniscus was found to be stable over a wide range of evaporation rates.

Further work of Renk and Wayner [236] and Renk and Wayner [237] reaffirmed that the meniscus profile was a function of heat flux. The change of meniscus profile drove the fluid flow which replenishes the liquid evaporated in a stationary meniscus. Given the achieved local evaporative heat flux, it was suggested that a stationary evaporation meniscus could be used as an effective local heat sink.

Impact from liquid films had been tested by Cook *et al.* [238]. They concentrated on the contact line region of an evaporating decane meniscus as a function of evaporative heat flux. Scanning microphotometer was utilized to measure the meniscus profile. The effect of heat flux on the meniscus suggested that fluid flow in the contact line region of an evaporating liquid film was induced by the change of the film thickness.

Wayner *et al.* [239] pointed out that the curvature gradient is a strong function of the evaporation rate and composition. It was also noted the temperature and concentration gradient can lead to interfacial shear stresses and fluid flows which improve the contact line stability.

Modelling of the meniscus in a channel is complicated due to the varying liquid film thickness and the meniscus shape. Efforts have been made to develop theoretical models to describe the evaporating meniscus (DasGupta *et al.* [240], Wayner [241], DasGupta *et al.* [242], Stephan [232], Nilson *et al.* [243], Wang *et al.* [83]). The Yong-Laplace equation gives the static equilibrium of the meniscus. The augmented Young-Laplace equation provides the liquid-vapour pressure difference and has been used to evaluate the interface properties, to describe the meniscus shape, to predict the contact line motions, and to predict the dependency of meniscus shape and stability on the evaporative heat flux.

In the attempts to accurately acquire the thin liquid film profile, technologies including the interferogram and ellipsometric method were commonly employed. Measurements such as the film thickness, liquid drop edge spreading speed, isothermal profiles of the extended meniscus and the thin liquid film curvature and contact angle were obtained (Liu *et al.* [244], Zheng *et al.* [245], Zheng *et al.* [246], Panchamgam *et al.* [247]). Furthermore, the interfacial temperature is vital for the evaporation heat and mass transfer calculations (Wang *et al.* [234]). However, more difficulties were encountered when measuring the interfacial temperature due to the small scale. Instead of using the conventional thermocouples, technologies such as the thermochromic liquid crystal (TLC) and high-resolution infrared camera became more popular.

Buffone and Sefiane [248] acquired the temperature profile along the meniscus interface of volatile liquids in capillary tubes, the diameters of which ranged from 600 to 1630 μm. Thanks to the high spatial resolution (~ 30 μm) and the excellent sensitivity (20 mK at 30°C) of the infrared camera, the sink effect of meniscus triple line was captured. They reported increased sink effect with the reduced tube size and increased liquid volatility. Besides, liquid evaporated more at the meniscus wedge than in the middle of the meniscus, which resulted in the thermocapillary Marangoni convection.

In the continuous work of Buffone and Sefiane [249], the temperature of the n-pentane evaporation in a micro-tube (d_{in} = 1630 μm) was mapped onto the tube surface using the thermochromic liquid crystal (TLC). The authors extrapolated the heat flux

profile along the meniscus according to the temperature profile and managed to evaluate the evaporation flux.

Recently, Chauvet *et al.* [250] studies the evaporation of the thick liquid corner film in a square capillary tube (1 mm internal width) using the infrared thermography. When the tube was horizontally positioned, the evaporation rate was found to be at a stationary value, the capillary effect was dominating and the film thickness remained constant in the entrance region. However, when the tube was positioned vertically, the evaporation rate increased with the thinning of the corner film under the action of both gravity and viscous effects.

Moreover, the introduction of nanoparticles on the contact line made the study on meniscus evaporation even more complex. Nanoparticles have been identified to influence the fluid surface tension (Kim *et al.* [184], Chen *et al.* [251]) and the contact angle on the substrate (Kim *et al.* [184], Vafaei *et al.* [252], Munshi *et al.* [253], Sefiane *et al.* [254]). Besides, contact line stick-slip behaviour was observed during the evaporation of volatile drops (Moffat *et al.* [255]). The nanoparticle would migrate or pin at the contact line and the deposition on the solid surface would also change the surface structure.

Even though many studies have been conducted on the triple line and meniscus in confined space, the understanding of evaporation in micro-scale space is still far from enough owing to the lack of precise experimental measurements in the triple line region. Because of the appealing heat transfer potential of nanofluids and the significant role of thin liquid film evaporation and evaporative heat transfer in small pipes, the present study was conducted to acquire visualisation and thermographic results of a stationary meniscus confined in a high-aspect-ratio rectangular micro-channel with pure liquid and nanofluid. The meniscus was described as stationary when it is not moving upward or downward in the channel, but not necessarily mean the meniscus is non-deformed.

6.2 Experimental setup and procedure

The experimental facilities described in Chapter 3 session 3.2.4 were used in the present investigation of evaporating meniscus in vertical micro-channels. Three high aspect ratio micro-channels with the hydraulic diameters of 571 μm, 762 μm and 1454 μm were tested. An extra 727 μm with a 0.4 mm × 4.0 mm cross section was used when discussing

the evaporation rate per length on the contact line. Experiments were conducted within the plexiglass box at atmospheric pressure and an ambient temperature of 25°C. Transparent heating was utilised, providing controllable heat input on the channel. Pure ethanol and ethanol-based Al_2O_3 nanofluids were selected. So far, only the 0.01 vol.% nanofluid has been tested.

A meniscus was maintained in the vertical micro-channel. Controllable heat flux was applied on the channel outer surface, and the syringe pump flow rate was adjusted to keep the meniscus at a constant altitude within the channel. Therefore the flow rate could be considered as the evaporation rate at the meniscus. The evaporation rate as a function of heat flux was obtained. Meanwhile, the transient temperature profiles of the channel outer surface at and around the contact line region were acquired by the infrared (IR) camera which was operated at 7 fps and the ThermaCAM Researcher Professional® software was used to analyze the IR image sequences. The synchronous visualisation was provided by the high speed camera.

6.3 Results and discussions

6.3.1. Visualisation results of the meniscus

Before applying heat on the micro-channel, the meniscus was found receding in the channel due to evaporation. Then, the interface started to move upward in the channel when heat was applied uniformly on the channel outer surface. This could be explained as a result of the changed liquid surface tension, which decreases with increasing temperature. Then, further increase of heat flux achieved stationary meniscus. A stable meniscus was maintained with the help of a syringe pump, the pumping speed of which equalled to the liquid evaporation rate. Figure 6-2 shows two groups of meniscus in the channels with hydraulic diameter of 571 and 1454 μm respectively. The evaporation rates are both 0.01 $ml \cdot min^{-1}$. The “L” and “v” in the figures represent the liquid and the air-vapour sides respectively. The meniscus was considered as stable when it maintained at the same altitude in the channel without any deformation. Apparently the shapes of the meniscus are different in different-sized micro-channels. The meniscus shape is a consequence of the force balance at the interface. As illustrated in Figure 6-3, the liquid is absorbed on the channel wall due to strong intermolecular forces. The relative importance of different forces such as surface tension, the forces of adhesion and the

weight of the liquid determines the meniscus shape. Capillarity is more profound in the smaller micro-channel because of the less liquid weight.

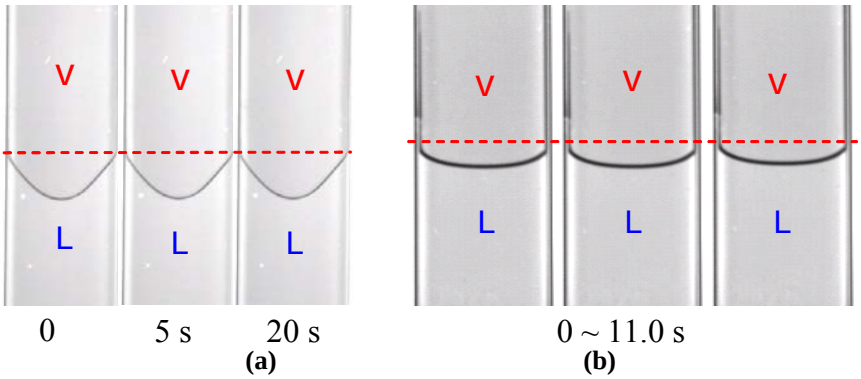

Figure 6-2. (a) Stable meniscus in the channel with d_h = 571 μm at evaporation rate 0.01 ml·min^{-1}, ethanol, (b) stable meniscus in the channel with d_h = 1454 μm at evaporation rate 0.01 ml·min^{-1}, ethanol; camera speed: 200 fps

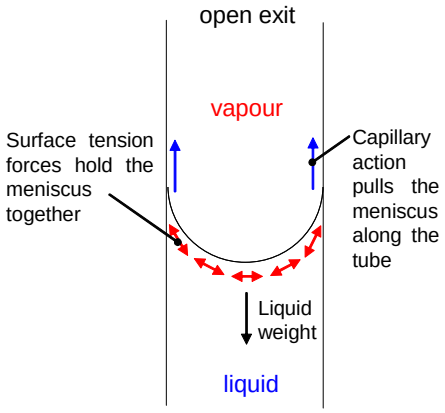

Figure 6-3. Schematic drawing of the forces at the meniscus in a vertical micro-channel

As the evaporation rate reaches higher levels, perturbed interfaces are observed, as shown in Figure 6-4. The interface instability is then followed by the onset of nucleation at the interface and then the large scale of vaporisation ensues (Figure 6-5). As the time scale of the nucleation incipient is too short, higher camera rate was necessary to capture the details. The camera speed was set at 1000 fps for the nucleation cases. However, owing to the reduced exposure time, the images appear darker at higher shutter speed. Therefore, the images in Figure 6-5 are processed using PCOPictures® by subtracting the dark background and adjusting the source image intensity scale.

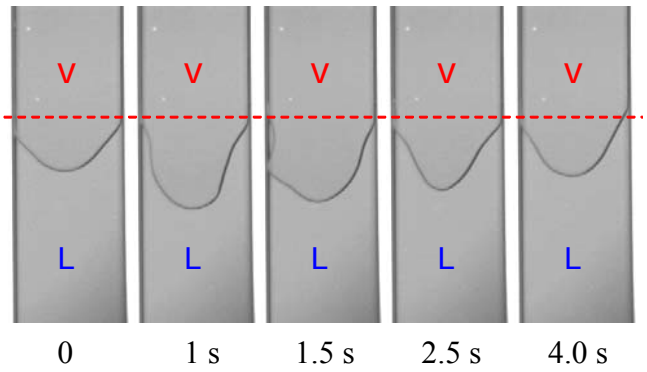

Figure 6-4. Deformed interface in the channel with d_h = 571 µm at evaporation rate 0.05 ml·min^{-1}, ethanol, camera speed: 200 fps

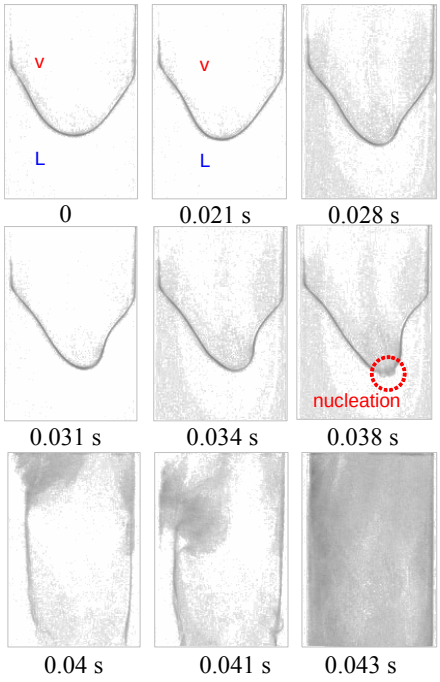

Figure 6-5. Nucleation at interface in the channel with d_h = 571 µm at evaporation rate 0.05 ml·min^{-1}, ethanol, camera speed: 1000 fps

The obtained results of pure ethanol were used as references when analyzing the ethanol-based nanofluids measurements. The meniscus of Al_2O_3-ethanol nanofluids was also observed. Similarly, stable meniscus was observed with nanofluid at relatively low evaporation rate. Figure 6-6 compares the stable meniscus obtained with 0.01 vol.% Al_2O_3-ethanol nanofluid and pure ethanol at the same evaporation rate 0.03 ml·min^{-1}. The contact angles on the channel side-wall are θ_{nano} and θ_{pure} respectively. The nanofluid has higher contact angle than pure ethanol. The meniscus in the channel was obtained carefully ensuring all the experimental conditions are the same except the nanoparticle concentration. The added particles increase the suspension density,

therefore the weight is larger. According to the force balance, higher capillarity is expected. Therefore the surface tension must be higher with a larger contact angle (*i.e.* lower $\cos\theta$). Correspondingly the wettability was decreased. However, further experiments with wider ranges of particle concentrations and different particle types are necessary to clarify the influence of nanoparticles on the contact angle.

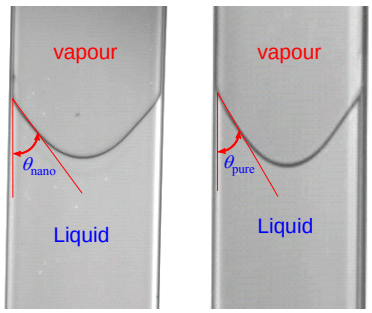

(a) **(b)**

Figure 6-6. Contact angle comparison in the channel with d_h = 571 μm, evaporation rate 0.03 ml·min^{-1} between (a) Al_2O_3-ethanol nanofluids, 0.01 vol.% and (b) pure ethanol; camera speed: 200 fps

Aside from the changed contact angle, the interface stability is also affected by the nanoparticles. Figure 6-7 presents the interfaces of pure ethanol and 0.01 vol.% Al_2O_3-ethanol nanofluids in the 571 μm micro-channel. At the evaporation rate of 0.04 ml·min^{-1}, the meniscus of pure ethanol is very unstable and is significantly deformed. However, the meniscus of the nanofluid at the same evaporation rate is more stable. The interface slightly oscillates up and down without being remarkably deformed. Besides, unstable meniscus of the nanofluid could be captured at an evaporation rate up to 0.07 ml·min^{-1} in the 571 μm micro-channel while the pure ethanol had already started nucleation. This shows that the nanoparticles substantially enhanced the meniscus stability even thought the particle volume fraction was only 0.01 vol.%.

Under heating conditions, the deposition and the building-up of a porous payer of nanoparticles on the surface become remarkable (Vafaei and Wen [256]). In the present study, it is also observed that as evaporation takes place, the nanoparticles deposit on the channel surface. Besides, the nanoparticles stay while the liquid reduces, resulting in increased local particle concentrations. Therefore, the local fluid viscosity is increased. The increased viscosity, the pinning effect of the nanoparticles at the meniscus and the change of surface condition might contribute to the improvement of meniscus stability. In the future work, nanofluids evaporation rate will be obtained to compare with that of pure ethanol to examine the effect of added particles. Beside, during the experiment,

large amount of nanoparticle depositions or fouling are found on the channel inner surfaces near the meniscus locations. Ultrasonic bath, flowing tap water and compressed air are used for cleaning. Sometimes new channels are used in each test to avoid the influence from the remained particle deposition. However, the fouling effect needs to be solved before the nanofluids evaporation and flow boiling can be practically used in wider applications.

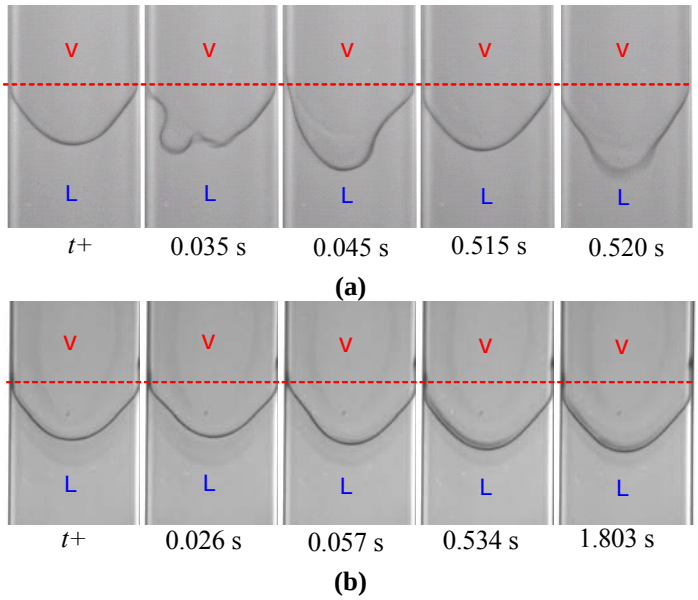

Figure 6-7. Interface stability in the 571 μm micro-channel (a) pure ethanol, camera speed: 200 fps, (b) 0.01 vol.% Al2O3-ethanol nanofluids at the evaporation rate of 0.04 ml·min^{-1}, camera speed 1000 fps

As mentioned above, during the transition from stable interface to the perturbed interface, the nanofluid meniscus was found moving up and down. It was observed that the meniscus recedes with step-slip as evaporation was taking place. Instead of staying at the same altitude, the meniscus drops down with short "step length", and then after dropping for a certain distance, the meniscus jumps back to the previous height. During the evaporation, the reduction of ethanol left the nanoparticles on the channel inner surface. Closer inspection reveals that the nanoparticle deposition appears line by line following the receding meniscus, as highlighted by the yellow arrow in Figure 6-8. The nanoparticle deposition line appears either from the edge to the middle of the meniscus or contrariwise. The temporal distance of the meniscus bottom to the top of the image was measured and plotted in Figure 6-9. It is worth mentioning that the measurement is a relative distance to the selected reference height on the channel. The aim is to highlight the step-slip phenomenon. During the slip, the meniscus slightly sticks on the channel

surface prior to the next step. Then, after falling for 0.55 mm – 0.60 mm, the meniscus jumps back to the previous height under the pumping pressure and begins the next step-slip recession. A similar "stick-slip" phenomenon was previously reported by Moffat *et al.* [255]. They described the stick-slip pinning behaviour of the triple line during the droplet evaporation and argued that the slip behaviour indicated the existence of hysteretic energy barriers and the stick behaviour was explained to be a result of locally increased viscosity or by the pinning of the deposited nanoparticles. In the present study, the meniscus sudden back-jump was observed when the liquid pressure conquers the joint resistance from the surface tension force and the pinning of the nanoparticles.

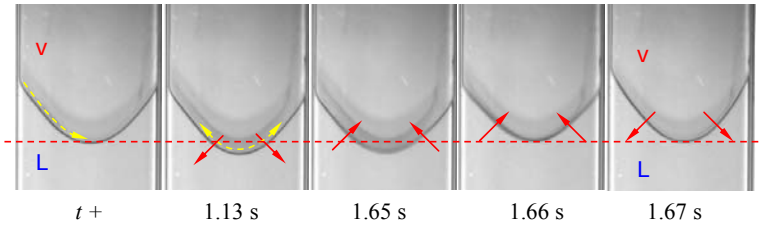

Figure 6-8. Stick-slip contact line of 0.01 vol.% Al_2O_3-ethanol nanofluid, d_h = 571 μm at evaporation rate 0.05 ml·min^{-1}, camera speed 100 fps

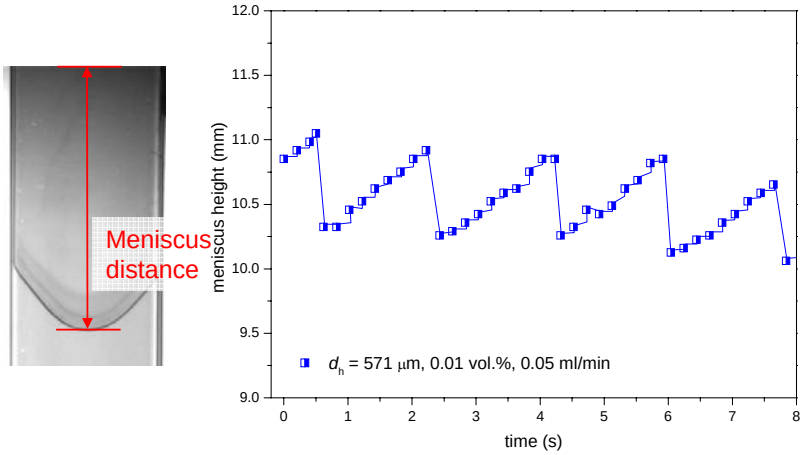

Figure 6-9. Meniscus distance measurement during step-slip, d_h = 571 μm, 0.01 vol.% Al_2O_3-ethanol nanofluids at evaporation rate 0.05 ml·min^{-1}

6.3.2. Meniscus evaporation rate

The meniscus evaporation rate measurements were reproduced for three times on different dates. Then the averaged results with error bars are plotted in Figure 6-10, in which the q is the heat flux on the channel outer surface. The dash lines are the incipient nucleation beyond which the large scale nucleation ensues. Apparently, the meniscus evaporation rate is an increasing function of heat flux. The channel dimension is also

influential on the evaporation rate when q > 1.2 kW·m^{-2}, showing an evaporation rate enhancement in larger micro-channel. This is as expected because the larger micro-channel has longer contact line, where most of the evaporation takes place (Buffone and Sefiane [248]). However, for q < 1.2 kW·m^{-2}, the evaporation rate is insensitive to the increasing heat flux. Similar with the analysis in Chapter 5, for the meniscus evaporation at very low heat flux, the heat can be considered to be stored in a superheated liquid layer near the interface before rapid evaporation occurs. Thus heat loss to the liquid is more profound at low heat flux conditions.

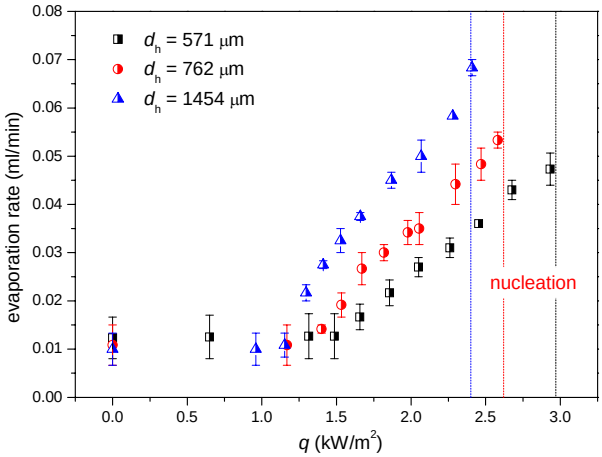

Figure 6-10. Meniscus evaporation rate versus heat flux in three micro-channels; pure ethanol

The evaporation rate per length, named as the specific evaporation rate in the present study, was also obtained by dividing the evaporation rate with the contact line length. To estimate the contact line length, electron microscope was used to measure the micro-channels cross-section. Figure 6-11 gives an example of the measurement of the cross-section of the 762 μm channel. The radius of the corner is around 101.84 μm, which is negligible compared with the channel width and depth. Therefore, the channel inner perimeter can be simply calculated as $2(W_{in} + d_{in})$ and the contact line length approximately equals to the inner perimeter. As in Figure 6-12, the curves of evaporation rate per length in the 571 μm and 762 μm channels almost overlap, showing that the evaporation rate in the rectangular micro-channel is proportional to the length of the contact line. However, the specific evaporation rate in the 1454 μm is slightly higher than the other two curves. The distinguishing specific evaporation rate in the 1454 μm channel is probably caused by the different channel cross-sectional aspect ratio. For

comparison, an extra 727 μm channel (0.4 mm ×4.0 mm) cross section, which had the same aspect ratio with the 1454 μm channel was used to testify the dependency of specific evaporation rate on channel aspect ratio and good agreement with 1454 μm channel is achieved as shown in Figure 6-12. The specific evaporation rate is higher when the channel aspect ratio is lower. Here the aspect ratio is defined as $\frac{\mathrm{MAX}(W_{\mathrm{in}}, d_{\mathrm{in}})}{\mathrm{MIN}(W_{\mathrm{in}}, d_{\mathrm{in}})}$.

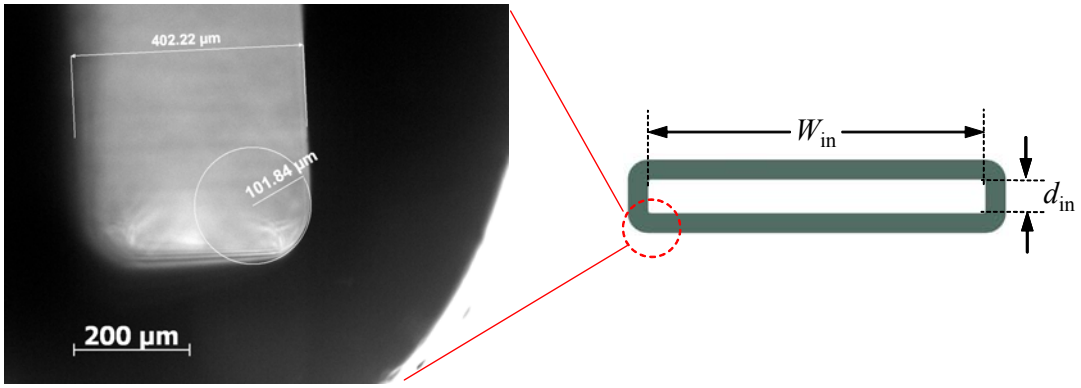

Figure 6-11. Microscopic photo of the channel cross-sectional corner, d_h = 762 μm

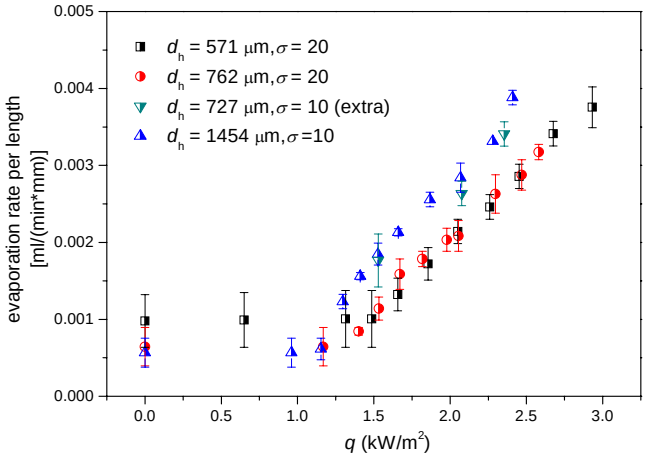

Figure 6-12. Evaporation rate per unit length versus heat flux

6.3.3. Infrared measurements at and around the meniscus

The infrared measurements of the channel surface temperature profiles are presented in this session to demonstrate the sink effect at the meniscus triple line. Figure 6-13 (a) gives an example of the IR image of the channel surface when a heat flux of 1.098 kW·m^{-2} is applied on the surface and the evaporation rate is 0.01 ml·min^{-1}. A stable interface without any deformation is observed. Because the evaporation peaks at the meniscus contact line, the local channel surface is cooled to a lower temperature than the

rest of the channel where the liquid and vapour are occupying. The temperature string data are extracted using the ThermaCAM Researcher Professional® software and plotted in 3-dimensional coordinate as in Figure 6-13 (b).

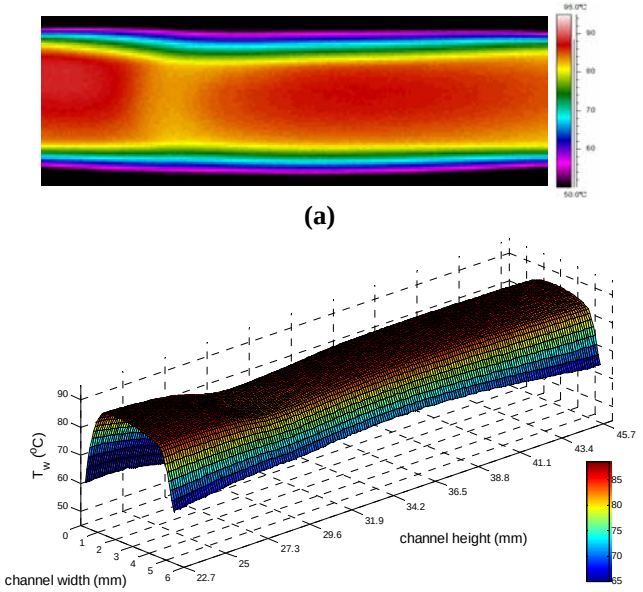

Figure 6-13. (a) IR image of the temperature profile in the channel with d_h = 571 μm at evaporation rate of 0.01 ml·min^{-1} and q = 1.098 kW·m^{-2}, stable interface, ethanol, (b) 3-dimensional plot

The meniscus sink effect was captured in all the tested cases. Selected IR images obtained in the 571 μm micro-channel are presented in Figure 6-14 – Figure 6-17, the corresponding interface transfer from stable to deformed unstable interface and the evaporation rate increases from 0.02 ml·min^{-1} to 0.06 ml·min^{-1}. It can be seen that as the evaporation rate increases, the temperature gradient across the meniscus becomes higher. This is because when higher evaporation rate is reached, the latent heat of the liquid is drawn from the air at a higher rate. Thus lower vapour temperature is achieved while the liquid interface is at the saturation temperature, therefore a higher temperature gradient is observed. The air and vapour mixture is then heated by the upper channel, and the vapour temperature increases from the meniscus.

Besides, according to the temperature profiles across the channel surface around the meniscus region, it is noticed that the temperature gradient varies along the meniscus, showing that the temperature gradient is higher at the meniscus wedge than the middle of the meniscus. This agrees with Buffone and Sefiane [248]. The consequent uneven surface tension on the meniscus brings the hot liquid to the colder region and results in the thermocapillary Marangoni convection. The temperature gradient along the meniscus

is more obvious at higher evaporation rate. During the experiment, some intense convection can be visualized by the high speed camera, but more precise measurements using Particle image velocimetry *(*PIV*)* are necessary to demonstrate the Marangoni convection.

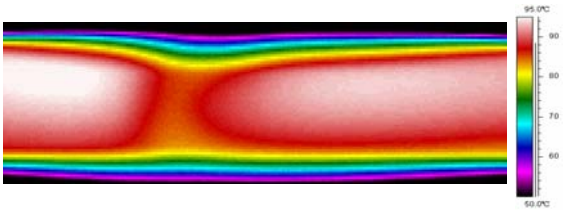

(a)

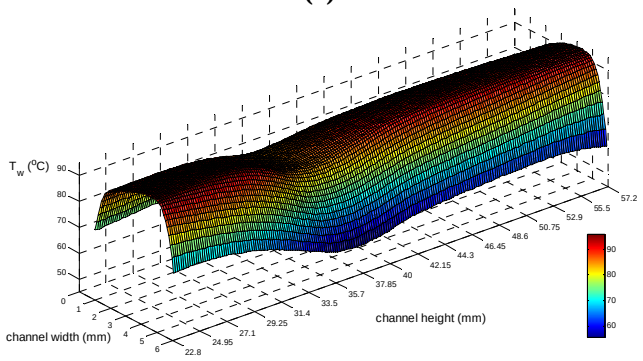

(b)

Figure 6-14. (a) IR image of the temperature profile in the channel with d_h = 571 μm at evaporation rate of 0.02 ml·min^{-1} and q = 1.357 kW·m^{-2}, stable interface, ethanol, (b) 3-dimensional plot

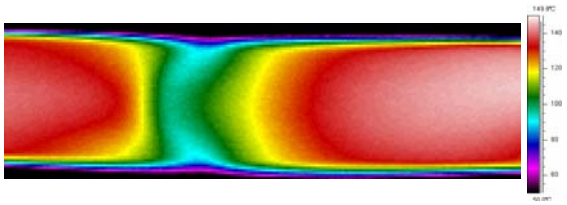

(a)

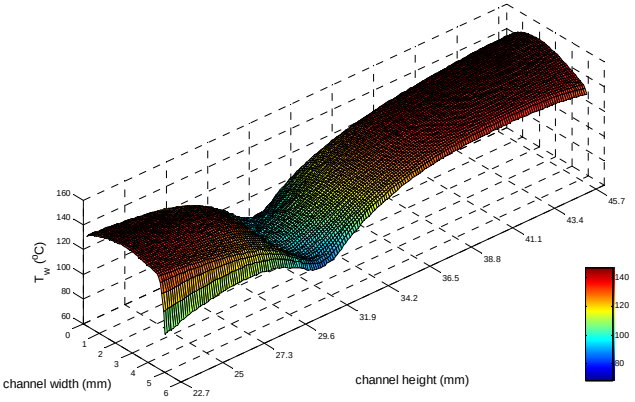

(b)

Figure 6-15. (a) IR image of the temperature profile in the channel with d_h = 571 μm at evaporation rate of 0.04 ml·min^{-1} and q = 2.132 kW·m^{-2}, unstable interface, ethanol, (b) 3-dimensional plot

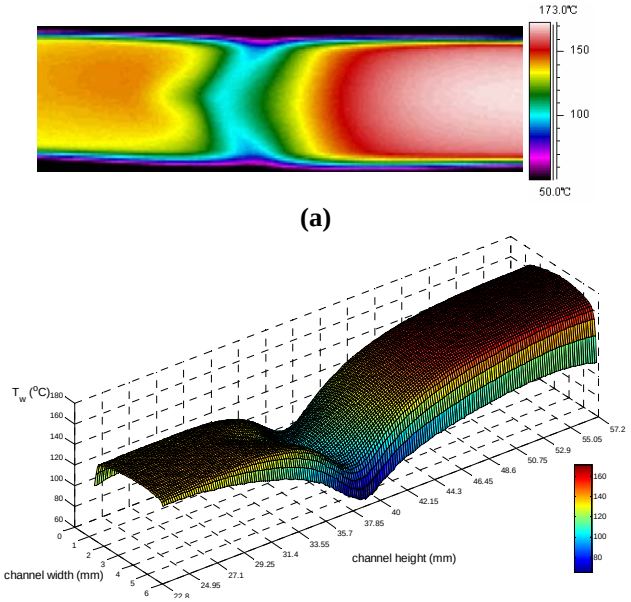

Figure 6-16. (a) IR image of the temperature profile in the channel with d_h = 571 μm at evaporation rate of 0.05 ml·min^{-1} and q = 2.969 kW·m^{-2}, unstable interface, ethanol, (b) 3-dimensional plot

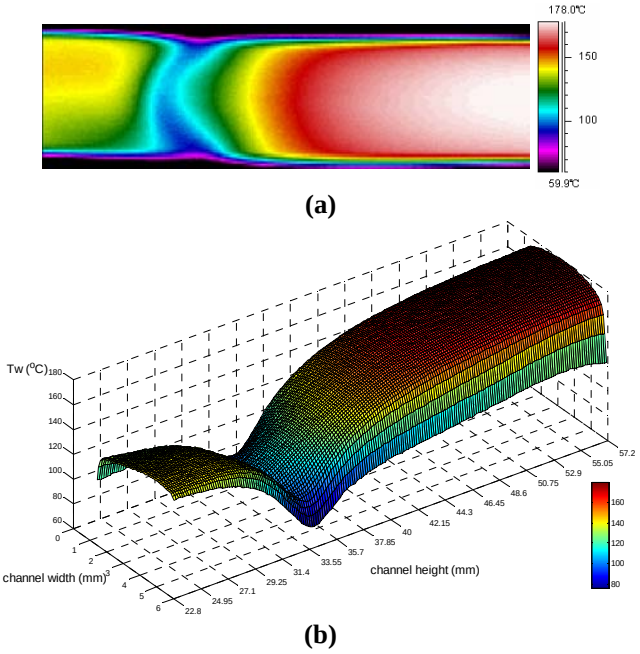

Figure 6-17. (a) IR image of the temperature profile in the channel with d_h = 571 μm at evaporation rate of 0.06 ml·min^{-1} and q = 3.318 kW·m^{-2}, unstable interface, ethanol, (b) 3-dimensional plot

The sink effect was further analyzed by extracting data across the axial line which passes through the meniscus bottom (see Figure 6-18 (a)). Figure 6-18 (b) and (c) are the acquired axial channel wall temperature profiles at different evaporation rates in the 571

μm and the 1454 μm channels. It is important to note that the presented results are the averaged string data of the entire infrared video.

Difference can be found between the stable and unstable interfaces. A temperature valley is observed from the liquid phase to the vapour phase. When the interface is stable, the temperature profiles along the central line show less deep and wider-mouth valley. Besides, the liquid temperature gradually increases as the evaporation rate increases, resulting from a higher heat flux.

Furthermore, the temperature difference between the liquid phase and the minimum vapour temperature at the profile valley is noted as ΔT_{sink}, as illustrated in Figure 6-18 (b). The dependencies of ΔT_{sink} on evaporation rate in different channels are plotted in Figure 6-19. The liquid and vapour temperature difference ΔT_{sink} is apparently an increase function of evaporation rate. In detail, the sink effect significantly increases when the meniscus is stable. However, only mild increase of sink effect is found after the meniscus becomes deformed. The influence of the micro-channel hydraulic diameter is not conclusive. More experiments are essential to explore the influencing factors on the meniscus sink effect.

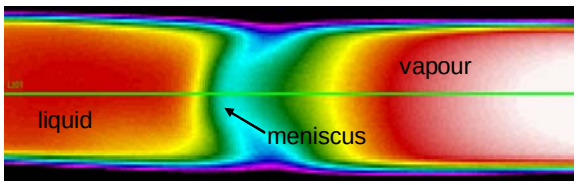

(a)

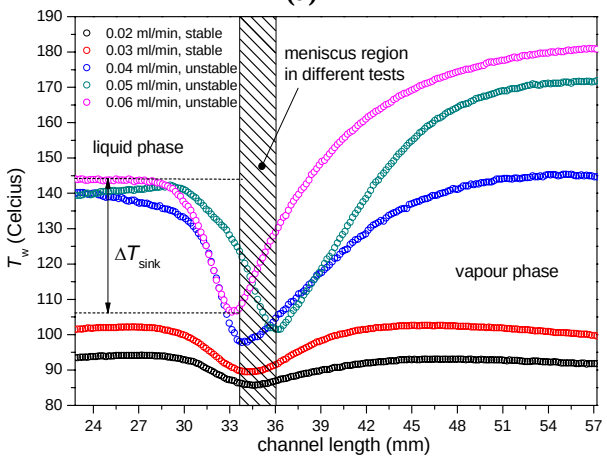

(b)

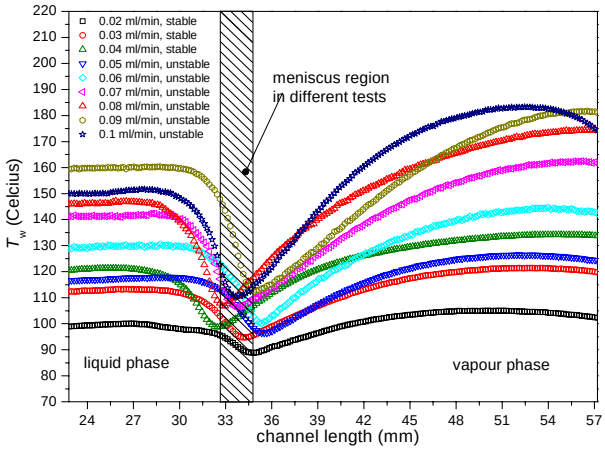

(c)

Figure 6-18. (a) line for axial temperature profile, (b) temperature profiles along the channel central line in the channel with d_h = 571 μm, (c) temperature profiles along the channel central line in the channel with d_h = 1454 μm; ethanol

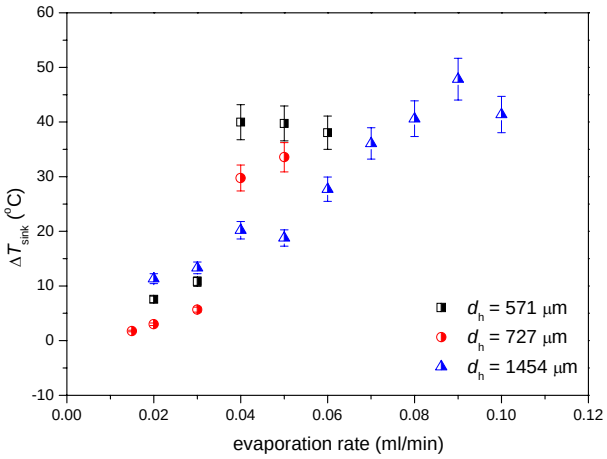

Figure 6-19. Sink effect versus evaporation rate in three micro-channels

6.4 Conclusions

In this chapter, visualisation and thermographic measurements at and around the meniscus triple line region in vertical high aspect ratio rectangular micro-channels were presented. Three high aspect ratio micro-channels with the hydraulic diameters of 571 μm, 762 μm and 1454 μm were tested for pure ethanol, and only the 571 μm channel was used in the ethanol-based Al_2O_3 nanofluids (0.01 vol.%) tests so far. The interface stability, effect of nanoparticles on the meniscus behaviours and the sink effect of the meniscus triple line were discussed. The following characteristics of the meniscus are gathered:

The shape of the meniscus in the micro-channel is determined by the joint effect of surface tension, the forces of adhesion and the weight of the liquid. Capillarity pulls the

meniscus to a higher distance in the smaller micro-channel because of less liquid weight. The meniscus interface becomes deformed when the evaporation rate increases. The interface perturbation is then followed by nucleation.

The use of nanofluids can largely enhance the interface stability even though the added particle volume fraction is as low as 0.01 vol.%. At the evaporation rate of 0.04 $ml \cdot min^{-1}$, the meniscus of pure ethanol is significantly deformed but stable meniscus with slight oscillation is observed with nanofluids. Unstable meniscus of the nanofluid are captured at an evaporation rate up to 0.07 $ml \cdot min^{-1}$ in the 571 μm micro-channel while the pure ethanol has already started nucleation. Besides, the additional nanoparticles increase the apparent contact angle. It can be inferred that the surface tension of the suspension is increased, thus the wettability is decreased.

An interesting "stick-slip and back-jump" behaviour of the nanofluid meniscus is captured during the transition from stable to deformed interface. The interface stick-slip recession lasts for 0.55 mm – 0.60 mm then the interface jumps back to the previous height when the liquid pressure conquers the joint resistance due to surface tension force and the pinning of the nanoparticles.

The meniscus evaporation rate is an increasing function of heat flux and channel dimension. Furthermore, based on the electron microscope measurement of the channel cross section, the channel corner curvature is negligible. Thus the meniscus contact line is approximated as the inner perimeter of the channel cross section. The evaporation rate per length in the channels with the same aspect ratio almost overlap, verifying that the evaporation rate is proportional to the length of contact line, which reaffirms that the evaporation peaks at the contact line. Evaporation rate per length is higher when channel aspect ratio is lower.

Sink effect of the meniscus triple line is captured via the infrared camera. The temperature gradient across the meniscus becomes higher as the evaporation rate increases. Moreover, the temperature gradient is higher at the meniscus wedge than the middle of the meniscus. The consequent uneven surface tension on the meniscus brings the hot liquid to the colder region and results in the thermocapillary Marangoni convection.

Chapter 7

Two-phase flow instabilities in single micro-channels

7.1. Introduction

Flow instabilities encountered during two-phase flow boiling were found to cause severe non-uniformities of surface temperature (Hetsroni *et al.* [257]) and to reduce the boiling heat transfer coefficients (Qu and Mudawar [258]). Flow instabilities would also result in pressure drop fluctuation and lead to high amplitude temperature oscillation (Bogojevic *et al.* [259] and Barber *et al.* [93]). In micro-channel flow boiling, two-phase flow instabilities are even more intense than in conventional channels owing to the confined space for vapour bubble growth. Bergles and Kandlikar [260] also reported reduced critical heat flux (CHF) accompanied with the flow instabilities. These instabilities might be catastrophic if followed by dry-out and could lead to heat exchanger burnout and system failure. Thus, before bringing the micro-channel flow boiling into wider applications, issues of flow instabilities must be addressed to better understand the occurrence of flow instabilities, the impact factors, and the possible options to control and reduce the instabilities.

In this chapter, flow instabilities are analyzed based on the two-phase pressure drop and channel surface temperature fluctuations as well as the synchronous visualization results.

7.2. Experimental setup and procedure

The experimental setups described in Chapter 3 session 3.2.1 and 3.2.2 were used in the present investigation of two-phase flow instabilities. All the experiments were conducted at atmospheric pressure. FC-72 and ethanol were used as the working liquids. Liquids were vigorously degassed for one hour to remove the dissolved gases prior to entering the flow loop. Meanwhile, the plexiglass box was heated up and maintained at 25°C. Then the working liquid was delivered into the flow loop by a syringe pump at desired flow rates. Transparent heating was utilised, providing controllable heat input on the channel. The liquids were eventually collected in a reservoir after passing the test section. The inlet and outlet pressures of the micro-channel test section were acquired via a National Instruments® Data Acquisition card at a predetermined acquisition frequency of 200 Hz. The offset pressures resulted from the background noises were recorded prior to

each test when the channel was filled with stagnant working fluid. Then the offset pressures were subtracted from the acquired raw data. Meanwhile, the boiling process was synchronously visualized by the high speed camera and analyzed with the Image Pro.® software. Besides, the transient temperature profiles of the channel outer surface were acquired by the infrared (IR) camera which was operated at 7 fps. The camera speed was high enough to capture the temperature fluctuations induced by the long-period recoiling and re-wetting cycles, the period of which was around 0.5 s. ThermaCAM Researcher Professional® software was used to analyze the IR image sequences. Table 7-1 lists the test conditions of the present study.

Table 7-1. Experimental conditions for the investigation on flow instabilities in single micro-channels

FC-72			ethanol		
channel d_h [μm]	Heat flux q [kW·m^{-2}]	Mass flux G [kg·m^{-2}·s^{-1}]	channel d_h [μm]	Heat flux q [kW·m^{-2}]	Mass flux G [kg·m^{-2}·s^{-1}]
571 762 1454	0 – 18.31	11.2, 22.4 and 44.8	1454	0 – 15.0	11.2 and 22.4

It is worth noting that the exhibited inlet and outlet pressure data in this chapter are the pressure data without subtracting the minor losses discussed in Chapter 4, session 4.3.1. Pressure drop fluctuation was firstly associated with the synchronous visualisation results to show liquid-vapour behaviours in time domain. Subsequently, Fast Fourier Transformation (FFT) was performed on the pressure drop results in Origin® software to assess the pressure drop fluctuation in frequency domain. The pressure drop fluctuation was also associated with the channel wall temperature oscillation based on the infrared thermographic measurements.

7.3. Results and discussions

7.3.1. Two-phase pressure and synchronous visualisation results

After boiling incipient, the two-phase pressures were found to be fluctuating with high amplitude. The fluctuations were believed to be triggered by the liquid-vapour two-phase flow according to the comparison with single phase pressure measurements in Figure 7-1.

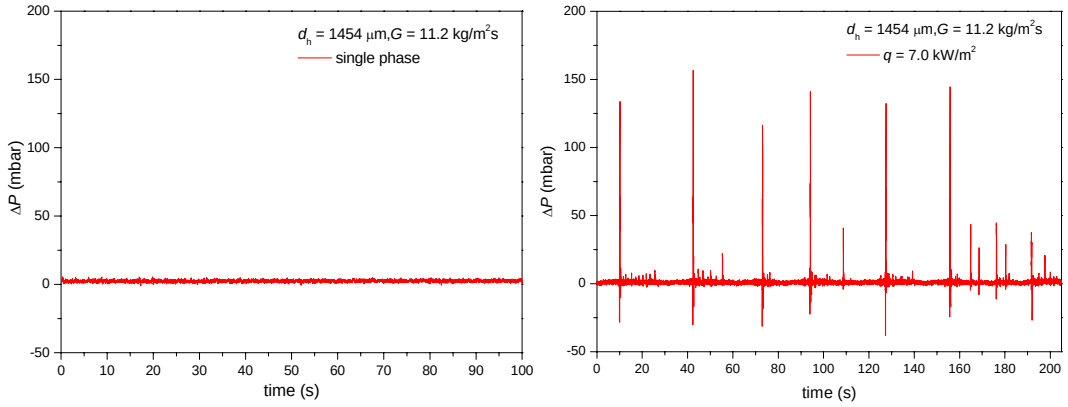

Figure 7-1. Pressure drop measurements, d_h = 1454 μm, G = 11.2 kg·m^{-2}·s^{-1}, (a) single phase flow without heating, (b) two-phase flow at q = 7.0 kW·m^{-2}; ethanol

Generally, the alternation from single phase liquid to liquid-vapour two-phase flow will lead to oscillation of the pressure drop across the channel. Transient pressure measurements accompanied with the visualisation results are exhibited as follows to discuss the different fluctuation types and the corresponding two-phase flow behaviours at various mass fluxes and heat fluxes.

First of all, low mass flux and low heat flux conditions are studied. Figure 7-2 (b) shows the time interval between two pressure oscillation peaks in Figure 7-2 (a). The results were obtained in the channel with d_h = 571 μm at G = 11.2 kg·m^{-2}·s^{-1} and q = 2.86 kW·m^{-2}. Two types of fluctuations are identified: the one with longer period (~ 14.33 s) has higher amplitude. This low-frequency high-amplitude fluctuation is considered as the major fluctuation due to the reverse flow. According to the visualisation, the low-frequency high-amplitude fluctuation is caused by the rapid vapour expansion and recoiling after nucleation. Figure 7-3 shows a series of the corresponding high speed camera sequences. After being filled with vapour, the channel is re-wetted by upstream fresh liquid, accompanied by a group of pressure oscillations with shorter period (0.20 s – 0.25 s) and lower amplitude. This high-frequency low-amplitude fluctuation can be considered as the minor fluctuation which normally takes place after the major fluctuation. From the visualization results, a cluster of vapour slugs are observed from upstream during re-wetting. The inlet and outlet pressures are consequently disturbed when the series of vapour collision occurs at downstream. As the length of vapour slug is reduced gradually, the amplitude of the minor fluctuation gets lower till the entire vapour slug cluster passes through and the channel is re-wetted by single phase liquid. Then the major fluctuation occurs again when the next nucleation cycle stars.

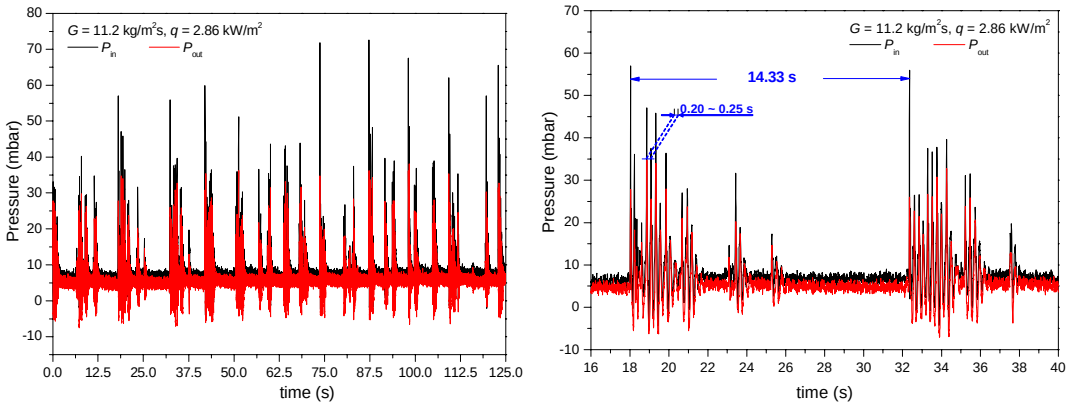

Figure 7-2. Inlet and outlet pressures, d_h = 571 μm, G = 11.2 kg·m^{-2}·s^{-1}, q = 2.86 kW·m^{-2}; FC-72

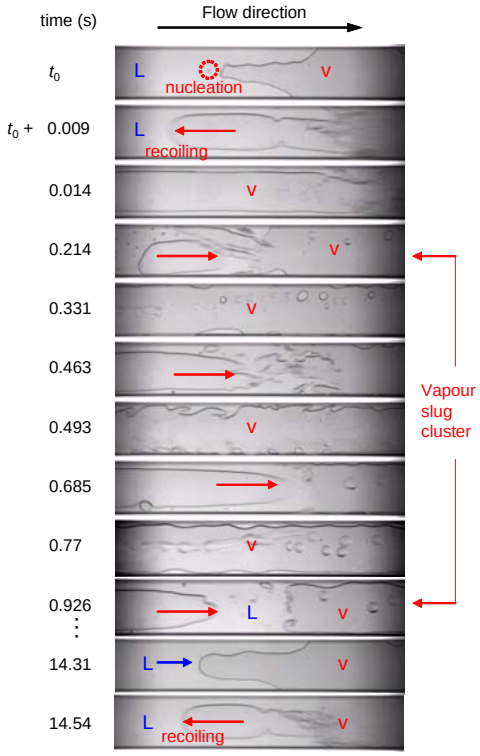

Figure 7-3. Visualisation of the flow boiling, d_h = 571 μm, G = 11.2 kg·m^{-2}·s^{-1}, q = 2.86 kW·m^{-2}; FC-72, camera speed: 1500 fps

At the same mass flux but a higher heat flux, the frequency of the low-frequency high-amplitude fluctuation is increased. As shown in Figure 7-4, heat flux increases to 3.47 kW·m^{-2}. The period of the major fluctuation is about 4.98 s, indicating a shorter period of the recoiling-rewetting cycle at a higher heat flux. The minor fluctuations caused by vapour slug cluster (Figure 7-5) are still observed. However, the period of the minor fluctuation is still around 0.20 s – 0.26 s.

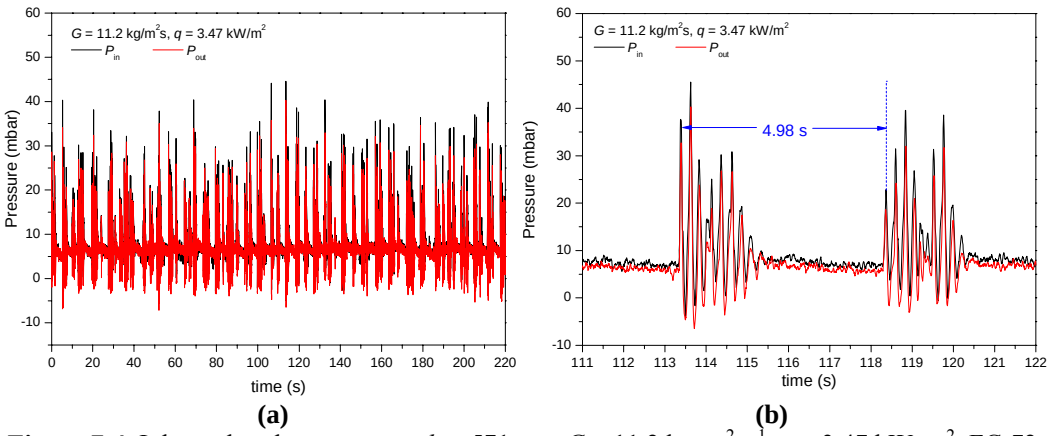

Figure 7-4. Inlet and outlet pressures, d_h = 571 μm, G = 11.2 kg·m^{-2}·s^{-1}, q = 3.47 kW·m^{-2}; FC-72

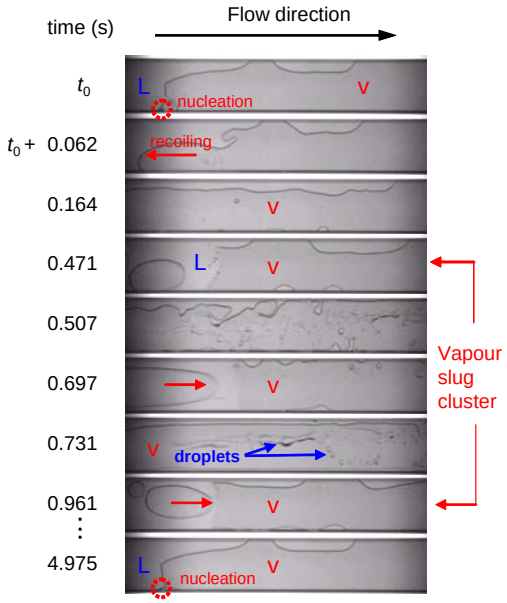

Figure 7-5. Visualisation of the flow boiling, d_h = 571 μm, G = 11.2 kg·m^{-2}·s^{-1}, q = 3.47 kW·m^{-2}; FC-72, camera speed: 2000 fps

Further increase of heat flux results in more intense boiling. In Figure 7-6, when heat flux increases to 3.88 kW·m^{-2}, large amount of vapour exists in the channel with high moving speed. Consequently large numbers of liquid droplets are entrained in the vapour core and are evaporating intensely. Partial dry-out spots on the inner channel surface are observed. Vapour collision is the cause of the high-frequency low-amplitude fluctuation, the frequency of which seems unaffected by increasing heat flux. At q = 3.88 kW·m^{-2}, the period maintains about 0.22 s.

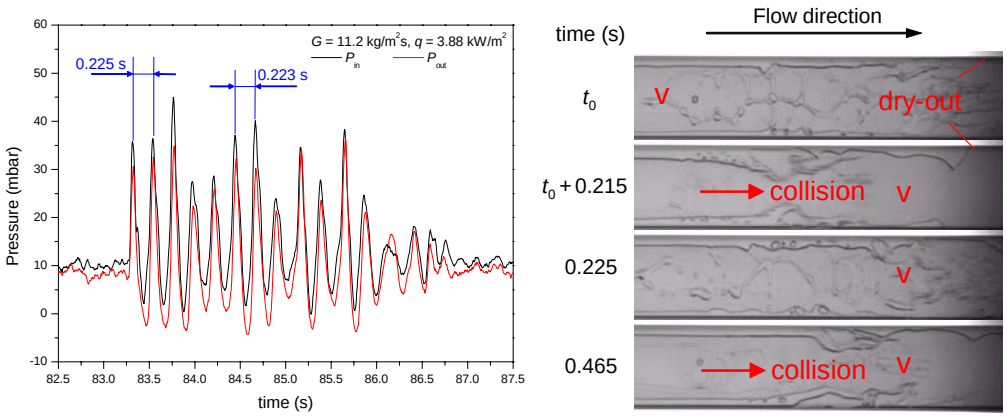

Figure 7-6. (a) Minor fluctuations of the inlet and outlet pressures, d_h = 571 μm, G = 11.2 kg·m^{-2}·s^{-1}, q = 3.88 kW·m^{-2}. (b) Corresponding visualisation of vapour collisions; FC-72, camera speed: 2500 fps

Mass flux is found to be influential on the pressure fluctuation. In the present study, a higher mass flux G = 44.8 kg·m^{-2}·s^{-1} is tested. The corresponding pressure shows one type of fluctuation mode. Only the high-frequency low-amplitude fluctuation is captured. Figure 7-7 presents the flow regimes in the channel with d_h = 571 μm at G = 44.8 kg·m^{-2}·s^{-1} and q = 6.90 kW·m^{-2}. Vapour slug cluster is observed after the initiation of nucleation. The vapour slug cluster passage lasts for a longer time than at the lower mass flux. Moreover, the amplitudes of the fluctuations are almost constant (Figure 7-8), only with slight decrease when approaching the end of the vapour slug cluster. The period of the minor fluctuation is 0.23 s – 0.24 s. Then the inlet and outlet pressures shortly stay stable when the channel is temporarily re-wetted by single phase liquid prior to the passage of the next vapour slug cluster. Figure 7-9 shows the flow regimes in the 571 μm channel at G = 44.8 kg·m^{-2}·s^{-1} and q = 10.31 kW·m^{-2}. Increased heat flux slightly shortened the fluctuation period, which becomes 0.195 s – 0.21 s. Similar flow regimes are observed (Figure 7-10). This reinforced that the increase of heat flux has minor effect on the high-frequency low-amplitude fluctuation.

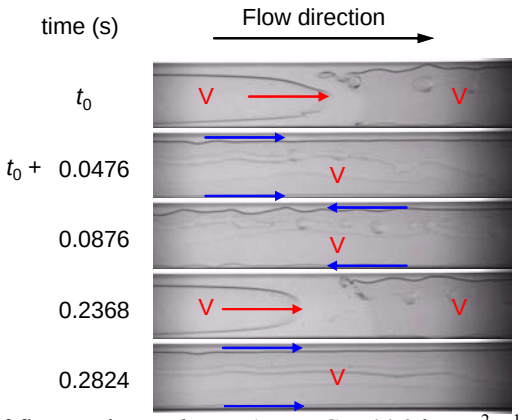

Figure 7-7. Visualisation of flow regimes, d_h = 571 μm, G = 44.8 kg·m^{-2}·s^{-1}, q = 6.90 kW·m^{-2}; FC-72, camera speed: 2500 fps

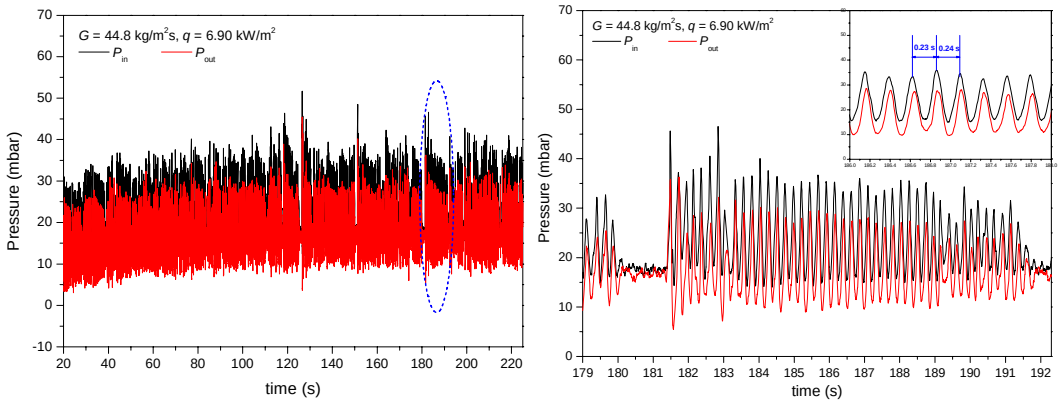

(a) **(b)**

Figure 7-8. Inlet and outlet pressures, d_h = 571 μm, G = 44.8 kg·m^{-2}·s^{-1}, q = 6.90 kW·m^{-2}; FC-72

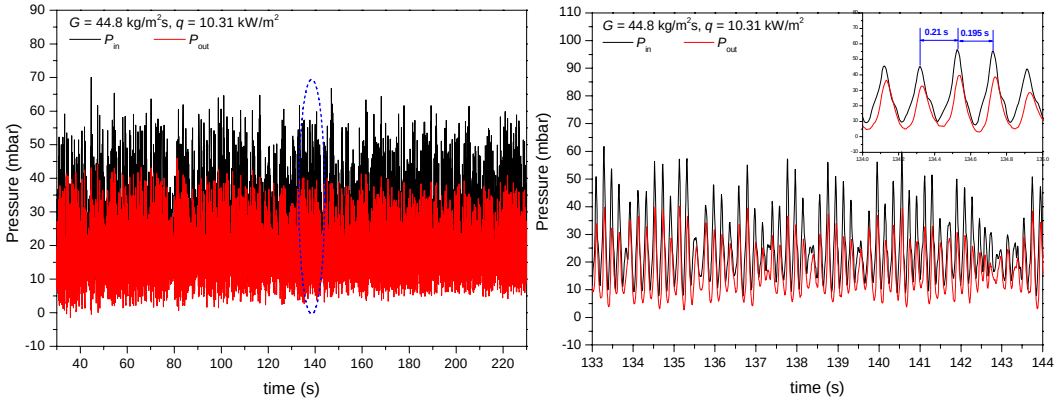

(a) **(b)**

Figure 7-9. Inlet and outlet pressures, d_h = 571 μm, G = 44.8 kg·m^{-2}·s^{-1}, q = 10.31 kW·m^{-2}; FC-72

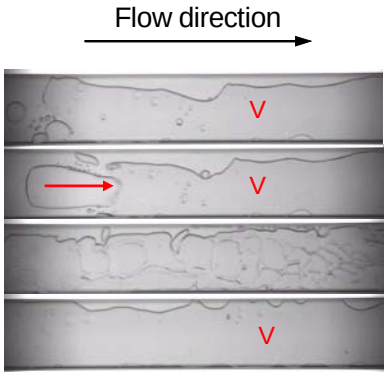

Figure 7-10. Visualisation of the flow boiling, d_h = 571 μm, G = 44.8 kg·m^{-2}·s^{-1}, q = 10.31 kW·m^{-2}; FC-72, camera speed: 2500 fps

It is also noticed in Figure 7-11 (a) that there are some tiny pressure disturbances after the high-frequency low-amplitude pressure fluctuation peak (highlighted in red circle). The period of the tiny fluctuation is in the order of 0.01 s. The answer can be found from the visualization results in Figure 7-11 (b). While large amount of vapour slugs move rapidly from upstream, liquid films with tiny nucleating bubbles are formed on the channel side-wall. The growth and expansion of these small bubbles will deform the liquid-vapour interface, and will consequently affect the pressures if the interface deformation propagates to the channel inlet and/or outlet. The cavities on channel side-walls are newly activated because of the reduced local pressure. This kind of tiny disturbances is seldomly captured in the 571 μm channel. The increase of channel cross-sectional area provides larger space for thicker liquid film which gives rise to the liquid film nucleation.

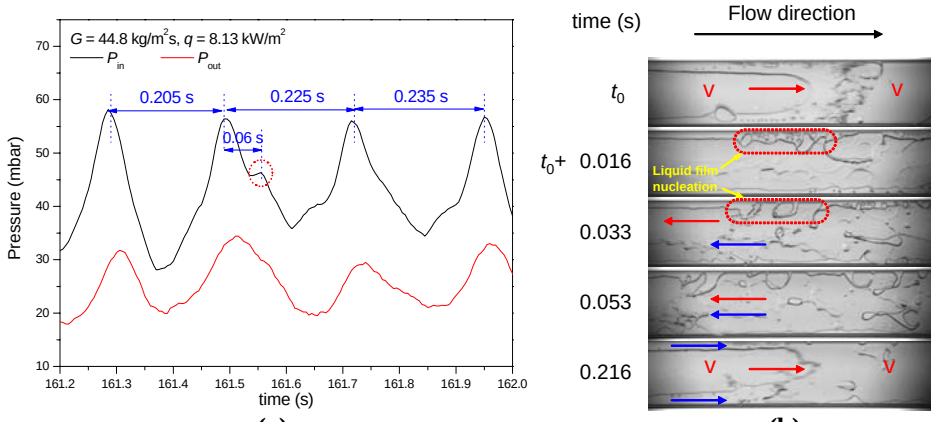

Figure 7-11. (a) Inlet and outlet pressure, d_h = 762 μm, G = 44.8 kg·m^{-2}·s^{-1}, q = 8.13 kW·m^{-2}, (b) Corresponding visualisation of liquid film nucleation and reverse flow; FC-72, camera speed: 2000 fps

Chaotic boiling ensues when the channel size further increases. The major fluctuation in the 1454 μm channel is still a result of the vapour collision. However, the larger cross-sectional area increases the complexity of the flow field. Figure 7-12 presents the typical flow regimes in the 1454 μm channel at G = 44.8 kg·m^{-2}·s^{-1}. Notable nucleation within the thick liquid film and the fiercely-evaporating droplets entrained in the fast-moving vapour core are observed.

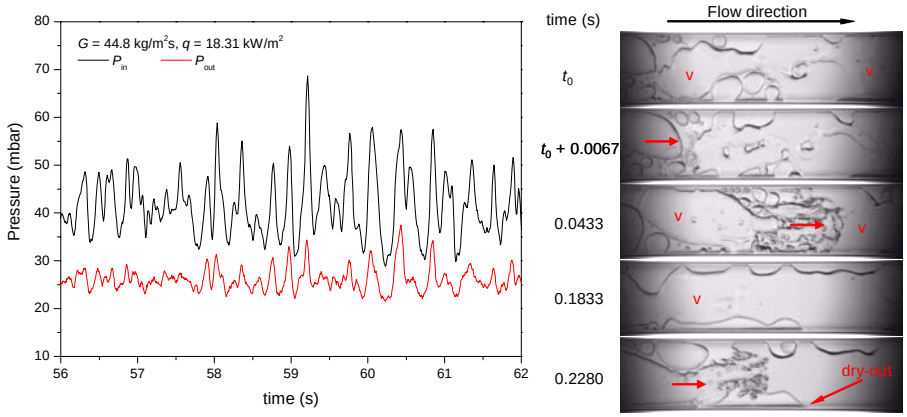

Figure 7-12. (a) Inlet and outlet pressures, d_h = 1454 μm, G = 44.8 kg·m^{-2}·s^{-1}, q = 18.31 kW·m^{-2}; FC-72, (b) Corresponding visualisation showing nucleation within liquid film and vapour collision, camera speed: 3000 fps

7.3.2. Analysis on two-phase pressure drop

Two-phase pressure drop data are analyzed to discuss the effects of heat flux, mass flux and the channel dimension on the fluctuation frequency and amplitude. First of all, the averaged pressure drop is plotted against heat flux in Figure 7-13. All the pressure drop data acquired in the micro-channels with d_h = 571 μm, 762 μm and 1454 μm at G = 11.2 kg·m^{-2}·s^{-1}, 22.4 kg·m^{-2}·s^{-1} and 44.8 kg·m^{-2}·s^{-1} are included. For each flow rate, the applied heat fluxes are limited in certain ranges, which are restricted by the onset of boiling and the critical heat flux. Generally, the averaged pressure drop increases with increasing heat flux. All the pressure drop data are fitted to a linear line illustrated in Figure 7-13. Meanwhile, the pressure drop becomes higher as the mass flux increases from 11.2 kg·m^{-2}·s^{-1} to 44.8 kg·m^{-2}·s^{-1}. This is as expected because the higher averaged pressure drop is induced by the increased flow resistance at higher mass flux. It is worth mentioning that the pressure drop results presented in this chapter are the total pressure drop measurements during two-phase flow. Thus the pressure drop consists of the pressure drop due to wall friction, pressure drop due to sudden contraction and expansion at the

micro-channel connections and the pressure drop due to acceleration which depends on the averaged void fraction and density change (Kawahara *et al.* [261]). According to Kawahara *et al.* [261], the contraction and acceleration pressure drops only take small parts of the total pressure drop in circular micro-channels (0.05% – 9% and 0% – 4.5% respectively). Thus the main contribution of the pressure drop is from the friction pressure drop during the flow. However, in the present study, large amount of vapour exists in the high aspect ratio channel during the slug-annular flow and/or annular flow. Thus the accelerational pressure drop is expected to be more considerable than that in the regular channel geometries.

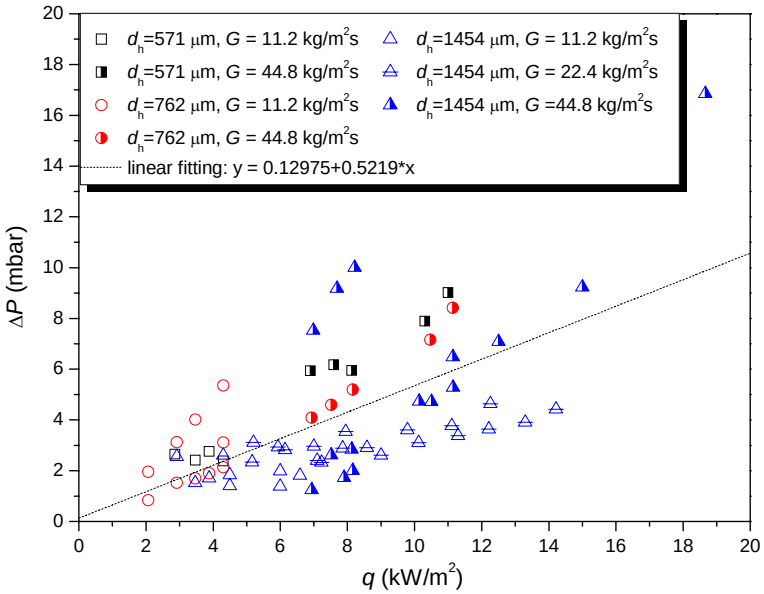

Figure 7-13. Average pressure drop versus applied heat flux in the three micro-channels at G = 11.2 kg·m^{-2}·s^{-1}, 22.4 kg·m^{-2}·s^{-1} and 44.8 kg·m^{-2}·s^{-1}; FC-72

Then, Origin® software was used to perform the signal analysis of the pressure drop fluctuation. Fast Fourier Transform (FFT) was used as the algorithm to compute the Discrete Fourier Transform (DFT), transforming the time domain pressure drop data into frequency domain data.

The DFT is defined by the formula (OriginLab [262]):

$$X_k = \sum_{n=0}^{N-1} x_n \exp\left(-i 2\pi k \frac{n}{N}\right), \quad \begin{matrix} n = 0, \cdots, N-1 \\ k = 0, \cdots, N-1 \end{matrix} \qquad \textbf{(7-1)}$$

where N represents the number of data points, x_n is the time domain data value, i is a complex number, X_k are the amplitudes in frequency domain after the transform, while the frequency f_k is computed from:

$$f_k = \frac{k}{N\tau},\ \tau \text{ is an equal interval} 1/2\pi \tag{7-2}$$

Frequency spectrums of the pressure drop at each tested heat fluxes and mass fluxes were obtained. Figure 7-14 gives the frequency spectrums of the pressure drop signals during single phase and two-phase flows. Apparently, the differences between single phase and two-phase pressure drop frequency spectrums are distinguishable. The frequencies with high amplitude are considered to be the consequence of two-phase flow instabilities. Frequencies with considerable amplitude are mostly lower than 10 Hz. Therefore the remaining part of frequency distribution is not shown in the plots. For two-phase pressure drop, the frequencies with the highest amplitudes were marked as the dominant frequencies. The amplitudes of the dominating frequencies at each heat flux are summarized in Table 7-2. As can be seen in Figure 7-14 and Table 7-2, there are mainly two types of fluctuations, the frequencies of which are in the order of 0.1 Hz and 1 Hz, namely low-frequency fluctuation and high-frequency fluctuation. This is consistent with the previous analysis. The occurrence of each type of fluctuation is sensitive to the thermal and flow conditions. For lower mass flux (G = 11.2 kg·m^{-2}·s^{-1}), the low-frequency pressure drop fluctuation shows increasing frequency as the heat flux increases, the corresponding amplitude is also generally increasing. As listed in Table 7-2, within the same heat flux range, the low-frequency amplitudes increase from 0.79 to 1.36 in the 571 μm channel and from 1.72 to 3.08 in the 762 μm channel. The increase of fluctuation amplitude is less obvious in the d_h = 1454 μm channel, which stays around 0.42 – 0.49, indicating that for a given mass flux, the pressure drop fluctuation amplitudes of low frequencies are more sensitive to heat flux in smaller micro-channels. For the high-frequency fluctuation, the amplitude is relatively lower than those of the low-frequency at a certain heat flux and mass flux. Besides, the amplitudes of high-frequency fluctuations are only slightly increased by increasing heat flux. However, the two types of fluctuations do not occur in every test. Take the 762 μm channel for instance, f = 4.48 Hz and 4.52 Hz are detected only once at q = 3.87 kW·m^{-2} and 4.30 kW·m^{-2} and G = 11.2 kg·m^{-2}·s^{-1}, while in the 1454 μm channel, the low-frequency

fluctuation only occurs twice. Visualisation reveals that the pressure drop fluctuation is strongly related with the local flow conditions and liquid-vapour distribution, which could be different even at the same heat flux and mass flux. The role of the channel dimension must be highlighted. The low-frequency oscillations are prone to take place in smaller channels.

It can be found in Table 7-2 that at G = 44.8 kg·m^{-2}·s^{-1}, low-frequency high-amplitude fluctuation is largely suppressed. Pressure drop fluctuates at a relatively steady frequency and amplitude range. Therefore it can be concluded that the increase of mass flux could suppress reverse flow. This is as expected because the reverse flow is caused by insufficient upstream-liquid energy to overcome the downstream high pressure resistance (Singh *et al.* [89], Wang *et al.* [263]). The liquid could only re-enter the channel when the upstream liquid has enough potential to provide a sufficiently high pressure. At a higher mass flux, upstream liquid has higher potential to suppress the reverse flow.

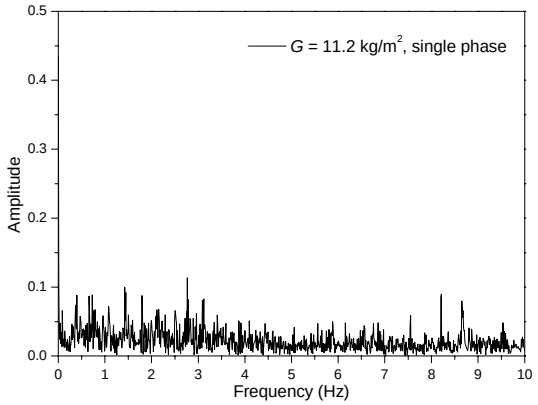

(a)

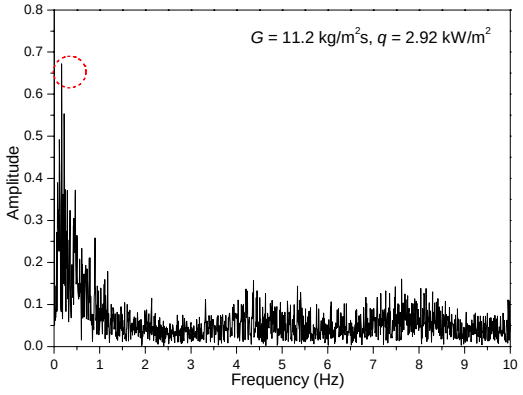

(b)

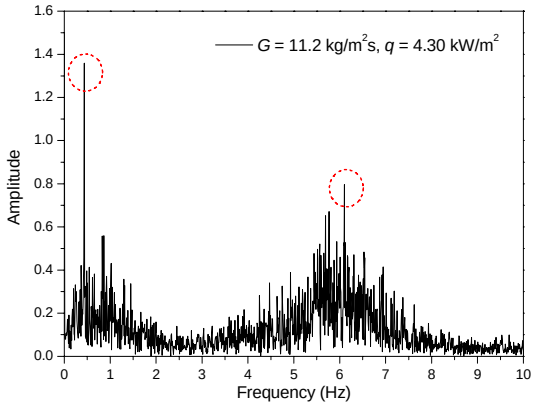

(c)

Figure 7-14. Pressure drop fluctuation frequency spectrums; d_h = 571 μm G = 11.2 kg·m^{-2}·s^{-1}; FC-72; (a) single phase flow, (b) two-phase flow, q = 2.92 kW·m^{-2}, (c) two-phase flow, q = 4.30 kW·m^{-2}

Table 7-2. The dominant frequencies of pressure drop fluctuation in the three micro-channels under ranges of heat fluxes at two mass fluxes; FC-72

d_h (μm)	G = 11.2 kg·m^{-2}·s^{-1}			G = 44.8 kg·m^{-2}·s^{-1}		
	q (kW·m^{-2})	frequency (Hz)	amplitude	q (kW·m^{-2})	frequency (Hz)	amplitude
571	2.07	0.27	0.79	6.94	0.80, 4.82	0.53, 0.60
	2.92	0.28 5.47	0.56 0.41	7.52	1.27, 4.86	0.55, 0.35
	3.47	0.41 5.48	0.81 0.55	8.16	1.32, 5.56	0.62, 0.33
	3.88	0.42, 6.06	0.81, 0.62	10.47	1.47, 5.80	0.66, 0.77
	4.30	0.44, 6.10	1.36, 0.80	11.14	6.65	0.65
762	2.07	0.12	1.27	6.94	0.37, 3.02	0.43, 0.512
	2.92	0.14	2.84	7.52	0.48, 3.86	0.46, 0.50
	3.47	0.18, 0.66	2.32, 1.88	8.16	0.17, 4.33	0.56, 0.59
	3.87	0.41, 4.48	2.16, 0.312	10.47	0.40 4.832	0.43 0.712
	4.30	0.59, 4.25	2.46, 0.52	11.14	0.46, 5.23	0.679, 0.86
	6.0	0.58	3.08			
1454	2.92	1.77, 2.75	0.48, 0.45	7.52	1.76, 3.32	0.51, 0.36
	3.47	2.36	0.70	8.13	1.80, 2.80	0.60, 0.81
	3.88	2.60, 3.12	0.63, 0.57	10.40	1.20, 2.40, 3.36	0.97, 1.06, 0.90

4.30	0.24, 1.95, 2.29	0.42, 0.46, 0.42	11.14	1.33, 2.67, 3.81	0.96, 0.94, 0.92
6.0	0.54, 3.18	0.49, 0.50			

Furthermore, pressure drop fluctuation is evaluated via the coefficient of variation of the pressure drop. The coefficient of variation is a commonly used measurement of variability or diversity, revealing the variation of the data from the average value. It is defined as the ratio of the standard deviation (or root mean square) ΔP_{rms} to the mean value ΔP_{avg}. A high coefficient of variation indicates that the data are spread out over a large range of values ([264]). It is worth mentioning that this analysis method was also previously used by Singh *et al.* [89].

The standard deviation of the pressure drop ΔP_{rms} is calculates as:

$$\Delta P_{\text{rms}} = \sqrt{\sum_{i=1}^{N} (\Delta P_i - \Delta P_{\text{avg}})^2 / N} \tag{7-3}$$

where ΔP_{i} is the transient pressure drop, ΔP_{avg} is the arithmetically-averaged value of the pressure drop data string, and N is the number of the data point.

The coefficients of variation $\Delta P_{\text{rms}} / \Delta P_{\text{avg}}$ in three channels are plotted in Figure 7-15 (a)-(c) at two different mass fluxes. When G = 11.2 kg·m^{-2}·s^{-1}, $\Delta P_{\text{rms}} / \Delta P_{\text{avg}}$ generally increases with increasing heat flux. When G = 44.8 kg·m^{-2}·s^{-1}, however, only slight decrease of $\Delta P_{\text{rms}} / \Delta P_{\text{avg}}$ is found when heat flux increases. The $\Delta P_{\text{rms}} / \Delta P_{\text{avg}}$ data are linearly fitted. The slope of the line is decreased when channel hydraulic diameter increases from 571 μm to 1454 μm, indicating the decreasing trend of pressure drop diversity at low mass flux.

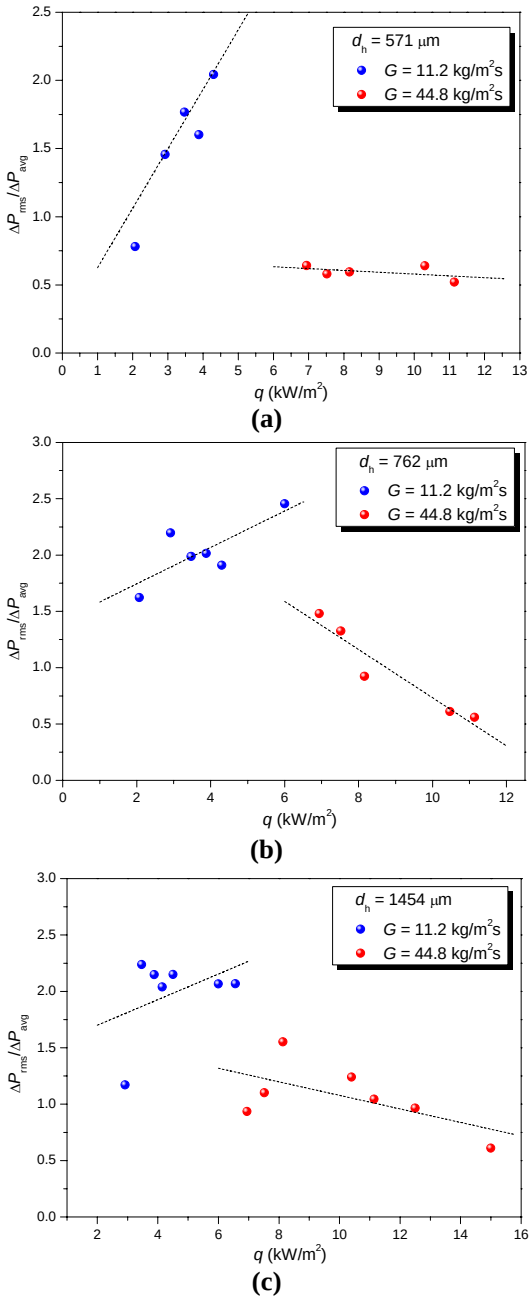

Figure 7-15. Coefficients of variation obtained at ranges of heat fluxes and two mass fluxes; FC-72. (a) d_h = 571 μm, (b) d_h = 762 μm, (c) d_h = 1454 μm

Besides, in order to highlight the effect of channel hydraulic diameter, Figure 7-16 (a) and (b) plot the $\Delta P_{rms}/\Delta P_{avg}$ versus q at G = 11.2 kg·m^{-2}·s^{-1} and 44.8 kg·m^{-2}·s^{-1}. At G = 44.8 kg·m^{-2}·s^{-1}, $\Delta P_{rms}/\Delta P_{avg}$ increases as the channel hydraulic diameter increases from 571 μm to 1454 μm. At G = 11.2 kg·m^{-2}·s^{-1} in Figure 7-16 (a), however, the increase of $\Delta P_{rms}/\Delta P_{avg}$ is more profound in low heat flux region, beyond which the data in three channels merge together. The experimental range was limited by the heat input power

and pumping capacity. Further investigations with wider experimental ranges are essential to explore the influences on the pressure fluctuation.

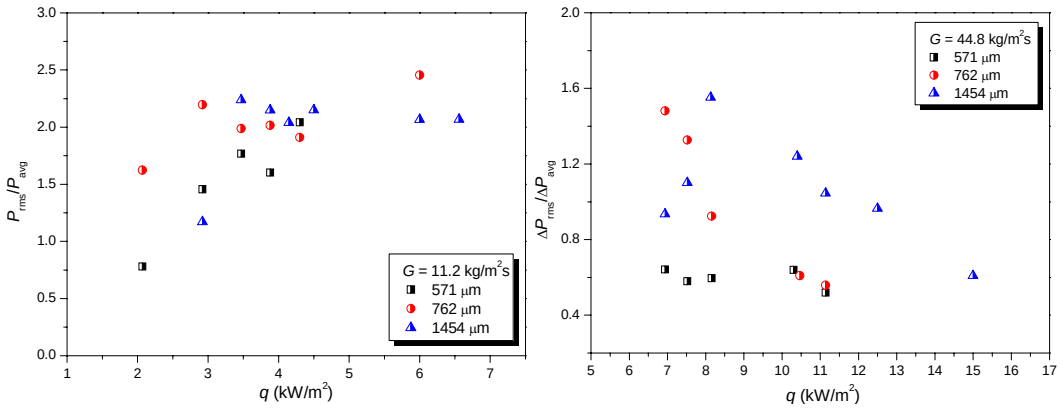

(a) **(b)**

Figure 7-16. Coefficients of variation obtained in three channels at ranges of heat fluxes; FC-72. (a) G = 11.2 kg·m^{-2}·s^{-1}, (b) G = 44.8 kg·m^{-2}·s^{-1}

7.3.3. Channel wall temperature fluctuation of FC-72 and ethanol

During the two-phase flow, periodic partial dry-out occasionally occurs on the channel inner surface as a result of the succeeding process including nucleation, vapour expansion and confinement, periodic reverse and rewetting flow. Thus the temperature on the channel inner surface is oscillating. As discussed in Chapter 3, the channel inner surface temperature profile could be reflected by the outer surface temperature thanks to the low Biot number. Infrared images presented in this chapter are the measurements of channel outer surface temperatures with the aid of Thermovision® 900 infrared camera.

Figure 7-17 (a) gives an example of infrared measurement of the channel surface temperature profile during single phase liquid flow when the channel is uniformly heated. Before the boiling incipient, the channel wall temperature maintains at a stable state. The temperature gradually increases from channel inlet to outlet. Higher temperature is achieved at the channel side-wall. Heat is transferred from the channel wall to the bulk liquid via conduction and convection.

The channel wall temperature distributions are significantly different in the two-phase flow boiling. Figure 7-17 (b) is the infrared sequence when there is vapour staying near the channel exit after boiling. The temperature at liquid-vapour interface maintains at around 56 °C, *i.e.* the saturation temperature of FC-72. The most obvious difference is that in liquid-vapour two-phase flow, the channel wall temperature is higher near the channel centre but opposite profile is found in single phase flow, liquid temperature

decreases from channel side-wall to the channel central line. Moreover, Figure 7-17 also reinforces that two-phase flow has higher heat dissipation capacity because the channel wall temperatures in Figure 7-17 (a) and (b) are at similar heights but the heat flux dissipated in two-phase flow is almost three times that in single phase flow.

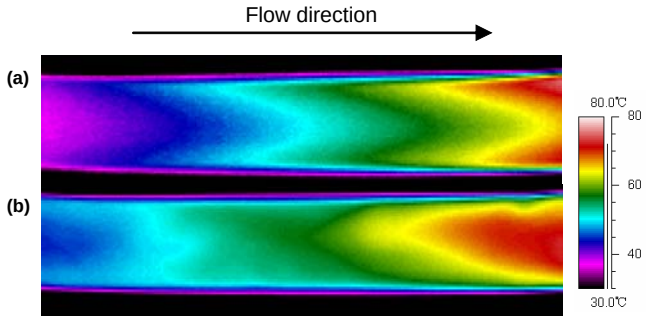

Figure 7-17. Micro-channel surface temperature profiles; d_h = 571 μm, G = 44.8 kg·m^{-2}·s^{-1}(a) q = 2.91 kW·m^{-2}, single phase liquid flow, (b) q = 8.16 kW·m^{-2}, two-phase flow boiling

Channel wall temperature is found to be fluctuating after boiling started. The deposition on the micro-channel exterior wall was uniformly coated, hence the applied heat flux was uniform. So the temperature fluctuations captured at the wall were merely caused by the two-phase flow occurring inside the micro-channel. The periodic temperature fluctuation is evidently related with the liquid-vapour distribution within the channel and is a consequence of the periodic reverse and rewetting flow. Figure 7-18 is the channel wall temperature map during the reverse and rewetting flow. The 3-dimensional coordinates provide a more quantitative perspective of the temperature profiles. This corresponds to the low-frequency high-amplitude fluctuation. As the liquid temperature gradually increases, vapour firstly appears near the channel exit. Then the rapid vapour expansion triggers the reverse flow with the recoiling propagating towards upstream. At the locations occupied by vapour phase, the liquid layer beneath the vapour bubble keeps on evaporating and partial dry-out appears before being replenished by fresh liquid. Therefore the channel wall temperatures at these dry-out spots jump to a much higher level. As the vapour expands, the high-temperature spot also expands till the upstream liquid has sufficient potential to conquer the high vapour pressure and to rewet the channel surface. Consequently channel surface is cooled down by the liquid rewetting.

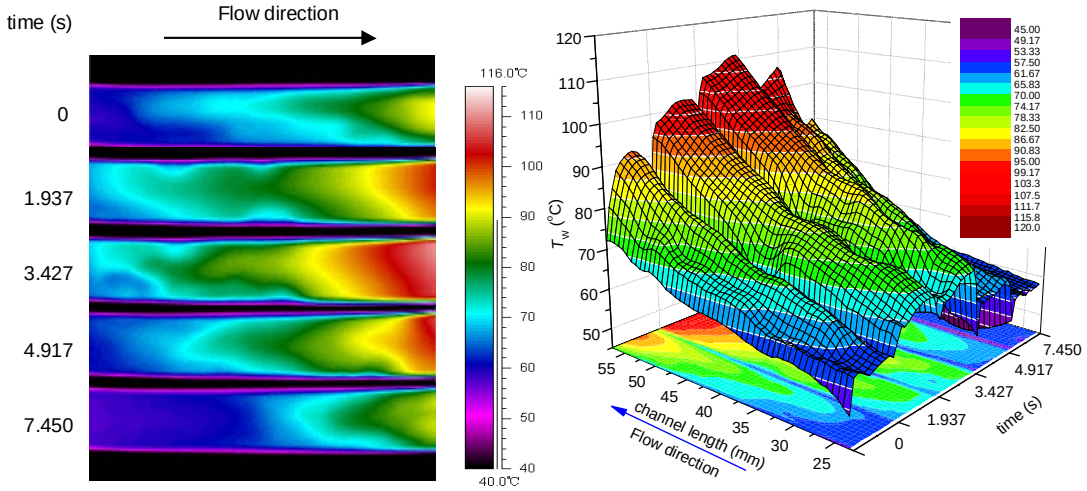

Figure 7-18. Infrared sequences of channel surface temperatures and the 3-dimensional plot; d_h = 571 μm, G = 11.2 kg·m^{-2}·s^{-1}, q = 2.07 kW·m^{-2}; FC-72

When the high-frequency low-amplitude fluctuation is encountered in the flow, the channel surface temperature distributes differently. As can be seen from Figure 7-19, a higher heat flux q = 4.30 kW·m^{-2} is applied on the channel surface, temperature still gradually grows along the channel stream-wise direction, very high T_w is achieved near the channel exit where large amount of vapour exists. The temperature fluctuation between frames is not as remarkable as in Figure 7-18. No reverse flow is observed from the high speed camera. Instead, nucleation is taking place within the liquid film, vapour collision is the major fluctuation source and the entrained liquid in the vapour core is evaporating fiercely due to high heat flux. Because the reverse flow is largely suppressed by higher mass flux, the vapour-occupied portion in the channel constantly exists. In this circumstance, the high temperature area should be monitored with special attention because the constantly high channel wall temperature could easily result in surface destruction.

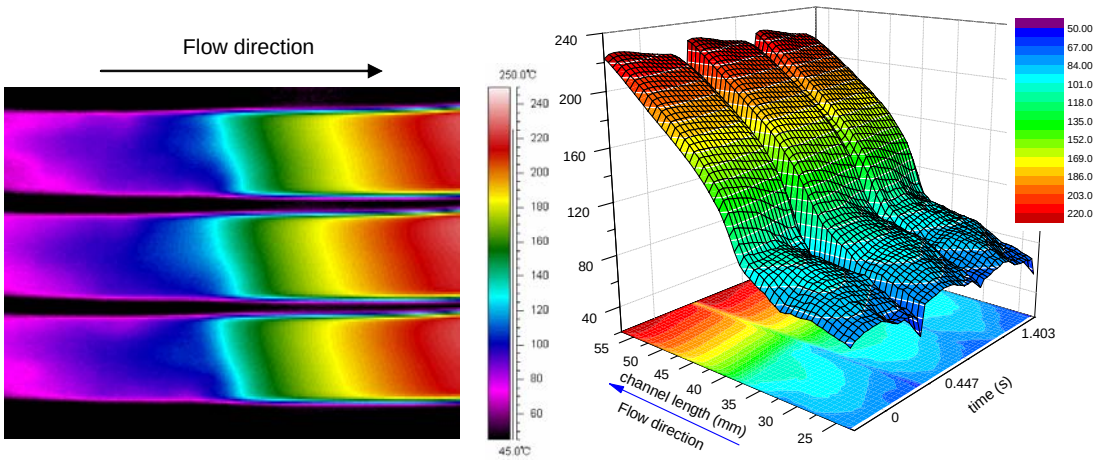

Figure 7-19. Infrared sequences of channel surface temperatures and the 3-dimensional plot; d_h = 571 μm, G = 11.2 kg·m^{-2}·s^{-1}, q = 4.30 kW·m^{-2}; FC-72

As a result of the dependency on the liquid and vapour behaviours in the channel, the peak and valleys of wall temperature and channel inlet and outlet pressures show strong relations. Based on the visualization results, the pressure peak occurs when the reverse flow takes place in the micro-channel. Consequently the majority of the channel is occupied by vapour phase. Partial dry-out easily appears and the channel wall temperature rise to a high level. As expected, in Figure 7-20 and Figure 7-21, the channel wall temperature jumps to a high value when the pressure drop reaches a peak. The wall temperature drops during the channel re-wetting, meanwhile the corresponding pressure drop falls back from the peak. Low frequency high amplitude pressure drop fluctuation and the averaged channel wall temperature fluctuation are in-phase because both of them are caused by the periodic recoiling and re-wetting in the channel.

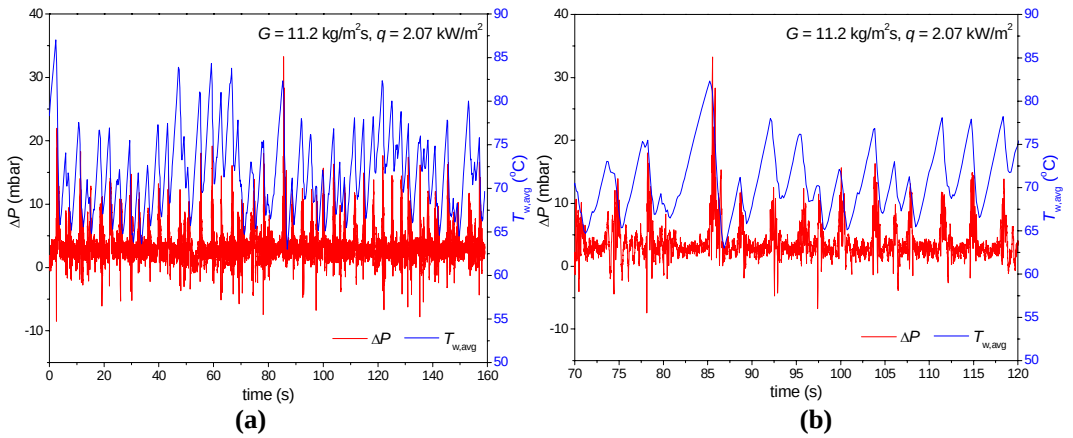

Figure 7-20. Pressure drop fluctuation and synchronous channel wall temperature fluctuations in two time scales, d_h = 571 μm, G = 11.2 kg·m^{-2}·s^{-1}, q = 2.07 kW·m^{-2}; FC-72

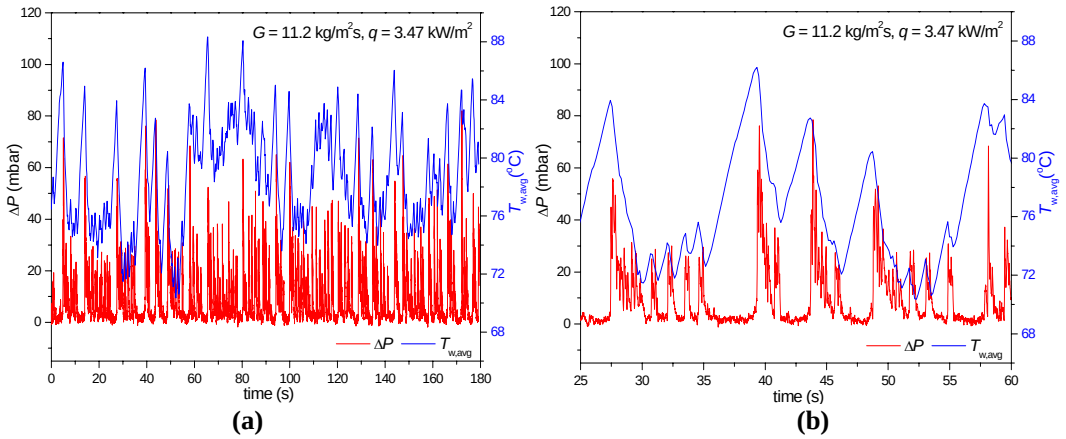

Figure 7-21. Pressure drop fluctuation and synchronous channel wall temperature fluctuations in two time scales, d_h = 762 μm, G = 11.2 kg·m^{-2}·s^{-1}, q = 3.47 kW·m^{-2}; FC-72

The channel wall temperature fluctuation can be clearer viewed in Figure 7-22. Figure 7-22 (a) is the channel wall temperature profiles obtained at G = 11.2 kg·m^{-2}·s^{-1} and q = 2.07 kW·m^{-2}. Three averaged temperatures at upstream, middle-stream and downstream, the distances of which to the channel inlet are z = 22.8 mm, z = 40.0 mm and z = 57.2 mm respectively are plotted in Figure 7-22 (b), noted as $T_{w,low}$, $T_{w,medium}$ and $T_{w,high}$. It can be seen that the temperature fluctuation amplitude is higher at downstream. This is because the downstream channel is more likely to be occupied by the vapour phase, thus is easier to be affected by the liquid and vapour distribution.

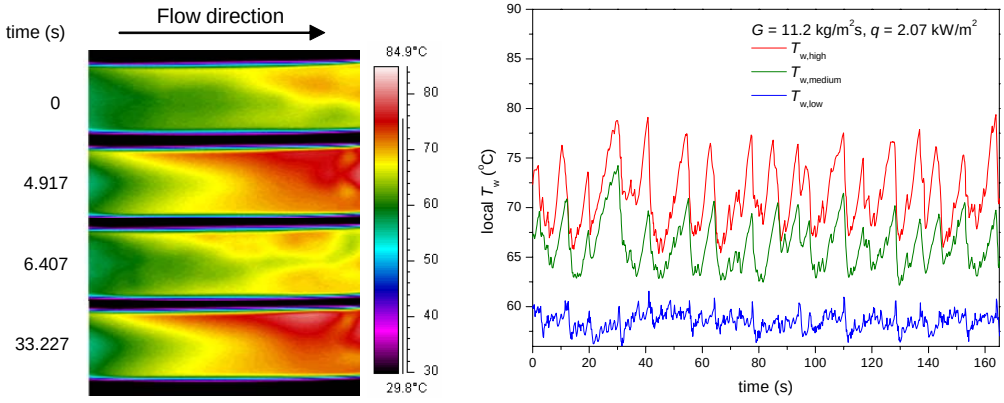

Figure 7-22. (a) Infrared sequences of channel surface temperatures and the 3-dimensional plot; d_h = 762 μm, G = 11.2 kg·m^{-2}·s^{-1}, q = 2.07 kW·m^{-2}, (b) corresponding channel wall temperature measurements; FC-72

Figure 7-23 shows the channel wall temperature measurements when FC-72 is boiling in the 1454 μm channel at G = 11.2 kg·m^{-2}·s^{-1}, q = 2.92 kW·m^{-2} and 6.0 kW·m^{-2}. Channel wall temperatures rise with increasing heat flux. Meanwhile, the fluctuation

frequency is higher at higher heat flux, exhibiting a more chaotic channel wall temperature profile. Wall temperature fluctuation magnitude is relatively low, which stays within the range of ±10°C.

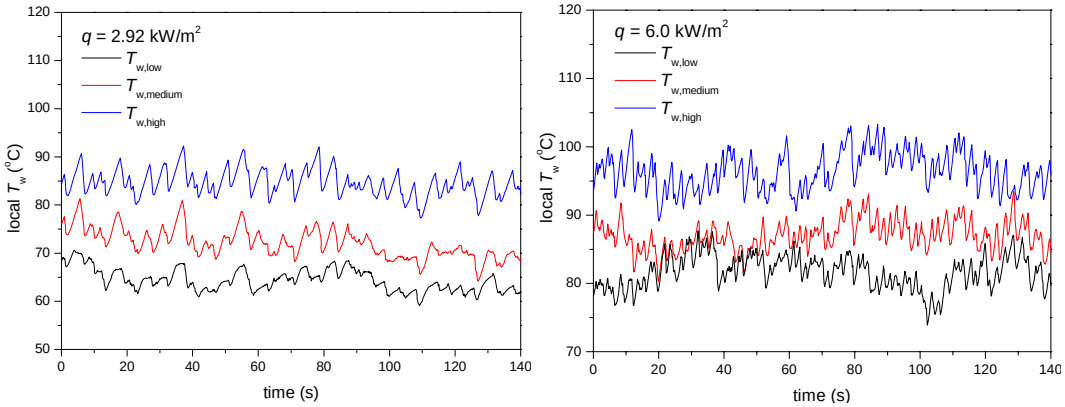

Figure 7-23. Channel wall temperature fluctuation; d_h = 1454 µm, G = 11.2 kg·m^{-2}·s^{-1}, (a) q = 2.92 kW·m^{-2}, (b) q = 6.0 kW·m^{-2}; FC-72

At a higher mass flux (G = 44.8 kg·m^{-2}·s^{-1}), the pressure drop fluctuates at high-frequency low-amplitude mainly due to the fast moving vapour slug cluster. Hence the wall temperature shows no distinctive high-amplitude fluctuation peak. As in Figure 7-24 at G = 44.8 kg·m^{-2}·s^{-1} and q = 7.52 kW·m^{-2}, the average channel wall temperature is oscillating within less then ± 5 °C.

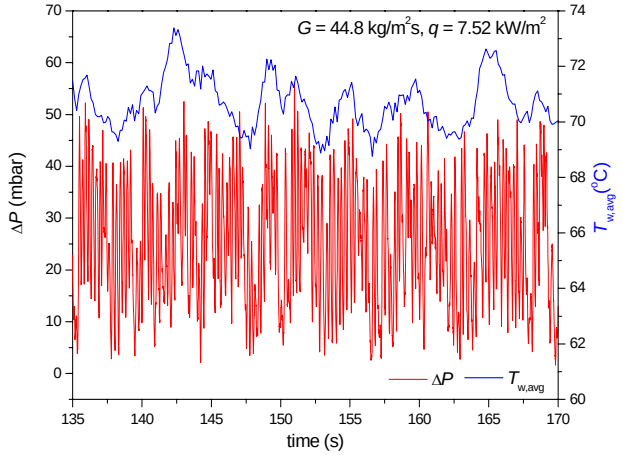

Figure 7-24. Pressure drop fluctuation and synchronous channel wall temperature fluctuations, FC-72, d_h = 762 µm, G = 44.8 kg·m^{-2}·s^{-1}, q = 7.52 kW·m^{-2}; FC-72

Results of ethanol flow boiling in micro-channels show some variations from those of FC-72. Compared with FC-72, the pressure drop and temperature fluctuations of ethanol at low heat fluxes are much more regular. Pressure fluctuations of ethanol also

show the aforementioned two types of fluctuations. The low-frequency high-amplitude major fluctuation is clearly seen in Figure 7-25 (a) and the high-frequency low-amplitude fluctuation is highlighted in Figure 7-25 (b).

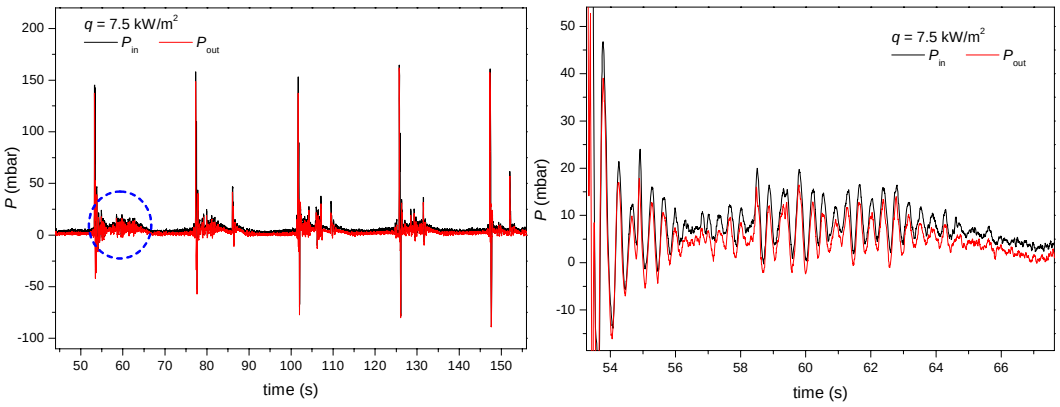

Figure 7-25. Inlet and outlet pressures fluctuations, d_h = 1454 μm, G = 11.2 kg·m^{-2}·s^{-1}, q = 7.5 kW·m^{-2}; ethanol, (a) low-frequency high-amplitude fluctuation, (b) high-frequency low-amplitude fluctuation

Besides, the channel wall temperature fluctuation obtained with ethanol are more regular than FC-72. As shown in Figure 7-26 and Figure 7-27, wall temperature T_w is fluctuating periodically. The high T_w fluctuation amplitude implies the much longer recoiling and re-wetting period of ethanol than FC-72. However, as long as the fresh liquid re-enters the channel and re-wets the channel inner surface, channel wall temperature distributes uniformly. After dropping from the peak, all the three local T_w remain almost the same before recoiling again. This is a very stable fluctuation mode. When the channel is occupied by liquid-vapour phases, channel wall temperature is uniformly distributed and is maintained at a low value around the boiling point of ethanol. The difference in wall temperature distribution between ethanol and FC-72 could be partly explained by the very low surface tension of FC-72 and its complete wetting of glass walls.

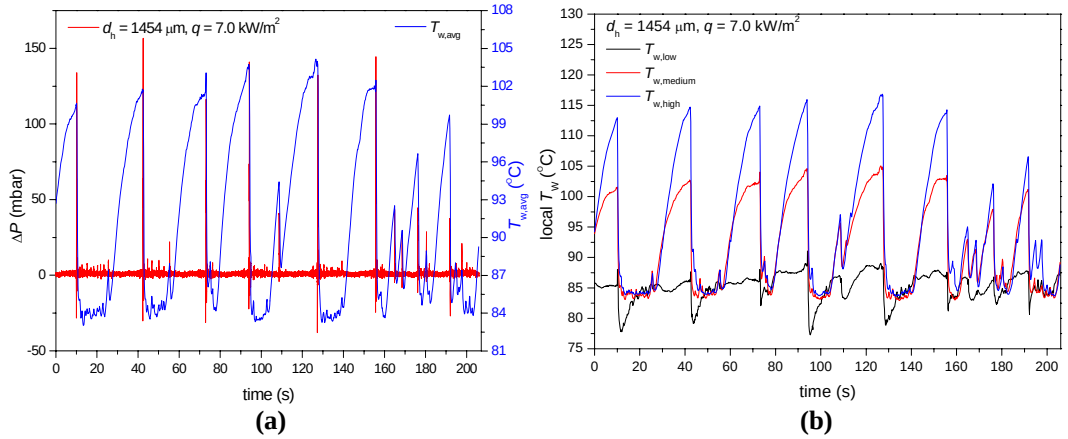

(a) **(b)**

Figure 7-26. (a) Pressure drop fluctuation and synchronous channel wall temperature fluctuations, (b) corresponding channel wall temperature measurements; d_h = 1454 μm, G = 11.2 kg·m^{-2}·s^{-1}, q = 7.0 kW·m^{-2}; ethanol

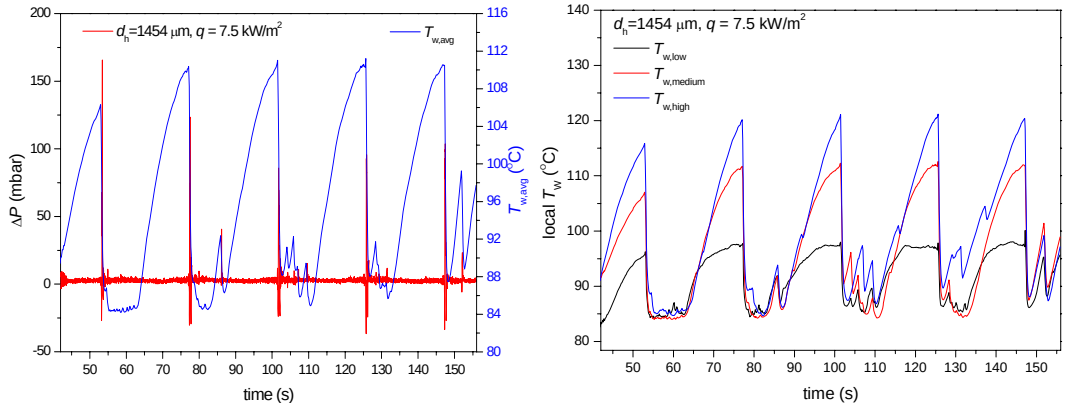

(a) **(b)**

Figure 7-27. (a) Pressure drop fluctuation and synchronous channel wall temperature fluctuations, (b) corresponding channel wall temperature measurements; d_h = 1454 μm, G = 11.2 kg·m^{-2}·s^{-1}, q = 7.5 kW·m^{-2}; ethanol

Thermographic results corresponding to the regular temperature fluctuation are exhibited in Figure 7-28. The low-frequency high-amplitude instabilities are resulted from the recoiling and rewetting. Uniform temperature profiles during rewetting can be found. In addition, more intense fluctuation is triggered by increasing the heat flux as in Figure 7-29 where the heat flux is increased to 9.0 kW·m^{-2}. Meanwhile, the temperature gradient along the channel is lessened. As the heat flux increases, the pressure drop fluctuation and channel wall temperature oscillation become increasingly chaotic. There appear some low-amplitude instabilities, which are caused by the random bubble nucleation and vapour collision. A series of infrared sequences are listed in Figure 7-30, showing the temperature profiles while a bubble is growing, filling the channel and finally be suppressed by the upstream liquid in the 1454 μm channel at G = 11.2 kg·m^{-2}·s^{-1} and q = 9.0 kW·m^{-2}.

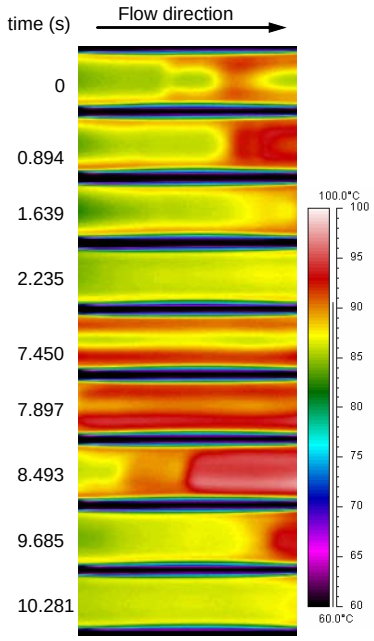

Figure 7-28. Transient channel wall temperature profile during periodic recoiling and rewetting; d_h = 1454 μm, G = 11.2 kg·m^{-2}·s^{-1}, q = 7.5 kW·m^{-2}; ethanol

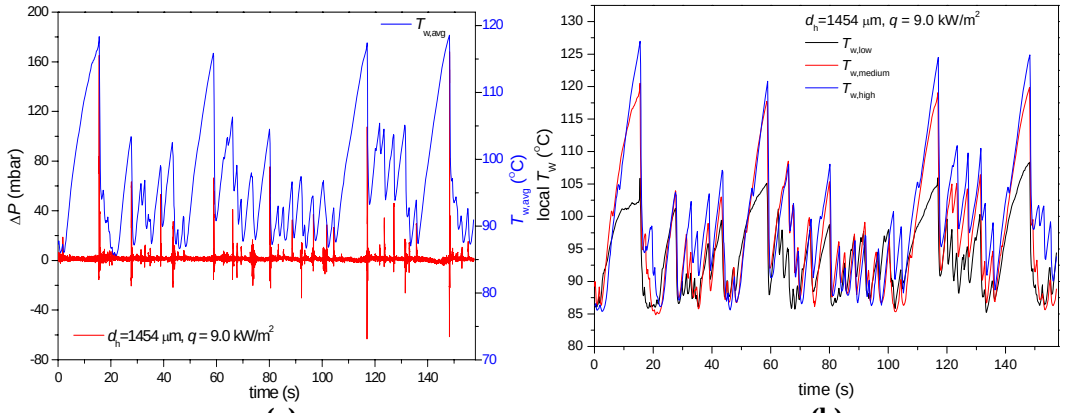

Figure 7-29. (a) Pressure drop fluctuation and synchronous channel wall temperature fluctuations, (b) corresponding channel wall temperature measurements; d_h = 1454 μm at G = 11.2 kg·m^{-2}·s^{-1} and q = 9.0 kW·m^{-2}; ethanol

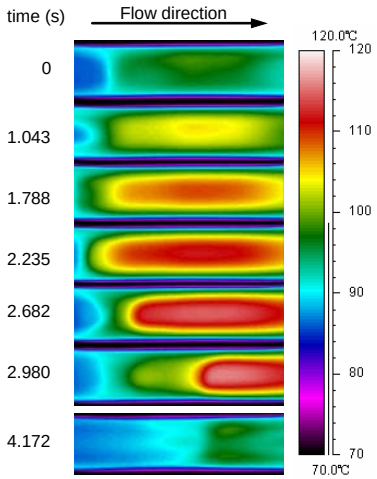

Figure 7-30. Transient channel wall temperature fluctuation due to local bubble growth; d_h = 1454 μm, G = 11.2 kg·m^{-2}·s^{-1}, q = 9.0 kW·m^{-2}; ethanol

7.4. Conclusions

Two-phase flow instabilities in single high-aspect-ratio rectangular micro-channels were experimentally investigated. Degassed FC-72 and ethanol were tested in the micro-channels with the hydraulic diameters of 571 μm, 762 μm and 1454 μm at the liquid mass fluxes 11.2 kg·m^{-2}·s^{-1}, 22.4 kg·m^{-2}·s^{-1} and 44.8 kg·m^{-2}·s^{-1} and ranges of heat fluxes. The pressure drop across the micro-channels is recorded over a wide range of heat input. Fast Fourier Transform (FFT) was performed to transform the transient pressure drop data into frequency domain for frequency spectrum analysis. Synchronous channel surface temperature profiles as well as the visualization results were also obtained. In light of the present study, the following outcomes are gathered.

Low-frequency fluctuation and high-frequency fluctuation are identified. Normally the amplitude of the low frequency is higher than that of the high frequency. Based on the visualization results, the low-frequency high-amplitude fluctuation is the major fluctuation mode at lower mass flux, and resulted from the periodic reverse and rewetting flow. The high-frequency low-amplitude fluctuation, on the other hand, is caused by the vapour slug cluster passage during the rewetting flow and the vapour collision at downstream. The high-frequency low-amplitude fluctuation is the minor fluctuation mode at lower mass flux, but becomes dominant at higher mass flux. Low-frequency oscillation is largely suppressed by the increasing mass flux.

For lower mass flux (G = 11.2 kg·m^{-2}·s^{-1}), low frequencies of the pressure drop fluctuation increase with increasing heat flux, the corresponding amplitudes are also

generally increased. However, heat flux shows minor influence on the high-frequency low-amplitude fluctuation, the period of which maintains within 0.195 – 0.26 s when heat flux increases from 2.86 – 10.31 $kW \cdot m^{-2}$, and the amplitudes show insignificant variation.

The averaged pressure drop increases with increasing heat flux and mass flux. Besides, based on the FFT computation, it is found that the pressure drop fluctuation amplitudes of low frequencies are more sensitive to heat flux in smaller micro-channels for a given mass flux.

The coefficient of variation of the pressure drop data $\Delta P_{rms} / \Delta P_{avg}$ is calculated as a measurement of the pressure drop fluctuation. For G = 11.2 $kg \cdot m^{-2} \cdot s^{-1}$, $\Delta P_{rms} / \Delta P_{avg}$ increases with increasing heat flux, the increasing rate of $\Delta P_{rms} / \Delta P_{avg}$ with heat flux increases as the channel size reduces. The increase of coefficient of variation is more profound merely at low heat flux region, beyond which the data in three channels merge together. Channel dimension is also influential on the pressure drop deviation at G = 44.8 $kg \cdot m^{-2} \cdot s^{-1}$, the pressure drop seems more divergent in larger micro-channel. The coefficient of variation increases as the channel hydraulic diameter increases from 571 μm to 1454 μm.

Channel surface temperature is fluctuating owing to the periodic reverse and rewetting flow and the consequent local partial dry-out. It is found that the low frequency high amplitude pressure drop and the averaged channel wall temperature fluctuations are in-phase. Temperature fluctuation amplitude is higher at downstream where the vapour phase exists. In addition, channel wall temperature distribution of FC-72 is remarkably different from ethanol. Ethanol flow boiling shows very stable fluctuation mode where the pressure drop and temperature oscillate regularly. Very high T_w fluctuation amplitude is reached, implying the much longer recoiling and re-wetting period of ethanol than FC-72. The channel wall temperature gradient is lessened by increasing heat flux. For FC-72, T_w fluctuates chaotically with low amplitudes while the wall temperature gradient exists in the channel axial direction. For ethanol, however, T_w fluctuates regularly with high fluctuation amplitudes and low channel wall temperature gradient appears during the rewetting period. The very low surface tension of FC-72 and its complete wetting of glass walls probably explain the observed differences.

Chapter 8

Flow boiling heat transfer in single micro-channels

8.1. Introduction

Flow boiling in micro-scale devices has been attractive in the rapid development of the microelectronic industry because of its high heat removal ability in applications such as miniature power systems, compact heat exchangers, chemical reactors and Micro-Electro-Mechanical Systems (MEMS). Small scale flow passages such as micro-channels become popular thanks to numerous advantages such as high heat dissipation capacity, small size and the flexibility of design. In particular, great efforts have been made to explore the flow boiling heat transfer mechanisms in small scale, as these tend to deviate from known mechanisms at the macro-scale.

There are several exhaustive reviews which comprehensively cover micro-channel heat transfer experimental studies and applications (Kandlikar [13], Thome [15], Cheng and Mewes [265], Thome [16], Cheng *et al.* [17], Lin *et al.* [266] and Wong *et al.* [267]). Different heat transfer characteristics were reported due to various experimental conditions such as working liquid, saturation pressure and the applied heat flux and mass flux. Besides, heat transfer characteristics were also found influenced by liquid properties and channel geometry (Tran *et al.* [95], Yen *et al.* [120] and Harirchian and Garimella [121]). For rectangular channel, channel cross-section aspect ratio was also an influential factor. Moreover, boiling number range could be an indicator or a criterion candidate of different heat transfer mechanisms, further experimental investigations of which are needed. Meanwhile, a large number of two-phase heat transfer correlations have been developed from existing experimental databases. Some of the flow boiling heat transfer correlations have been overviewed in Chapter 2, session 2.4.4. However, most of the micro-channels used in previous studies were circular, trapezoidal, square and low aspect ratio rectangular micro-channels (*i.e.* $\mathrm{MAX}(W_{\mathrm{in}}, d_{\mathrm{in}}) / \mathrm{MIN}(W_{\mathrm{in}}, d_{\mathrm{in}}) < 10$ or $\mathrm{MIN}(W_{\mathrm{in}}, d_{\mathrm{in}}) / \mathrm{MAX}(W_{\mathrm{in}}, d_{\mathrm{in}}) > 0.1$). Studies with high aspect ratio micro-channels are very limited. More efforts on flow boiling in high aspect ratio micro-channels are necessary. High aspect ratio micro-channels can be potentially used in various industrial applications because first, high aspect ratio channels have a large surface-to-volume ratio. This can reduce the working liquid consumption while providing large cooling area. Second, high aspect ratio channels can reduce vapour side pressure drop and increase vapour side heat transfer (Mokrani *et al.* [53]). Despite the potential of the specific

geometry, there is limited work in literature using high aspect ratio micro-channels. In order to bridge this gap, an experimental investigation on flow boiling heat transfer in high aspect ratio micro-channels has been undertaken. Visualization results obtained using transparent heating and the thermographic channel wall temperature profiles were gathered. The primary objective was to explore the heat transfer characteristics during flow boiling in high aspect ratio micro-channels and to elucidate the heat transfer mechanisms, to assess some existing heat transfer correlations and to look for a better correlation based on the measured data.

8.2. Experimental setup and procedure

The experimental facilities described in Chapter 3 session 3.2.1 and session 3.2.2 were used in the present investigation of flow boiling heat transfer in single micro-channels. All the experiments were conducted at atmospheric pressure. Vigorously degassed FC-72 and ethanol were used as the working liquids. Transparent heating was utilised, providing controllable heat input on the channel. During the flow boiling, the fluid inlet and outlet temperatures were measured. Meanwhile, the boiling process was synchronously visualized by the high speed camera. Image Pro.® software helped to analyze the visualization results. Besides, the transient temperature profiles of the channel outer surface were acquired by the infrared (IR) camera which was operated at 7 fps and the ThermaCAM Researcher Professional® software was used to analyze the IR image sequences. Table 8-1 lists the test conditions of the present study.

Table 8-1. Experimental conditions for the investigation of flow boiling heat transfer in single micro-channels

FC-72			ethanol		
channel d_h [μm]	Heat flux q [kW·m^{-2}]	Mass flux G [kg·m^{-2}·s^{-1}]	channel d_h [μm]	Heat flux q [kW·m^{-2}]	Mass flux G [kg·m^{-2}·s^{-1}]
571 762 1454	0 – 18.31	11.2, 22.4 and 44.8	1454	0 – 15.0	11.2 and 22.4

In the flow boiling heat transfer experiment, a constant environmental temperature was maintained at 25°C and the effect of liquid inlet subcooling was not one of the main

interests because it has been verified by previous study that inlet subcooling has minor influence on flow boiling heat transfer characteristics (Consolini and Thome [268]).

In this chapter, some visualization results of FC-72 and ethanol were exhibited to show the typical flow regimes in the high aspect ratio micro-channels. More importantly, the flow regimes were also tightly associated with the heat transfer mechanisms. The steady state of the flow boiling was analyzed by plot the boiling curves. Beside, the local heat transfer coefficients along the flow direction were obtained. Finally, the experimental heat transfer results were compared with the predictions from ten existing heat transfer correlations for macro- or micro-channels. After the assessment, the correlation which best fit the measured data was selected and modified based upon the measured data.

8.3. Data reduction

8.3.1. Heat transfer coefficient

The heat transfer coefficient was calculated based on the channel wall temperature measurements. The channel was partially mapped by the IR camera due to the limited focus distance and field of view. In the experiment, the thermally observed area covered the central channel length from 22.8 mm to 57.2 mm from the channel entrance, the schematic drawing of which can be found in Figure 8-1.

As discussed in Chapter 3, session 3.3.3, the Biot number values in the present study is very low ($Bi << 1$), thus the difference between the inner and outer wall temperatures can be neglected. The local heat transfer coefficient along the channel axial direction is estimates as:

$$h_{\text{local}} = \frac{q}{T_{\text{W,local}} - T_{\text{L,local}}} \tag{8-1}$$

where $T_{\text{W,local}}$ is the local temperature of the channel outer surface, $T_{\text{L,local}}$ is the local liquid temperature.

In the present study, inlet and outlet fluid temperatures were detected with inserted thermocouples (accurate to ± 0.05°C), but the local liquid temperatures along channel axial direction were not experimentally measured due to the fragility of the channel and

the consequent inconvenience of thermocouple installation, which would not only deteriorate the transparency but also damage the glass surface. The local liquid temperature was calculated based on the assumption that all the effective applied heat flux was used to heat up the liquid. This led to the following energy balance:

$$2z(W_{\text{in}} + d_{\text{in}})q = C_p G A_{\text{c}}(T_{\text{L},z} - T_{\text{in}}) \tag{8-2}$$

so the liquid temperature can be written as

$$T_{\text{L},z} = \frac{2q(W_{\text{in}} + d_{\text{in}})}{C_p G W_{\text{in}} d_{\text{in}}} z + T_{\text{in}} \tag{8-3}$$

where $T_{\text{L},z}$ (or $T_{\text{L,local}}$) is the local liquid temperature at a distance z (mm) from the channel inlet, and T_{in} is the inlet liquid temperature, q is heat flux, G is mass flux, W_{in} and d_{in} are the channel inner width and inner depth respectively, and C_p is the liquid specific heat.

The distance required for the liquid to reach saturation temperature is noted as z_0, which can be calculated in eq. (8-4). When $z > z_0$, liquid temperature is considered to be at the saturation temperature since boiling ensues. The saturation temperature decreases due to local pressure drop. According to the measurements of the two-phase pressure drop across the channel in Chapter 7, the maximum pressure drop is below 20 mbar within the tested conditions. The corresponding temperature drop is calculated to be around 0.6°C based on the Antoine Equation. Compared with the saturation temperature of FC-72 and ethanol, the temperature decrease is negligible. The liquid temperature along the channel axial direction is also shown in Figure 8-1.

$$z_0 = \frac{A_{\text{c}} G C_p (T_{\text{sat}} - T_{\text{in}})}{2q(W_{\text{in}} + d_{\text{in}})} \tag{8-4}$$

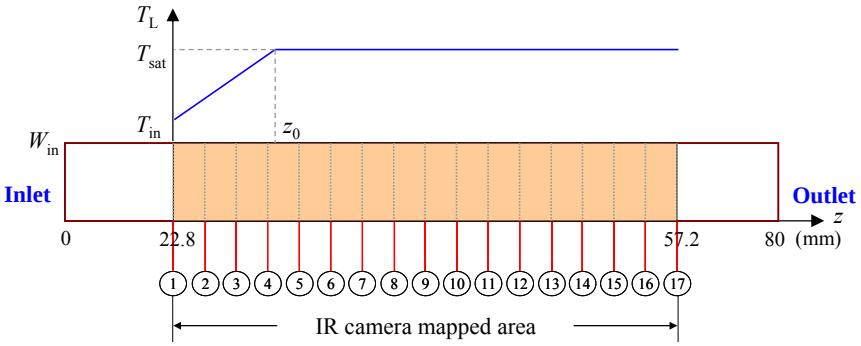

Figure 8-1. Schematic drawing of the channel, showing the IR mapped area, selected locations and local liquid temperature along the channel axial direction

In addition to the direct heat transfer calculation using eq. (8-1), inverse heat method was also implemented. The inverse heat method is commonly used to determine the thermal conditions on an inaccessible surface by measuring the temperature on an accessible boundary. The inverse heat method takes into account the heat conduction due to temperature spatial gradient in both channel width and length directions.

In the present study, the power supply on the channel outer surface and the corresponding temperature profiles were used to calculate the local heat transfer coefficient at the channel internal surface. The study of heat transfer using inverse heat method was accomplished in collaboration with Prof. Souad Harmand and her group in the Université de Valenciennes et du Hainaut-Cambrésis, who developed a Matlab® program for inverse heat method computation.

The channel wall was divided into several small grids, the size of which depended on the mesh density of the domain. To obtain the local heat transfer coefficient at the channel internal surface, an initial heat transfer coefficient h_0 was firstly given. After providing a liquid reference temperature, a new outer wall temperature could be calculated using the initial heat transfer coefficient and the applied heat flux based on the equation which was the same as the direct heat transfer method (eq. (8-1)). The sum of the differences between the calculated and measured wall temperature was necessary for obtaining a "sensitivity matrix" S which represented the sensitivity of wall temperature to the heat transfer coefficient. The minimum of the sensitivity matrix provided a heat transfer coefficient increment Δh, and $h_{i+1} = h_i + \Delta h$ was used in the next cycle of computation. Eventually the computation terminated when $\Delta h << \varepsilon$, where ε is an extremely small value.

The flow chart of the Matlab® program is given in Figure 8-2.

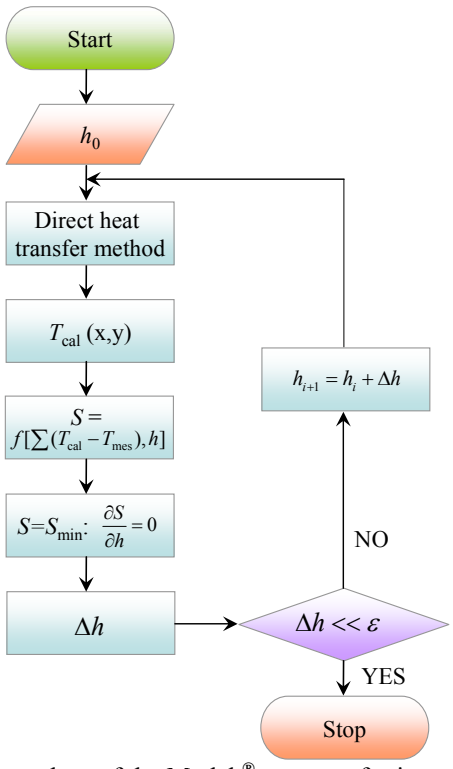

Figure 8-2. Flow chart of the Matlab® program for inverse heat method

The advantage of using the inverse method is that only the temperature data measured at some locations of the accessible channel outer surface are required to calculate the heat transfer coefficients on the inaccessible side. Other information such as the properties of the cooling media, which are necessary in the direct approach when using empirical correlations, is not required in the inverse method (Kim and Oh [269]). Besides, Biot number in the channel width and length directions were estimated. The method was described in Chapter 3. It was found that for different channel dimensions, the Biot number ranged from 1.13 – 2.16 across the channel width and ranged from 5.66 – 14.41 across the entire channel length. Apparently, the consideration of width and length temperature gradients could improve the accuracy of the heat transfer results.

In the present study, the local heat transfer coefficient results discussed below are all obtained using the direct heat method. Some samples of two-dimensional heat transfer coefficient maps calculated using inverse heat method are presented for comparison.

8.3.2. Local vapour quality

Local vapour quality x_z along the channel stream-wise is estimated following Bao *et al.* [96], Bertsch *et al.* [115] and Hamdar *et al.* [119]:

$$x_z = \frac{2q(z - z_0)(W_{in} + d_{in})}{A_c G h_{fg}}, z > z_0 \quad (8\text{-}5)$$

where q is heat flux, G is mass flux, W_{in}, d_{in} and A_c are the channel inner width, inner depth and channel cross-sectional area respectively, h_{fg} is the latent heat of vaporisation of the liquid, and the subscript z is the stream-wise distance from channel inlet. For $z < z_0$, liquid is under subcooled condition, hence vapour quality $x = 0$.

8.4. Results and discussions

8.4.1. Visualization results of FC-72 and ethanol

The use of transparent heating offers a real advantage when it gets to visualisation. With the aid of the high speed camera, vapour dynamics inside the micro-channels were visualized. Comparisons between FC-72 and ethanol did not show significant differences in the main flow regimes. Figure 8-3 (a) shows the typical flow regimes of FC-72 boiling in the channel with d_h = 1454 μm. Shortly after bubble nucleation, confined bubbly flow is found. Slug flow appears too shortly to be captured and the flow turns into slug-annular flow rapidly. As more vapour occupies the channel, annular flow is observed. Successively, liquid droplets are entrained in fast-moving vapour core and wispy-annular flow with evaporating film can be achieved. The high aspect ratio channel cross section causes the rapid transition from bubble nucleation to annular flow. As shown in Figure 8-3 (b), upstream recoiling and re-wetting as well as downstream vapour collisions are captured, during which the thin liquid film between bubble interface and channel inner surface is evaporating.

Similar vapour dynamics for ethanol are shown in Figure 8-4. Vapour fills the channel after growing bubbles and elongation following nucleation. Periodic recoiling and re-wetting cycles are the major causes of flow instabilities, which result in channel wall temperature fluctuations (Barber *et al.* [93] and Bogojevic *et al.* [259]).

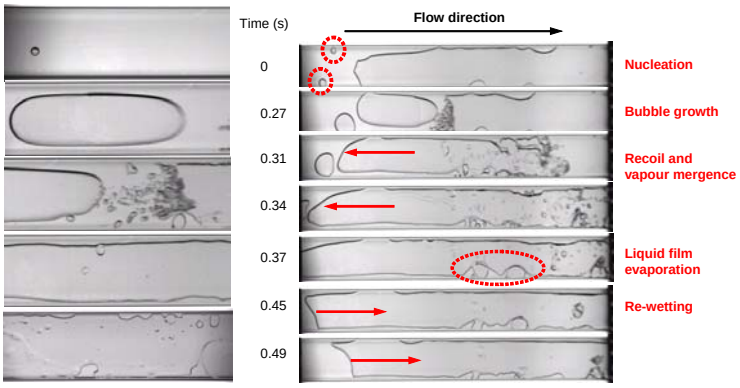

Figure 8-3. Flow regimes of FC-72 boiling in the channel with d_h = 1454 μm, (a) slug and annular flow, camera speed: 1500 fps, (b) wispy-annular flow at G = 22.4 kg·m^{-2}·s^{-1} and q = 8.13 kW·m^{-2}, camera speed: 1000 fps

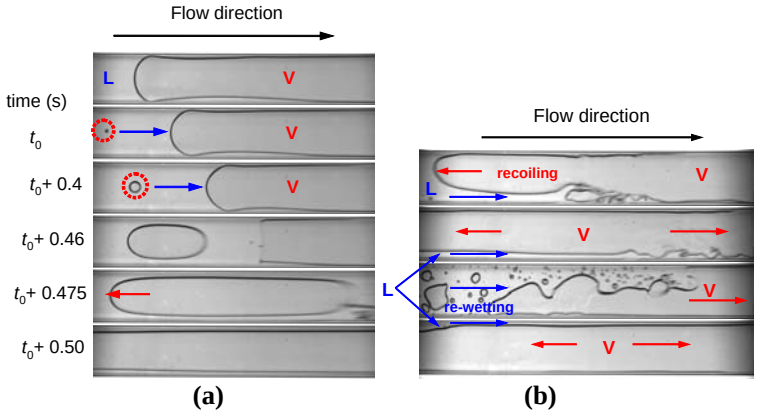

Figure 8-4. Flow regimes of ethanol boiling in the channel with d_h = 1454 μm, (a) slug and annular flow at G = 11.2 kg·m^{-2}·s^{-1} and q = 11.0 kW·m^{-2}, camera speed: 1000 fps, (b) wispy-annular flow at G = 11.2 kg·m^{-2}·s^{-1} and q = 15.0 kW·m^{-2}, camera speed: 1000 fps

8.4.2. Analysis of data in steady state

Boiling curves of FC-72 at three different mass fluxes for each tested channel were firstly obtained. It is shown in Figure 8-5 that in the single phase region, higher mass flux can dissipate higher heat flux at a given wall temperature. As the wall temperature keeps on increasing, cavities within the channel were activated and single bubble or large amount of bubbles were captured via the high speed camera and noted as the onset of nucleate boiling (ONB). ONB is marked in Figure 8-5. Apparently ONB increases with increasing mass flux. As higher flow velocity strengthens the convective heat transfer, the corresponding channel wall temperature becomes lower. Therefore, higher heat flux is required to initiate nucleation.

Since all the boiling curves are obtained by increasing the heat flux, apparent temperature overshoot at the boiling onset was detected. This temperature overshoot,

which is also named as incipient hysteresis, was a result of a sudden reduction of wall temperature when boiling started.

The incipient of nucleation is then followed by dramatic changes of heat transfer. It is observed in Figure 8-5 that there is an increase in the slopes of the boiling curves shortly after ONB. This stage is the transition from partial nucleate boiling to fully developed nucleate boiling. In the present study, due to the narrow channel gap, vapour bubbles filled the channel depth and width directions in a very short span of time and became confined and elongated rapidly. Thus the transition to fully developed nucleation was completed in such a short period that it was difficult to be visually captured.

It is also noticed that boiling curve is largely affected by mass flux in both single phase and two-phase regions. This is different from some previous studies (e.g. Tran *et al.* [95] and Bertsch *et al.* [115]) which found that mass flux is only influential in single phase region but the boiling curves almost collapse onto a single curve at different mass fluxes. The unique channel geometry utilised in the present study was considered as the major cause of the discrepancy from previous studies. As the channels have very high aspect ratio ($\sigma = 10$ and 20), abrupt transition from bubble nucleation to annular flow occurred. During the annular flow, large portion of the channel was occupied by vapour with some entrained droplets while only a thin layer of liquid film was on the channel wall. The large amount of existing vapour in the channel remarkably suppressed nucleate boiling. Instead, forced convection boiling performed as the dominant heat transfer mechanism. The heat flux increases until further slight increases of heat flux will cause substantial jump of channel surface superheating. The corresponding heat flux is considered as the critical heat flux (CHF) in the present study. In the present mass flux ranges of 11.2 $kg \cdot m^{-2} \cdot s^{-1}$, 22.4 $kg \cdot m^{-2} \cdot s^{-1}$ and 44.8 $kg \cdot m^{-2} \cdot s^{-1}$, the CHF is found to be below 20 $kW \cdot m^{-2}$.

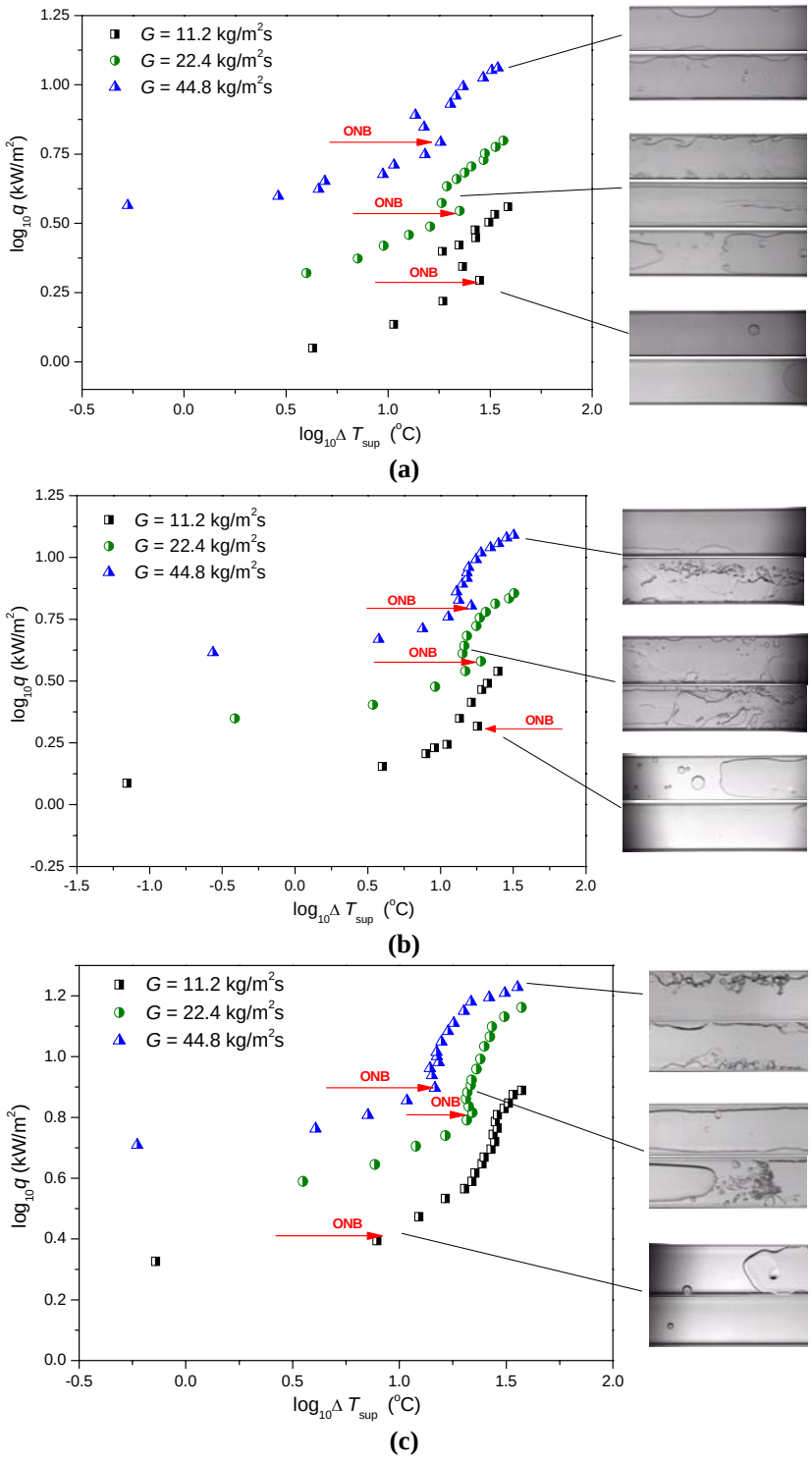

Figure 8-5. Boiling curves at three mass fluxes in micro-channels with (a) d_h = 571 μm, (b) d_h = 762 μm, (c) d_h = 1454 μm; FC-72

The boiling curves for ethanol in the 1454 μm channel were also obtained. The comparison of boiling curves between FC-72 and ethanol at G = 11.2 kg·m^{-2}·s^{-1} in the channel with d_h = 1454 μm is shown in Figure 8-6. For ethanol, remarkable overshoot is found at ONB. In addition, ethanol can dissipate much higher heat fluxes than FC-72 at a

certain channel wall superheat. It is noticed that the CHF for ethanol is greater than for FC-72. However, the corresponding wall superheat of ethanol is lower than that of FC-72.

The differences in heat transfer characteristics of FC-72 and ethanol can be explained based on the liquid physical property comparisons in Figure 8-7. FC-72 was selected as the reference by setting its properties as 100 (%), then the corresponding property percentages of ethanol can be calculated. It is found that latent heat of vaporization of ethanol is more than nine times higher than FC-72. This probably explains the higher CHF of ethanol. Moreover, the surface tension of ethanol is 133.9% higher than that of FC-72. The high surface tension of ethanol largely prolongs the dry-out period as higher resistance would be encountered during dry-out area spreading. Consequently when CHF is reached, the channel wall superheating for ethanol is at a lower level than FC-72.

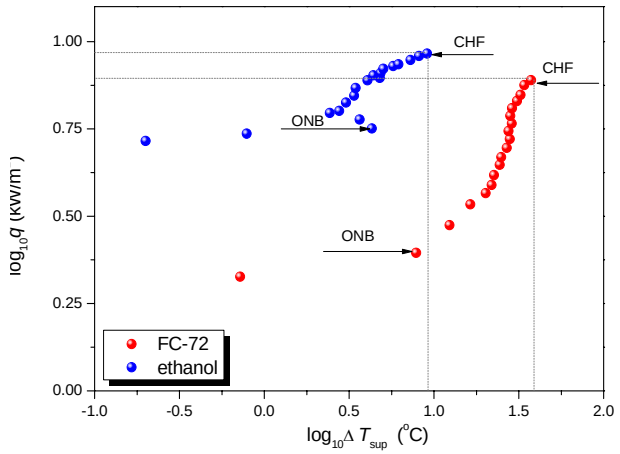

Figure 8-6. Boiling curve comparison between FC-72 and ethanol at G = 11.2 kg·m^{-2}·s^{-1} in the channel with d_h = 1454 μm

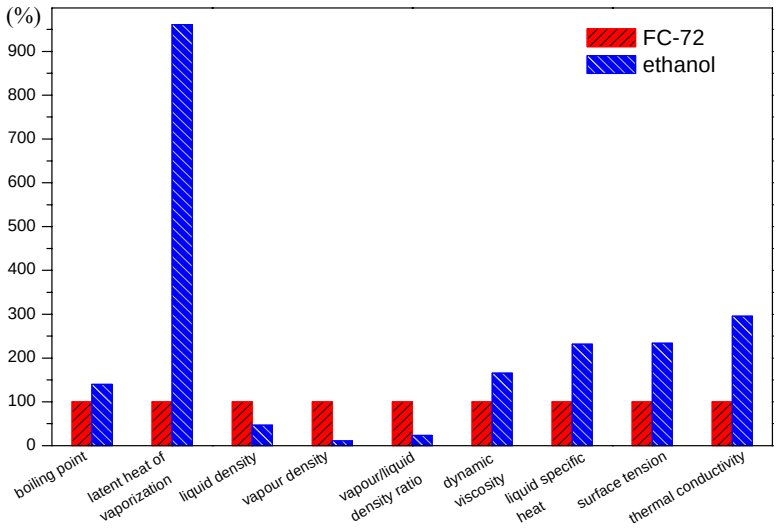

Figure 8-7. Percentage comparisons of the physical properties of FC-72 and ethanol

8.4.3. Local heat transfer coefficient versus vapour quality

Local heat transfer coefficients were obtained as a function of vapour quality. Figure 8-8 - Figure 8-10 show the results of FC-72 in all the three tested channels at G = 11.2 kg·m^{-2}·s^{-1} and 44.8 kg·m^{-2}·s^{-1}. Vapour quality is in the range of 0 – 1.43. For most of the vapour quality ranges, heat transfer coefficient h_{local} is a strong decreasing function of vapour quality. This indicates that the dominant heat transfer mechanism is not nucleate boiling because heat transfer coefficient is normally insensitive to vapour quality in nucleate boiling. The similar decreasing trend of heat transfer coefficient versus vapour quality was also reported by Sumith *et al.* [270] and Agostini *et al.* [111] even though low aspect ratio rectangular channels were used in their studies (231 μm × 713 μm by Sumith *et al.* [270] and 223 μm × 680 μm by Agostini *et al.* [111].

It can be found that h_{local} decreases with x from x = 0 or shortly after x > 0. The vapour quality at which h_{local} starts to decrease is named as critical vapour quality (CVQ) in the present study (CVQ was previously mentioned by Yun *et al.* [106]). Figure 8-8 – Figure 8-10 show higher CVQ in larger micro-channel. Besides, CVQ is higher at higher mass flux.

According to Figure 8-8 – Figure 8-10, heat transfer coefficient also depends on heat flux. For most of the cases, h_{local} increases with increasing q. Moreover, the effect of heat flux is more profound in high vapour quality region as the curves become more divergent as x increases. It is also noticed that h_{local} starts to decrease with further increase of q since q = 3.87 kW·m^{-2} in Figure 8-9 (a). Intermittent dry-out prior to CHF

probably has caused the deterioration of heat transfer. The similar trend of heat transfer coefficient decreases with further increase of heat flux was also reported by Agostini *et al.* [111].

It is worth mentioning that, according to the calculation in eq. (8-1), the local heat transfer coefficients are obtained by using the transient and time-averaged channel surface temperatures. Besides, the liquid saturation temperature is considered to be constant because of the low average pressure drop values during the two-phase flow. However, the pressure drop is fluctuating and the transient pressure drop is high at fluctuation peaks, consequently inducing transient local saturation temperature drop. In the experiment, the highest pressure drop fluctuation amplitude reaches 100 mbar when using ethanol. The corresponding saturation temperature is calculated to be 75.4°C according to Antoine Equation. Thus the maximum saturation temperature reduction is 3K, which will cause slightly higher local heat transfer coefficients than the presented results in Figure 8-8 to Figure 8-10 during the two-phase flow boiling.

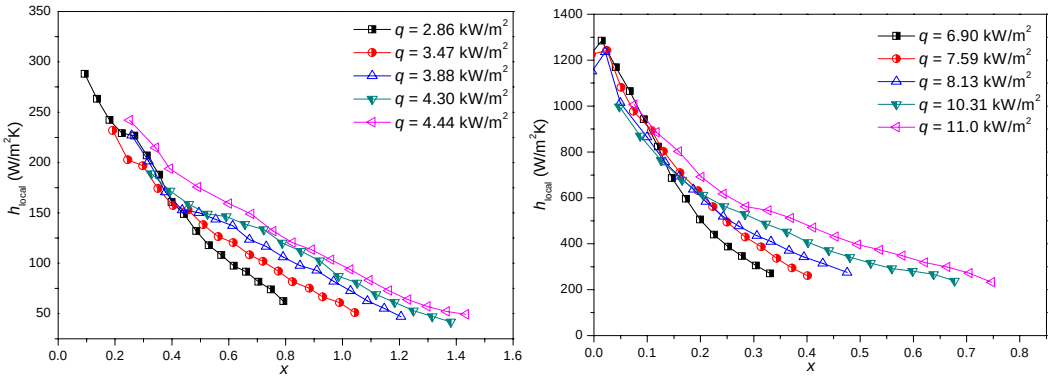

(a) **(b)**

Figure 8-8. Local heat transfer coefficients at different heat fluxes in the channel with d_h = 571 μm; FC-72: (a) G = 11.2 kg·m^{-2}·s^{-1}, (b) G = 44.8 kg·m^{-2}·s^{-1}

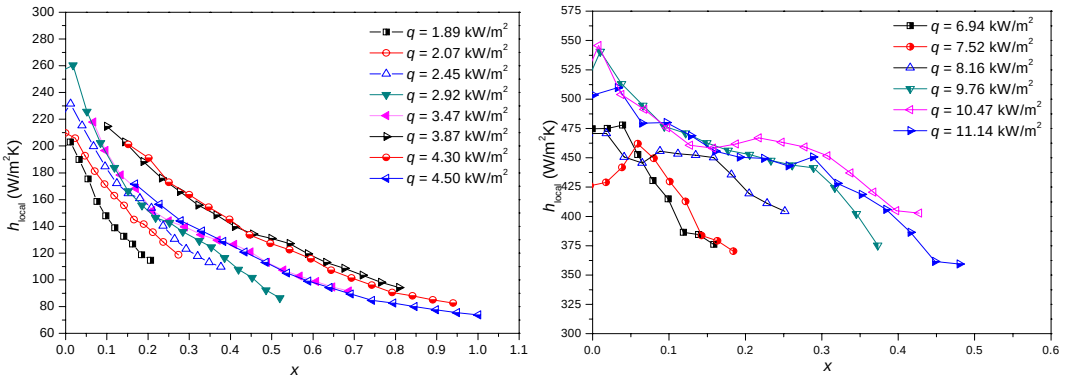

(a) **(b)**

Figure 8-9. Local heat transfer coefficients at different heat fluxes in the channel with d_h = 762 μm; FC-72: (a) G = 11.2 kg·m^{-2}·s^{-1}, (b) G = 44.8 kg·m^{-2}·s^{-1}

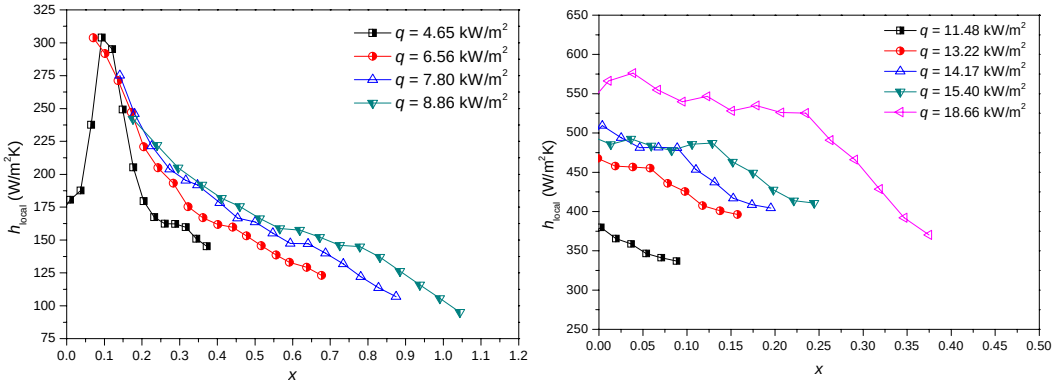

(a) **(b)**

Figure 8-10. Local heat transfer coefficients at different heat fluxes in the channel with d_h = 1454 μm; FC-72: (a) G = 11.2 kg·m^{-2}·s^{-1}, (b) G = 44.8 kg·m^{-2}·s^{-1}

Comparisons between different channels emphasized the impact of channel hydraulic diameter on local heat transfer. As shown in Figure 8-11, local heat transfer coefficients at the same mass flux and the same heat flux range in both 571 μm and 762 μm micro-channels are compared. The results in 1454 μm channel are not included in the plot due to different heat flux range. It is shown that h_{local} increases with decreasing d_h. Moreover, the effect of d_h is more significant when mass flux is higher.

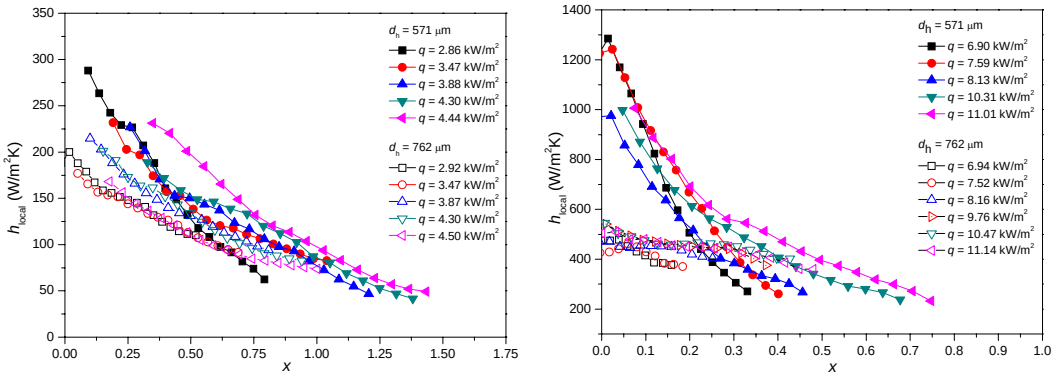

(a) **(b)**

Figure 8-11. Effect of channel diameter on local heat transfer coefficient; FC-72: (a) G = 11.2 kg·m^{-2}·s^{-1}, (b) G = 44.8 kg·m^{-2}·s^{-1}

The effect of channel hydraulic diameter on the local heat transfer could be explained based on the visualization results. The typical flow regimes under similar flow and heat conditions in each channel were shown in Figure 8-12. Even at the similar heat flux and mass flux, flow conditions were different in different channels. As shown in Figure 8-12 (a), in the 571 μm channel, annular flow prevails, and regular vapour collisions are observed, the period of which depends on the heating condition. Due to

large amount of existing vapour, nucleation is evidently suppressed. The liquid film thickness is reduced downstream and dry-out appears near the channel exit.

In Figure 8-12 (b), in the 762 μm channel, similar annular flow with downstream entrained droplets is observed. However, the liquid film is thicker in the 762 μm channel compared with the 571 μm channel, resulting in a higher thermal resistance. Therefore liquid film evaporation is weaker in the 762 μm channel. Thus the heat transfer enhancement in the 571 μm channel is understandable.

When d_h = 1454 μm (Figure 8-12 (c)), thick liquid exists between vapour and the channel wall. For moderate heat flux, more intense nucleation takes place in the liquid while the liquid film is evaporating and diminishing as approaching the channel exit. In the 1454 μm channel, the higher CVQ could be considered as a result of the more intense nucleation. Nevertheless, negligible nucleation was found in liquid film when d_h = 571 μm and 762 μm and abrupt transition from single phase to slug-annular flow was observed, the corresponding CVQ of which almost equal to zero.

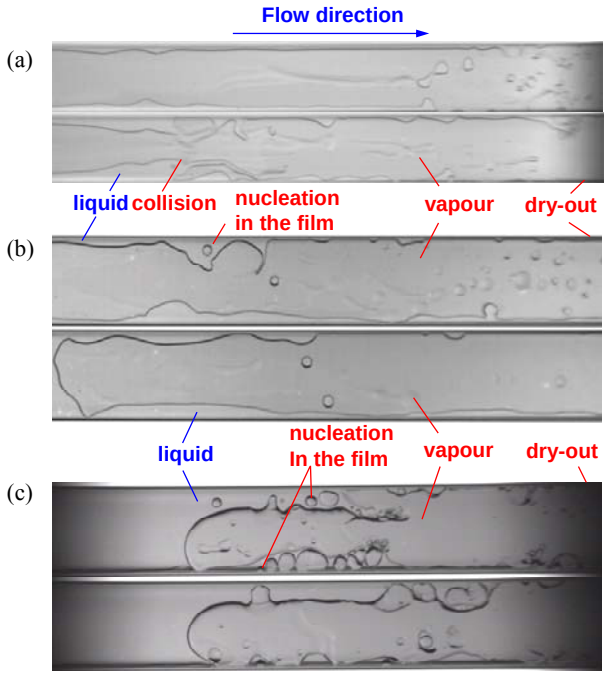

Figure 8-12. Two-phase flow regimes of FC-72: (a) d_h = 571 μm, G = 44.8 kg·m^{-2}·s^{-1}, q = 6.0 kW·m^{-2}, camera speed: 1000 fps, (b) d_h = 762 μm, G = 44.8 kg·m^{-2}·s^{-1}, q = 5.95 kW·m^{-2}, camera speed: 1500 fps, (c) d_h = 1454 μm, G = 44.8 kg·m^{-2}·s^{-1}, q = 7.56 kW·m^{-2}, camera speed: 2000 fps.

As aforementioned, heat transfer coefficient was estimated using both direct and inverse heat methods. Some of the results calculated by inverse heat method are presented for comparison.

Figure 8-13 shows two examples of the local heat transfer coefficients across the channel surface obtained using the inverse heat method. Grids were drawn on the channel surface and the averaged local temperatures at all the nodes were extracted using ThermaCAM Researcher Professional® software. The measured-temperature-matrices were then used in the Matlab program. A 6×17 and 8×17 grid was employed upon the 571 μm and 1454 μm channels respectively. The computed local heat transfer coefficient maps are plotted as in Figure 8-13. The two dimensional matrices can provide more accurate local heat transfer details. The heat transfer results obtained using both direct and inverse methods are compared in Figure 8-14, where h_{inverse} is the average value of each column in the matrix. Even though it was found that for different channel dimensions, the present Biot number ranged from 1.13 – 2.16 across the channel width and ranged from 5.66 – 14.41 across the channel length, the calculated heat transfer results using direct and inverse heat methods show minor difference (within ± 5.2%). The discrepancy is more remarkable approaching the channel exit where the wall temperature gradient is more considerable.

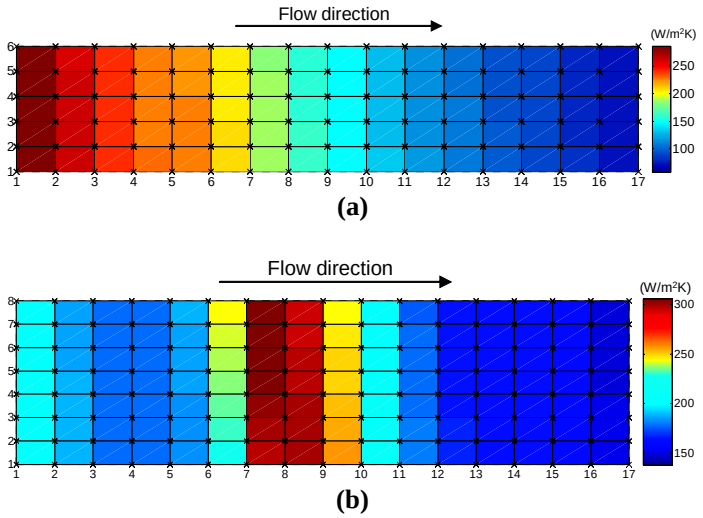

Figure 8-13. Inverse heat method calculated local heat transfer coefficient distribution (a) d_h = 571 μm, G = 11.2 kg·m^{-2}·s^{-1}, q = 2.86 kW·m^{-2}, (b) d_h = 1454 μm, G = 11.2 kg·m^{-2}·s^{-1}, q = 4.65 kW·m^{-2}

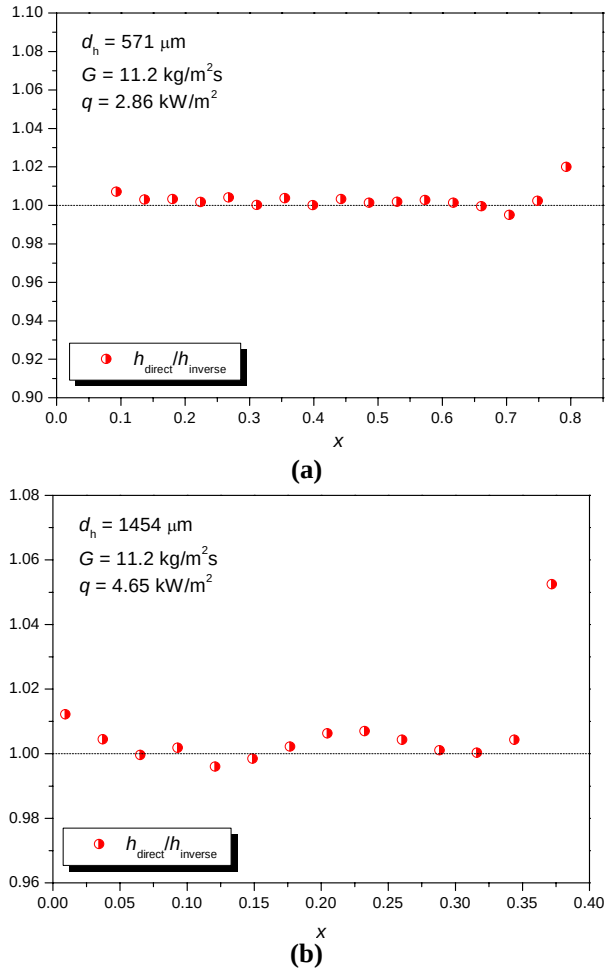

Figure 8-14. Comparisons between the heat transfer coefficients obtained using direct method and inverse heat method (a) d_h = 571 μm, G = 11.2 kg·m^{-2}·s^{-1}, q = 2.86 kW·m^{-2}, (b) d_h = 1454 μm, G = 11.2 kg·m^{-2}·s^{-1}, q = 4.65 kW·m^{-2} (maximum deviation case)

8.4.4. Heat transfer correlation assessment

Experimental heat transfer results acquired with FC-72 (426 data points) and ethanol (251 data points) were compared with several correlations for macro-, mini- and micro-channels. Ten existing correlations (Chen [131], Shah [132], Kandlikar [134], Liu and Winterton [136], Lazarek and Black [140], Tran *et al.* [95], Lee and Lee [137] Warrier *et al.* [98], Kandlikar and Balasubramanian [135] and Bertsch *et al.* [139], as included in Table 8-2) were selected. These correlations were also included in the literature review in Chapter 2. The first four correlations were suitable for macro-channels and the others were developed and applicable for rectangular mini- and micro-channels at wide ranges of experimental conditions.

Generally, most of the correlations included a single phase item h_{sp} expressed as the Dittus-Boelter correlation. Some correlations considered both nucleate boiling and

convective boiling terms (Chen [131], Liu and Winterton [136] and Bertsch *et al.* [139]). Liquid properties such as liquid and vapour density, surface tension, thermal conductivity, latent heat of vaporization, viscosity and specific heat have been taken into account. Besides, the effect of channel orientation in macro-scale was discussed in the macro-channel correlations (Shah [132] and Kandlikar [134]); Moreover, channel aspect ratio (Lee and Lee [137]) and channel surface roughness (Bertsch *et al.* [139]) were also considered.

All the experimental local heat transfer data were plotted against the calculated heat transfer coefficients in Figure 8-15 (a)-(t). The predictive accuracy of the correlations is measured by the mean absolute error (MAE), defined as:

$$\mathrm{MAE} = (1/N)\cdot\sum\left(\left|h_{\mathrm{exp.}} - h_{\mathrm{cor.}}\right| / h_{\mathrm{exp.}}\right)\times 100\% \qquad \textbf{(8-6)}$$

where N is the amount of data points.

Table 8-2. Summary of selected correlations for saturated flow boiling heat transfer in macro-, mini- and micro-channels

Reference (Year)	Parameter ranges	Correlation for local h
Chen [131] (1966)	water and organic fluids; vertical tubes; u_L = 0.061-4.481 m·s^{-1}; x = 0.01-0.71; P = 0.56-35.28 bar; macro-tube and annulus	$h_{tp} = Fh_{sp} + Sh_{nb}$ $h_{sp} = 0.023(Re_L)^{0.8}\cdot(Pr_L)^{0.4}\cdot(k_L/D)$ $h_{nb} = 0.00122\left(\frac{k_L^{0.79}C_{p,L}^{0.45}\rho_L^{0.49}g_c^{0.25}}{\sigma^{0.5}\mu_L^{0.29}h_{fg}^{0.24}\rho_v^{0.24}}\right)\cdot(\Delta T)^{0.24}\cdot(\Delta P)^{0.75}$ $F = (1+1/X^{0.5})^{1.78}$, $S = 0.9622 - 0.5822\left[\tan^{-1}\left(\frac{Re_L F^{1.25}}{6.18\times10^4}\right)\right]$ X: Martinelli parameter , $X = \left(\frac{1-x}{x}\right)^{0.9}\cdot\left(\frac{\rho_v}{\rho_L}\right)^{0.5}\cdot\left(\frac{\mu_L}{\mu_v}\right)^{0.5}$ $Re_L = \frac{G(1-x)d_h}{\mu_L}$, $Pr_L = \frac{C_{p,L}\cdot\mu_L}{k_L}$, ΔT : effective superheat of the flow, ΔP : difference in vapour pressure corresponding to the wall superheat
Shah [132] (1982)	water and refrigerants (R11, R12,R22, R502); vertical and horizontal tubes; d = 5.0-15.8 mm; G = 70-11071 kg·m^{-2}·s^{-1}; q = 90-1215 kW·m^{-2}; x = 0-0.7; macro-channels	$h_{tp} = \max(F,S)h_{sp}$ $h_{sp} = 0.023(Re_L)^{0.8}\cdot(Pr_L)^{0.4}\cdot(k_L/D)$ For N >1.0, $S = 1.8/N^{0.8}$, $F = 230Bl^{0.5}$ for $Bl > 3\times10^{-5}$, or $F = 1+46Bl^{0.5}$ for $Bl < 3\times10^{-5}$ For $0.1 < N \le 1.0$, $S = 1.8/N^{0.8}$, $F = E\cdot Bl^{0.5}\exp(2.74N^{-0.1})$

		For $N \le 0.1$ $S = 1.8/N^{0.8}$, $F = E \cdot Bl^{0.5}\exp(2.74N^{-0.15})$ where E = 14.7 for $Bl \ge 11\times10^{-4}$ or E = 15.43 for $Bl < 11\times10^{-4}$ $N = Co$ for $Fr_L \ge 0.04$ or $N = 0.38Fr_L^{-0.3}Co$ for $Fr_L < 0.04$ $Bl = \frac{q}{Gh_{fg}}$, $Co = \left(\frac{1-x}{x}\right)^{0.8}\cdot\left(\frac{\rho_v}{\rho_L}\right)^{0.5}$, $Fr = \frac{G^2}{\rho_L^2 gd}$
Kandlikar [134] (1990)	water, refrigerants, neon and nitrogen; vertical and horizontal; d_h = 4.6-32 mm; G = 13-8179 kg·m^{-2}·s^{-1}; q = 0.3-2280 kW·m^{-2}; x = 0.001-0.987; P = 0.6-64.2 bar; macro-channels	$h_{tp} = \max(F,S)\cdot h_{sp}$ $h_{sp} = 0.023(Re_L)^{0.8}\cdot(Pr_L)^{0.4}\cdot(k_L/D)$ For convective boiling: $F = 1.136Co^{-0.9}f(Fr_L) + 667.2Bl^{0.7}$ For nucleate boiling: $S = 0.6683Co^{-0.2}f(Fr_L) + 1058Bl^{0.7}$ $Co = \left(\frac{1-x}{x}\right)^{0.8}\cdot\left(\frac{\rho_v}{\rho_L}\right)^{0.5}$ F_{fL}: fluid-dependent parameter; Co: convection number $f(Fr_L) = 1$ for $Fr_L \ge 0.04$ or $f(Fr_L) = (25\,Fr_L)^{0.3}$ for $Fr_L < 0.04$ Extension of the correlation (Kandlikar and Balasubramanian [135]) neglects channel orientation in mini-channels, thus Froude number effect is deleted.
Liu and Winterton [136] (1991)	d_h = 2.95-32 mm; G = 12.4-8179.3 kg·m^{-2}·s^{-1}; q = 0.349-2620 kW·m^{-2}; x = 0.0-0.948; superheat: 0.2-62.2 K, T_{sub} = 0.1-173.7 K, Fr = 2.66×10^{-4} -2240 reduced pressure: 0.0023-0.895,Re = 568.9-875000; macro-channels	$h_{tp} = Fh_{sp} + Sh_{nb}$ $h_{sp} = 0.023(Re_L)^{0.8}\cdot(Pr_L)^{0.4}\cdot(k_L/D)$ $F = \left[1 + xPr_L\left(\frac{\rho_L}{\rho_v} - 1\right)\right]^{0.35}$ $h_{nb} = 55P_r^{0.12}\cdot(-\log_{10}P_r)^{-0.55}\cdot M^{-0.5}\cdot q^{0.67}$ $S = 1/(1 + 0.055F^{0.2}Re_L^{0.16})$ For horizontal tube and Froude number Fr < 0.05: $F = F\cdot Fr^{(0.1-2Fr)}$ and $S = S\sqrt{Fr}$
Lee and Lee [137] (2001)	R113; single, rectangular with aspect ratio: 0.1, 0.05 and 0.02; d_{in} = 0.4-2.0 mm, W_{in} = 20 mm; G = 50-200 kg·m^{-2}·s^{-1}; q = 0-15 kW·m^{-2}; x =0.15-0.75; mini- and micro-channels	$h_{tp} = F\cdot h_{sp}$ $h_{sp} = 8.235\left(\begin{matrix}1 - 2.0421\alpha + 3.0853\alpha^2 - 2.4765\alpha^3\\ +1.0578\alpha^4 - 0.1861\alpha^5\end{matrix}\right)$ $F = 10.3\alpha^{0.398}\phi_L^{0.598}$, $Re_L \le 200$, α: channel aspect ratio; $\phi_L^2 = 1 + \frac{C}{X} + \frac{1}{X^2}$, X: Martinelli parameter $C = 6.185\times10^{-2}Re_L^{0.726}$
Warrier *et al.* [98] (2002)	FC-84; 5 parallel, rectangular; d_h = 0.75 mm; G = 557-1600 kg·m^{-2}·s^{-1}; q = 0-59.9 kW·m^{-2}; x =0-0.55; T_{in} = 26, 40 and 60 °C; mini- and micro-channels	$h_{tp}/h_{sp\_FD} = 1 + 6.0Bl^{1/16} - 5.3(1 - 855Bo)x^{0.65}$ h_{sp_FD}: fully developed single phase heat transfer coefficient for laminar flow

Bertsch *et al.* [139] (2009)	water, refrigerants, FC-77 and nitrogen; circular and rectangula; d_h = 0.16-2.92 mm; G = 20-3000 kg·m^{-2}·s^{-1}; q = 0.4-115 kW·m^{-2}; T_{sat} = -194-97 °C; x = 0-1; confinement number: 0.3-4.0; mini- and micro-channels	$h_{tp} = h_{nb} \cdot (1-x) + h_{conv,tp} \cdot \left[1 + 80(x^2 - x^6) \cdot e^{-0.6Co}\right]$ $h_{nb} = 55 P_r^{0.12-0.2\log_{10} R_p} \cdot (-\log_{10} P_r)^{-0.55} M^{-0.5} q^{0.67}$, R_p : surface roughness parameter, μm P_r : reduced pressure $h_{conv,tp} = h_{conv,L} \cdot (1-x) + h_{conv,v} \cdot x$ $h_{conv,L} = \left(3.66 + \frac{0.0668 \frac{d_h}{L} Re \cdot Pr}{1 + 0.04 \cdot \left[\frac{d_h}{L} Re \cdot Pr\right]^{2/3}} \right) \cdot \frac{k_L}{d_h}$ $h_{conv,v}$ is calculated using the properties of saturated vapour instead

Reference (Year)	Parameter ranges	Correlation for global *h*
Lazarek and Black [140] (1982)	G = 125-750 kg·m^{-2}·s^{-1}; q = 14-380 kW·m^{-2}; static pressure: 1.3-4.1 bar *Re*: 860-5500 *Bl*: 2.3×10^4 - 76×10^4 ; mini- and micro-channels	$h_{tp} = 30 Re^{0.857} Bl^{0.714} k_L / d_h$ $Re = \frac{GD}{\mu_L}$ $Bl = \frac{q}{G h_{fg}}$
Tran *et al.* [95] (1996)	R12; single, circular and rectangular; d_h = 2.4-2.92 mm; G = 44-832 kg·m^{-2}·s^{-1}; q = 3.6-129 kW·m^{-2}; x =0-0.94 reduced pressure: 0.045-0.20 bar nucleate boiling dominant; mini-channels	$h = (8.4\times10^5)(Bl^2 We_L)^{0.3} \cdot \left(\frac{\rho_L}{\rho_v}\right)^{-0.4}$

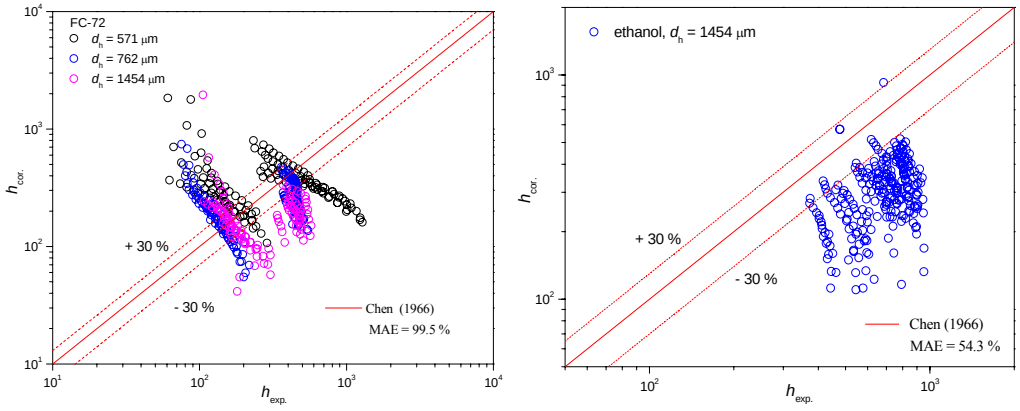

(a) **(b)**

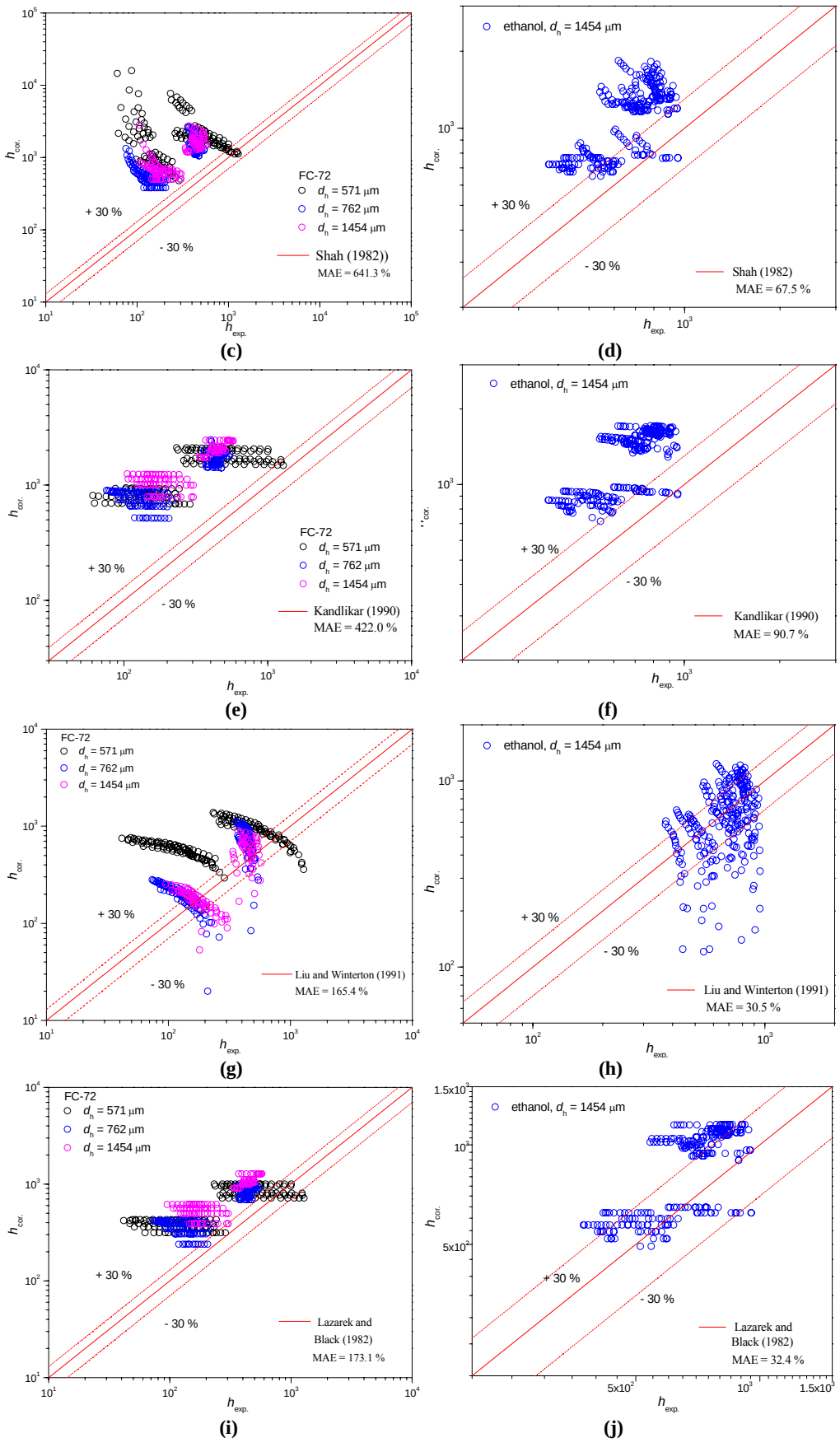
FC-72
d_h = 571 μm
d_h = 762 μm
d_h = 1454 μm
+ 30 %
- 30 %
Shah (1982))
MAE = 641.3 %
(c)
ethanol, d_h = 1454 μm
+ 30 %
- 30 %
Shah (1982)
MAE = 67.5 %
(d)
FC-72
d_h = 571 μm
d_h = 762 μm
d_h = 1454 μm
+ 30 %
- 30 %
Kandlikar (1990)
MAE = 422.0 %
(e)
ethanol, d_h = 1454 μm
+ 30 %
- 30 %
Kandlikar (1990)
MAE = 90.7 %
(f)
FC-72
d_h = 571 μm
d_h = 762 μm
d_h = 1454 μm
+ 30 %
- 30 %
Liu and Winterton (1991)
MAE = 165.4 %
(g)
ethanol, d_h = 1454 μm
+ 30 %
- 30 %
Liu and Winterton (1991)
MAE = 30.5 %
(h)
FC-72
d_h = 571 μm
d_h = 762 μm
d_h = 1454 μm
+ 30 %
- 30 %
Lazarek and Black (1982)
MAE = 173.1 %
(i)
ethanol, d_h = 1454 μm
+ 30 %
- 30 %
Lazarek and Black (1982)
MAE = 32.4 %
(j)

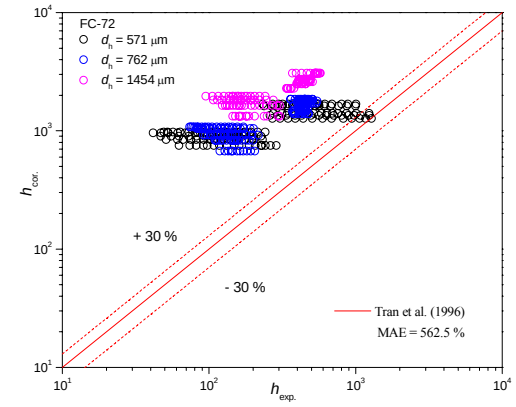
FC-72
d_h = 571 μm
d_h = 762 μm
d_h = 1454 μm
+ 30 %
- 30 %
Tran et al. (1996)
MAE = 562.5 %
$h_{cor.}$
$h_{exp.}$

(k)

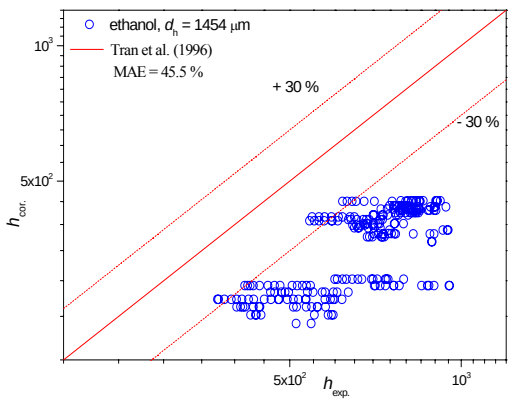
ethanol, d_h = 1454 μm
Tran et al. (1996)
MAE = 45.5 %
+ 30 %
- 30 %
$h_{cor.}$
$h_{exp.}$

(l)

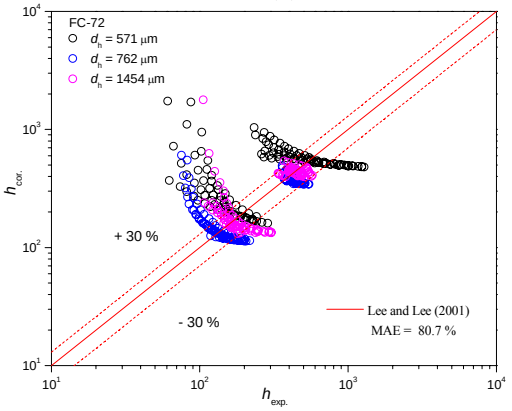
FC-72
d_h = 571 μm
d_h = 762 μm
d_h = 1454 μm
+ 30 %
- 30 %
Lee and Lee (2001)
MAE = 80.7 %
$h_{cor.}$
$h_{exp.}$

(m)

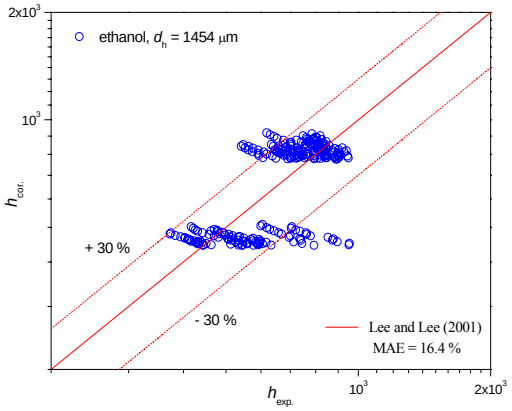
ethanol, d_h = 1454 μm
+ 30 %
- 30 %
Lee and Lee (2001)
MAE = 16.4 %
$h_{cor.}$
$h_{exp.}$

(n)

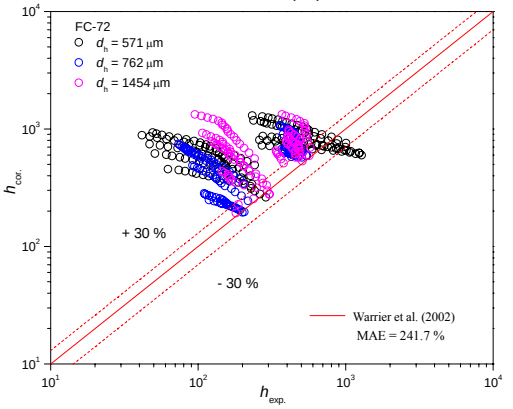
FC-72
d_h = 571 μm
d_h = 762 μm
d_h = 1454 μm
+ 30 %
- 30 %
Warrier et al. (2002)
MAE = 241.7 %
$h_{cor.}$
$h_{exp.}$

(o)

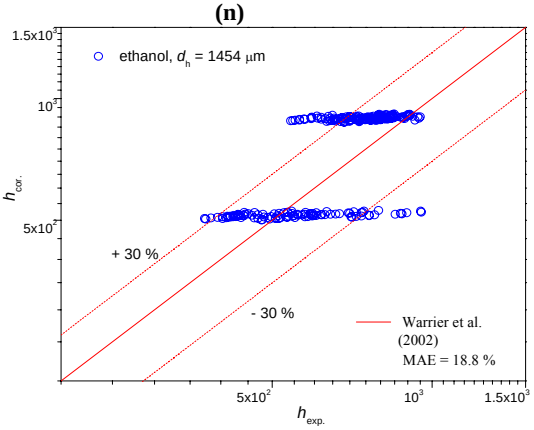
ethanol, d_h = 1454 μm
+ 30 %
- 30 %
Warrier et al. (2002)
MAE = 18.8 %
$h_{cor.}$
$h_{exp.}$

(p)

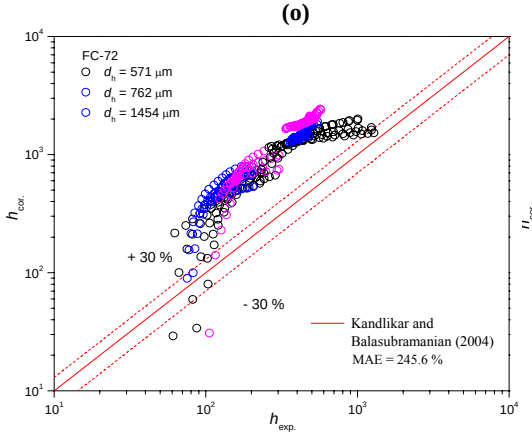
FC-72
d_h = 571 μm
d_h = 762 μm
d_h = 1454 μm
+ 30 %
- 30 %
Kandlikar and Balasubramanian (2004)
MAE = 245.6 %
$h_{cor.}$
$h_{exp.}$

(q)

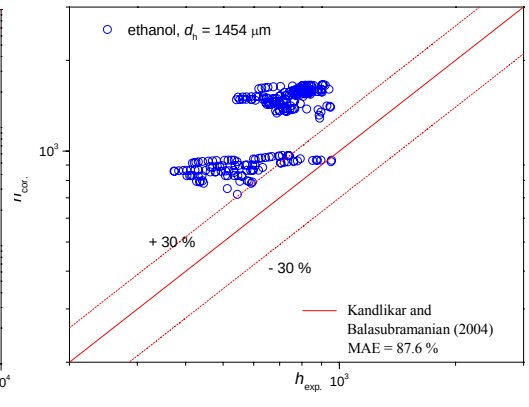
ethanol, d_h = 1454 μm
+ 30 %
- 30 %
Kandlikar and Balasubramanian (2004)
MAE = 87.6 %
$h_{cor.}$
$h_{exp.}$

(r)

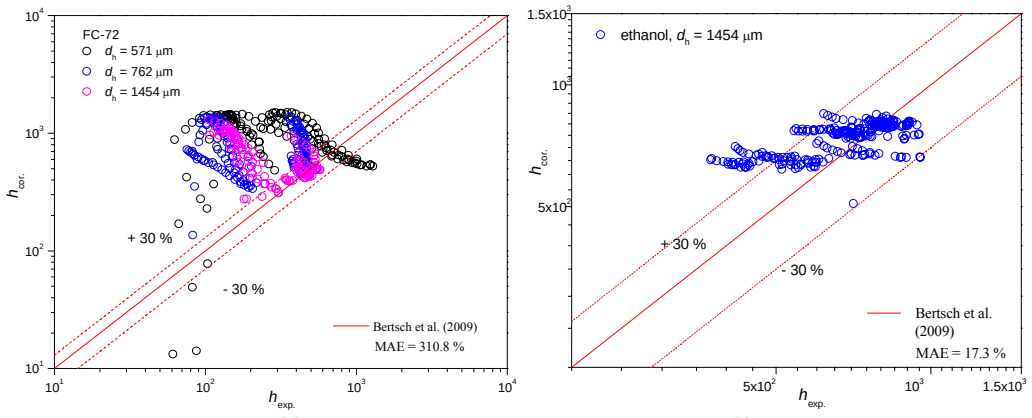

Figure 8-15. Comparison of experimental heat transfer coefficient data with predictions based on (a)-(b): Chen [131]; (c)-(d): Shah [132]; (e)-(f): Kandlikar [134]; (g)-(h): Liu and Winterton [136]; (i)-(j): Lazarek and Black [140]; (k)-(l):Tran *et al.* [95]; (m)-(n): Lee and Lee [137]; (o)-(p): Warrier *et al.* [98]; (q)-(r): Kandlikar and Balasubramanian [135] and (s)-(t): Bertsch *et al.* [139]

As evidenced in Figure 8-15, most correlations show better agreement with ethanol results than FC-72. Among all the comparisons, most of ethanol data points fall in ± 30%, while only less than 15% of FC-72 data fall in the range of ± 30%. The use of Dittus-Boelter correlation might partly contribute to the discrepancy because Dittus-Boelter correlation is well-known for turbulent flow. In the micro-channel tests, however, liquid flows are mostly laminar.

MAEs of the ten selected correlations are summarized in Table 8-3. Apparently, the correlations provide more accurate predictions for ethanol. High prediction accuracies are achieved by Lee and Lee [137] (MAE = 16.4%), Warrier *et al.* [98] (MAE = 18.8%) and Bertsch *et al.* [139] (MAE = 17.3%). However, all the ten correlations have poor agreements with FC-72 data, even the lowest MAE is as high as 80.7% (Lee and Lee [137]).

Efforts have been made to find a heat transfer expression which is suitable for both FC-72 and ethanol boiling in the high aspect ratio rectangular micro-channels. The aim is to use the best-fit correlation according to the above comparisons and make the modification base on the experimental data obtained in the present study.

First of all, it is essential to calculate the vapour Reynolds number Re_v ranges in the present study. For FC-72, Re_v ranges from 889.457 to 9059.69 and for ethanol, Re_v ranges from 1565.846 to 3131.69. Therefore the best-fit correlation Lee and Lee [137], which is suitable for laminar (liquid) - turbulent (vapour) flow can be selected for further amendment.

The effects of channel aspect ratio and liquid properties were emphasized by modifying the parameter F in the Lee and Lee [137] correlation and a modified parameter $F = 10.3\alpha^{0.984}\phi_L^{-0.806}$ is proposed based on the present data. The modified correlation is rewritten as follows:

FC-72 and ethanol; single, rectangular micro-channels with aspect ratio: 10 and 20; d_{in} = 571, 762, 1454 μm, G = 11.2, 22.4, 44.8 kg·m^{-2}·s^{-1} q = 0~18.6 kW·m^{-2} x = 0~1	$h_{tp} = F \cdot h_{sp}$ $h_{sp} = 8.235\left(\begin{array}{l}1 - 2.0421\alpha + 3.0853\alpha^2 - 2.4765\alpha^3 \\ +1.0578\alpha^4 - 0.1861\alpha^5\end{array}\right)$ $F = 10.3\alpha^{0.984}\phi_L^{-0.806}$, α: channel aspect ratio ($\alpha < 1$); d_h: micro-channel hydraulic diameter $\phi_L^2 = 1 + \frac{C}{X} + \frac{1}{X^2}$, X: Martinelli parameter $C = 6.185 \times 10^{-2} Re_L^{0.726}$

As can be seen in Figure 8-16, the modified correlation agrees with the experimental data within ± 23.6% for both FC-72 and ethanol.

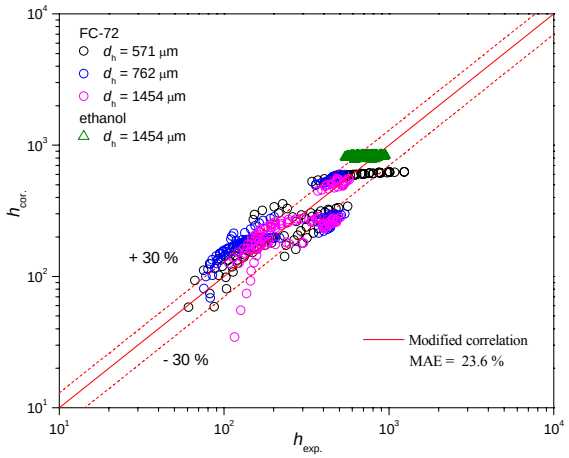

Figure 8-16. Comparison of experimental heat transfer coefficient data with the modified correlation

Table 8-3. Summary of MAE of the experimental heat transfer data comparison with the predictions based on selected correlations and the modified correlation in the present study

Selected correlations	MAE (%) FC-72	MAE (%) ethanol
Macro-channel correlations		
Chen [131]	99.5	54.3
Shah [132]	641.3	67.5
Kandlikar [134]	422.0	90.7

Liu and Winterton [136]	165.4	30.5
Mini- and micro-channel correlations		
Lazarek and Black [140]	173.1	32.4
Tran *et al.* [95]	562.5	45.5
Lee and Lee [137]	80.7	16.4
Warrier *et al.* [98]	241.7	18.8
Kandlikar and Balasubramanian [135]	245.6	87.6
Bertsch *et al.* [139]	310.8	17.3
Modified correlation	23.6	

8.5. Conclusions

Experimental investigation on flow boiling heat transfer in high aspect ratio rectangular micro-channels was carried out. Three channels with different hydraulic diameters and aspect ratios were used. FC-72 and ethanol were used as working liquids. Visualization results, boiling curves and the local heat transfer coefficients were obtained. Direct heat transfer calculation and inverse heat method were employed and compared for the local heat transfer coefficient computation. Furthermore, ten existing heat transfer correlations were assessed using the experimental heat transfer data. A modified correlation based on the present database for flow boiling heat transfer in high aspect ratio micro-channels was presented. In conclusion:

FC-72 and ethanol show similar vapour dynamics during flow boiling in micro-channels. Flow regimes including bubble nucleation, confined bubbly flow which rapidly turns into slug-annular flow, annular flow and wispy-annular flow with evaporating film are successively observed. Besides, periodic recoiling and re-wetting are captured for both liquids.

Heat transfer characteristics including boiling curves and local heat transfer coefficients are discussed. According to the boiling curves, incipient hysteresis occurs at the boiling onset. Besides, boiling curves are largely influenced by mass flux in both single phase and two-phase regions. The unique high aspect ratio channel geometry caused the abrupt transition from single phase to annular flow, during which convective boiling is the dominant heat transfer mechanism. ONB and CHF increase with increasing mass flux. Moreover, CHF is higher for ethanol than for FC-72. However, the corresponding wall superheat of ethanol at CHF is lower than FC-72. The significant differences in latent heat of vaporization and surface tension between ethanol and FC-72 probably explain the observed differences.

Local heat transfer coefficient decreases with vapour quality from $x = 0$ or shortly after $x > 0$. The vapour quality at which h_{local} starts to decrease is named as critical vapour quality (CVQ) and CVQ is higher at higher mass flux and/or in larger channel due to less suppressed nucleation. Moreover, local heat transfer coefficient increases with increasing heat flux, the effect of which is more profound as vapour quality becomes higher. Interestingly, h_{local} starts to decrease with further increase of heat flux since $q = 3.87$ kW·m^{-2} in the 762 μm micro-channel. Intermittent dry-out prior to CHF probably has deteriorated the local heat transfer.

Heat transfer is enhanced by the decreasing channel hydraulic diameter. The effect of channel diameter is more considerable when mass flux is higher. During annular flow, thicker liquid film exists in larger channel, resulting higher thermal resistance and weaker evaporation. Within one channel, however, heat transfer coefficient decreases as the liquid film diminishes. The partial dry-out is believed to deteriorate the local heat transfer.

In addition, the results from inverse heat method and direct heat calculation show minor deviation even though the Biot numbers range from 1.13 – 2.16 and 5.66 – 14.41 in the channel width and length directions respectively. As expected, the deviation is more remarkable near the channel exit where the wall temperature is higher.

Furthermore, according to the heat transfer correlation assessment, three micro-channel correlations show fairly good predictive accuracy for ethanol data: Lee and Lee [137] (MAE = 16.4%), Warrier *et al.* [98] (MAE = 18.8%) and Bertsch *et al.* [139] (MAE = 17.3%). However, all the ten correlations poorly predict the FC-72 data, evidenced by very high MAE ranging from 80.7% – 641.3%. Effects of channel aspect ratio and liquid properties need to be emphasized to develop more accurate correlations for flow boiling heat transfer in high aspect ratio micro-channels. A modified correlation based on Lee and Lee [137] is proposed. The modified correlation covers the experimental data of both FC-72 and ethanol with ± 23.6% mean deviation.

Chapter 9

Conclusions

9.1. Conclusions

Liquid-vapour phase change and multiphase flow heat transfer in single micro-channels were experimentally investigated. An experimental system has been built to study the vapour dynamics, flow boiling instabilities, micro-scale heat transfer and the meniscus evaporation in single high-aspect-ratio rectangular micro-channels. Micro-channels with three different hydraulic diameters (571 μm, 762 μm and 1454 μm) and cross-sectional aspect ratio (20, 20 and 10) were tested. A thin (~ 45 Angstroms) tantalum layer was sputtered on the micro-channels exterior surfaces for transparent heating, which enabled simultaneous visualisation. FC-72, n-pentane, ethanol and ethanol-based Al_2O_3 nanofluids (particle volume fractions: 0.01 vol.%, 0.05 vol.%, 0.1 vol.% and 0.5 vol.%) were selected as working fluids. High speed camera, infrared camera, pressure transducers and thermocouples were installed for data acquisition. A summary of the major findings from the measured results is given below:

Single phase pressure drop is an increasing function of Reynolds number and a decreasing function of the micro-channel hydraulic diameter. Single phase friction factors with pure liquids in the 571 μm and 762 μm micro-channels agree with the conventional friction theory within ±10% – ±20%, indicating the validity of the set-ups. The discrepancies in the 1454 μm channel are associated with hydrodynamic developing flow and the early transition to turbulent flow. The critical Reynolds number for the liquid to drift away from laminarity ranges from 600 – 700. Moreover, nanofluids show slightly lower friction factor than pure ethanol especially at high Reynolds numbers, possibly owing to the reduced contacting area between the working fluid and the channel inner surface. In addition, the nanoparticle concentration has minor impact on the single phase friction, but the friction factors of nanofluids agree with the predictions within ±30%, implying that nanofluids can be treated as homogeneous fluids and the conventional friction factor correlations can be extended to nanofluids within the tested nanoparticle concentration range.

Liquid-vapour phase change occurs as the applied heat flux increases. The heat flux required for the onset of nucleation increases with increasing mass flux and micro-channel size. The unique high aspect ratio micro-channel geometry accelerates the rapid transition from bubbly flow to slug and annular flow. The main flow regimes are slug

and annular flow, annular flow and wispy-annular flow with evaporating liquid film and entrained liquid droplets due to rapid vapour core movement.

Special attention is dedicated to the single vapour bubble growth. The bubble growth rate increases with plate superheating and the increasing plate gap when growing between two parallel plates (with 114 μm and 250 μm gaps) without flow. During flow boiling, on the other hand, a typical three-stage bubble growth mode is revealed. The first stage where bubble grows proportional to the square root of time is terminated by the channel depth confinement. The bubble linear growth is dominated by the liquid inertia force and the exponential growth is dominated by the heat transfer via liquid film evaporation. Transition from linear growth to exponential growth is accelerated by higher heat flux and lower mass flux. Bell-shape bubbles are observed and are attributed to the non-uniform liquid velocity distribution along the channel width-wise due to no-slip boundary condition. Furthermore, bubble aspect ratio ($\sigma = W_b/L_b$) firstly maintains at 1 within ± 10% – 20% and then drops drastically when bubble width occupies 78% – 90% of the channel width. From the slopes of the aspect ratio curves, heat flux and mass flux do not significantly affect the heat transfer mechanisms during bubble growth but only change the bubble evolution speed. However, bubble geometry progression is sensitive to the channel cross-sectional geometry. Bubble elongation is promoted in smaller channels. Based on the bubble growth rate, the evaporation heat flux is obtained, which increases with increasing heat flux and decreasing mass flux. Interestingly, evaporation heat flux finally becomes larger than the total applied heat flux because of the local saturation temperature reduction due to sudden pressure drop.

In order to explore the details of the evaporation in micro-scale space, a stationary meniscus in vertical micro-channels has been examined. The meniscus deteriorates due to the increasing evaporation rate but the use of nanofluids largely enhances the interface stability even though the added particle volume fraction is as low as 0.01 vol.%. Additionally, meniscus evaporation rate is an increasing function of heat flux and channel dimension. Specific evaporation rate, *i.e.* the evaporation rate per length in the micro-channels with the same aspect ratio almost overlap, verifying that the evaporation rate is proportional to the length of contact line, and reaffirming that the evaporation mostly takes place on the contact line.

Step-slip and back-jump behaviour of the nanofluid meniscus is captured during the transition from stable to deformed interface. The interface stick-slip recession lasts for 0.55 – 0.60 mm then the interface jumps back to the previous height when the liquid

pressure conquers the joint resistance from the surface tension force and the pinning of the nanoparticles.

Additionally, sink effect of the meniscus triple line is more profound at higher evaporation rate. Moreover, the temperature gradient is higher at the meniscus wedge than the middle of the meniscus. The consequent uneven surface tension on the meniscus is believed to initiate the thermocapillary Marangoni convection.

Two-phase flow instabilities have been extensively analyzed. Low-frequency high-amplitude fluctuation which results from the periodic reverse-rewetting flow, and high-frequency low-amplitude fluctuation which is caused by the vapour slug cluster passage and the vapour collision at downstream, are identified. Heat flux is only influential on the low frequency fluctuation at low mass flux. Fluctuation amplitudes of low frequencies are more sensitive to heat flux in smaller micro-channels. However, high mass flux drives high frequencies, the amplitudes of which are insensitive to heat flux.

The averaged pressure drop increases with increasing heat flux and mass flux. The coefficient of variation is chosen as a measurement of the pressure drop fluctuation. Increase of heat flux and channel dimension intensifies the pressure drop fluctuation. Meanwhile the averaged channel wall temperature T_w and the two-phase pressure drop fluctuations are in-phase. Different wettabilities of FC-72 and ethanol on the glass walls result in different T_w fluctuation behaviours.

Heat transfer has been particularly concentrated on during flow boiling in the high aspect ratio micro-channels. According to the obtained boiling curves, incipient hysterisis occurs at the boiling onset. Besides, boiling curves are largely influenced by mass flux, indicating the dominance of convective boiling heat transfer. ONB and CHF increase with increasing mass flux. Moreover, CHF of ethanol is higher than that of FC-72. However, the corresponding wall superheat of ethanol at CHF is lower than FC-72. The significant differences in latent heat of vaporization and surface tension between ethanol and FC-72 probably explain the observed differences.

Local heat transfer coefficient decreases with vapour quality from $x = 0$ or shortly after $x > 0$. The vapour quality at which h_{local} starts to decrease is named as critical vapour quality (CVQ) and CVQ is higher at higher mass flux and/or in larger channel due to less suppressed nucleation. Additionally, the local heat transfer coefficient increases with increasing heat flux, the effect of which is more profound as vapour quality becomes higher. Local heat transfer coefficient starts to decrease with further

increase of heat flux since q = 3.87 kW·m^{-2} in the 762 μm micro-channel. Intermittent dry-out prior to CHF probably has deteriorated the local heat transfer at high heat fluxes.

Heat transfer is enhanced by the decreasing channel hydraulic diameter and the effect of channel hydraulic diameter is more significant at higher mass flux. During annular flow, thicker liquid film exists in larger micro-channels, resulting in weaker evaporation. Within one channel, however, the partial dry-out is believed to deteriorate the local heat transfer as the liquid film diminishes.

Direct heat transfer calculation and inverse heat method for the local heat transfer coefficient computation are compared, showing minor deviation even though the Biot numbers range from 1.13 – 2.16 and 5.66 – 14.41 in the channel width and length directions respectively. Furthermore, ten existing heat transfer correlations have been assessed using the present experimental heat transfer data. Three micro-channel correlations show fairly good predictive accuracy for ethanol data. However, all the ten correlations poorly predict the FC-72 data. Significant roles of channel aspect ratio and liquid properties are emphasized and a modified correlation based on the best-agreed correlation is proposed for high aspect ratio micro-channels. The modified correlation covers the experimental data with ±23.6% mean deviation.

9.2. Future work

Single phase flow in micro-channels can be extensively investigated by using a higher pumping capacity to achieve higher Reynolds number, so that the transition from laminar flow to turbulent flow in different micro-channels can be captured. Besides, wider ranges of channel dimension and inner surface roughness levels are important to clarify the deviation from the conventional friction theory observed in some of the micro-channel tests.

In addition, more experiments are required to look for the explanations of the reduced friction factors of nanofluids at higher Reynolds numbers. It will also be helpful to be able to probe the inner surface condition to unveil how the nanoparticles distribute and deposit on the channel surfaces during and after the flow.

More importantly, nanofluids should be used as the main working fluids in the future work in order to investigate the influences on evaporation and flow boiling heat transfer characteristics in the unique channel geometry. In the present study, the use of

nanofluids was limited to the single phase pressure drop experiments and the evaporating meniscus in vertical micro-channels. The investigation on the effects of additional nanoparticles on hydrodynamic and thermal characteristics in high aspect ratio micro-channels is only at an early stage. It is vital to enlarge the nanofluids database. Then, fundamental experiments on the nanofluids meniscus evaporation and the nanofluids flow boiling heat transfer in micro-channels should be conducted. Different selections of base liquids and nanoparticles, and wider ranges of particle concentrations should be used.

Reference

1. D. Clark, "*Apple iPad Taps Familiar Component Suppliers - WSJ.com*." Online.wsj.com. Retrieved 2010-04-05.
2. "*Chipworks Confirms Apple A4 iPad chip is fabbed by Samsung in their 45-nm proces*." Chipworks.
3. R. Smith, *Current Packaging Trends*. Proceedings of the Cooling Electronics The Next Decade conference, Marlborough, MA, USA 2001.
4. M.K. Sung and I. Mudawar, *Single-Phase and Two-Phase Hybrid Cooling Schemes for High-Heat-Flux Thermal Management of Defense Electronics*. Journal of Electronic Packaging, 2009.131(2):p. 021013.
5. S. Kakac, L. Vasiliev and Y. Bayazitoglu, *Microscale Heat Transfer: Fundamentals And Applications*,2005. Springer-Verlag
6. J.P. Petit, *Dissipation thermique dans les systèmes électroniques, Techniques de l'ingénieur, Ref E3952*.
7. C. Gillot, *Etude et réalisation d'une fonction interrupteur en technologie hybride à haute intégration*. Thèse de doctorat de l'INP Grenoble, 2000.
8. D. Wen, G. Lin, S. Vafaei and K. Zhang, *Review of nanofluids for heat transfer applications*. Particuology, 2009.7(2):p. 141-150.
9. J.C. Maxwell, *A Treatise on Electricity and Magnetism*,1873. Oxford : Clarendon Press
10. S.G. Kandlikar, M. Shoji and V.K. Dhir, *Handbook of Phase Changes:Boiling and Condenation*,1999. Taylor and Francis
11. J.R. Thome, *Chapter 20 Two-Phase Flow and Flow Boiling in Microchannels*. Wolverine Heat Transfer Engineering Data book III. Switzerland.
12. S.S. Mehendale, A.M. Jacobi and R.K. Shah, *Fluid Flow and Heat Transfer at Micro- and Meso-Scales With Application to Heat Exchanger Design*. Applied Mechanics Reviews, 2000.53(7):p. 175-193.
13. S.G. Kandlikar, *Fundamental issues related to flow boiling in minichannels and microchannels*. Experimental Thermal and Fluid Science, 2002.26(2-4):p. 389-407.
14. A.E. Bergles, J.H. Lienhard, G.E. Kendall and P. Griffith, *Boiling and Evaporation in Small Diameter Channels*. Heat Transfer Engineering, 2003.24(1):p. 18 - 40.
15. J.R. Thome, *Boiling in microchannels: a review of experiment and theory*. International Journal of Heat and Fluid Flow, 2004.25:p. 128-139.
16. J.R. Thome, *State-of-the-Art Overview of Boiling and Two-Phase Flows in Microchannels*. Heat Transfer Engineering, 2006.27(9):p. 4-19.
17. P. Cheng, G. Wang and X. Quan, *Recent Work on Boiling and Condensation in Microchannels*. Journal of Heat Transfer, 2009.131(4):p. 043211-15.
18. Y.-Y. Yan and T.-F. Lin, *Evaporation heat transfer and pressure drop of refrigerant R-134a in a small pipe*. International Journal of Heat and Mass Transfer, 1998.41(24):p. 4183-4194.
19. W. Owhaib, C. Martín-Callizo and B. Palm, *Evaporative heat transfer in vertical circular microchannels*. Applied Thermal Engineering, 2004.24(8-9):p. 1241-1253.

20. L. Consoli, *Convective Boiling Heat Transfer in a Single Microchannel*. PhD, École Polytechnique Federale de Lausanne, Switzerland. 2008.
21. W. Qu and I. Mudawar, *Measurement and correlation of critical heat flux in two-phase micro-channel heat sinks*. International Journal of Heat and Mass Transfer, 2004.47(10-11):p. 2045-2059.
22. S.G. Kandlikar and W.J. Grande, *Evolution of Microchannel Flow Passages--Thermohydraulic Performance and Fabrication Technology*. Heat Transfer Engineering, 2003.24(1):p. 3 - 17.
23. L. Lin and A.P. Pisano, *Bubble forming on a micro line heater*. D. Cho (Ed.), Micromechanical Sensors, Actuators, and Systems, ASME, DSC, 1991. 32:p. 147-164.
24. M. Suo and P. Griffith, *Two-phase flow in capillary tubes*. Transaction of the ASME, Journal of Basic Engineering, 1964.86:p. 576-582.
25. P.A. Kew and K. Cornwell, *Correlations for the prediction of boiling heat transfer in small-diameter channels*. Applied Thermal Engineering, 1997.17(8-10):p. 705-715.
26. N. Brauner and D.M. Maron, *Identification of the range of 'small diameters' conduits, regarding two-phase flow pattern transitions*. International Communications in Heat and Mass Transfer, 1992.19(1):p. 29-39.
27. A.M. Jacobi and J.R. Thome, *Heat Transfer Model for Evaporation of Elongated Bubble Flows in Microchannels*. Journal of Heat Transfer, 2002.124(6):p. 1131-1136.
28. P. Cheng, H.Y. Wu, J.P.H.A.B.-C. George A. Greene and I.C. Young, *Mesoscale and Microscale Phase-Change Heat Transfer*. Advances in Heat Transfer, Elsevier. 2006. Volume 39:p. 461-563.
29. W. Li and Z. Wu, *A general criterion for evaporative heat transfer in micro/mini-channels*. International Journal of Heat and Mass Transfer, 2010.53(9-10):p. 1967-1976.
30. N. Zuber, *Hydrodynamic aspects of boiling heat transfer*. Research Laboratory, Los Angeles and Ramo-wooldridge Corporation. Doctor of Philosophy, University of California. 1959.
31. V.K. Dhir, *BOILING HEAT TRANSFER*. Annual Review of Fluid Mechanics, 1998.30(1):p. 365-401.
32. J. Straub, *Bubble — bubbles — boiling*. Microgravity Science and Technology, 2005.16(1):p. 242-248.
33. A.J. Robinson and R.L. Judd, *Bubble growth in a uniform and spatially distributed temperature field*. International Journal of Heat and Mass Transfer, 2001.44(14):p. 2699-2710.
34. S. Kandlikar, V. Mizo and M. Cartwright, *Investigation of bubble departure mechanism in subcooled flow boiling of water using high-speed photography*. 1995.
35. O. Zeitoun and M. Shoukri, *Bubble Behavior and Mean Diameter in Subcooled Flow Boiling*. Journal of Heat Transfer, 1996.118(1):p. 110-116.
36. X.F.Peng, H.Y. Hu and B.X.Wang, *Boiling nucleation during liquid flow in microchannels*. International Journal of Heat and Mass Transfer, 1998.41(1):p. 101-106.
37. G.E. Thorncroft, J.F. Klausner and R. Mei, *An experimental investigation of bubble growth and detachment in vertical upflow and downflow boiling*. International Journal of Heat and Mass Transfer, 1998.41(23):p. 3857-3871.

38. F. Moshe, T. Zehev and S. Raphael, *Bubble growth in a viscous liquid in a simple shear flow*. AIChE Journal, 1999.45(4):p. 691-695.
39. R. Maurus, V. Ilchenko and T. Sattelmayer, *Study of the bubble characteristics and the local void fraction in subcooled flow boiling using digital imaging and analysing techniques*. Experimental Thermal and Fluid Science, 2002.26(2-4):p. 147-155.
40. G.Hetsroni, A.Mosyak, Z.Segal and E.Pogrebnyak, *Two- phase flow patterns and heat transfer in parallel microchannels*. Journal of Thermal Science, 2002.11(4):p. 353-358.
41. T. Cubaud and C.-M. Ho, *Transport of bubbles in square microchannels*. Physics of Fluids, 2004.16(12):p. 4575-4585.
42. P.C. Lee, F.G. Tseng and C. Pan, *Bubble dynamics in microchannels. Part I: single microchannel*. International Journal of Heat and Mass Transfer, 2004.47(25):p. 5575-5589.
43. H.Y. Li, F.G. Tseng and C. Pan, *Bubble dynamics in microchannels. Part II: two parallel microchannels*. International Journal of Heat and Mass Transfer, 2004.47(25):p. 5591-5601.
44. R. Situ, T. Hibiki, M. Ishii and M. Mori, *Bubble lift-off size in forced convective subcooled boiling flow*. International Journal of Heat and Mass Transfer, 2005.48(25-26):p. 5536-5548.
45. X. Frank, N. Dietrich, J. Wu, R. Barraud and H.Z. Li, *Bubble nucleation and growth in fluids*. Chemical Engineering Science, 2007.62(24):p. 7090-7097.
46. W. Owhaib, B. Palm and C. Martin-Callizo, *A Visualization Study of Bubble Behavior in Saturated Flow Boiling through a Vertical Mini-Tube*. Heat Transfer Engineering, 2007.28(10):p. 852-860.
47. B. Agostini, R. Revellin and J.R. Thome, *Elongated bubbles in microchannels. Part I: Experimental study and modeling of elongated bubble velocity*. International Journal of Multiphase Flow, 2008.34(6):p. 590-601.
48. R. Revellin, B. Agostini and J.R. Thome, *Elongated bubbles in microchannels. Part II: Experimental study and modeling of bubble collisions*. International Journal of Multiphase Flow, 2008.34(6):p. 602-613.
49. W. Wu, P. Chen, B.G. Jones and T.A. Newell, *A study on bubble detachment and the impact of heated surface structure in subcooled nucleate boiling flows*. Nuclear Engineering and Design, 2008.238(10):p. 2693-2698.
50. J. Lee and I. Mudawar, *Critical heat flux for subcooled flow boiling in micro-channel heat sinks*. International Journal of Heat and Mass Transfer, 2009.52(13-14):p. 3341-3352.
51. G. Duhar, G. Riboux and C. Colin, *Vapour bubble growth and detachment at the wall of shear flow* Heat and Mass Transfer, 2009.45:p. 847-855.
52. D.B. Tuckerman and R.F.W. Pease, *High-performance heat sinking for VLSI*. Electron Device Letters, IEEE, 1981.2(5):p. 126-129.
53. O. Mokrani, B. Bourouga, C. Castelain and H. Peerhossaini, *Fluid flow and convective heat transfer in flat microchannels*. International Journal of Heat and Mass Transfer, 2009.52(5-6):p. 1337-1352.
54. J. Barber, D. Brutin, K. Sefiane and L. Tadrist, *Bubble confinement in flow boiling of FC-72 in a "rectangular" microchannel of high aspect ratio*. Experimental Thermal and Fluid Science, 2010.34(8):p. 1375-1388.
55. A. Serizawa, Z. Feng and Z. Kawara, *Two-phase flow in microchannels*. Experimental Thermal and Fluid Science, 2002.26:p. 703-714.

56. S. Saisorn, J. Kaew-On and S. Wongwises, *Flow pattern and heat transfer characteristics of R-134a refrigerant during flow boiling in a horizontal circular mini-channel*. International Journal of Heat and Mass Transfer, 2010.53(19-20):p. 4023-4038.
57. J.L. Xu, P. Cheng and T.S. Zhao, *Gas-liquid two-phase flow regimes in rectangular channels with mini/micro gaps*. International Journal of Multiphase Flow, 1999.25(3):p. 411-432.
58. T. Harirchian and S.V. Garimella, *An investigation of flow boiling regimes in microchannels of different sizes by means of high-speed visualization*. Thermal and Thermomechanical Phenomena in Electronic Systems, 2008. ITHERM 2008. 11th Intersociety Conference on 2008.p. 197-206.
59. A.A. Arcanjo, C.B. Tibiriçá and G. Ribatski, *Evaluation of flow patterns and elongated bubble characteristics during the flow boiling of halocarbon refrigerants in a micro-scale channel*. Experimental Thermal and Fluid Science, 2010.34(6):p. 766-775.
60. A. Megahed and I. Hassan, *Two-phase pressure drop and flow visualization of FC-72 in a silicon microchannel heat sink*. International Journal of Heat and Fluid Flow, 2009.30(6):p. 1171-1182.
61. J.G. Collier, *CONVECTIVE BOILING AND CONDENSATION*. Oxford, UK,1972. McGRAW-HILL
62. X. Huo, L. Chen, Y.S. Tian and T.G. Karayiannis, *Flow boiling and flow regimes in small diameter tubes*. Applied Thermal Engineering, 2004.24(8-9):p. 1225-1239.
63. N. Ichikawa, K. Hosokawa and R. Maeda, *Interface motion of capillary-driven flow in rectangular microchannel*. Journal of Colloid and Interface Science, 2004.280(1):p. 155-164.
64. C. Huh and M.H. Kim, *Pressure Drop, Boiling Heat Transfer and Flow Patterns during Flow Boiling in a Single Microchannel*. Heat Transfer Engineering, 2007.28(8):p. 730 - 737.
65. S.G. Kandlikar, *Scale effects on flow boiling heat transfer in microchannels: A fundamental perspective*. International Journal of Thermal Sciences, 2010.p. 1-13.
66. T. Harirchian and S.V. Garimella, *A comprehensive flow regime map for microchannel flow boiling with quantitative transition criteria*. International Journal of Heat and Mass Transfer, 2010.53(13-14):p. 2694-2702.
67. S. In and S. Jeong, *Flow boiling heat transfer characteristics of R123 and R134a in a micro-channel*. International Journal of Multiphase Flow, 2009.35(11):p. 987-1000.
68. A. Kawahara, M. Sadatomi, K. Nei and H. Matsuo, *Experimental study on bubble velocity, void fraction and pressure drop for gas-liquid two-phase flow in a circular microchannel*. International Journal of Heat and Fluid Flow, 2009.30(5):p. 831-841.
69. G.P. Celata, S.K. Saha, G. Zummo and D. Dossevi, *Heat transfer characteristics of flow boiling in a single horizontal microchannel*. International Journal of Thermal Sciences, 2010.49(7):p. 1086-1094.
70. G. Chen and P. Cheng, *Nucleate and film boiling on a microheater under pulse heating in a microchannel*. International Communications in Heat and Mass Transfer, 2009.36(5):p. 391-396.

71. J. Wu, M. Shi, Y. Chen and X. Li, *Visualization study of steam condensation in wide rectangular silicon microchannels*. International Journal of Thermal Sciences, 2010.49(6):p. 922-930.
72. M. Ledinegg, *Instability of Flow During Natural and Forced Circulation*. Die Wärme, 1938.61(48):p. 891-898.
73. J.A. Boure, A.E. Bergles and L.S. Tong, *Review of two-phase flow instability*. Nuclear Engineering and Design, 1973.25(2):p. 165-192.
74. L. Tadrist, *Review on two-phase flow instabilities in narrow spaces*. International Journal of Heat and Fluid Flow, 2007.28(1):p. 54-62.
75. S. Kakac and B. Bon, *A Review of two-phase flow dynamic instabilities in tube boiling systems*. International Journal of Heat and Mass Transfer, 2008.51(3-4):p. 399-433.
76. S.G. Kandlikar, M. Shoji and V.K. Dhir, *Two-Phase Flow Instabilities*. *Handbook of Phase Changes:Boiling and Condenation*, Taylor and Francis. 1999.p. 263.
77. P.A. Kew and K. Cornwell, *Confined bubble flow and boiling in narrow spaces*. IHTC 10, Brighton, England 1994.p. 473-478.
78. J.E. Kennedy, J.G.M. Roach, M.F. Dowling, S.I. Abdel-Khalik, S.M. Ghiaasiaan, S.M. Jeter and Z.H. Quershi, *The Onset of Flow Instability in Uniformly Heated Horizontal Microchannels*. Journal of Heat Transfer, 2000.122(1):p. 118-125.
79. L. Zhang, E.N. Wang, K.E. Goodson and T.W. Kenny, *Phase change phenomena in silicon microchannels*. International Journal of Heat and Mass Transfer, 2005.48(8):p. 1572-1582.
80. G. Hetsroni, A. Mosyak, Z. Segal and G. Ziskind, *A uniform temperature heat sink for cooling of electronic devices*. International Journal of Heat and Mass Transfer, 2002.45(16):p. 3275-3286.
81. D. Brutin, F. Topin and L. Tadrist, *Experimental study of unsteady convective boiling in heated minichannels*. International Journal of Heat and Mass Transfer, 2003.46(16):p. 2957-2965.
82. K.H. Chang and C. Pan, *Two-phase flow instability for boiling in a microchannel heat sink*. International Journal of Heat and Mass Transfer, 2007.50(11-12):p. 2078-2088.
83. G. Wang, P. Cheng and H. Wu, *Unstable and stable flow boiling in parallel microchannels and in a single microchannel*. International Journal of Heat and Mass Transfer, 2007.50(21-22):p. 4297-4310.
84. G. Wang and P. Cheng, *An experimental study of flow boiling instability in a single microchannel*. International Communications in Heat and Mass Transfer, 2008.35(10):p. 1229-1234.
85. P. Balasubramanian and S.G. Kandlikar, *Experimental Study of Flow Patterns, Pressure Drop, and Flow Instabilities in Parallel Rectangular Minichannels*. Heat Transfer Engineering, 2005.26(3):p. 20 - 27.
86. R. Muwanga, I. Hassan and R. MacDonald, *Characteristics of Flow Boiling Oscillations in Silicon Microchannel Heat Sinks*. Journal of Heat Transfer, 2007.129(10):p. 1341-1351.
87. D. Brutin and L. Tadrist, *Pressure drop and heat transfer analysis of flow boiling in a minichannel: influence of the inlet condition on two-phase flow stability*. International Journal of Heat and Mass Transfer, 2004.47(10-11):p. 2365-2377.

88. Y. Ding, S. Kakaç and X.J. Chen, *Dynamic instabilities of boiling two-phase flow in a single horizontal channel*. Experimental Thermal and Fluid Science, 1995.11(4):p. 327-342.
89. S.G. Singh, R.R. Bhide, S.P. Duttagupta, B.P. Puranik and A. Agrawal, *Two-Phase Flow Pressure Drop Characteristics in Trapezoidal Silicon Microchannels*. Components and Packaging Technologies, IEEE Transactions on, 2009.32(4):p. 887-900.
90. R.R. Bhide, S.G. Singh, A. Sridharan, S.P. Duttagupta and A. Agrawal, *Pressure drop and heat transfer characteristics of boiling water in sub-hundred micron channel*. Experimental Thermal and Fluid Science, 2009.33(6):p. 963-975.
91. G. Hetsroni, A. Mosyak, E. Pogrebnyak and Z. Segal, *Explosive boiling of water in parallel micro-channels*. International Journal of Multiphase Flow, 2005.31(4):p. 371-392.
92. H.J. Lee and S.-c. Yao, *System instability of evaporative micro-channels*. International Journal of Heat and Mass Transfer, 2010.53(9-10):p. 1731-1739.
93. J. Barber, K. Sefiane, D. Brutin and L. Tadrist, *Hydrodynamics and heat transfer during flow boiling instabilities in a single microchannel*. Applied Thermal Engineering, 2009.29(7):p. 1299-1308.
94. X.F. Peng and B.X. Wang, *Forced convection and flow boiling heat transfer for liquid flowing through microchannels*. International Journal of Heat and Mass Transfer, 1993.36(14):p. 3421-3427.
95. T.N. Tran, M.W. Wambsganss and D.M. France, *Small circular- and rectangular-channel boiling with two refrigerants*. International Journal of Multiphase Flow, 1996.22(3):p. 485-498.
96. Z.Y. Bao, D.F. Fletcher and B.S. Haynes, *Flow boiling heat transfer of Freon R11 and HCFC123 in narrow passages*. International Journal of Heat and Mass Transfer, 2000.43(18):p. 3347-3358.
97. S. Lin, P.A. Kew and K. Cornwell, *Flow Boiling of Refrigerant R141B in Small Tubes*. Chemical Engineering Research and Design, 2001.79(4):p. 417-424.
98. G.R. Warrier, V.K. Dhir and L.A. Momoda, *Heat transfer and pressure drop in narrow rectangular channels*. Experimental Thermal and Fluid Science, 2002.26(1):p. 53-64.
99. W. Yu, D.M. France, M.W. Wambsganss and J.R. Hull, *Two-phase pressure drop, boiling heat transfer, and critical heat flux to water in a small-diameter horizontal tube*. International Journal of Multiphase Flow, 2002.28(6):p. 927-941.
100. W. Qu and I. Mudawar, *Flow boiling heat transfer in two-phase micro-channel heat sinks--I. Experimental investigation and assessment of correlation methods*. International Journal of Heat and Mass Transfer, 2003.46(15):p. 2755-2771.
101. T.-H. Yen, N. Kasagi and Y. Suzuki, *Forced convective boiling heat transfer in microtubes at low mass and heat fluxes*. International Journal of Multiphase Flow, 2003.29(12):p. 1771-1792.
102. M.E. Steinke and S.G. Kandlikar, *An Experimental Investigation of Flow Boiling Characteristics of Water in Parallel Microchannels*. Journal of Heat Transfer, 2004.126(4):p. 518-526.
103. A. Greco and G.P. Vanoli, *Flow boiling heat transfer with HFC mixtures in a smooth horizontal tube. Part I: Experimental investigations*. Experimental Thermal and Fluid Science, 2005.29(2):p. 189-198.
104. J. Lee and I. Mudawar, *Two-phase flow in high-heat-flux micro-channel heat sink for refrigeration cooling applications: Part II--heat transfer characteristics*. International Journal of Heat and Mass Transfer, 2005.48(5):p. 941-955.

105. S. Saitoh, H. Daiguji and E. Hihara, *Effect of tube diameter on boiling heat transfer of R-134a in horizontal small-diameter tubes*. International Journal of Heat and Mass Transfer, 2005.48(23-24):p. 4973-4984.
106. R. Yun, Y. Kim and M. Soo Kim, *Flow boiling heat transfer of carbon dioxide in horizontal mini tubes*. International Journal of Heat and Fluid Flow, 2005.26(5):p. 801-809.
107. T. Chen and S.V. Garimella, *Flow Boiling Heat Transfer to a Dielectric Coolant in a Microchannel Heat Sink*. IEEE Transactions on Components and Packaging Technologies, 2007.30(1):p. 24-31.
108. K.-I. Choi, A.S. Pamitran and J.-T. Oh, *Two-phase flow heat transfer of CO2 vaporization in smooth horizontal minichannels*. International Journal of Refrigeration, 2007.30(5):p. 767-777.
109. M.C. Díaz and J. Schmidt, *Experimental investigation of transient boiling heat transfer in microchannels*. International Journal of Heat and Fluid Flow, 2007.28(1):p. 95-102.
110. D. Liu and S.V. Garimella, *Flow Boiling Heat Transfer in Microchannels*. Journal of Heat Transfer, 2007.129:p. 1321-1332.
111. B. Agostini, J.R. Thome, M. Fabbri, B. Michel, D. Calmi and U. Kloter, *High heat flux flow boiling in silicon multi-microchannels - Part I: Heat transfer characteristics of refrigerant R236fa*. International Journal of Heat and Mass Transfer, 2008.51(21-22):p. 5400-5414.
112. B. Agostini, J.R. Thome, M. Fabbri, B. Michel, D. Calmi and U. Kloter, *High heat flux flow boiling in silicon multi-microchannels - Part II: Heat transfer characteristics of refrigerant R245fa*. International Journal of Heat and Mass Transfer, 2008.51(21-22):p. 5415-5425.
113. S.S. Bertsch, E.A. Groll and S.V. Garimella, *Refrigerant flow boiling heat transfer in parallel microchannels as a function of local vapor quality*. International Journal of Heat and Mass Transfer, 2008.51(19-20):p. 4775-4787.
114. P.-S. Lee and S.V. Garimella, *Saturated flow boiling heat transfer and pressure drop in silicon microchannel arrays*. International Journal of Heat and Mass Transfer, 2008.51(3-4):p. 789-806.
115. S.S. Bertsch, E.A. Groll and S.V. Garimella, *Effects of heat flux, mass flux, vapor quality, and saturation temperature on flow boiling heat transfer in microchannels*. International Journal of Multiphase Flow, 2009.35(2):p. 142-154.
116. R.J. da Silva Lima, J.M. Quibén and J.R. Thome, *Flow boiling in horizontal smooth tubes: New heat transfer results for R-134a at three saturation temperatures*. Applied Thermal Engineering, 2009.29(7):p. 1289-1298.
117. V. Kuznetsov and A. Shamirzaev, *Flow Boiling Heat Transfer in Two-Phase Micro Channel Heat Sink at Low Water Mass Flux*. Microgravity Science and Technology, 2009.21(0):p. 305-311.
118. C.L. Ong and J.R. Thome, *Flow boiling heat transfer of R134a, R236fa and R245fa in a horizontal 1.030mm circular channel*. Experimental Thermal and Fluid Science, 2009.33(4):p. 651-663.
119. M. Hamdar, A. Zoughaib and D. Clodic, *Flow boiling heat transfer and pressure drop of pure HFC-152a in a horizontal mini-channel*. International Journal of Refrigeration, 2010.33(3):p. 566-577.
120. T.-H. Yen, M. Shoji, F. Takemura, Y. Suzuki and N. Kasagi, *Visualization of convective boiling heat transfer in single microchannels with different shaped cross-sections*. International Journal of Heat and Mass Transfer, 2006.49(21-22):p. 3884-3894.

121. T. Harirchian and S.V. Garimella, *The critical role of channel cross-sectional area in microchannel flow boiling heat transfer*. International Journal of Multiphase Flow, 2009.35(10):p. 904-913.
122. S. Oktay and A. Schmekenbecher, *Method for Forming Heat Sinks on Semiconductor Device Chips*. US.1972. Patent No. 3706127.
123. H. Honda, H. Takamastu and J.J. Wei, *Enhanced Boiling of FC-72 on Silicon Chips With Micro-Pin-Fins and Submicron-Scale Roughness*. Journal of Heat Transfer, 2002.124(2):p. 383-390.
124. H. Honda and J.J. Wei, *Enhanced boiling heat transfer from electronic components by use of surface microstructures*. Experimental Thermal and Fluid Science, 2004.28(2-3):p. 159-169.
125. A. Ma, J. Wei, M. Yuan and J. Fang, *Enhanced flow boiling heat transfer of FC-72 on micro-pin-finned surfaces*. International Journal of Heat and Mass Transfer, 2009.52(13-14):p. 2925-2931.
126. M. Yuan, J. Wei, Y. Xue and J. Fang, *Subcooled flow boiling heat transfer of FC-72 from silicon chips fabricated with micro-pin-fins*. International Journal of Thermal Sciences, 2009.48(7):p. 1416-1422.
127. L. Shou-Shing Hsieh and Chih-Yi, *Subcooled convective boiling in structured surface microchannels*. Journal of Micromechanics and Microengineering, 2010.20(1):p. 015027.
128. G. Hetsroni, D. Mewes, C. Enke, M. Gurevich, A. Mosyak and R. Rozenblit, *Heat transfer to two-phase flow in inclined tubes*. International Journal of Multiphase Flow, 2003.29(2):p. 173-194.
129. M. Misale, G. Guglielmini and A. Priarone, *HFE-7100 pool boiling heat transfer and critical heat flux in inclined narrow spaces*. International Journal of Refrigeration, 2009.32(2):p. 235-245.
130. M.E. Steinke and S.G. Kandlikar, *Control and effect of dissolved air in water during flow boiling in microchannels*. International Journal of Heat and Mass Transfer, 2004.47(8-9):p. 1925-1935.
131. J.C. Chen, *Correlation for Boiling Heat Transfer to Saturated Fluids in Convective Flow*. Industrial & Engineering Chemistry Process Design and Development, 1966.5(3):p. 322-329.
132. M.M. Shah, *Chart correlation for saturated boiling heat transfer: equation and further study*. ASHRAE Trans., 1982.88:p. 185-196.
133. K.E. Gungor and R.H.S. Winterton, *A general correlation for flow boiling in tubes and annuli*. International Journal of Heat and Mass Transfer, 1986.29(3):p. 351-358.
134. S.G. Kandlikar, *A General Correlation for Saturated Two-Phase Flow Boiling Heat Transfer Inside Horizontal and Vertical Tubes*. Journal of Heat Transfer, 1990.112(1):p. 219-228.
135. S.G. Kandlikar and P. Balasubramanian, *An Extension of the Flow Boiling Correlation to Transition, Laminar, and Deep Laminar Flows in Minichannels and Microchannels*. Heat Transfer Engineering, 2004.25(3):p. 86-93.
136. Z. Liu and R.H.S. Winterton, *A general correlation for saturated and subcooled flow boiling in tubes and annuli, based on a nucleate pool boiling equation*. International Journal of Heat and Mass Transfer, 1991.34(11):p. 2759-2766.
137. H.J. Lee and S.Y. Lee, *Heat transfer correlation for boiling flows in small rectangular horizontal channels with low aspect ratios*. International Journal of Multiphase Flow, 2001.27(12):p. 2043-2062.

138. W. Zhang, T. Hibiki and K. Mishima, *Correlation for flow boiling heat transfer in mini-channels*. International Journal of Heat and Mass Transfer, 2004.47(26):p. 5749-5763.
139. S.S. Bertsch, E.A. Groll and S.V. Garimella, *A composite heat transfer correlation for saturated flow boiling in small channels*. International Journal of Heat and Mass Transfer, 2009.52(7-8):p. 2110-2118.
140. G.M. Lazarek and S.H. Black, *Evaporative heat transfer, pressure drop and critical heat flux in a small vertical tube with R-113*. International Journal of Heat and Mass Transfer, 1982.25(7):p. 945-960.
141. J.D. Schwarzkopf, S.G. Penoncello and P. Dutta, *Enhanced boiling heat transfer in mesochannels*. International Journal of Heat and Mass Transfer, 2009.52(25-26):p. 5802-5813.
142. J.R. Thome, V. Dupont and A.M. Jacobi, *Heat transfer model for evaporation in microchannels. Part I: presentation of the model*. International Journal of Heat and Mass Transfer, 2004.47(14-16):p. 3375-3385.
143. V. Dupont, J.R. Thome and A.M. Jacobi, *Heat transfer model for evaporation in microchannels. Part II: comparison with the database*. International Journal of Heat and Mass Transfer, 2004.47(14-16):p. 3387-3401.
144. A. Bejan and A.D. Kraus, *Heat Transfer Handbook*,2003. John Wiley & Sons
145. S.K. Das, S.U.S. Choi, W. Yu and T.Pradeep, *Nanofluids Science and Technology*,2007. WILEY-INTERSCIENCE
146. S.U.S. Choi and J.A. Eastman, *Enhancing thermal conductivity of fluids with nanoparticles*. International mechanical engineering congress and exhibition, San Francisco, CA (United States) 1995.p. 8.
147. J.A. Eastman, S.U.S. Choi, S. Li, W. Yu and L.J. Thompson, *Anomalously increased effective thermal conductivities of ethylene glycol-based nanofluids containing copper nanoparticles* Applied Physics Letters, 2001.78(6):p. 718-720.
148. S. Lee, S.U.S. Choi, S. Li and J.A. Eastman, *Measuring Thermal Conductivity of Fluids Containing Oxide Nanoparticles*. Journal of Heat Transfer, 1999.121(2):p. 280-289.
149. X. Wang, X. Xu, S.U.S. Choi, T. Energy and U. Purdue, *Thermal conductivity of nanoparticle-fluid mixture*. Journal Name: J. Thermophys. Heat Transf.; Journal Volume: 13; Journal Issue: 13 ; Oct.-Dec. 1999, 1999.p. Medium: X; Size: 474-80.
150. Y. Xuan and W. Roetzel, *Conceptions for heat transfer correlation of nanofluids*. International Journal of Heat and Mass Transfer, 2000.43(19):p. 3701-3707.
151. S.U.S. Choi, Z.G. Zhang, W. Yu, F.E. Lockwood and E.A. Grulke, *Anomalous thermal conductivity enhancement in nanotube suspensions*. Applied Physics Letters, 2001.79(14):p. 2252-2254.
152. H. Xie, J. Wang, T. Xi, Y. Liu and F. Ai, *Dependence of the thermal conductivity of nanoparticle-fluid mixture on the base fluid*. Journal of Materials Science Letters, 2002.21(19):p. 1469-1471.
153. S. Kumar Das, N. Putra, P. Thiesen and W. Roetzel, *Temperature Dependence of Thermal Conductivity Enhancement for Nanofluids*. Journal of Heat Transfer, 2003.125(4):p. 567-574.
154. Y.J. Hwang, Y.C. Ahn, H.S. Shin, C.G. Lee, G.T. Kim, H.S. Park and J.K. Lee, *Investigation on characteristics of thermal conductivity enhancement of nanofluids*. Current Applied Physics, 2006.6(6):p. 1068-1071.
155. Garg, J, Poudel, B, Chiesa, M, Gordon, B. J, Ma, J. J, Wang, B. J, Ren, F. Z, Kang, T. Y, Ohtani, H, Nanda, J, McKinley, H. G, Chen and G, *Enhanced*

thermal conductivity and viscosity of copper nanoparticles in ethylene glycol nanofluid. Melville, NY, ETATS-UNIS,2008. American Institute of Physics
156. J.-H. Lee, K.S. Hwang, S.P. Jang, B.H. Lee, J.H. Kim, S.U.S. Choi and C.J. Choi, *Effective viscosities and thermal conductivities of aqueous nanofluids containing low volume concentrations of Al2O3 nanoparticles*. International Journal of Heat and Mass Transfer, 2008.51(11-12):p. 2651-2656.
157. X.F. Li, D.S. Zhu, X.J. Wang, N. Wang, J.W. Gao and H. Li, *Thermal conductivity enhancement dependent pH and chemical surfactant for Cu-H2O nanofluids*. Thermochimica Acta, 2008.469(1-2):p. 98-103.
158. S.M.S. Murshed, K.C. Leong and C. Yang, *Investigations of thermal conductivity and viscosity of nanofluids*. International Journal of Thermal Sciences, 2008.47(5):p. 560-568.
159. J. Wensel, B. Wright, D. Thomas, W. Douglas, B. Mannhalter, W. Cross, H. Hong, J. Kellar, P. Smith and W. Roy, *Enhanced thermal conductivity by aggregation in heat transfer nanofluids containing metal oxide nanoparticles and carbon nanotubes*. Applied Physics Letters, 2008.92(2):p. 023110-023110-3.
160. Y. Xuan and Q. Li, *Heat transfer enhancement of nanofluids*. International Journal of Heat and Fluid Flow, 2000.21(1):p. 58-64.
161. Patel, E. Hrishikesh, Das, K. Sarit, Sundararajan, T, N. Sreekumaran, A, George, Beena, Pradeep and T, *Thermal conductivities of naked and monolayer protected metal nanoparticle based nanofluids: Manifestation of anomalous enhancement and chemical effects*. Melville, NY, ETATS-UNIS,2003. American Institute of Physics
162. T.-K. Hong, H.-S. Yang and C.J. Choi, *Study of the enhanced thermal conductivity of Fe nanofluids*. Journal of Applied Physics, 2005.97(6):p. 064311-064311-4.
163. H. Zhu, C. Zhang, S. liu, Y. Tang and Y. Yin, *Effects of nanoparticle clustering and alignment on thermal conductivities of Fe_3O_4aqueous nanofluids*. 2006.89.
164. K.S. Hwang, S.P. Jang and S.U.S. Choi, *Flow and convective heat transfer characteristics of water-based Al2O3 nanofluids in fully developed laminar flow regime*. International Journal of Heat and Mass Transfer, 2009.52(1-2):p. 193-199.
165. U. Rea, T. McKrell, L.-W. Hu and J. Buongiorno, *Laminar convective heat transfer and viscous pressure loss of alumina-water and zirconia-water nanofluids*. International Journal of Heat and Mass Transfer, 2009.52(7-8):p. 2042-2048.
166. W. Duangthongsuk and S. Wongwises, *An experimental study on the heat transfer performance and pressure drop of TiO2-water nanofluids flowing under a turbulent flow regime*. International Journal of Heat and Mass Transfer, 2010.53(1-3):p. 334-344.
167. W. Williams, J. Buongiorno and L.-W. Hu, *Experimental Investigation of Turbulent Convective Heat Transfer and Pressure Loss of Alumina/Water and Zirconia/Water Nanoparticle Colloids (Nanofluids) in Horizontal Tubes*. Journal of Heat Transfer, 2008.130(4):p. 042412.
168. M. Chopkar, A. Das, I. Manna and P. Das, *Pool boiling heat transfer characteristics of ZrO_2–water nanofluids from a flat surface in a pool*. Heat and Mass Transfer, 2008.44(8):p. 999-1004.
169. V. Trisaksri and S. Wongwises, *Nucleate pool boiling heat transfer of TiO_2-R141b nanofluids*. International Journal of Heat and Mass Transfer, 2009.52(5-6):p. 1582-1588.

170. K.-J. Park and D. Jung, *Enhancement of nucleate boiling heat transfer using carbon nanotubes*. International Journal of Heat and Mass Transfer, 2007.50(21-22):p. 4499-4502.
171. K.-J. Park and D. Jung, *Boiling heat transfer enhancement with carbon nanotubes for refrigerants used in building air-conditioning*. Energy and Buildings, 2007.39(9):p. 1061-1064.
172. Y. Li, J.e. Zhou, S. Tung, E. Schneider and S. Xi, *A review on development of nanofluid preparation and characterization*. Powder Technology, 2009.196(2):p. 89-101.
173. K.V. Sharma, L.S. Sundar and P.K. Sarma, *Estimation of heat transfer coefficient and friction factor in the transition flow with low volume concentration of Al2O3 nanofluid flowing in a circular tube and with twisted tape insert*. International Communications in Heat and Mass Transfer, 2009.36(5):p. 503-507.
174. L. Dong and Y. Leyuan, *Single-Phase Thermal Transport of Nanofluids in a Minichannel*. Journal of Heat Transfer, 2011.133(3):p. 031009.
175. Y. Xuan and Q. Li, *Investigation on Convective Heat Transfer and Flow Features of Nanofluids*. Journal of Heat Transfer, 2003.125(1):p. 151-155.
176. S.M. Fotukian and M. Nasr Esfahany, *Experimental study of turbulent convective heat transfer and pressure drop of dilute CuO/water nanofluid inside a circular tube*. International Communications in Heat and Mass Transfer, 2010.37(2):p. 214-219.
177. Q. Li and Y. Xuan, *Convective heat transfer and flow characteristics of Cu-water nanofluid*. Science in China Series E: Technological Sciences, 2002.45(4):p. 408-416.
178. K.S. Pawan, T. Sundararajan and K.D. Sarit, *Hydrodynamic Study of Nanofluids in Microchannel*. ASME Conference Proceedings, 2009.2009(43895):p. 467-473.
179. P. Vassallo, R. Kumar and S. D'Amico, *Pool boiling heat transfer experiments in silica-water nano-fluids*. International Journal of Heat and Mass Transfer, 2004.47(2):p. 407-411.
180. S.M. You, J.H. Kim and K.H. Kim, *Effect of nanoparticles on critical heat flux of water in pool boiling heat transfer*. Applied Physics Letters, 2003.83(16):p. 3374-3376.
181. I.C. Bang and H.C. Soon, *Boiling heat transfer performance and phenomena of Al2O3-water nano-fluids from a plain surface in a pool*. International Journal of Heat and Mass Transfer, 2005.48(12):p. 2407-2419.
182. D. Milanova and R. Kumar, *Role of ions in pool boiling heat transfer of pure and silica nanofluids*. APPLIED PHYSICS LETTERS, 2005.87(233107):p. 3 pages.
183. H. Kim, J. Kim and M.H. Kim, *Effect of nanoparticles on CHF enhancement in pool boiling of nano-fluids*. International Journal of Heat and Mass Transfer, 2006.49(25-26):p. 5070-5074.
184. S.J. Kim, I.C. Bang, J. Buongiorno and L.W. Hu, *Surface wettability change during pool boiling of nanofluids and its effect on critical heat flux*. International Journal of Heat and Mass Transfer, 2007.50(19-20):p. 4105-4116.
185. S.K. Das, N. Putra and W. Roetzel, *Pool boiling characteristics of nano-fluids*. International Journal of Heat and Mass Transfer, 2003.46(5):p. 851-862.
186. S. Witharana, *Boiling of refrigerants on enhanced surfaces and boiling of nanofluids*. Ph.D., Royal Institute of Technology. 2003.

187. Z.-h. Liu, J.-g. Xiong and R. Bao, *Boiling heat transfer characteristics of nanofluids in a flat heat pipe evaporator with micro-grooved heating surface*. International Journal of Multiphase Flow, 2007.33(12):p. 1284-1295.
188. S. Vafaei and D. Wen, *Critical Heat Flux (CHF) of Subcooled Flow Boiling of Alumina Nanofluids in a Horizontal Microchannel*. Journal of Heat Transfer, 2010.132(10):p. 102404-7.
189. T.I. Kim, Y.H. Jeong and S.H. Chang, *An experimental study on CHF enhancement in flow boiling using Al2O3 nano-fluid*. International Journal of Heat and Mass Transfer, 2010.53(5-6):p. 1015-1022.
190. K. Henderson, Y.-G. Park, L. Liu and A.M. Jacobi, *Flow-boiling heat transfer of R-134a-based nanofluids in a horizontal tube*. International Journal of Heat and Mass Transfer, 2010.53(5-6):p. 944-951.
191. C. Höhmann and P. Stephan, *Microscale temperature measurement at an evaporating liquid meniscus*. Experimental Thermal and Fluid Science, 2002.26(2-4):p. 157-162.
192. J.C. Barber, *Hydrodynamics, Heat Transfer and Flow Boiling Instabilities in Microchannels*. Doctor of Philosophy, University of Edinburgh, U.K.and Université d'Aix-Marseille I, France. 2009.
193. I. Mudawar and D.E. Maddox, *Enhancement of Critical Heat Flux From High Power Microelectronic Heat Sources in a Flow Channel*. Journal of Electronic Packaging, 1990.112(3):p. 241-248.
194. L. Consolini, *CONVECTIVE BOILING HEAT TRANSFER IN A SINGLE MICRO-CHANNEL*. M.Sc., University of Illinois. 2008.
195. C.L. Yaws, *Chemical Properties Handbook*, McGraw-Hill.1999.
196. R. Butt, *Introduction to Numerical Analysis Using MATLAB*,2008. MATHEMATICS SERIES
197. L. Malter and D.B. Langmuir, *Resistance, Emissivities and Melting Point of Tantalum*. Physical Review, 1939.55(8):p. 743-747.
198. R.D. Allen, L.F. Glasier and P.L. Jordan, *Spectral Emissivity, Total Emissivity, and Thermal Conductivity of Molybdenum, Tantalum, and Tungsten above 2300°K*. Journal of Applied Physics, 1960.31(8):p. 1382-1387.
199. N.D. Milošević, G.S. Vuković, D.Z. Pavičić and K.D. Maglić, *Thermal Properties of Tantalum Between 300 and 2300 K*. International Journal of Thermophysics, 1999.20(4):p. 1129-1136.
200. R.K. Shah and A.L. London, *Laminar flow forced convection in ducts: a source book for compact heat exchanger analytical data*,1978. Academic Press. New York.San Francisco. London
201. M.Thirumaleshwar, *Transient Heat Conduction*. Fundamentals of Heat and Mass Transfer, INCLUDES MATHCAD-BASED SOLUTIONS TO PROBLEMS, Dorling Kindersley (India) Pvt. Ltd.,licenses of Pearson Eduacation in South Asia. 2006.p. 269.
202. J. R.Taylor, *An introduction to error analysis*,1997. University Science Books
203. K. Sefiane, V.V. Wadekar, S. Kakaç, L.L. Vasiliev, Y. Bayazitoğlu and Y. Yener, *Role of Microscale Heat Transfer in Understanding Flow Boiling Heat Transfer and Its Enhancement Microscale Heat Transfer Fundamentals and Applications*, Springer Netherlands. 2005. 193:p. 429-444.
204. S. Johannes, T.F.I.Y.I.C. James P. Hartnett and A.G. George, *Boiling heat transfer and bubble dynamics in microgravity*. Advances in Heat Transfer, Elsevier. 2001. Volume 35:p. 57-172.

205. I. Papautsky, T. Ameel and A.B. Frazier, *A review of laminar single-phase flow in microchannels*. 2001 ASME International Mechanical Engineering Congress and Exposition, New York 2001.
206. G.L. Morini, *Single-phase convective heat transfer in microchannels: a review of experimental results*. International Journal of Thermal Sciences, 2004.43(7):p. 631-651.
207. M.E. Steinke and S.G. Kandlikar, *Single-phase liquid friction factors in microchannels*. International Journal of Thermal Sciences, 2006.45(11):p. 1073-1083.
208. J. Harley, H. Bau, J.N. Zemel and V. Dominko, *Fluid flow in micron and submicron size channels*. Micro Electro Mechanical Systems, 1989, Proceedings, An Investigation of Micro Structures, Sensors, Actuators, Machines and Robots. IEEE 1989.p. 25-28.
209. M.M. Rahman and F. Gui, *Experimental measurements of fluid flow and heat transfer in microchannel cooling passages in a chip substrate*. The ASME International Electronics Packaging Conference, Binghamton, NY; USA 1993. Vol. 29 Sept.-02 Oct. 1993:p. 685-692.
210. X.F. Peng and G.P. Peterson, *Convective heat transfer and flow friction for water flow in microchannel structures*. International Journal of Heat and Mass Transfer, 1996.39(12):p. 2599-2608.
211. G.M. Mala and D. Li, *Flow characteristics of water in microtubes*. International Journal of Heat and Fluid Flow, 1999.20(2):p. 142-148.
212. M.M. Rahman, *Measurements of heat transfer in microchannel heat sinks*. International Communications in Heat and Mass Transfer, 2000.27(4):p. 495-506.
213. J. Pfahler, J. Harley, H. Bau and J. Zemel, *Liquid transport in micron and submicron channels*. Sensors and Actuators A: Physical, 1989.22(1-3):p. 431-434.
214. B. X.Wang and X. F.Peng, *Experimental investigation on liquid forced-convection heat transfer through microchannels*. International Journal of Heat and Mass Transfer, 1994.37:p. 73-82.
215. X.F. Peng and G.P. Peterson, *The effect of thermofluid and geometrical parameters on convection of liquids through rectangular microchannels*. International Journal of Heat and Mass Transfer, 1995.38(4):p. 755-758.
216. X.F. Peng and G.P. Peterson, *Forced convection heat transfer of single-phase binary mixtures through microchannels*. Experimental Thermal and Fluid Science, 1996.12(1):p. 98-104.
217. P.-X. Jiang, M.-H. Fan, G.-S. Si and Z.-P. Ren, *Thermal-hydraulic performance of small scale micro-channel and porous-media heat-exchangers*. International Journal of Heat and Mass Transfer, 2001.44(5):p. 1039-1051.
218. A. Bucci, G.P. Celata, M. Cumo, E. Serra and G. Zummo, *Water Single-Phase Fluid Flow and Heat Transfer in Capillary Tubes*. ASME Conference Proceedings, 2003.2003(36673):p. 319-326.
219. F.M. White, *Fluid Mechanics*,1986. McGraw-Hill
220. R.K. Shah and A.L. London, *Laminar flow forced convection in ducts : a source book for compact heat exchanger analytical data*. New York,1978. Academic Press
221. H.C. Brinkman, *The Viscosity of Concentrated Suspensions and Solutions*. The Journal of Chemical Physics, 1952.20(4):p. 571.

222. X.F. Peng, G.P. Peterson and B.X. Wang, *Frictional flow characteristics of water flowing through rectangular microchannels* Experimental Heat Transfer, 1994.7(4):p. 249-264.
223. V.P. Carey, *Liquid-Vapor Phase-Change Phenomena An Introduction to the Thermophysics of Vaporization and Condensation Processes in Heat Transfer Equipment*,2008. Taylor&Francis
224. Y.-Y. Hsu and R.W. Graham, *Transport processes in boiling and two-phase systems, including near-critical fluids*,1986. American Nuclear Society (La Grange Park, Ill., USA)
225. S.M. Ghiaasiaan, *Two-Phase Flow, Boiling, and Condensation: In Conventional and Miniature Systems*,2008. New York : Cambridge University Press
226. V.P. Carey, *Heterogeneous nucleation and bubble growth in liquids*. Liquid-Vapor Phase-Change Phenomena An Introduction to the Thermophysics of Vaporization and Condensation Processes in Heat Transfer Equipment, Taylor&Francis. 2008.p. Page 221.
227. H.C. Lee, J. Kim, B.D. Oh and M.H. Kim, *Single bubble growth in saturated pool boiling of binary mixtures*. International Journal of Multiphase Flow, 2004.30(6):p. 697-710.
228. C.E. Brennen, *Cavitation and Bubble Dynamics*,1995. Oxford University Press, New York
229. M. Potash Jr and P.C. Wayner Jr, *Evaporation from a two-dimensional extended meniscus*. International Journal of Heat and Mass Transfer, 1972.15(10):p. 1851-1863.
230. K.D. Hemanth, V.G. Suresh and Y.M. Jayathi, *Microscale Temperature Measurements Near the Triple Line of an Evaporating Thin Liquid Film*. Journal of Heat Transfer, 2009.131(6):p. 061501.
231. P. Stephan and J. Hammer, *A new model for nucleate boiling heat transfer*. Heat and Mass Transfer, 1994.30(2):p. 119-125.
232. K. Stephan, *Influence of dispersion forces on phase equilibria between thin liquid films and their vapour*. International Journal of Heat and Mass Transfer, 2002.45(24):p. 4715-4725.
233. K. Park, K.-J. Noh and K.-S. Lee, *Transport phenomena in the thin-film region of a micro-channel*. International Journal of Heat and Mass Transfer, 2003.46(13):p. 2381-2388.
234. H. Wang, Z. Pan and Z. Chen, *Thin-liquid-film evaporation at contact line*. Frontiers of Energy and Power Engineering in China, 2009.3(2):p. 141-151.
235. G. Preiss and J.P.C. Wayner, *Evaporation From a Capillary Tube*. Journal of Heat Transfer, 1976.98(2):p. 178-181.
236. F.J. Renk and J.P.C. Wayner, *An Evaporating Ethanol Meniscus---Part I: Experimental Studies*. Journal of Heat Transfer, 1979.101(1):p. 55-58.
237. F.J. Renk and J.P.C. Wayner, *An Evaporating Ethanol Meniscus---Part II: Analytical Studies*. Journal of Heat Transfer, 1979.101(1):p. 59-62.
238. R. Cook, C.Y. Tung and J.P.C. Wayner, *Use of Scanning Microphotometer to Determine the Evaporative Heat Transfer Characteristics of the Contact Line Region*. Journal of Heat Transfer, 1981.103(2):p. 325-330.
239. J.P.C. Wayner, C.Y. Tung, M. Tirumala and J.H. Yang, *Experimental Study of Evaporation in the Contact Line Region of a Thin Film of Hexane*. Journal of Heat Transfer, 1985.107(1):p. 182-189.

240. S. DasGupta, J.A. Schonberg and J.P.C. Wayner, *Investigation of an Evaporating Extended Meniscus Based on the Augmented Young--Laplace Equation*. Journal of Heat Transfer, 1993.115(1):p. 201-208.
241. J.P.C. Wayner, *Thermal and Mechanical Effects in the Spreading of a Liquid Film Due to a Change in the Apparent Finite Contact Angle*. Journal of Heat Transfer, 1994.116(4):p. 938-945.
242. S. DasGupta, I.Y. Kim and J.P.C. Wayner, *Use of the Kelvin-Clapeyron Equation to Model an Evaporating Curved Microfilm*. Journal of Heat Transfer, 1994.116(4):p. 1007-1015.
243. R.H. Nilson, S.W. Tchikanda, S.K. Griffiths and M.J. Martinez, *Steady evaporating flow in rectangular microchannels*. International Journal of Heat and Mass Transfer, 2006.49(9-10):p. 1603-1618.
244. A.-H. Liu, J.P.C. Wayner and J.L. Plawsky, *Image scanning ellipsometry for measuring nonuniform film thickness profiles*. Appl. Opt., 1994.33(7):p. 1223-1229.
245. L. Zheng, Y.-X. Wang, J.L. Plawsky and P.C. Wayner, *Accuracy of measurements of curvature and apparent contact angle in a constrained vapor bubble heat exchanger*. International Journal of Heat and Mass Transfer, 2002.45(10):p. 2021-2030.
246. L. Zheng, J.L. Plawsky, J.P.C. Wayner and S. DasGupta, *Stability and Oscillations in an Evaporating Corner Meniscus*. Journal of Heat Transfer, 2004.126(2):p. 169-178.
247. S.S. Panchamgam, J.L. Plawsky and J.P.C. Wayner, *Spreading Characteristics and Microscale Evaporative Heat Transfer in an Ultrathin Film Containing a Binary Mixture*. Journal of Heat Transfer, 2006.128(12):p. 1266-1275.
248. C. Buffone and K. Sefiane, *IR measurements of interfacial temperature during phase change in a confined environment*. Experimental Thermal and Fluid Science, 2004.29(1):p. 65-74.
249. C. Buffone and K. Sefiane, *Temperature measurement near the triple line during phase change using thermochromic liquid crystal thermography*. Experiments in Fluids, 2005.39(1):p. 99-110.
250. F. Chauvet, S. Cazin, P. Duru and M. Prat, *Use of infrared thermography for the study of evaporation in a square capillary tube*. International Journal of Heat and Mass Transfer, 2010.53(9-10):p. 1808-1818.
251. R.-H. Chen, T.X. Phuoc and D. Martello, *Surface tension of evaporating nanofluid droplets*. International Journal of Heat and Mass Transfer, 2011.54(11-12):p. 2459-2466.
252. S. Vafaei, T. Borca-Tasciuc, M.Z. Podowski, A. Purkayastha, G. Ramanath and P.M. Ajayan, *Effect of nanoparticles on sessile droplet contact angle*. Nanotechnology, 2006.17(10):p. 2523-2527.
253. A.M. Munshi, V.N. Singh, M. Kumar and J.P. Singh, *Effect of nanoparticle size on sessile droplet contact angle*. Journal of Applied Physics, 2008.103(8):p. 084315.
254. K. Sefiane, J. Skilling and J. MacGillivray, *Contact line motion and dynamic wetting of nanofluid solutions*. Advances in Colloid and Interface Science, 2008.138(2):p. 101-120.
255. J.R. Moffat, K. Sefiane and M.E.R. Shanahan, *Effect of TiO2 Nanoparticles on Contact Line Stick−Slip Behavior of Volatile Drops*. The Journal of Physical Chemistry B, 2009.113(26):p. 8860-8866.

256. S. Vafaei and D. Wen, *Flow boiling heat transfer of alumina nanofluids in single microchannels and the roles of nanoparticles*. Journal of Nanoparticle Research, 2010.p. 1-11.
257. G. Hetsroni, A. Mosyak and Z. Segal, *Nonuniform temperature distribution in electronic devices cooled by flow in parallel microchannels*. Components and Packaging Technologies, IEEE Transactions on, 2001.24(1):p. 16-23.
258. W. Qu and I. Mudawar, *Measurement and prediction of pressure drop in two-phase micro-channel heat sinks*. International Journal of Heat and Mass Transfer, 2003.46(15):p. 2737-2753.
259. D. Bogojevic, K. Sefiane, A.J. Walton, H. Lin and G. Cummins, *Two-phase flow instabilities in a silicon microchannels heat sink*. International Journal of Heat and Fluid Flow, 2009.30(5):p. 854-867.
260. A.E. Bergles and S.G. Kandlikar, *On the Nature of Critical Heat Flux in Microchannels*. ASME Conference Proceedings, 2003.2003(37149):p. 701-707.
261. A. Kawahara, P.M.Y. Chung and M. Kawaji, *Investigation of two-phase flow pattern, void fraction and pressure drop in a microchannel*. International Journal of Multiphase Flow, 2002.28(9):p. 1411-1435.
262. OriginLab, Origin Reference v8.
263. Y. Wang, K. Sefiane and R. Bennacer, *Investigation of boiling and bubble confinement in a high aspect ratio micro-channel*. Applied Thermal Engineering, 2010.In Press, Corrected Proof.
264. http://en.wikipedia.org/wiki/Coefficient_of_variation.
265. L. Cheng and D. Mewes, *Review of two-phase flow and flow boiling of mixtures in small and mini channels*. International Journal of Multiphase Flow, 2006.32(2):p. 183-207.
266. S. Lin, K. Sefiane and J.R.E. Christy, *Prospects of confined flow boiling in thermal management of microsystems*. Applied Thermal Engineering, 2002.22(7):p. 825-837.
267. C.P. Wong, K.-S. Moon, Y. Li, Y. Joshi, X. Wei, B. Dang and K. Kota, *Some Aspects of Microchannel Heat Transfer*. Nano-Bio- Electronic, Photonic and MEMS Packaging, Springer US. 2010.p. 431-477.
268. L. Consolini and J.R. Thome, *Micro-channel flow boiling heat transfer of R-134a, R-236fa, and R-245fa*. Microfluidics and Nanofluidics, 2009.6(6):p. 731-746.
269. H.K. Kim and S.I. Oh, *Evaluation of heat transfer coefficient during heat treatment by inverse analysis*. Journal of Materials Processing Technology, 2001.112(2-3):p. 157-165.
270. B. Sumith, F. Kaminaga and K. Matsumura, *Saturated flow boiling of water in a vertical small diameter tube*. Experimental Thermal and Fluid Science, 2003.27(7):p. 789-801.
271. R.P. Madding, *Emissivity measurement and temperature correction accuracy considerations*. Part of the SPIE Conference on Thermosense XXI . Orlando, Florida, April,1999, SPIE, 1999. Vol. 3700:p. 393-401.

Appendix A Channel surface emissivity and how the infrared camera works

The radiation that impinged on the IR camera lens comes from three different sources, as in Figure A-1: (1) radiation from the surroundings which has been reflected onto the object surface; (2) radiation from the target object. Meanwhile, both of these radiation components are attenuated when passing through the atmosphere (as illustrated in Figure A-1, (3)) between the lens and the target object. Therefore, temperature measurement of the object could only be obtained based on the following parameters:

One of the commonly performed methods for measuring the emissivity of opaque targets (Madding [271]) is to rise the target into two different and known temperatures, and the emissivity can be determined as:

$$\varepsilon = \frac{T_{\mathrm{IR1}} - T_{\mathrm{IR2}}}{T_1 - T_2} \tag{A-1}$$

where T_{IR1} and T_{IR2} are the infrared camera temperature measurements of the known temperatures T_1 and T_2.

The micro-channel segment was attached on a flexible heater (OMEGA® SRFR-4/5 Round Silicone Rubber Heater) and was maintained at two temperature levels by adjusting the power supply of the heater. An accurate thermocouple was inserted between the heater and the channel segment to acquire the actual temperatures whilst the IR camera was recording the temperature profile across the channel surface. The emissivity of the channel wall could be estimated according to eq. (A-1). In all the tests, emissivity fell in the range of 0.76 – 0.84, therefore an average 0.80 was set as the channel wall emissivity.

The other parameters which are essential for temperature measurements includes the object distance to the front lens of the scanner, the relative humidity of the atmosphere between the object and the scanner and the reflected ambient temperature, which is the mean value of the temperature surrounding the object. The reflected ambient temperature is considered to be the same as the atmosphere temperature.

It is important that the above object parameters (including the channel emissivity, and the channel distance from the IR camera lens) and the atmospheric conditions

(humidity and temperature of the atmosphere) are correctly input into the IR camera software ThermaCAM Researcher Professional®.

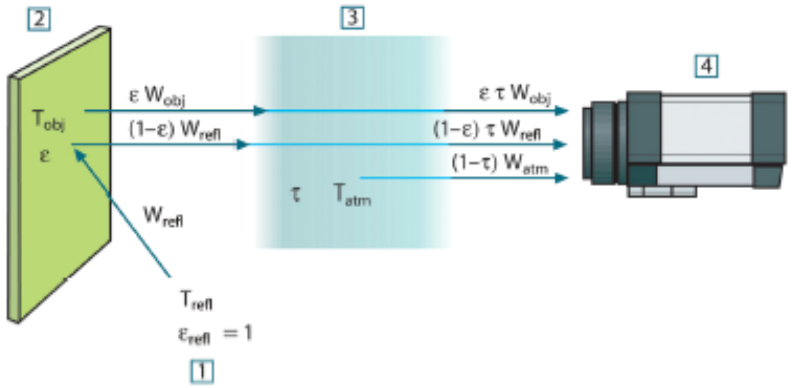

Figure A-1. Schematic drawing of the thermographic Infrared camera measurement mechnisms

Appendix B Experimental setup components calibrations

B.1 Syringe pump calibration

The syringe pump was calibrated by comparing the desired flow rate with the measured actual flow rate. The pump was set to run at a certain volume flow rate, meanwhile the time it took for the pump to deliver a known volume of liquid was recorded to calculate the actual volume flow rate. Data were collected in Table B-1, as can be seen that even there was uncertainty for the timing (±0.01 s), the averaged accuracy for syringe pump volume flow rate was still as high as 0.996. In the present study, the pump flow rate uncertainty was neglected and all the volume flow rates were the desired values set on the syringe pump. Figure B-1 shows the measured flow rate and set flow rate comparison and good agreement is achieved.

Table B-1. Syringe pump calibration data and the averaged accuracy

Volume (ml)	time (s)	measured flow rate ($ml \cdot min^{-1}$)	desired flow rate ($ml \cdot min^{-1}$)	volume flow rate accuracy	averaged accuracy
50	41.89	71.6161375	72	0.994668576	0.996567
50	50.29	59.6540068	60	0.994233446	
50	60.28	49.7677505	50	0.99535501	
50	75.04	39.978678	40	0.999466951	
50	100.28	29.9162345	30	0.997207818	
50	149.82	20.0240288	20	1.001201442	
100	41.9	143.198091	144	0.994431185	
100	50.3	119.284294	120	0.994035785	
100	60.09	99.8502247	100	0.998502247	

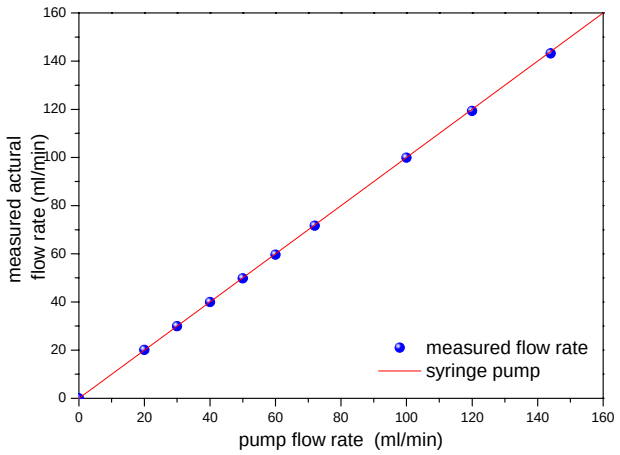

Figure B-1. Comparison between the syringe pump set volume flow rate and the actually measured flow rate

B.2 Pressure transducer calibration

Pressure transducer generates an electrical signal as a function of the measured pressure. In the present study, the voltage signal was obtained via NI® Data Acquisition System. In order to reveal the pressure values, a simplified calibration system (see Figure B-2 (a)) was built to convert the voltage back to pressure. A syringe was connected to a manometer (SPER SCIENTIFIC® Model 840083, Figure B-2 (b)) and the pressure transducer at the same time. The manometer has an accuracy of 0.3% of full scale at 25°C and a response time of 0.5 s. First of all, the syringe was fully charged with air. Then all the connections were highly sealed to avoid leakage. The leakproofness was good enough to maintain steady pressures by compressing the air in the syringe into smaller volumes. Then the synchronous voltages were recorded. Finally, the measured pressure versus voltage curve was linearly fitted as in Figure B-3 (a) and (b). The fitting equations for inlet and outlet pressure transducers were used as the functions in the Labview program to obtain pressure data.

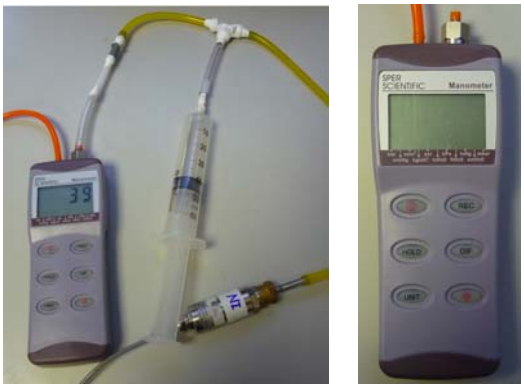

(a) (b)

Figure B-2. (a) Pressure transducer calibration system; (b) manometer used for pressure calibration: SPER SCIENTIFIC® Model 840083

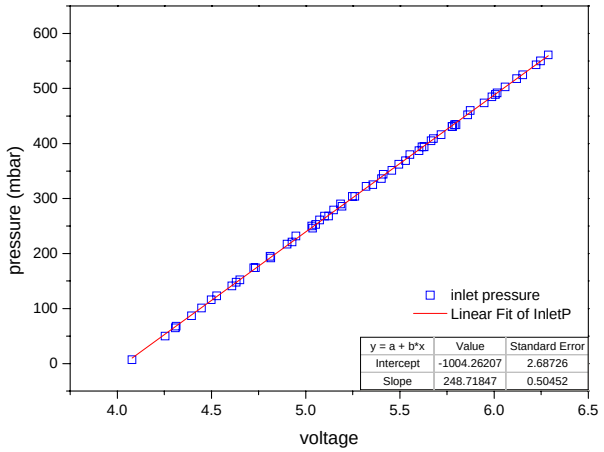

(a)

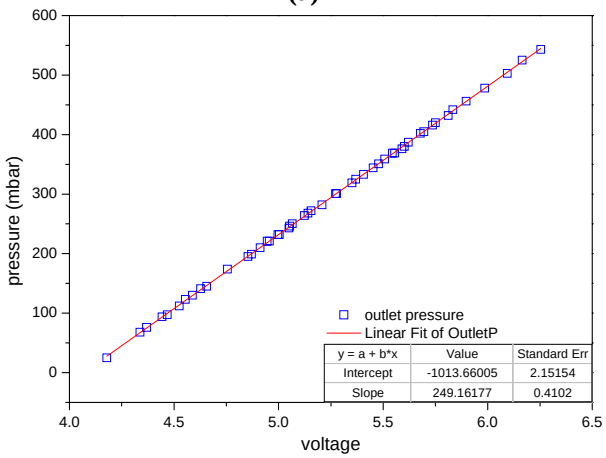

(b)

Figure B-3. Pressure transducer calibration charts: (a) inlet pressure transducer, (b) outlet pressure transducer

Appendix C Labview software interface and block diagram

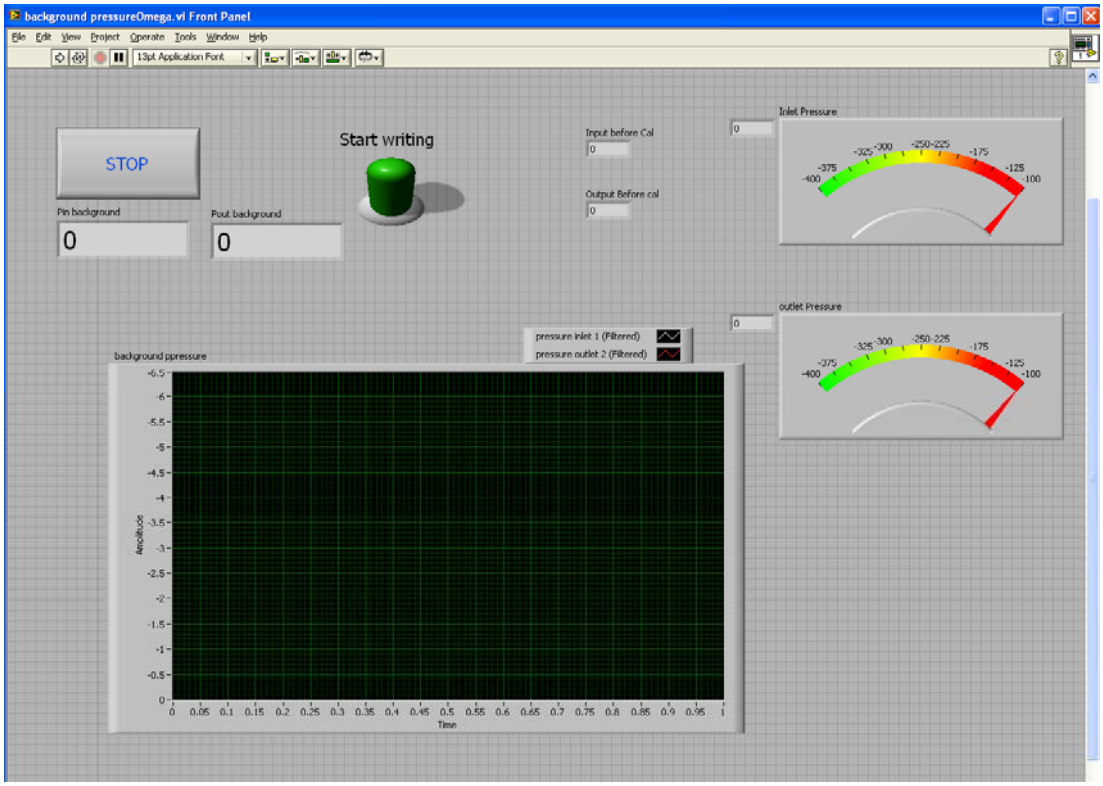

(a)

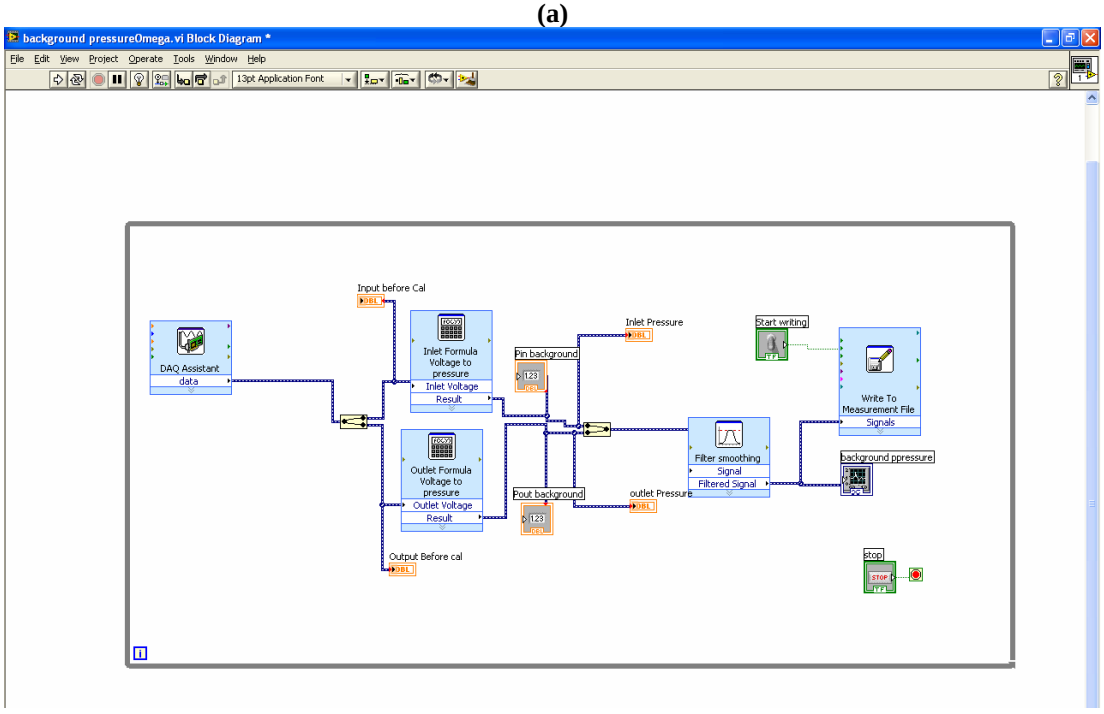

(b)

Figure C-1. Offset pressure measurements (a) Labview software interface, (b) Labview block diagram

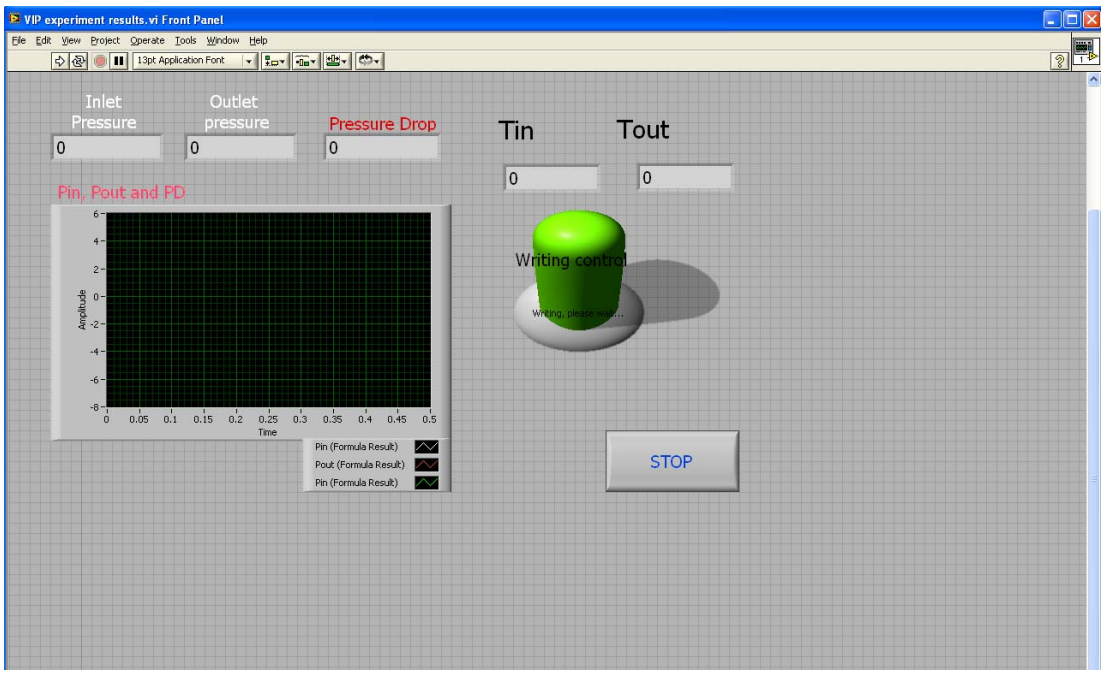

(a)

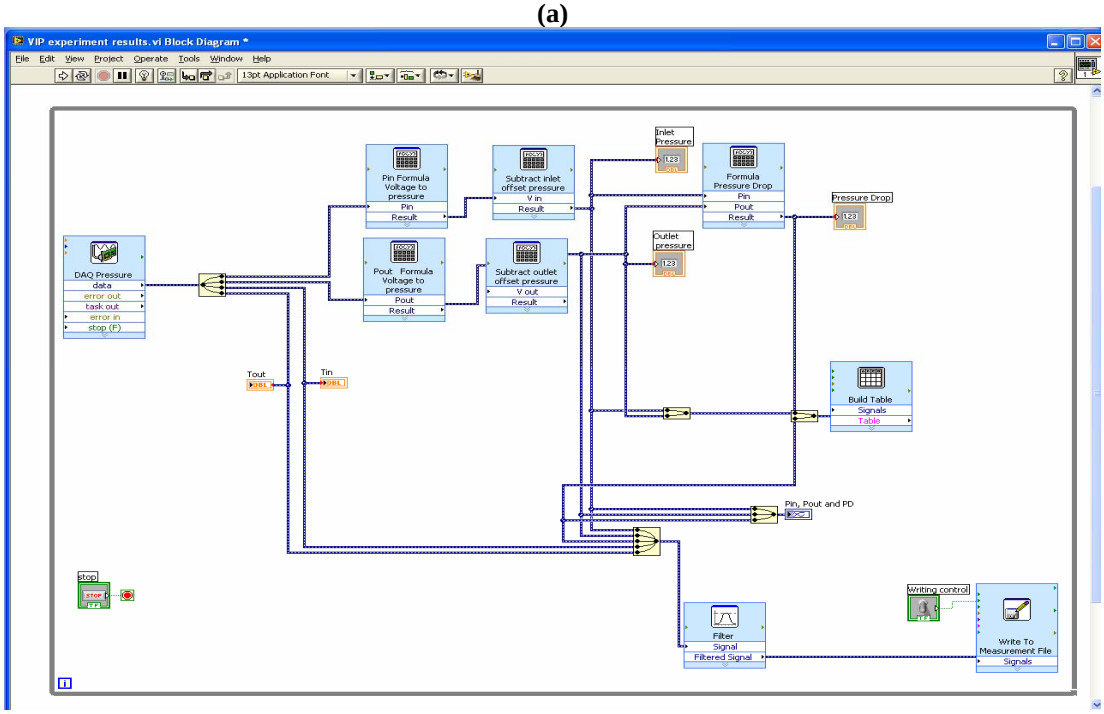

(b)

Figure C-2. Pressure and temperature measurements (a) Labview software interface, (b) Labview block diagram

Appendix D Vapour dynamic results

D.1 Single bubble growth between two parallel plates

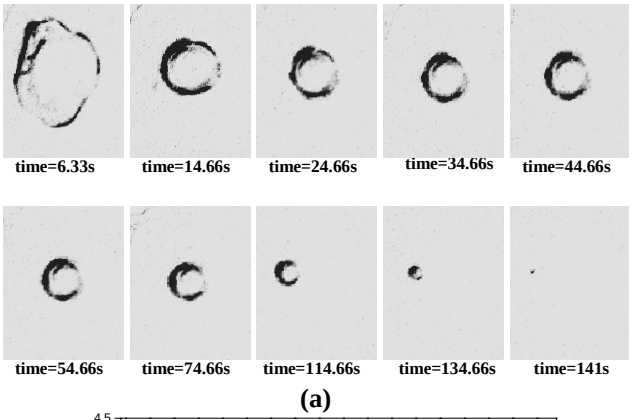

(a)

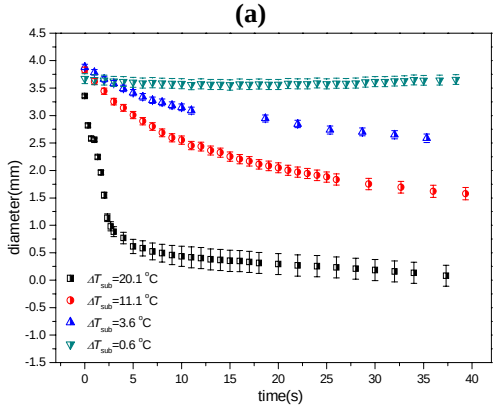

(b)

Figure D-1. (a) n-pentane vapour bubble shrinks between subcooled plates, $\Delta T_{sub} = -11.1\,°C$, plates gap = 114 μm, (b) bubble diameter measurements, plates gap = 114 μm

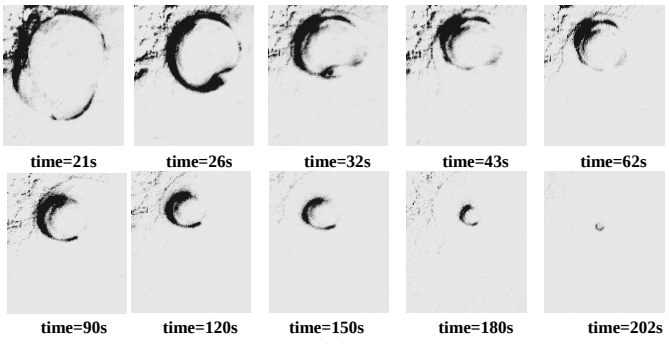

(a)

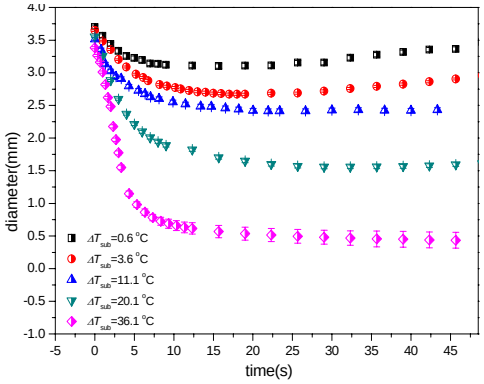

(b)

Figure D-2. (a) FC-72 vapour bubble shrinks between subcooled plates, $\Delta T_{sub} = -36.1\,°C$, plates gap = 114 μm, (b) bubble diameter measurements, plates gap = 114 μm

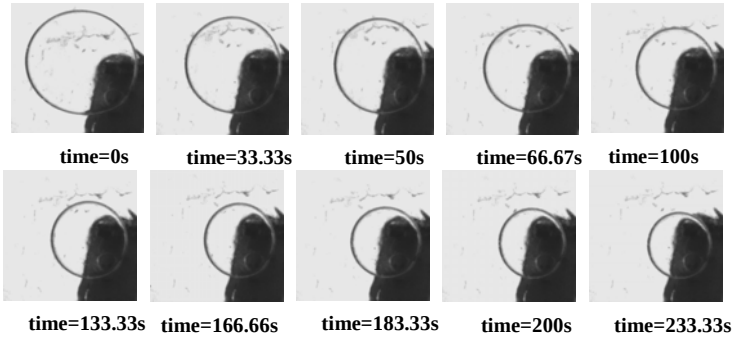

(a)

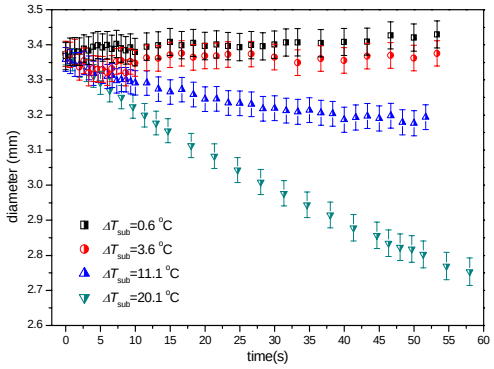

(b)

Figure D-3. (a) n-pentane vapour bubble shrinks between subcooled plates, $\Delta T_{sub} = 20.1\,°C$, plates gap = 250 μm, (b) bubble diameter measurements, plates gap = 250 μm

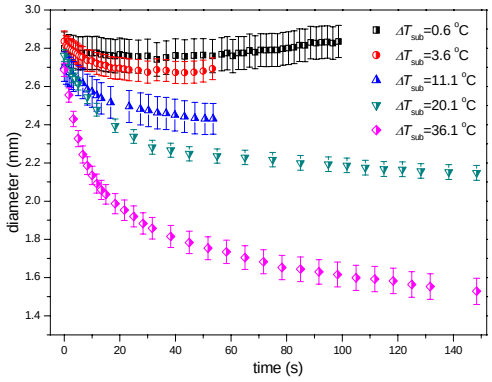

Figure D-4. FC-72 bubble diameter measurements between subcooled plates, plates gap = 250 μm

D.2 Single bubble growth during flow boiling in micro-channels: results of ethanol

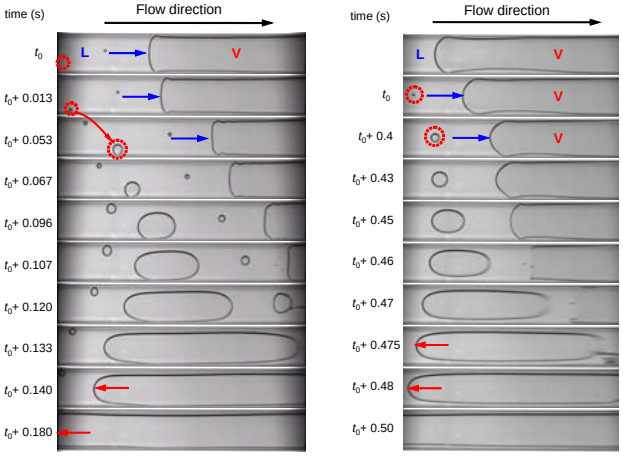

Figure D-5. Bubble growth visualization results in 1454 µm channel, (a) side-wall bubble at G = 22.4 kg·m^{-2}·s^{-1} and q = 12.0 kW·m^{-2}, (b) centre bubble at G = 11.2 kg·m^{-2}·s^{-1} and q = 9.0 kW·m^{-2}, ethanol

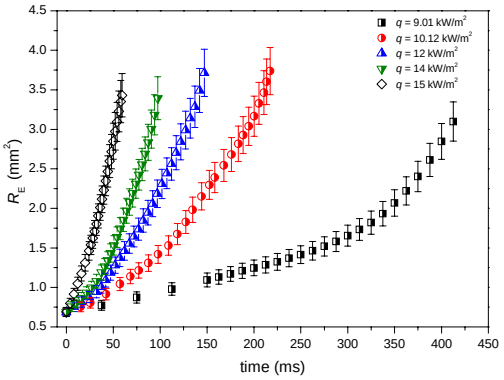

Figure D-6. Bubble equivalent radius at different heat fluxes in 1454 µm channel, G = 22.4 kg·m^{-2}·s^{-1}, ethanol

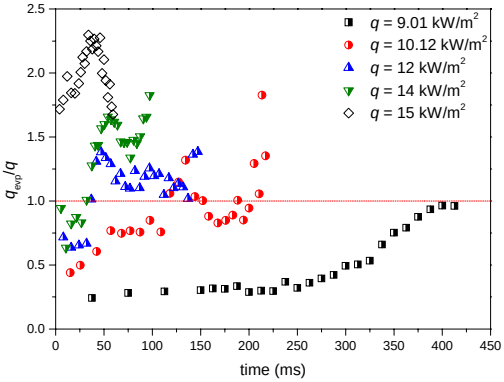

Figure D-7. Bubble evaporation heat flux at different heat fluxes in 1454 µm channel, G = 22.4 kg·m^{-2}·s^{-1}, ethanol

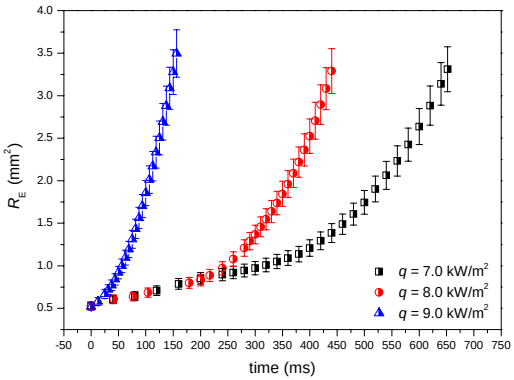

Figure D-8. Bubble equivalent radius at different heat fluxes in 1454µm channel, G = 11.2 kg·m^{-2}·s^{-1}, ethanol

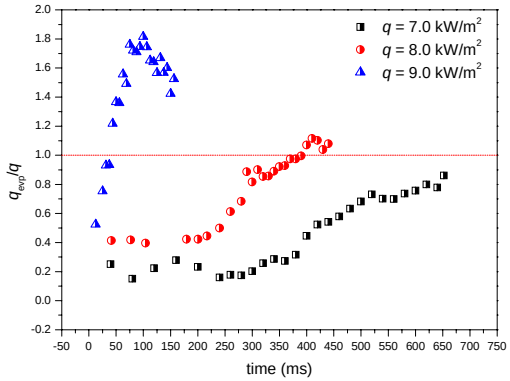

Figure D-9. Bubble evaporation heat flux at different heat fluxes in 1454 µm channel, G = 11.2 kg·m^{-2}·s^{-1}, ethanol

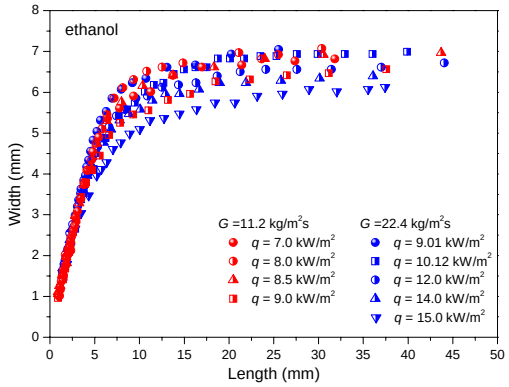

Figure D-10. Bubble width versus length during flow boiling in the 1454 µm channel, G = 11.2 kg·m^{-2}·s^{-1} and 22.4 kg·m^{-2}·s^{-1}, ethanol

Publications

Journals

Y. Wang, K. Sefiane, R. Bennacer; *"Investigation of Boiling and Bubble Confinement in A High Aspect Ratio Micro-Channel"*, Applied Thermal Engineering, **31**, 610-618, 2011

Y. Wang, K. Sefiane; *"Confined Bubble and Heat Transfer during Flow Boiling In a High Aspect Ratio Mini-Channel"*, Defect and Diffusion Forum, **312-315**, 548-553, 2011

Conferences

Y. Wang, K. Sefiane; *"Confined bubble and heat transfer in high aspect ratio micro-channel during saturated flow boiling"*, 6th International Conference on Diffusion in Solids and Liquids:Mass Transfer, Heat Transfer and Microstructure and Properties,05-07 JULY, 2010 / Paris - FRANCE

Y. Wang, K. Sefiane, R. Bennacer; *"Pressure Drop and Two Phase Flow during Boiling of FC-72"*, the 14th International Heat Transfer Conference (IHTC), Washington D.C. from August 7-13, 2010, USA, IHTC14-23336

Y. Wang, K. Sefiane, J. Barber, S.K. Wilson; *"Investigation of a Single Vapour Bubble Confined Between Superheated or Subcooled Parallel Plates"*, 2nd Micro and Nano Flows Conference MNF2009, 1 – 2 September, Brunel University, West London, UK, 2009, ISSN ISBN:978-1-902316-7

Book

Y. Wang, K. Sefiane, S. Harmand, R. Bennacer; *"Two-Phase Flow and Heat Transfer in Micro-Channels and Their Applications in Micro-System Cooling, in Heat and Mass Transfer in Porous Media"*, 2011